

THE UNIVERSITY OF HULL

**Pyridine Assisted CO<sub>2</sub> Reduction to Methanol at  
High Pressure**

Being a Thesis submitted for the Degree of

*Doctor of Philosophy (PhD)*

in the University of Hull

by

Dalila Touhami

BSc. MSc.

September 2015

## ABSTRACT

Significant research efforts have been directed towards exploring electrocatalysts for the selective reduction of CO<sub>2</sub> to fuels such as methanol. Bocarsly et al (Princeton University) have recently reported the use of aromatic amines (e.g. pyridine (C<sub>5</sub>H<sub>5</sub>N)) as electrocatalysts in aqueous electrolytes for the reduction of CO<sub>2</sub> at low overpotentials (50-150 mV). Importantly, the CO<sub>2</sub>-pyridine reduction process was claimed to selectively produce methanol with Faradaic efficiencies of ~100% on p-GaP electrode and 22-30% on Pt and Pd electrodes. Moreover, the initially proposed mechanism based on a radical intermediate interaction with CO<sub>2</sub> as a key step toward the production of methanol was subsequently disproved. In this project, methanol formation by the CO<sub>2</sub>-pyridine (C<sub>5</sub>H<sub>5</sub>N) system was assessed by conducting electrolysis under various conditions at platinum electrodes. High pressure CO<sub>2</sub> was used with the aim of increasing the methanol yield. In the course of the present study, the bulk electrolysis confirmed the methanol production at 1 bar and at 55bar of CO<sub>2</sub> in the presence of pyridine. However, the methanol yield was found to be persistently limited to sub-ppm level (<1ppm) under all conditions investigated. The observed methanol yield limitation could not be overcome by the electrode reactivation techniques used. Moreover, the methanol formation seemed unaffected by the current density or the biasing mode. This was an indication of the independence of methanol production from the charge transfer on the electrode. In agreement with these observations, analysis of the voltammetric data supported by simulation revealed that the CO<sub>2</sub>-pyridine reduction system is mainly pyridinium assisted molecular hydrogen production under all conditions investigated. In particular, protonated pyridine (C<sub>5</sub>H<sub>5</sub>N) 'pyridinium' was confirmed to behave as a weak acid on platinum. It was found that CO<sub>2</sub> is merely a proton source of pyridine reprotonation via the hydration reaction followed by carbonic acid dissociation. The reprotonation reaction coupled to the electrode reaction ultimately leads to the dihydrogen production. No direct contribution of CO<sub>2</sub> in the reduction process was observed. The production of methanol seems to occur chemically rather than directly driven by the charge transfer on the electrode. The role of pyridine (C<sub>5</sub>H<sub>5</sub>N) appears to be restricted to assisting in the generation of the hydrogen necessary for the alcohol production.

## **ACKNOWLEDGEMENTS**

I am deeply indebted to my research advisors Dr Sergey Rybchenko and Prof Stephanie Haywood for their constant encouragement, thought provoking discussions and guidance at every stage of the research programme. I am privileged to have been associated with them. I thank them for their patient guidance, open discussions, constant encouragement, unbounded enthusiasm and interest.

I express my sincere thanks to Dr Jay Wadhawan for his support, advice and the facilities provided in carrying out this project. I gratefully acknowledge the departmental financial support (fee waiver) for this research project. The experience I gained during my study at Hull University will always be remembered. I would also like to thank the Engineering and Chemistry departments staff for their support and assistance.

Last but not least I owe everything to my parents and sisters for their constant support, encouragement and continuous prayers, without them it would have been impossible for me to complete this work.

# TABLE OF CONTENTS

<b>ABSTRACT</b>	<b>I</b>
<b>ACKNOWLEDGEMENTS</b>	<b>II</b>
<b>TABLE OF CONTENTS</b>	<b>III</b>
<b>LIST OF TABLES</b>	<b>VI</b>
<b>LIST OF FIGURES</b>	<b>VIII</b>
<b>LIST OF SYMBOLS</b>	<b>XVI</b>
<b>GREEK SYMBOLS</b>	<b>XVIII</b>
<b>ABBREVIATIONS</b>	<b>XIX</b>
<b>CHAPTER 1 INTRODUCTION</b>	<b>1</b>
<b>CHAPTER 2 BACKGROUND THEORY</b>	<b>9</b>
<b>2.1 Introduction</b>	<b>9</b>
<b>2.2 Equilibria</b>	<b>9</b>
2.2.1 Chemical Equilibrium	9
2.2.2 Electrochemical Equilibrium	10
<b>2.3 Electrochemical Cells</b>	<b>14</b>
2.3.1 Types of Electrochemical Cells	14
2.3.2 Three Electrode Set Up	14
2.3.3 Electrolyte solutions	17
<b>2.4 Mass Transfer</b>	<b>18</b>
2.4.1 Migration	18
2.4.2 Diffusion	19
2.4.3 Convection	21
<b>2.5 Electrode – Solution Interface</b>	<b>22</b>
2.5.1 Electrical Double Layer	22
<b>2.6 Electrochemical Kinetics</b>	<b>25</b>
2.6.1 Arrhenius Equation	26
<b>2.7 Butler-Volmer Model of Electrode Kinetics</b>	<b>28</b>

<b>2.8 Electroanalytical Techniques</b>	<b>31</b>
2.8.1 Cyclic Voltammetry (CV)	31
2.8.2 Potential Step Chronoamperometry (CA)	44
2.8.3 Gas Chromatography (GC)	45
2.8.4 Mass Spectrometry (MS)	46
2.8.5 Headspace Gas Chromatography (HSGC)	48
2.8.6 GCMS Analysis Method	48
<b>CHAPTER 3 OVERVIEW OF THE RECENT LITERATURE</b>	<b>53</b>
<b>3.1 Electrochemical CO<sub>2</sub> Reduction</b>	<b>53</b>
3.1.1 Direct Electrochemical CO <sub>2</sub> Reduction	56
3.1.2 Catalytic Electrochemical Reduction of CO <sub>2</sub>	62
3.1.3 Reduction of Nitrogen-Heterocycles: Pyridine and Derivatives	74
3.1.4 Summary	77
<b>CHAPTER 4 EXPERIMENTAL METHODS AND TECHNIQUES</b>	<b>86</b>
<b>4.1 High Pressure Experimental Setup</b>	<b>86</b>
4.1.1 High Pressure Vessel	87
4.1.2 CO <sub>2</sub> Pump and Back Pressure Regulator (BRP)	93
4.1.3 Potentiostat	95
<b>4.2 Reaction Cells for Ambient Pressure</b>	<b>95</b>
4.2.1 Experimental Specification and Conditions	95
<b>4.3 Electrodes</b>	<b>96</b>
4.3.1 Working Electrodes (WE)	97
4.3.2 Counter Electrodes (CE)	99
4.3.3 Reference Electrodes (RE)	100
<b>4.4 Reagents</b>	<b>103</b>
<b>4.5 Product Analysis by Gas Chromatography-Mass Spectrometry (GCMS) in Selected Ion Monitoring (SIM) Mode</b>	<b>104</b>
4.5.1 Method Development	104
<b>4.6 Numerical Simulations of Cyclic Voltammograms</b>	<b>121</b>
<b>CHAPTER 5 IONIC EQUILIBRIA OF PYRIDINE-CO<sub>2</sub> SYSTEM</b>	<b>123</b>
<b>5.1 Calculation of Ionic Species Concentrations in Aqueous Pyridine Solution</b>	<b>123</b>
<b>5.2 Calculation of Ionic Species in the Pyridine-Acid System</b>	<b>125</b>
5.2.1 Concentration of Pyridine Species in the Presence of a Strong Acid	125
5.2.2 Concentration of Pyridine and CO <sub>2</sub> Species at elevated CO <sub>2</sub> pressure	128
<b>CHAPTER 6 PYRIDINIUM BEHAVIOUR AT PLATINUM ELECTRODE IN THE ABSENCE AND THE PRESENCE OF CO<sub>2</sub></b>	<b>135</b>

<b>6.1 Introduction</b> .....	<b>135</b>
6.1.1 Review of the CO <sub>2</sub> -Pyridine Mechanistic Picture .....	135
<b>6.2 CV Studies in the Absence of CO<sub>2</sub></b> .....	<b>139</b>
6.2.1 Cyclic Voltammetry of Pyridinium at Platinum Electrodes .....	139
6.2.2 pH Dependence Study of the Pyridinium System .....	151
<b>6.3 CV Studies in the Presence of CO<sub>2</sub></b> .....	<b>157</b>
6.3.1 Current Enhancement at Atmospheric Pressure (1 bar of CO <sub>2</sub> ) .....	157
6.3.2 Effect of High Pressure CO <sub>2</sub> on Pyridinium Voltammetric Behaviour at Platinum .....	164
<b>6.4 Summary</b> .....	<b>172</b>
<b>CHAPTER 7 PYRIDINIUM ASSISTED CO<sub>2</sub> REDUCTION ON PT ELECTRODE AT 1BAR AND 55 BAR</b> .....	<b>177</b>
<b>7.1 Introduction</b> .....	<b>177</b>
<b>7.2 Optimization of the Experimental Conditions</b> .....	<b>179</b>
7.2.1 Effect of RE and CE Electrodes Isolation .....	179
7.2.2 Effect of Pyridine Purity on the Electrolysis .....	183
7.2.3 Effect of Electrolyte Purification (Pre-Electrolysis) .....	184
<b>7.3 Results and Discussion</b> .....	<b>186</b>
7.3.1 Direct Electrolysis of CO <sub>2</sub> (in the absence of pyridine) at 55bar .....	186
7.3.2 CO <sub>2</sub> -Pyridine Reduction at 1bar: Alcohol Faradaic Yields (FY) .....	190
7.3.3 CO <sub>2</sub> -Pyridinium Reduction at High Pressure: Alcohol Faradaic Yields (FY) .....	196
<b>CONCLUSIONS</b> .....	<b>216</b>
<b>APPENDIX A</b> .....	<b>219</b>
<b>APPENDIX B</b> .....	<b>223</b>
<b>APPENDIX C</b> .....	<b>225</b>
<b>APPENDIX D</b> .....	<b>228</b>

## LIST OF TABLES

<i>Table 2.1 Cation fragments of methanol (CH<sub>3</sub>OH) detected in MS system</i> .....	46
<i>Table 3.1 Reduction potential and formation energy for various CO<sub>2</sub> reduced products (Aresta 2003, p. 279)</i> .....	54
<i>Table 3.2 Reduction potential and energy stored per mole of CO<sub>2</sub> for various products and water reduction processes</i> .....	55
<i>Table 3.3 Metal electrode reductions of CO<sub>2</sub> in aqueous electrolyte, grouped by reduction product (Adapted from Hori, et al)</i> .....	58
<i>Table 3.4 Summary of methanol production by electrochemical or photoelectrochemical reduction of CO<sub>2</sub> on several metals and materials</i> .....	65
<i>Table 4.1 Compounds with their most abundant ions</i> .....	108
<i>Table 4.2 Headspace (HS) selected ion monitoring gas chromatography (SIM GC) initial conditions for the method development</i> .....	110
<i>Table 4.3 GCMS Manual Headspace Methods</i> .....	113
<i>Table 4.4 HS SIM GCMS operating conditions</i> .....	114
<i>Table 4.5 SIM GCMS operating conditions for liquid injections</i> .....	116
<i>Table 4.6 Retention time of the target compounds</i> .....	116
<i>Table 4.7 Calculated GC peak areas of standard methanol concentrations</i> .....	118
<i>Table 4.8 LOD and LOQ concentrations for target analytes</i> .....	119
<i>Table 5.1 Pyridinium and non-protonated pyridine (C<sub>5</sub>H<sub>5</sub>N) concentrations at pH5.5 for pyridine range 5-200mM of concentration (C) (calculated data)</i> .....	128
<i>Table 5.2 Pyridinium <b>PyH</b> + and non-protonated pyridine [Py] concentrations in 0-7 pH range in 10mM total pyridine (C<sub>5</sub>H<sub>5</sub>N) concentration (calculated data)</i> .....	128
<i>Table 5.3 Carbon dioxide constants at 20°C and 25°C (1 bar) (Butler 1991)</i> .....	130
<i>Table 5.4 CO<sub>2</sub> concentrations (M) at different pressure at 20°C and 25°C (calculated using Diamond program)</i> .....	131
<i>Table 5.5 Species concentrations in 10mM of pyridine containing solutions saturated with CO<sub>2</sub> at different pressure (1-55bar)</i> .....	133
<i>Table 6.1 Diffusion coefficient calculated at scan rates ≤500mV/s obtained from the plot of the cathodic peak current as a function of the square root of the scan rate (I<sub>p</sub> vs. v)</i> .....	144

<i>Table 6.2 Diffusion coefficient calculated at different pyridine concentration obtained from the plot of the cathodic current as a function of pyridinium concentration (<b><i>I<sub>pvs</sub></i></b>[<b><i>PyH</i></b><sup>+</sup>]).....</i>	<i>145</i>
<i>Table 6.3 Apparent chemical and kinetic parameters used in the CV simulations.....</i>	<i>150</i>
<i>Table 6.4 Species concentrations in 3mM pyridine-CO<sub>2</sub> system .....</i>	<i>161</i>
<i>Table 6.5 Pyridinium and CO<sub>2</sub> concentrations in 10mM pyridine-containing aqueous solution at 20°C and varying pressure .....</i>	<i>166</i>
<i>Table 6.6 Simulation parameter (<math>E^{0\text{ app}}_{\text{H}^+/\text{H}}</math>, <math>k_S = 0.3</math>, <math>\alpha = 0.5</math>) for CV data at 55 bar of CO<sub>2</sub> and different analytical concentrations of pyridine. ....</i>	<i>167</i>
<i>Table 7.1 Methanol Faradaic efficiencies for electrolyses at controlled potential of 10mM pyridine in 0.5M KCl under CO<sub>2</sub> (1 bar, 25°C) at Pt 2.6cm<sup>2</sup> .....</i>	<i>192</i>

## LIST OF FIGURES

<i>Figure 2.1 The electronic energy diagram in metal electrode –solution (a) before electron transfer (b) after electron transfer (Compton Richard G 2010)</i>	11
<i>Figure 2.2 (a) An electrolytic electrochemical cell, (b) A galvanic electrochemical cell (Zoski 2007)(Bard &amp; Faulkner 2002)</i>	14
<i>Figure 2.3 Simulated cyclic voltammograms of a simple E reaction at planar electrode (1cm<sup>2</sup>) and 100mV/s (DigiSim.3.03) showing the effect of capacity and solution resistance. (a) reversible cyclic voltammogram, (b) with effect of capacity, and (c) with additional resistance, R=10Ω.</i>	15
<i>Figure 2.4 Schematic diagram of mass transfer modes at an electrode surface (Compton Richard G 2010)</i>	18
<i>Figure 2.5 Effect of the electrode geometry on the shape of reversible cyclic voltammograms and schematic drawings of the corresponding transition from a planar semi-infinite to a spherical diffusion (Compton Richard G 2010) (Scholz 2010).</i>	20
<i>Figure 2.6 Schematic diagram of an electric double layer between an electrolyte and a cathode (metal). Where x is the distance between the two. IHP is inner Helmholtz plane and OHP is outer Helmholtz plane (Zoski 2007).</i>	22
<i>Figure 2.7 The distance of closest approach, a, for an ion i and an atmosphere ion j, and the Debye length, 1/κ radius of the ion atmosphere (Bard &amp; Faulkner 2002).</i>	25
<i>Figure 2.8 Energy potential variation adopted from Bard and Faulkner (Bard &amp; Faulkner 2002)</i>	27
<i>Figure 2.9 Schematic diagram of Butler-Volmer kinetics: a detailed view of the potential effect on free activation energies (Bard &amp; Faulkner 2002)(Wang 2006)</i>	29
<i>Figure 2.10 Triangular cyclic voltammetric form. The slope designate the scan rate (V/s)(Bockris et al. 2001)</i>	31
<i>Figure 2.11 A representative cyclic voltammogram</i>	32
<i>Figure 2.12 Cyclic voltammogram (a) reversible, (b) quasi-reversible , and (c) irreversible system (Zoski 2007)</i>	36
<i>Figure 2.13 Normalised voltammograms for E<sub>rev</sub> C<sub>rev</sub> reaction for different values of kinetic parameter psi ( <math>\psi = \mathbf{Ka/l}</math> )(Nicholson &amp; Shain 1964)</i>	39

<i>Figure 2.14 Nicholson and Shain criteria for <math>E_{rev}C_{rev}</math>. (a) Ratio of anodic to cathodic current as function of kinetic parameters. (b) Variation of the peak potential as function of kinetic parameters <math>Ka/l</math> and <math>\psi = Ka/l</math> (Nicholson &amp; Shain 1964)</i>	40
<i>Figure 2.15 Normalised voltammograms for <math>E_{rev}C_{irrev}</math> reaction for different values of <math>k_f/a</math> (Nicholson &amp; Shain 1964).</i>	41
<i>Figure 2.16 Nicholson and Shain criteria for <math>E_{rev}C_{irrev}</math>. Ratio of anodic to cathodic current as function of the kinetic parameters (Nicholson &amp; Shain 1964).</i>	41
<i>Figure 2.17 Normalised voltammograms to the scan rate for EC' catalytic reaction (Nicholson &amp; Shain 1964)</i>	43
<i>Figure 2.18 Nicholson and Shain criteria for EC' catalytic. (a) Ratio of kinetic to diffusive current as function of kinetic parameters. (b) Variation of the peak potential as function of kinetic parameters (Nicholson &amp; Shain 1964).</i>	44
<i>Figure 2.19 Schematic representation of chronoamperometry (a) Potential variation as function of time, (b) current variation as function of time.</i>	45
<i>Figure 2.20 Characteristic methanol (<math>CH_3OH</math>) cations mass spectrum</i>	47
<i>Figure 2.21 Signal-to-noise examples of (a) 10:1 and (b) 3:1 (Shrivastava &amp; Gupta 2011)</i>	50
<i>Figure 3.1 Qualitative reaction scheme for <math>CO_2</math> conversion. Catalysts and electrolytes acting as co-catalysts can lower the energy of the intermediate and thus improve the energetic efficiency of the conversion. (Redrawn from Whipple and Kens review)(Whipple &amp; Kenis 2010)</i>	62
<i>Figure 3.2 Bocarsly initial mechanism of <math>CO_2</math> reduction to methanol via pyridinyl formation (Barton et al. 2008)</i>	70
<i>Figure 4.1 Schematic diagram of the high pressure set up</i>	86
<i>Figure 4.2 Schematic diagram of the glass liner (inserted in the high pressure vessel) with the three electrode arrangement</i>	88
<i>Figure 4.3 Section view 2D drawing of the high pressure vessel (design by Parr<sup>®</sup>)</i>	91
<i>Figure 4.4 Parr<sup>®</sup> high pressure vessel, left close view of the vessel cap</i>	92
<i>Figure 4.5 PTFE electrode holder inserted in the glass liner(100ml)</i>	92
<i>Figure 4.6 <math>CO_2</math> Liquid Delivery Pump JASCO<sup>®</sup> (PU-2080-<math>CO_2</math>)</i>	93
<i>Figure 4.7 Back Pressure Regulator JASCO<sup>®</sup> (PB-2080)</i>	95
<i>Figure 4.8 Glass reaction cells used in the ambient pressure experiments</i>	96
<i>Figure 4.9 Schematic diagram of macro-electrode Metrohm<sup>®</sup> Pt disk</i>	97

<i>Figure 4.10 Schematic diagram of the home-made working electrode: Pt wire electrode.</i>	98
<hr/>	
<i>Figure 4.11 Schematic diagram of a near micro- size electrode</i>	99
<i>Figure 4.12 Schematic diagram of Metrohm<sup>®</sup> glassy carbon electrode (2D drawing)</i>	99
<i>Figure 4.13 Schematic diagram of Russel<sup>®</sup> saturated calomel electrode (SCE)</i>	101
<i>Figure 4.14 Schematic diagram of Metrohm<sup>®</sup> Silver/Silver Chloride electrode (2D drawn)</i>	102
<hr/>	
<i>Figure 4.15 Equilibrium concentrations of methanol in the headspace as function of the initial liquid samples volume</i>	107
<i>Figure 4.16 Mass spectrum of isopropanol (C<sub>3</sub>H<sub>8</sub>O)</i>	107
<i>Figure 4.17 Chromatogram of methanol, ethanol, isopropanol, butanol, and pyridine peaks and their corresponding elution time</i>	108
<i>Figure 4.18 Chromatograms of methanol (500µg/l, 5ppm) run on (a) method 1 and (b) method 3 described in Table 4.3.</i>	109
<i>Figure 4.19 Effect of pressure on the peak height and retention time of air (first peak) and methanol (second peak)</i>	111
<i>Figure 4.20 Effect of initial column temperature on peak height and retention time of</i>	111
<hr/>	
<i>Figure 4.21 Effect of the initial column temperature on methanol peak shape</i>	112
<i>Figure 4.22 Repeatability of three injection replicas of three different methanol concentrations (a) 500µg/l (0.5ppm), (b) 2000µg/l (2ppm), and (c) 5000µg/l (5ppm)</i>	117
<i>Figure 4.23 Methanol Limit of Detection (LOD)</i>	118
<i>Figure 4.24 Methanol Limit of Quantification</i>	119
<i>Figure 4.25 Chromatograms of butanol standard samples at 300, 400, 500 and 1000µg/l</i>	120
<hr/>	
<i>Figure 4.26 Calibration graphs of the alcohols: (a) methanol, (b) ethanol, (c) Isopropanol and (d) butanol. A: is the corrected area of the relevant alcohol to pyridine area ratio. Error bars were estimated form repeatability of three injections replica for each concentration within each alcohol</i>	121
<i>Figure 5.1 Ionic species equilibrium concentrations of protons and pyridine/pyridinium in 10mM of total pyridine concentration as function of pH in the range 0-7 (calculated data)</i>	127

<i>Figure 5.2 Ionic species equilibrium concentrations of protons, pyridine species and carbonic acid in pyridine (<math>10^{-10}</math>-1M) aqueous solutions at 20°C and 55bar of CO<sub>2</sub></i>	132
<i>Figure 6.1 Bocarsly's Model: Scheme of the initially proposed mechanism of pyridinium assisted CO<sub>2</sub> reduction to methanol on Pt electrode. The key step of this mechanism is the radical formation (Reaction 2).(Barton Cole et al. 2010)</i>	136
<i>Figure 6.2 Savéant's Model: Scheme of the mechanism proposed of pyridinium catalytic role for HER in the presence of CO<sub>2</sub> on Pt electrode. HA: acid (Costentin et al. 2013)</i>	137
<i>Figure 6.3 Bocarsly-Barista Model: Scheme of the newly proposed reaction pathways for the CO<sub>2</sub>-pyridinium reduction system on Pt electrode. HA: acid (Barton Cole et al. 2014)</i>	138
<i>Figure 6.4 Scan rate dependence CVs of 10mM pyridine in 0.5M KCl (at pH 5.5) on Pt electrode (0.07cm<sup>2</sup>) at 10-2000 mV/s. Inset: Cathodic current as function of the square root of the scan rate (10-500mV/s).</i>	140
<i>Figure 6.5 The ratio of the anodic peak current to the cathodic peak current (<b>I<sub>pa</sub>/I<sub>pc</sub></b>) as function of the scan rate (mV/s) for the 10mM pyridine dataset under N<sub>2</sub></i>	143
<i>Figure 6.6 CV of Pyridine in 0.5 KCl solution at pH = 5.5. (top) 10mM, (bottom) 50mM at 10, 100, and 1000mV/s . Experiment (a and c), simulation (b and d) (Model of Scheme 6.5)</i>	149
<i>Figure 6.7 Cathodic peak current of CVs at different pyridine concentrations and scan rates in 0.5M KCl solution at pH = 5.5. Under N<sub>2</sub>. Circles - experiment, lines - simulation.</i>	151
<i>Figure 6.8 Cyclic voltamograms of 10mM pyridine in 0.5M KCl under N<sub>2</sub> at 100mV/s. The acidity varies between pH 2.0-5.3. (a) experiment, (b) simulation. Horizontal arrows- scanning direction, vertical arrow- pH increment</i>	153
<i>Figure 6.9 Peak current of 10mM pyridine in 0.5MKCl at 100mV/s as function of protons concentration (a) experimental, (b) simulation. Inset: Peak current of protons as function of the proton concentration</i>	154
<i>Figure 6.10 Simulated peak current as function of pyridine concentration at pH1-7</i>	154
<i>Figure 6.11 CVs under N<sub>2</sub> hydrochloric acid (HCl) adjusted pH at 100mV/s: (a) CV of ~10μM pyridine at pH 3, (b) CV with no pyridine at pH 5</i>	155
<i>Figure 6.12 Pourbaix diagram for 10mM analytical pyridine concentration</i>	156

<i>Figure 6.13 CVs of 10mM pyridine in 0.5MKCl at atmospheric pressure 1bar and 20°C (blue) under N<sub>2</sub>, (green) under CO<sub>2</sub> at (a) 5mV/s, (b) 50mV/s and (c) 500mV/s on Pt disk (100µm diameter).</i>	158
<i>Figure 6.14 Plot of the cathodic peak current under CO<sub>2</sub> and under N<sub>2</sub> at 100mM pyridine and Pt disk (100µm diameter)</i>	159
<i>Figure 6.15 Cyclic voltammograms of: 10mM pyridine under CO<sub>2</sub> pH5.3 (dashed line), 10mM pyridine under N<sub>2</sub> adjusted using HCl to pH5.3 (grey), CO<sub>2</sub> in the absence of pyridine pH 4(black) (a) 500mV/s, and (b) 5mV/s collected on Pt (0.07cm<sup>2</sup>).</i>	163
<i>Figure 6.16 CV of ~10µM pyridine in 0.5M KCl aqueous electrolyte in the presence of CO<sub>2</sub> at 55bar and 10mV/s</i>	164
<i>Figure 6.17 CV waves of 10mM pyridine in 0.5M KCl at 5mV/s at CO<sub>2</sub> saturated electrolyte (1-55 bar range). Inset: reduction peak/limiting current versus CO<sub>2</sub> pressure (for the same data series as shown on the main graph). Line-simulation, dots-cathodic peak current. Positive values represent the reduction in this case.</i>	165
<i>Figure 6.18 Cathodic peak current as function of pyridine total concentration for CVs at 55 bar CO<sub>2</sub>. Dots - experiment, lines - simulation</i>	168
<i>Figure 6.19 CVs of ~10µM pyridine at 55bar of CO<sub>2</sub> on Pt 0.07cm<sup>2</sup> at 300-5000mV/s scan rates. Pre-peaks preceding the usual CV wave are observed at -0.32±0.02V</i>	169
<i>Figure 6.20 Normalised cyclic voltammograms by the square root of the scan rate on Pt 0.07cm<sup>2</sup> at 55 bar CO<sub>2</sub> of (a and b) 10mM pyridine, (c and d) 100mM pyridine at 1000mV/s (blue), 100mV/s (red), and 10mV/s (black). Left images - experiment, right - simulation. Positive values of the current represent reduction in this case.</i>	170
<i>Figure 6.21 Nicholson and Shain criteria for EC' mechanism. The variation of the half peak potential with log λ. λ=k<sub>f</sub>/a, with a = nFv/RT. line-Nicholson characteristic curve for EC', symbols-this work data. (k<sub>f</sub> is the forward rate)</i>	171
<i>Figure 7.1 Cyclic voltammogram of 10mM pyridine in 0.5M KCl with a glass frit isolation on WE: Pt foil (7cm<sup>2</sup>).</i>	180
<i>Figure 7.2 Effect of the counter electrode isolation on the electrolysis (-0.5V) current. Electrolyte: 10mM pyridine in 0.5M KCl. Conditions: in the presence of CO<sub>2</sub> (1bar,25°C). WE: Pt foil, 7cm<sup>2</sup></i>	182
<i>Figure 7.3 Effect of electrolyte purity on electrolysis current (-0.7V). Electrolyte: 10mM pyridine in 0.5M KCl. Conditions: in the presence of CO<sub>2</sub> (1bar, 25°C). WE: on Pt foil, 7cm<sup>2</sup></i>	183

- Figure 7.4 Effect of electrolytic electrolyte purification at (-0.7V). (Blue) without prior pre-electrolysis effect, (Black) with pre-electrolysis. Electrolyte: 10mM pyridine in 0.5M KCl. Conditions: in the presence of CO<sub>2</sub>(1bar, 25°C). WE: on Pt ,ca. 2.8 x10<sup>4</sup>A/cm<sup>2</sup> \_\_\_\_\_ 185
- Figure 7.5 Direct electrochemical CO<sub>2</sub> reduction (55bar,25°C): Cyclic voltammograms at 100mV/s in 0.5M KCl at Pt wire (2.6cm<sup>2</sup>) (a) cathodic CV wave before electrolysis, (b) Chronoamperometry (-0.7V) of direct CO<sub>2</sub>, (c) cathodic CV wave after electrolysis and (d) anodic CV wave. Horizontal arrows illustrate the scanning direction. Vertical arrows show the voltammetric cycling direction. \_\_\_\_\_ 187
- Figure 7.6 Direct CO<sub>2</sub> electrolysis at -0.7V in initially acidic electrolyte (becoming basic electrolyte after CO<sub>2</sub> supply cut off) at Pt wire (2.6cm<sup>2</sup>) electrode. Inset: anodic CV wave after electrolysis (55bar, 25°C) \_\_\_\_\_ 189
- Figure 7.7 Chronoamperometric (potentiostatic) measurements at: -0.5V, -0.6V and -0.7V. Electrolyte: 10mM pyridine, 0.5 M KCl aqueous solution. Conditions: 25°C and 1bar CO<sub>2</sub>. WE: Pt wire 2.6cm<sup>2</sup>. Inset on the right: A typical cyclic voltamogram recorded before the electrolysis at 100mV/s. Inset on the left: Detailed view of the electrolysis at -0.5V. \_\_\_\_\_ 191
- Figure 7.8 Methanol Faradaic yields and their corresponding concentrations as a function of time in potentiostatic electrolysis -0.7V: Red –Methanol concentrations (ppm), Black – Methanol Faradaic yield (%). Electrolyte: 10mM pyridine, 0.5M KCl aqueous solution. Conditions: 25°C and 1bar CO<sub>2</sub>. LOD – limit of detection. \_\_\_\_\_ 193
- Figure 7.9 Methanol Faradaic efficiencies and their corresponding concentrations as a function of the passed charge: current densities ~0.4-1.3 mA/cm<sup>2</sup>. Electrolyte: 10 mM pyridine, 0.5 M KCl aqueous solution. Conditions: 25°C and 1bar CO<sub>2</sub>. WE:Pt (3.8cm<sup>2</sup>). LOD-limit of detection \_\_\_\_\_ 194
- Figure 7.10 Alcohol concentrations (ppm) as function of the passed charge in potentiostatic electrolysis -0.7V: black –MeOH concentrations, Red–ethanol (C<sub>2</sub>H<sub>6</sub>O) and Green–isopropanol. Electrolyte: 10mM pyridine, 0.5 M KCl aqueous solution. Conditions: 25°C and 1bar CO<sub>2</sub>. WE: Pt (3.8cm<sup>2</sup>). LOD – limit of detection. \_\_\_\_\_ 195
- Figure 7.11 Chronoamperometric (potentiostatic) electrolyses: -0.5-0.7V. Electrolyte: 10mM pyridine, 0.5M KCl aqueous solution. Conditions: 25°C and 55bar CO<sub>2</sub>. WE: Pt 3cm<sup>2</sup>. \_\_\_\_\_ 196

Figure 7.12 Methanol Faradaic yields and concentrations as function of the reduction potential in potentiostatic electrolysis: blue – MeOH concentrations (ppm), Black – MeOH Faradaic yield (%). Electrolyte: 10mM pyridine, 0.5 M KCl aqueous solution. Conditions: 25°C and 55bar CO<sub>2</sub>. Error bars indicate data scatter over three experiments at -0.7V. Other data represent single experimental runs. \_\_\_\_\_ 197

Figure 7.13 Methanol Faradaic yields and the corresponding concentrations as function of the passed charge for fixed cathodic current: circles – 0.05mA/cm<sup>2</sup>, squares – 0.5mA/cm<sup>2</sup>. Electrolyte: 50mM pyridine, 0.5M KCl aqueous solution. Conditions: 25°C and 55bar CO<sub>2</sub>. Error bars are estimated from the errors in the GCMS analysis \_\_\_\_\_ 198

Figure 7.14 Methanol concentrations (ppm) as function of analytical pyridine concentration. Electrolyte: 0.5M KCl. Accumulation charge ≥9 C. Conditions: 25°C and 55bar CO<sub>2</sub>. Each symbol represents individual experiment: open circles – potentiostatic electrolysis at - 0.5-0.8V; filled circles – galvanostatic electrolysis at 50μA/cm<sup>2</sup> and 1.5mA/cm<sup>2</sup>. LOD – limit of detection. \_\_\_\_\_ 199

Figure 7.15 Alcohols yields (ppm) as function of the analytical pyridine concentrations. Electrolyte: 0.5M KCl. Accumulation charge ≥9 C. Conditions: 25°C and 55bar CO<sub>2</sub>. Each symbol represents Faradaic yield of the alcohol: open circles – potentiostatic electrolysis at - 0.5-0.8V; filled circles – galvanostatic electrolysis at 50μA/cm<sup>2</sup> and 1.5mA/cm<sup>2</sup>. Red-ethanol, Green- isopropanol and Blue-butanol concentrations (ppm). LOD – limit of detection. \_\_\_\_\_ 200

Figure 7.16 Alcohol Faradaic yields as function of the charge at analytical pyridine concentration of the range (5μM to 1M). Electrolyte: 0.5 M KCl aqueous solution. Accumulation charge ≥9 C. Conditions: 25°C and 55bar CO<sub>2</sub>. Each symbol represents total Faradaic yield of the alcohol specified: Red-ethanol, Green- isopropanol and Blue-butanol. \_\_\_\_\_ 201

Figure 7.17 Total alcohol Faradaic yields as function of the charge at analytical pyridine concentration (0.5μM to 1M). Electrolyte: 0.5 M KCl aqueous solution. Accumulation charge ≥9 C. Conditions: 25°C and 55bar CO<sub>2</sub>. Each symbol represents total Faradaic yield at each experiment: open circles – potentiostatic electrolysis; filled circles – galvanostatic electrolysis. LOD – limit of detection. \_\_\_\_\_ 202

Figure 7.18 Potentiostatic electrolysis at -0.7 V at Pt electrode, showing current variation with time. Inset on the right: Cyclic voltammograms: Blue curve– before the

*electrolysis, red curve—after electrolysis and Green curve—after the anodic stripping at +0.5V. Inset on the right: anodic wave. Electrolyte: 10mM of pyridine in 0.5M KCl. Conditions: 55bar of CO<sub>2</sub> at 25°C. Horizontal arrows illustrate the scanning direction.*

205

*Figure 7.19 Potentiostatic electrolysis at -0.7V with periodic anodic biasing as function of time. Electrolyte: 10mM pyridine in 0.5M KCl aqueous solution. Conditions: 25°C and 55bar CO<sub>2</sub>*

207

*Figure 7.20 Potentiostatic electrolyses at alternating potential as function of time. Electrolyte: 200mM pyridine in 0.5MKCl aqueous solution. Conditions: 25°C and 55bar CO<sub>2</sub>. (a) 0V-0.9V, (b) 0V-1V and (c) 0V-0.65V*

208

*Figure 7.21 Galvanostatic electrolysis (-150 $\mu$ A/cm<sup>2</sup>) at alternating CO<sub>2</sub> pressure (63-40bar) as function of time. Electrolyte: 200mM pyridine in 0.5 M KCl aqueous solution. Conditions: 25°C.*

209

*Figure 7.22 CO<sub>2</sub> macro bubbles formation corresponding to the galvanostatic electrolysis at alternating CO<sub>2</sub> pressure (63-40bar) of Figure 7.21. The formation proceeds in the following sequence: (1) top left, (2) top middle, (3) top right, (4) bottom left, (5) bottom middle and (6) bottom right. Electrolyte: 200mM pyridine in 0.5 M KCl aqueous solution. Conditions: 25°C.*

210

*Figure 7.23 Variation of the potential in (underpotential) galvanostatic electrolysis at 50 $\mu$ A/cm<sup>2</sup>: Electrolyte: 200mM pyridine in 0.5M KCl. Conditions: 55bar of CO<sub>2</sub> and 25°C.*

211

## LIST OF SYMBOLS

A	electrode area ( $\text{cm}^2$ )
$C_{\text{O}}^*$	concentration of pyridinium ( $\text{mol}/\text{cm}^3$ )
$C_{\text{g}}$	gas phase concentration (M)
$C_{\text{l}}$	liquid phase concentration (M)
$C_{\text{l}}^0$	initial concentration of methanol (M)
$D_{\text{O}}$	diffusion coefficient in $\text{cm}^2/\text{s}$
$E^0$	standard hydrogen potential (V)
F	Faraday's constant ( $96484.6 \text{ C mol}^{-1}$ )
$\Delta G$	Gibbs energy ( $\text{J. mol}^{-1}$ )
$\Delta G^\circ$	standard Gibbs energy ( $\text{J. mol}^{-1}$ )
$\Delta G_{\text{a}\ddagger}$	Gibbs free energy at anode ( $\text{J mol}^{-1}$ )
$\Delta G_{\text{c}\ddagger}$	Gibbs free energy at cathode ( $\text{J mol}^{-1}$ )
$\Delta G_{\text{a}\ddagger}^0$	standard Gibbs free energy at anode ( $\text{J mol}^{-1}$ )
$\Delta G_{\text{c}\ddagger}^0$	standard Gibbs free energy at cathode ( $\text{J mol}^{-1}$ )
$H_{\text{ci}}$	dimensionless Henry's constant or gas/liquid partition coefficient
i	current (A)
$I_{\text{p}}^{\text{a}}$	anodic peak current (A)
$I_{\text{p}}^{\text{c}}$	cathodic peak current (A)
$K_{\text{a}}$	equilibrium constant of pyridine
$k_{\text{p}}$	rate constant of protonation ( $\text{g mol}^{-1} \text{ s}^{-1}$ )
$k_{\text{dep}}$	rate constant of deprotonation ( $\text{s}^{-1}$ )
$K_{\text{H}}$	Henry's law constant
$k_{\text{s}}$	standard heterogeneous rate constant
$k_{\text{f}}$	rate constants of the forward reduction
$k_{\text{b}}$	rate constants of the backward reduction
$m_{\text{T}}$	mass transport coefficient
n	number of electrons transferres
N	number of moles (mol)
Q	The charge (C)
R	universal gas constant ( $8.314 \text{ J K}^{-1}\text{mol}^{-1}$ )

$R_i$	resistance ( $\Omega$ )
$t$	time (s)
$T$	temperature (K)
$t_i$	transport number
$v$	scan rate in (V/s)
$V_l$	initial volume of methanol in the liquid phase (ml)
$V_g$	volume of the headspace (ml)

## GREEK SYMBOLS

- $\alpha$  transfer coefficient
- $\delta$  diffusion layer thickness
- $\sigma$  charge density at the electrode surface
- $\epsilon_0$  permittivity
- $\epsilon$  dielectric constant
- $\kappa$  Conductivity ( $\Omega^{-1}\text{cm}^{-1}$ , or siemens  $\text{cm}^{-1}$ )
- $\phi$  Electrode potential

## ABBREVIATIONS

BPY	Bipyridine
BRP	Back pressure regulator
CPET	Concerted electron proton transfer
CE	Counter electrode
DFT	Density functional theory
DC	Direct current
DMF	Dimethylformamide
DMF	Dimethylformamide
DMSO	Dimethylsulfoxide
ET	Electron transfer
$E_{WE}$	Potential working electrode
ERC	Electroreduction of carbon dioxide technology
ESR	Electron spin-resonance
FY	Faradaic Yields
FEP	Fluoropolymer resin
GDE	Gas diffusion electrode
GCMS	Gas chromatograph mass spectrometer
HER	Hydrogen evolution reaction
HS	Head space
ICH	International conference on harmonisation
IHP	Inner Helmholtz plane
LOD	Limit of detection
LOQ	Limit of quantification
LCD	Liquid crystal display
MDE	Mercury drop electrode
OHP	Outer Helmholtz plane
PT	Proton transfer
PLOT	Porous layer open tubular
PCET	Proton coupled electron transfer
PCHT	Proton coupled hybrid transfer
$PyH^+$	Protonated pyridine ‘pyridinium’

RE	Reference electrode
RAM	<i>Random Access Memory</i>
ROM	<i>Read Only Memory</i>
SCE	Saturated calomel electrode ( $Hg/Hg_2Cl_2$ )
SHE	Standard hydrogen electrode
SIM	Selected ion monitoring
SSQD	Slow Suction-Quick Delivery
TS	Transition state
WE	Working electrode
CV	Cyclic voltamogram
NB	Nota bene

# Chapter 1 Introduction

The prosperity of our modern world and the consequent improvement to the quality of human life was initiated by the industrial revolution; an era where inexpensive and seemingly inexhaustible fossil fuel energy was discovered and exploited. The industrial revolution, initially fuelled by coal and then natural gas and oil, has entirely changed the way people live and utilize energy. Liquid fossil fuels such as petroleum and converted natural gas are of particular interest as they represent excellent feedstocks for chemicals and plastics production. Furthermore, the world's transportation systems are almost exclusively powered by refined petroleum, owing to its high energy density and portability. The exploitation of such fossil fuels has offered widespread electricity use, cleaner heating and cooling, improved housing and transportation among other benefits. While this form of energy continues to be the main power source (fossil fuels account for more than 80% of the world's energy (Aresta 2010) and it has propelled the world to high living standards, this brings a potential threat to the environment.

Average atmospheric temperatures have increased drastically since the industrial revolution. For instance a globally averaged warming of 0.85 °C (between 0.65 and 1.06 °C) was observed over the period 1880-2012 (IPCC 2014). According to the Intergovernmental Panel on Climate Change (IPCC) of the United Nations, the observed increase is likely to have occurred due to the increase in anthropogenic greenhouse gas (GHG) concentrations in the atmosphere. The phenomenon by which the GHGs (including CO<sub>2</sub>, water vapour, methane and nitrous oxide) absorb outgoing radiation, resulting in the increased temperature observed, has become known as global warming. There is a general consensus that the rising temperatures have triggered other changes such as the rise of the sea level, the frequency and intensity of extreme climate events, glacier retreat and greening of the desert among other serious environmental changes (IPCC 2014).

Carbon dioxide (CO<sub>2</sub>) has been identified as the most influential GHG due to its high radiative forcing (net change of the solar irradiation absorbed by the Earth surface and the energy radiated back to space). The extent of such an effect is determined by the gas concentration and its absorption capacity (Shine et al. 1990). CO<sub>2</sub> concentrations have risen by ca. 30% from pre-industrial levels of 280ppm (prior to 1750) to over 387ppm

today and they continue to rise by 2-3ppm/year (Aresta 2010). Such increases in atmospheric CO<sub>2</sub> are primarily caused by the combustion of fossil fuels in energy-related activities and industrial processes (Ganesh 2014) (Smith 2010).

Recently, many efforts have been directed toward to carbon capture and storage (CCS) as a mean of preventing the accumulation of atmospheric CO<sub>2</sub>. The CCS CO<sub>2</sub> mitigation route is concerned with the capture of the GHG primarily from industrial or power sector point sources such as fossil fuel power plants, refineries, iron, steel and chemical industries and its transport through dedicated pipelines to be finally stored in geological reservoirs, such as saline aquifers or depleted gas fields. CCS has been demonstrated to be high cost (e.g. requires 10-40% of the energy produced by a coal fired power station per kWh) (Smith 2010) for the capture part, yet the storage and the transport costs can be as significant as well, especially if the reservoir is far from the CO<sub>2</sub> source. Although in some countries the geological storage capacity is evaluated to be sufficient, a level of uncertainty remains in terms of the reservoirs' capacity and their capability of safely storing the GHG (Peter Styring 2011). In view of the high investment costs, uncertainty over potential storage capacity and leakage, which have unknown environmental and ecological impacts and risks, complementary options must also be considered. For example, the use of CO<sub>2</sub> as a building block in the production of chemicals for industrial applications can provide sustainable industries and consequently contribute to CO<sub>2</sub> emissions reduction. As such, carbon capture and utilisation (CCU) has been suggested as an alternative or complementary route to CCS.

CCU is a technology based on several potential routes. CO<sub>2</sub> transformation via mineral carbonation, biofuels from algae and chemical conversion all have great potential in addressing the CO<sub>2</sub> emission issue (Peter Styring 2011). Mineral carbonation involves the production of inert carbonates from CO<sub>2</sub> and minerals (usually calcium or magnesium silicates) and is potentially useful in providing construction materials. This route still requires optimisation of conditions at the industrial scale and the process is estimated at high cost (€60-100/t CO<sub>2</sub> stored) (Peter Styring 2011). Microalgae can use flue gases and CO<sub>2</sub> as a nutrient source to produce a wide range of products such as chemicals, fertilizers and biofuels. This route however is similar to mineral carbonation in that it still needs cost and energy reductions and is currently at the R&D stage (Peter Styring 2011).

The conversion of CO<sub>2</sub> into a chemical form, such as valuable organic compounds, hydrocarbons and transportable liquid fuels is a particularly attractive approach contributing to the establishment of a carbon energy cycle. In new CO<sub>2</sub> based cycles, energy from renewable sources, such as wind, solar, bio or nuclear power, should be utilized to produce fuels/valuable chemicals from captured CO<sub>2</sub>. Accordingly, additional CO<sub>2</sub> will not be released to the atmosphere during the generation of energy (e.g., heat, electricity), and thus the cycle can generate “carbon neutral” fuel or chemicals. Amongst various renewable energy utilisation routes, the renewable energy conversion into electrical energy is the most established and is currently commercialized.

In order to build the carbon energy cycle concept based on renewable energy, two main strategies are known. One is hydrogenation reaction in which H<sub>2</sub> generated by water splitting is used to convert CO<sub>2</sub> to useful chemicals. The other route is the direct electrochemical CO<sub>2</sub> reduction with a proton source to form valuable products such as fuels (Aresta 2010) (Appel et al. 2013). The electrochemical pathway is considered more practical in terms of the mild reaction conditions it offers as compared to chemical conversion (e.g. CO<sub>2</sub> hydrogenation to methanol (CH<sub>3</sub>OH) is performed at 125–525°C under 2–12MPa pressure). Furthermore, the electrochemical reduction of CO<sub>2</sub> is more convenient in terms of electrical energy storage in the form of liquid fuel. In this instance, the proton source is either molecular hydrogen or water and the by-product is water (Ganesh 2014). The electrochemical CO<sub>2</sub> reduction in aqueous electrolytes and under specific conditions can lead to the formation of CO, formic acid, alcohols, hydrocarbons (e.g. methane) and other valuable products. Being a high-energy product, convenient to store and transport, methanol (CH<sub>3</sub>OH) is one of the most attractive of these products. The alcohol has a high energy density per volume 15.6MJ/L which makes it an ideal portable liquid fuel for combustion and transportation (Ganesh 2011). Moreover, methanol (CH<sub>3</sub>OH) can be easily converted to gasoline or added as a reactant in transesterification of triglycerides to form biodiesel.

To reduce CO<sub>2</sub> electrochemically an external bias is required to supply electrons to the electrode. The potential energy supplied should be kept to a minimum (lowest overpotential possible to drive a reaction) for a given electrochemical CO<sub>2</sub> reduction system to be efficient and economically viable. In addition, a high Faradaic efficiency (defined as the ratio of the actual and theoretical amounts of product formed within the

same electrolysis time, based on the number of coulombs passed) and selectivity toward the desired product are also critical factors (Aresta 2010). The product selectivity is important in terms of saving energy needed for separation and purification. The industrial implementation, on the other hand, entails the use of high current densities (a measure of the rate of conversion) (Qiao et al. 2014).

The use of aqueous electrolytes represents an attractive approach as water is seen as a non-expensive proton source and is regarded as more economic than organic solvents (Hori 2008). However, the hydrogen evolution reaction (HER) usually competes with CO<sub>2</sub> reduction at a rate proportional to the proton activity in such an electrolyte at a given constant potential and at a given metal electrode (Hori 2008). In such systems, heterogeneous catalysts (e.g. metal oxides, metal complexes), at the electrode/electrolyte interface, are usually used to activate CO<sub>2</sub> to reduce the high overpotentials (Jhong et al. 2013). The development of homogeneous organic catalysts for the electrochemical reduction of CO<sub>2</sub> is a promising approach which is beginning to attract more researchers (Oh 2013). An efficient catalyst should (1) favour the CO<sub>2</sub> reduction over the competing hydrogen evolution reaction (HER) or ideally suppress it, (2) operate at reduction potentials close to those of the desired CO<sub>2</sub> reduced products (this minimises the overpotentials). Most electrochemical CO<sub>2</sub> reduction processes employing homogeneous catalysts demonstrated to date have been found to be impractical (Schwartz 1993). This is usually due to the competition with HER, low current densities, low Faradaic efficiencies and/or electrochemical product yields and/or poor selectivity toward the desired product.

Recently, protonated pyridine (C<sub>5</sub>H<sub>5</sub>N) 'pyridinium' was shown to catalyse a highly efficient electrochemical CO<sub>2</sub> reduction system to produce methanol (CH<sub>3</sub>OH) (Seshadri et al. 1994). In conjunction with semiconductor (p-GaP) or metal (Pt, Pd) surfaces pyridinium was reported to support CO<sub>2</sub> to methanol (CH<sub>3</sub>OH) conversion at ~>95% and 22-30% Faradaic efficiencies respectively. Bocarsly and co-workers have shown that the CO<sub>2</sub> reduction potential in acidified pyridine-containing electrolytes is close to the potential for CO<sub>2</sub> reduction to methanol (CH<sub>3</sub>OH), consequently the formation of the alcohol was achieved at low overpotentials (~100-200mV). The remarkably efficient system has stimulated several studies directed toward gaining further mechanistic insights; thus the implementation of this system on a large-scale could address some of the environmental issues associated with CO<sub>2</sub>-generating

technologies. Understanding the mechanism and hence the potential for scale-up is the key driver for the present work.

The CO<sub>2</sub> reduction process was suggested to proceed *via* the pyridinium electrochemical reduction to a radical intermediate which interacts with CO<sub>2</sub> to form a complex as a first step toward the production of methanol (CH<sub>3</sub>OH). However, some independent theoretical calculations have shown that the radical suggested cannot possibly form at the experimentally reported reduction potential and the conditions studied by the original group. Instead, the intermediate radical forms at least 0.6V more negatively than observed (J. a Keith & Carter 2013). This has accordingly ruled out the key step of the mechanism proposed and stimulated further investigations.

Alternative mechanisms based on experimental investigations together with numerical simulations (Costentin et al. 2013) and theoretical calculations (Ertem et al. 2013) (Liao et al. 2015) were suggested by independent groups. The first study, undertaken at Pt electrode and very similar conditions to the original group reports, indicated that the catalytic role of pyridinium at such condition is merely a weak acid behaviour leading exclusively to HER (Costentin et al. 2013). On the other hand, Barista and co-workers proposed a theoretical mechanism in which pyridinium catalyses the CO<sub>2</sub> reduction to formic acid on platinum electrode. These authors suggested that CO<sub>2</sub> is reduced by binding of hydrogen atoms to the Pt surface (Pt-H hybrid) that are transferred as hybrids to CO<sub>2</sub> in proton coupled hybrid transfer (PCHT) activated by pyridinium (Ertem et al. 2013) (Liao et al. 2015). Hence, the mechanism of this system is controversial to date.

Moreover, CO<sub>2</sub>-pyridinium system was reported only at low current densities ( $\sim 50\mu\text{A}/\text{cm}^2$ ) and low methanol (CH<sub>3</sub>OH) concentrations ( $\sim 1\text{ppm}$ ). Nonetheless, the CO<sub>2</sub>-pyridine (C<sub>5</sub>H<sub>5</sub>N) reduction system was investigated at other material electrodes such as Au (Lucio & Shaw 2015), TiO<sub>2</sub> passivated GaP (Zeng et al. 2014), Pt/C TiO<sub>2</sub> (de Tacconi et al. 2012) and iron pyrites (Bocarsly et al. 2012). Some of these studies confirmed the production of methanol (CH<sub>3</sub>OH) (Boston et al. 2013) (de Tacconi et al. 2012) (Zeng et al. 2014), while others could not detect the alcohol or any other carbon based products (Costentin et al. 2013)(Lucio & Shaw 2015). Intriguingly, methanol (CH<sub>3</sub>OH) was formed on TiO<sub>2</sub> passivated GaP even in the absence of pyridinium (Zeng et al. 2014). In view of the reported mechanisms which reached different conclusions in terms of the pyridine (C<sub>5</sub>H<sub>5</sub>N) catalytic activity in the CO<sub>2</sub> reduction system and the

controversy over the methanol ( $\text{CH}_3\text{OH}$ ) production, an experimentally based study along with numerical simulations of such system are reported herein.

The current work aims to answer two key questions: (a) Is there potential for methanol ( $\text{CH}_3\text{OH}$ ) formation by the  $\text{CO}_2$ -pyridinium system at reasonable reaction rates and concentrations? and (b) Can the controversy over the reduction mechanism of this system be solved? The approach to answering these questions is two-fold. First, a high pressure electrolysis study was conducted under various conditions aimed at increasing the methanol ( $\text{CH}_3\text{OH}$ ) yields and enhancing the current densities of the electrochemical reduction of  $\text{CO}_2$ . The concentration of dissolved gaseous  $\text{CO}_2$  is limited in aqueous solutions at 1bar; this restricts the  $\text{CO}_2$  availability at the electrode and hence limits the reduction rate. The concentration of the reactant,  $\text{CO}_2$ , can be enhanced by increasing its pressure. The abundance of this reactant near the electrode surface should maximise the current proportion contributing to  $\text{CO}_2$  reduction to methanol ( $\text{CH}_3\text{OH}$ ) and could also increase the operating current densities. Thus, in this project, electrochemical reduction in the  $\text{CO}_2$ -pyridinium system was extended to high  $\text{CO}_2$  pressure (50-55bar) at Pt electrodes.

Secondly, the role of pyridinium in the electrochemical  $\text{CO}_2$  reduction was investigated in the present project. In this context, a comparative approach of the two experimentally-derived mechanisms ‘Bocarsly and Savéant groups’ is adopted (Barton Cole et al. 2010) (Contentin et al. 2013). The mechanisms best describing this process in an inert atmosphere and under  $\text{CO}_2$  are derived from a detailed voltammetric study, numerical simulations and Nicholson based diagnostics.

The thesis is organised as follows: This Chapter presents the motivation for undertaking the present work. Chapter 2 provides an outline of the fundamental and experimental principles underpinning the electrochemical processes. Chapter 3 presents a comprehensive review of the recent literature of  $\text{CO}_2$  electrochemical reduction. The first part reports the un-catalysed direct  $\text{CO}_2$  electrochemical reduction, whereas the second part provides a summary of the studies reported on the electrocatalytic reduction of  $\text{CO}_2$  to methanol ( $\text{CH}_3\text{OH}$ ). The final section reports the early investigations of electroreduction by nitrogen bearing heterocycles. Chapter 4 describes the electrochemical techniques and methods used in this project. Chapter 5 presents the calculations of the ionic species concentrations in the  $\text{CO}_2$ -pyridine system. Chapter 6 and Chapter 7 report and discuss the results obtained in this project. Chapter 6

investigates the pyridinium role in the electrochemical CO<sub>2</sub> reduction system. Mechanisms of pyridinium reduction are proposed in both the absence and the presence of CO<sub>2</sub>. Chapter 7 reports the production of methanol (CH<sub>3</sub>OH) through the pyridinium-CO<sub>2</sub> reduction route at atmospheric pressure and at high CO<sub>2</sub> pressure. Finally, a summary of the research work and suggestions of future work are presented in the conclusion section.

## References of Chapter 1

- Appel, A.M. et al., 2013. Frontiers, opportunities, and challenges in biochemical and chemical catalysis of CO<sub>2</sub> fixation. *Chemical Reviews*, 113(8), pp.6621–6658.
- Aresta, M., 2010. *Carbon Dioxide as Chemical Feedstock* M. Aresta, ed., Weinheim, Germany: Wiley-VCH Verlag GmbH & Co. KGa.
- Boston, D.J. et al., 2013. Photochemical reduction of carbon dioxide to methanol and formate in a homogeneous system with pyridinium catalysts. *Journal of the American Chemical Society*, 135(44), pp.16252–5.
- Ganesh, I., 2014. Conversion of carbon dioxide into methanol – a potential liquid fuel: Fundamental challenges and opportunities (a review). *Renewable and Sustainable Energy Reviews*, 31, pp.221–257.
- Ganesh, I., 2011. Conversion of Carbon Dioxide to Methanol Using Solar Energy - A Brief Review. *Materials Sciences and Applications*, 02(10), pp.1407–1415.
- Hori, Y., 2008. Electrochemical CO<sub>2</sub> Reduction on Metal Electrodes. In *Modern Aspects of Electrochemistry*. pp. 89–189.
- Jhong, H.R.M., Ma, S. & Kenis, P.J., 2013. Electrochemical conversion of CO<sub>2</sub> to useful chemicals: Current status, remaining challenges, and future opportunities. *Current Opinion in Chemical Engineering*, 2(2), pp.191–199.
- Mairanovskii, S.G., 1963. The theory of catalytic hydrogen waves in organic polarography. *Journal of Electroanalytical Chemistry*, 6(2), pp.77–118.
- Qiao, J. et al., 2014. *A review of catalysts for the electroreduction of carbon dioxide to produce low-carbon fuels*, 43(2), pp.631–675.
- Schwartz, M., 1993. Carbon Dioxide Reduction to Alcohols using Perovskite-Type Electrocatalysts. *Journal of The Electrochemical Society*, 140(3), p.614.
- Seshadri, G., Lin, C. & Bocarsly, A.B., 1994. A new homogeneous electrocatalyst for the reduction of carbon dioxide to methanol at low overpotential. *Journal of Electroanalytical Chemistry*, 372(1-2), pp.145–150.
- Shine, K.P. et al., 1990. Radiative Forcing of Climate. In *Climate Change: The IPCC Scientific Assessment. Report prepared for Intergovernmental Panel on Climate Change by Working Group I*.
- Smith, Y., 2010. *Photo-electrochemical and Photo-catalytic Conversion of Carbon Dioxide*, Photo-Electrochemistry & Photo-Biology for the Sustainability.
- Zeng, G. et al., 2014. CO<sub>2</sub> Reduction to Methanol on TiO<sub>2</sub>-Passivated GaP Photocatalysts. *ACS Catalysis*, 4(10), pp.3512–3516.

# Chapter 2 Background Theory

## 2.1 Introduction

Electrochemistry usually involves the charge transfer between electron conductors (electrodes) and a solid ionic conductor or an electrolyte solution. It has a wide range of applications such as electroanalytical measurements, batteries and fuel cells as well as water treatment, and energy conversion technology; the latter being the subject of this thesis.

This Chapter provides an outline of the fundamental and experimental principles underpinning electrochemical processes. It covers the basics of electrochemical equilibria, the Nernstian system and the standard arrangement used in electrochemical cells. The theoretical and experimental aspects of controlled potential measurements, such as cyclic voltammetry and chronoamperometry used in this project are described in this Chapter. The Chapter also outlines the coupled chemical reactions, which provide mechanistic insights into a given electrochemical system.

## 2.2 Equilibria

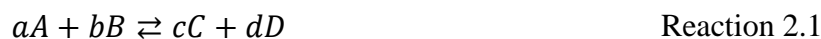
### 2.2.1 Chemical Equilibrium

In a broad sense, equilibrium is defined as the state of a system in which competing influences (e.g. forces) are balanced resulting in no net change. In chemical reactions, the equilibrium is the state at which both the reactants and the products have reached certain concentrations (Atkins & De Paula 2006). Thermodynamics is used to predict the change in energy and equilibrium composition of a chemical reaction. This section is concerned only with what is essential to describe thermodynamics in electrochemical systems.

Under equilibrium, the Gibbs energy of a system,  $G_{\text{sys}}$ , is minimized at constant temperature and pressure. This is mathematically written as:

$$dG_{\text{sys}} = 0 \qquad \text{Eq. 2.1}$$

The reaction of reactants A and B is considered to proceed to products C and D with stoichiometric coefficients a, b, c, and d, respectively (Reaction 2.1):



The standard Gibbs energy change of the reaction is expressed as a function of the equilibrium constant K:

$$\Delta G^0 = -RT \ln K \quad \text{Eq. 2.2}$$

where  $\Delta G^0$  is Gibbs energy change ( $\text{J} \cdot \text{mol}^{-1}$ ), R is the universal gas constant ( $8.314 \text{ J K}^{-1} \text{ mol}^{-1}$ ), and T is the temperature (K). The equilibrium constant, K, is described in Eq. 2.3 at a constant temperature

$$K = \frac{[C]^c [D]^d}{[A]^a [B]^b} \quad \text{Eq. 2.3}$$

The chemical equilibria of pyridine ( $\text{C}_5\text{H}_5\text{N}$ ) in the absence and the presence of  $\text{CO}_2$  are described in Chapter 5.

## 2.2.2 Electrochemical Equilibrium

An electrochemical equilibrium is established when an electron conductor (electrode) is brought into contact with an ionic conductor (electrolyte). Establishing electrochemical equilibrium usually involves an electron transfer at the electrode-electrolyte interface; this naturally results in an electrical charge difference between the two phases. Accordingly, a potential difference, E, between the electrode (e.g. metals) and the electrolyte (solution) develops. This may be used to drive a chemical reaction in solution, for example at the working electrode of an electrochemical cell. One of the two electrodes responds to the target reactant and thus is termed the working electrode (WE); the second electrode is the reference electrode (RE), which is independent of the properties of the electrolyte. The WE is of interest as the reactions take place between the interface of the latter and the electrolyte, which is usually a solution. If a general heterogeneous electron transfer reaction is considered, then:



where, O, symbolizes the oxidized species, R represents the reduced species, n is the number of electrons transferred and  $k_f$  and  $k_b$  are the rate constants of the reduction (forward reaction) and the oxidation (backward reaction) reactions respectively. The

establishment of equilibrium in this case implies that the rate constant of the forward reaction is balanced by the rate of the backward reaction. Once the equilibrium is attained no further change occurs, the concentration of the oxidized and reduced species remains unchanged as compared to the values prior the redox reactions (Atkins & De Paula 2006) (Compton Richard G 2010).

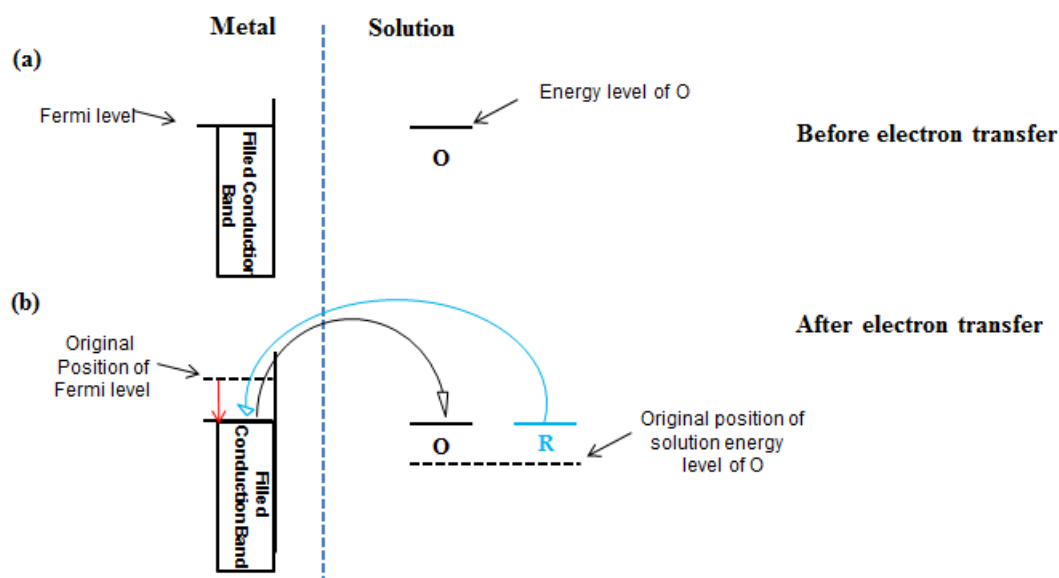


*Figure 2.1 The electronic energy diagram in metal electrode –solution (a) before electron transfer (b) after electron transfer (Compton Richard G 2010)*

Metals are comprised of closely packed atoms in which the outer valence electrons are free to move throughout the solid. In energy terms, these electrons are considered to occupy the ‘conduction band’. In an electronic conduction band, an effective continuum of levels is filled up to an energy maximum (Fermi-level). Figure 2.1 illustrates the energy level diagram for a metal electrode in solution and shows the change in the relative position of these energy levels. The scheme in Figure 2.1a shows the metal/solution state before charge transfer, the Fermi level is higher than the energy level within the molecule O in solution. It is therefore energetically favourable for an electron to leave the electrode and join the molecules O, reducing them to species R. Upon the electron transfer from the metal to the solution a positive charge builds up on the metal electrode and corresponding negative charge in the electrolyte. Hence, the electronic energy of the metal electrode is lowered (progressively lowering the Fermi-level) relative to the electrolyte (Figure 2.1b). Subsequently, the negative charge in the solution raises the energy levels of this latter. In this instance, a dynamic equilibrium takes place where the rate of electron transfer from the metal to O is matched with the

rate of the electron transfer from R back to the metal (species R becomes oxidised) (Wang 2006) (Compton Richard G 2010).

## 2.2.2.1 Nernst Equation

The reaction in Scheme 2.2 occurs in a potential region where the electron transfer is kinetically or thermodynamically favourable. In thermodynamically controlled systems, the Gibbs energy is related to the concentration of the electro-active species  $C_O(0, t)$ ,  $C_R(0, t)$  in the electrode process by:

$$\Delta G = \Delta G^0 + RT \ln \frac{C_O(0, t)}{C_R(0, t)} \quad \text{Eq. 2.4}$$

Eq. 2.4 is expressed in terms of concentrations of O and R species instead of their ionic activities (see the ionic activity Section 2.5.1.1). Usually an ideal solution of 1M is considered when describing energy/potential equations, since at such ideal state the ionic activity is identical with the molar concentration. Gibbs energy for Scheme 2.2 at equilibrium as a function of the potential difference is given by:

$$\Delta G = -QE = -nFE \quad \text{Eq. 2.5}$$

where  $E$  is the potential between the WE and RE,  $Q$  is the charge (C): which is the number of electrons transferred within the reaction,  $n$ , times the Faraday constant (96,484.6 C mol<sup>-1</sup>), this constant represents the charge of a mole of electrons. In the case of all substances are at unit activity, the equation (Eq. 2.5) is written as:

$$\Delta G^0 = -nFE^0 \quad \text{Eq. 2.6}$$

where,  $E^0$ , is the standard potential (V) of the reaction. Eq. 2.4, Eq. 2.5 and Eq. 2.6 give the relationship of the concentration of the electroactive species  $C_O(0, t)$ ,  $C_R(0, t)$  with the potential, known as the Nernst equation:

$$E = E^0 + \frac{RT}{nF} \ln \frac{C_O(0, t)}{C_R(0, t)} \quad \text{Eq. 2.7}$$

## 2.2.2.2 Faradaic and Non –Faradaic Processes

### 2.2.2.2.1. Electrode Processes

The current flowing in an electrochemical cell can be either Faradaic or non-Faradaic. The Faradaic currents are all the currents resulting from the reduction or oxidation of the species in the cell (Bard & Faulkner 2002). These currents are governed by Faraday's law:

$$i = \frac{dQ}{dt} = \frac{d}{dt}(nFN) = nF \frac{dN}{dt} \quad \text{Eq. 2.8}$$

where,  $t$ , is the time (s), and  $N$  is the number of moles reacted. All other processes not involving a charge transfer are considered non-Faradaic processes (e.g. adsorption/desorption processes). These reactions are usually caused by changes in the solution composition or the electrode surface, which lead to non-Faradaic current flow. Since no charge crosses the electrode interface, the electrode-solution behaviour is effectively similar to a capacitor, where at a given potential a charge builds up at the electrode and the corresponding charge in the solution. Therefore, such system is analogous to a capacitor in series with a resistor, the current as function of time is given by:

$$i = \frac{E}{R_s} e^{-t/R_s C} \quad \text{Eq. 2.9}$$

where,  $i$ , is the current (A),  $E$  is the potential (V),  $R$  is the solution resistance ( $\Omega$ ),  $C$  is capacitance and  $t$  is the time (s). Eq. 2.9 is derived from Ohm's law (Eq.2.10) and the capacitance (Eq. 2.11) as shown in Appendix A4.

$$i = \frac{E}{R} \quad \text{Eq. 2.10}$$

Capacitance is directly proportional to area of the conductors and inversely proportional to the separation distance between the conductors:

$$C = q/E \quad \text{Eq.2. 11}$$

## 2.3 Electrochemical Cells

### 2.3.1 Types of Electrochemical Cells

Electrochemical cells are devices capable of either generating electrical energy from chemical reactions known as ‘galvanic cells’ (e.g. batteries), or supplying electrical energy into a system to drive or facilitate chemical reactions such as electrolytic syntheses termed ‘electrolytic cells’. The galvanic cells are those whose reactions are spontaneously taking place at electrodes when connected *via* an external conductor (electricity is generated in this case), however electrolytic cells require an external potential that is higher than the potential of the cell to drive the electrochemical process (Zoski 2007). A typical example of a galvanic cell, Volta’s battery, is depicted in Figure 2.2b. It consists of stacked copper and zinc disks separated by paper soaked in an acidic solution. Figure 2.2a, however, illustrates a two-electrode arrangement electrolytic cell driven by an external energy, with copper as a cathode and platinum as an anode. In this thesis, the latter cell type is used to drive CO<sub>2</sub> reduction to methanol (CH<sub>3</sub>OH).

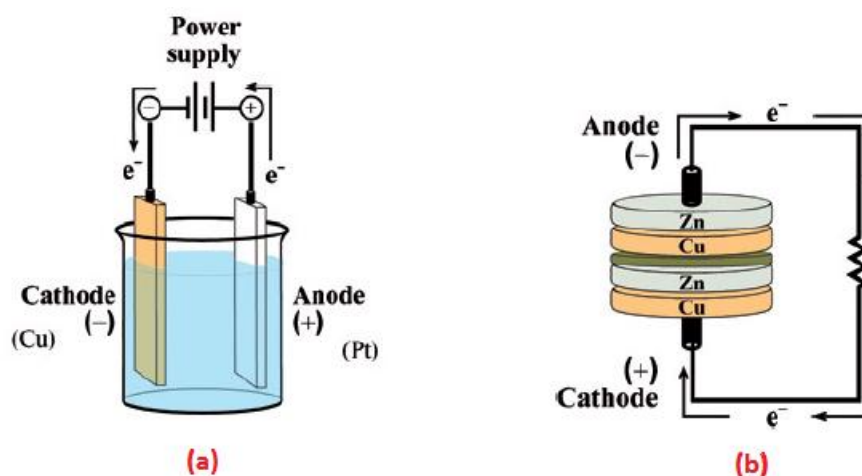


Figure 2.2 (a) An electrolytic electrochemical cell, (b) A galvanic electrochemical cell (Zoski 2007)(Bard & Faulkner 2002)

### 2.3.2 Three Electrode Set Up

Controlled potential techniques investigating kinetics often employ a three-electrode set up which consists of a WE, the electrode at which redox reactions occur, a RE provides a stable and reproducible reference potential and a counter electrode (CE) (or auxiliary),

that is a third electrode needed as a current carrier. The three electrodes are connected in a bulk electrolyte system and are controlled by a potentiostat. In such system, a potential is applied and controlled by the polarizing circuit between the WE and the RE, and the current through the cell is monitored by the measuring circuit. Since negligible current flows through the RE, and because this electrode has a constant potential, any changes in the potential are reflected as changes in the WE potential  $E_{WE}$ . During the passage of the current a voltage drop equal to  $iR$  is always included in the measured value (Eq. 2.12). The term  $iR$  reflects the electrical resistance of the bulk solution between the WE and RE electrodes (Zoski 2007)(Scholz 2010)(Bard & Faulkner 2002).

$$E_{app} = E_{WE} - E_{RE} - iR \quad \text{Eq. 2.12}$$

The working electrode capacitance gives rise to an additional non-Faradaic current (as described in the previous section), which contributes to both the forward and backward Faradaic current responses; this is due to the double layer, diffuse layer, and capacitance (discussed later in the electrical double layer section) (Scholz 2010) . On the other hand, the presence of the uncompensated resistance ( $iR$ ) causes a deviation of the applied potential from the true value as illustrated in Figure 2.3.

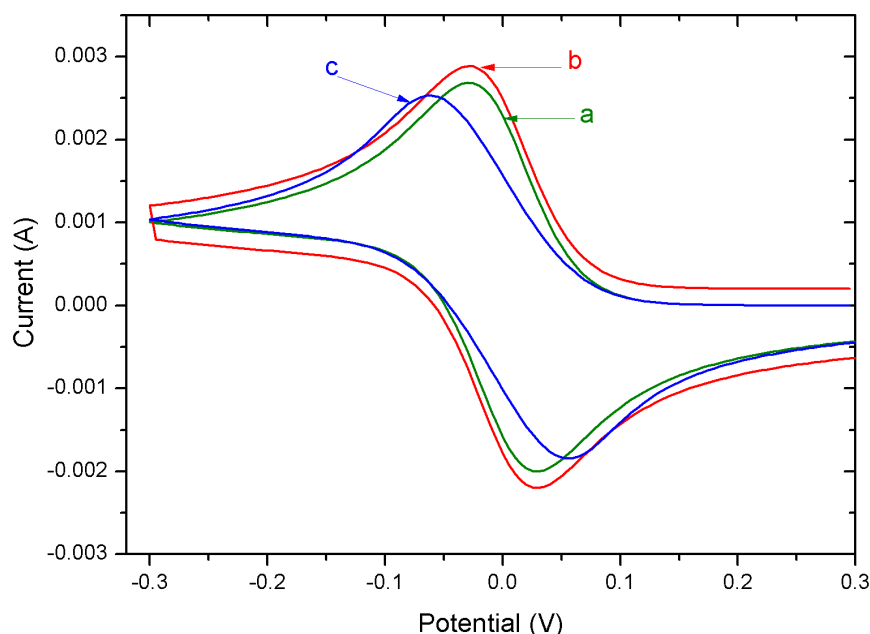


Figure 2.3 Simulated cyclic voltammograms of a simple E reaction at planar electrode ( $1\text{cm}^2$ ) and  $100\text{mV/s}$  (DigiSim.3.03) showing the effect of capacity and solution resistance. (a) reversible cyclic voltammogram, (b) with effect of capacity, and (c) with additional resistance,  $R=10\Omega$ .

### **2.3.2.1 Working Electrode (WE)**

The working electrode can be either a cathode or an anode depending whether a reduction or an oxidation takes place. The electrode material typically includes noble metals (e.g. Au, Pt), carbon (such as glassy carbon, carbon paste or nanotubes), liquid metals (mercury (Hg)) or doped semiconductors (e.g. Si, GaP). WEs can be chemically modified in order to increase their sensitivity toward specific species (e.g. chemical sensors) or to decrease the potential required to drive a particular reaction (e.g. catalyst). The WE can be designed at different geometrical shapes including, a hanging drop electrode, a disk or a wire electrode depending on the electrochemical technique employed or the specific application.

### **2.3.2.2 Reference Electrode (RE)**

Reference electrodes, as their name suggests, are employed to provide a stable and reproducible reference potential against which WE potential can be monitored. The stability and reproducibility of the potential should be maintained over time at ambient temperature, and not altered by perturbations of the measuring system such as passage of very small current. The most frequently used reference electrodes are saturated calomel electrode (SCE) and silver/silver chloride electrode (Ag/AgCl). Types of reference electrodes used in this thesis and the preparation of Ag/AgCl electrode are described in Chapter 4, Section 4.3.3.

### **2.3.2.3 Counter Electrode (CE)**

In a two-electrode configuration system, the passage of large current through the RE may induce chemical changes thus cause it to lose its ideal non-polarizable property, hence a three-electrode configuration is often used. The third electrode, a counter electrode (CE), is employed as a current sink to avoid the passage of high currents through the RE electrode. The CE serves to pass the same current as the induced current flowing through the WE. Accordingly, the potentiostat drives the CE to the voltage required to pass this current.

The CE is usually chosen to be an inert material with a large area. In electrolysis applications of high current densities, the CE is often separated from the WE

compartment by a glass frit to avoid the interferences of the products from CE with the products of interest at WE.

### 2.3.3 Electrolyte solutions

One of the most important properties a medium in electrochemistry must have is the ability to support the current flow. The electrolyte provides a medium for ions to flow near the electrodes to maintain a charge balance. Conductivity is, thus, the ability of a solution to support current flow by the motion of charged particles upon applying an electrical field. The conductivity ( $\Omega^{-1}\text{cm}^{-1}$ , or Siemens  $\text{cm}^{-1}$ ) of an electrolyte phase of uniform section of area  $A$ , resistance  $R$ , and length  $L$  is given by:

$$\kappa = \frac{1}{R} (L/A) \quad \text{Eq. 2.13}$$

Electrolytes of aqueous or non-aqueous (aprotic) nature are generally used in electrochemical systems. An electrolyte solution consists of a solvent and a supporting electrolyte (e.g. salt), the solvent should be electrochemically inert over a wide potential range. The supporting electrolytes are usually used to suppress migration effects (see the migration section), maintain a constant ionic strength (see ionic activity section), and minimize the resistance across the solution. The choice of the electrolyte usually depends on several factors such as the solubility and the redox nature of the analyte. The removal of dissolved molecular oxygen from the electrolyte is critical particularly for the reduction reactions, since the reduction of the oxygen often results in current arising which causes interferences in the measurements of the cathodic current. The electrochemical reduction of oxygen proceeds via a two-step mechanism (Reactions 2.3, 2.4). The first step involves a two-electron, proton coupled reaction occurring at  $\sim -0.1\text{V}$  vs. SCE, leading to the production of hydrogen peroxide. The second step involves the reduction of hydrogen peroxide to form water at  $-0.9\text{V}$  vs. saturated calomel electrode (SCE).



Furthermore, the products resulting from these reactions may affect the chemical processes under investigation. It is, therefore, prudent to remove dissolved oxygen from

the electrochemical cell. The most common approach is to purge the cell with an inert gas such as nitrogen or argon.

## 2.4 Mass Transfer

The movement of a material arises due to the difference of electrical or chemical potential between two locations in solution. The reactants must be transported from the bulk solution to the electrode surface for a reaction to take place. Mass transfer (Figure 2.4) plays a critical role in the electrochemical dynamics of a system (Compton Richard G 2010). Since, the rate of a reaction is determined by the rate at which the material is brought (from or to) the electrode surface (e.g. mass transfer) or by the electron transfer at the electrode. Three main mass transfer modes are reviewed in Figure 2.4.

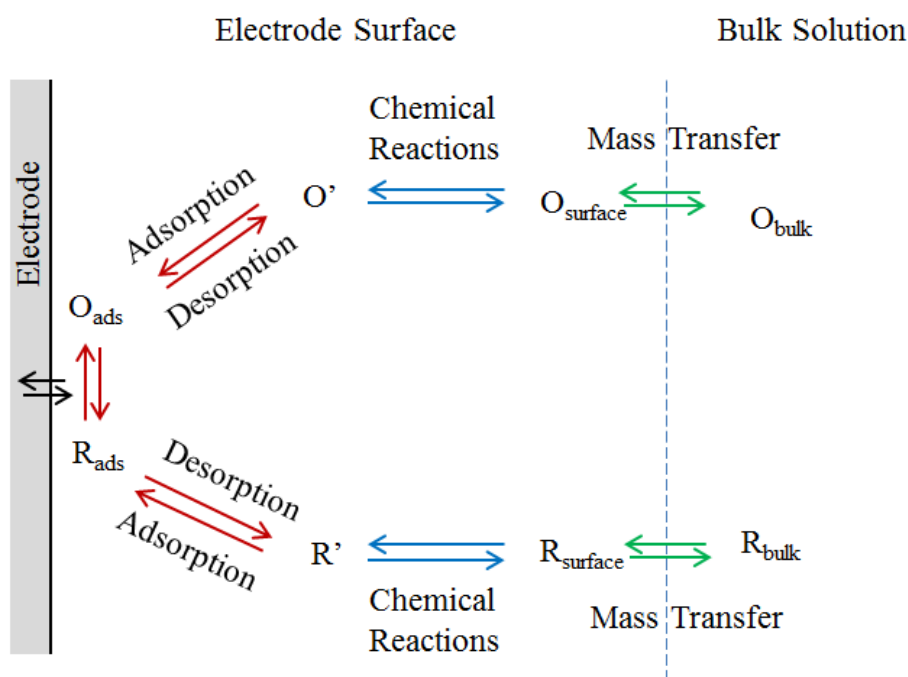


Figure 2.4 Schematic diagram of mass transfer modes at an electrode surface (Compton Richard G 2010)

### 2.4.1 Migration

The electromigration is defined as the movement of charged species under the influence of an electric field (Zoski 2007)(Compton Richard G 2010). In such an external field, for instance, positively charged species move toward the cathode. The migration of

electroactive species can be quantified by the transport number,  $t_i$ , of ions  $i$  relative to ions  $j$  both present in a given solution:

$$t_i = \frac{|z_i|u_i c_i}{\sum_{j=1}^n |z_j|u_j c_j} \quad \text{Eq. 2.14}$$

where,  $z$ ,  $u$ , and  $c$  are the charge, the mobility, and the concentration of species  $i$  and  $j$  respectively. The mobility of species  $i$ , is written as:

$$u_i = \frac{|z_i|FD_i}{RT} \quad \text{Eq. 2.15}$$

The transport number is proportional to the ratio of the mobilities of ions  $i$  and  $j$  as illustrated in Eq. 2.14. The Faradaic current flowing through a system consists of diffusion currents,  $i_d$ , and migration currents,  $i_m$ , reflecting the diffusive and migrational components to the electroactive species flux at the surface (Zoski 2007):

$$i = i_d + i_m \quad \text{Eq. 2.16}$$

The interplay of the migration and electrolysis of a given reaction often results in a complex physical transport processes. A charge transfer occurring at the electrode surface alters the electrical potential and the electric field of the electrode, affecting the surface concentration of the species. Consequently, the migration flux and the mass transport of the electroactive species are altered. Such variations can make the experimental results difficult to interpret. Therefore, it is necessary to eliminate the migration effects by the introduction of a high concentration of inert electrolyte. The high concentration of the electrolyte ions contributes to reducing the double charged layer such that the electroneutrality is maintained through the interfacial region since  $t_i \rightarrow 0$  leads to  $i_m \rightarrow 0$ . The excess of these ions prevents the electrical field build up as the reaction proceeds.

## 2.4.2 Diffusion

Diffusion is a spontaneous process driven by entropy whereby random species motion takes place to reach homogenization. Species move *via* a chemical potential gradient (i.e. concentration gradient). A diffusive flux at a given point  $x$  and time  $t$  of species  $O$  is dependent on the concentration gradient as described by 1<sup>st</sup> Fick's law:

$$J_O(x, t) = -D_O \frac{\partial C_O(x, t)}{\partial x} \quad \text{Eq. 2.17}$$

Where,  $J_o(x, t)$  is the molar flux in  $\text{mol cm}^{-2} \text{s}^{-1}$ ,  $D_o$  is the diffusion coefficient of species  $O$  to the electrode in  $\text{cm}^2 \text{s}^{-1}$ , and  $\frac{\partial C_o(x, t)}{\partial x}$  is the concentration gradient at point  $x$ . Since it is important to know how the concentration gradient at point  $x$  varies with time, Fick has derived his second law:

$$\frac{\partial C_o(x, t)}{\partial t} = D_o \frac{\partial^2 C_o(x, t)}{\partial x^2} \quad \text{Eq. 2.18}$$

This equation represents a simple linear diffusion for a planar electrode. In general, most practical and theoretical work on cyclic voltammetry is based on the use of macroscopic electrode disks. For such electrode geometry, a planar diffusion dominates. However, if the electrode size is reduced to a micro-disk, the diffusion layer thickness becomes comparable to the electrode radius, thus the diffusion becomes non-planar. Reducing the electrode size increases the mass flux and hence the current density as illustrated in Figure 2.5. In this case when a radial diffusion dominates sigmoidal shaped (S-shape) voltametric response is seen, for the same scan rate (Scholz 2010).

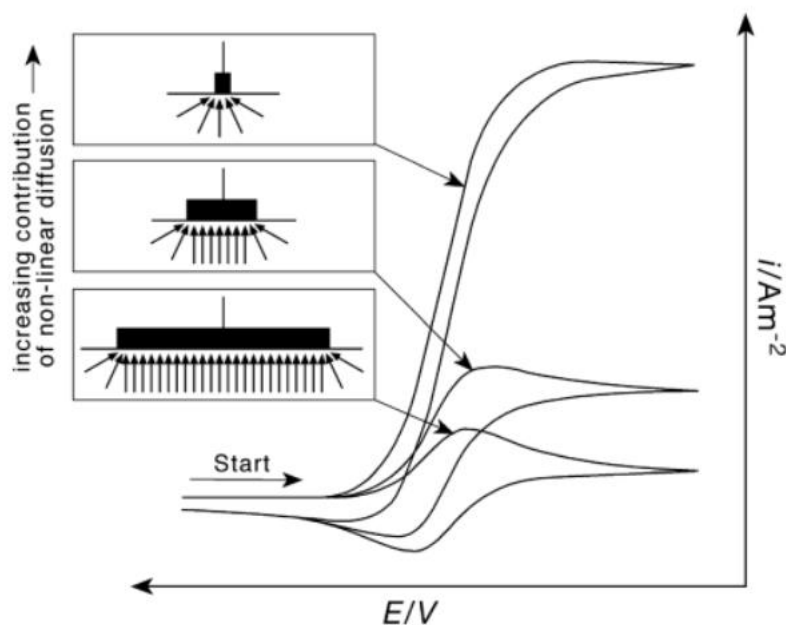


Figure 2.5 Effect of the electrode geometry on the shape of reversible cyclic voltammograms and schematic drawings of the corresponding transition from a planar semi-infinite to a spherical diffusion (Compton Richard G 2010) (Scholz 2010).

### 2.4.2.1 Spherical Correction

The boundary value problem of linear sweep voltammetry at a spherical electrode with a radius,  $r_0$ , is addressed in analogue manner as described in Section 2.8.1.1.1.1, the resulting current has a spherical correction term  $\phi [(nF/RT) vt]$ . The current for reversible system is written as:

$$i = i(\text{plane}) + \frac{nFAD_oC_o^*\phi[(nF/RT)vt]}{r_0} \quad \text{Eq. 2.19}$$

The correction term  $\phi [(nF/RT) vt]$  was calculated at various scan rates by Nicholson and Shain (Nicholson & Shain 1964). The higher the scan speed  $v$  the current,  $i(\text{plane})$ , becomes much larger than the spherical correction term, the electrode under these conditions can be considered planar. For irreversible redox systems (see irreversible system section) the current has a spherical correction factor  $\phi (\alpha f vt)$  and is written as:

$$i = i(\text{plane}) + \frac{FAD_oC_o^*\phi(\alpha f vt)}{r_0} \quad \text{Eq. 2.20}$$

It is not always practical to use electrode which gives planar diffusion (e.g. disks) in a given electrochemical application. Hence, it is important to take in consideration the spherical contribution when electrodes of non-planar shape are used. These would give rise to high spherical contribution as shown in Figure 2.5.

### 2.4.3 Convection

Convection is defined as the movement of species in solution under the influence of some forces. Convection can be described as natural or forced. Natural convection is caused by a density gradient or a thermal gradient. The density gradient causes the material to flow from a dense region to less dense region. The thermal gradient may result from the endo- or exo-thermicity of a given electrochemical process (Compton Richard G 2010). The forced convection is the result of external force exerted upon a solution usually by mechanical means. In such case, the convection dominates the mass transport in a given system. Since, the convection is induced deliberately its hydrodynamic behaviour is well defined (e.g. rotating disk voltammetry).

The convection of species, O, can be described by Fick's first law in one dimension (Eq. 2.18):

$$j_{convection} = C_0 V(x) \quad \text{Eq. 2.21}$$

where,  $V(x)$  is the fluid velocity at a point  $x$  ( $\text{cm s}^{-1}$ ). The relationship between the time,  $t$ , the position,  $x$ , and the concentration of the species is given by:

$$\frac{\partial C_0}{\partial t} = -V(x) \frac{\partial C_0}{\partial x} \quad \text{Eq. 2.22}$$

## 2.5 Electrode – Solution Interface

### 2.5.1 Electrical Double Layer

It is essential to take a close look at the electrode-electrolyte interfacial layer structure, which determines many properties of a given system and inevitably affects the kinetics of the reactions taking place at this interface. In electrochemical systems, the electrode-electrolyte layer consists of a build-up of ionic species in the solution for the excess charge compensation on the electrode (Compton Richard G 2010). Such layer is made up of charged particles of opposite sign to the corresponding electrode.

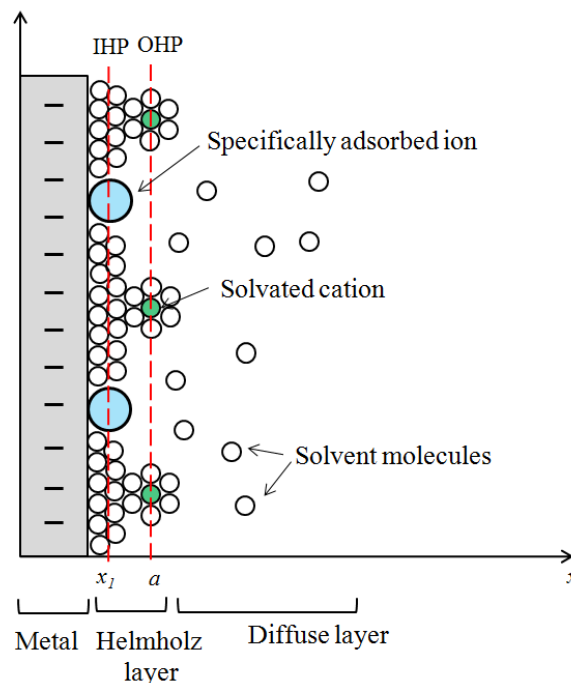


Figure 2.6 Schematic diagram of an electric double layer between an electrolyte and a cathode (metal). Where  $x$  is the distance between the two. IHP is inner Helmholtz plane and OHP is outer Helmholtz plane (Zoski 2007).

Figure 2.6 illustrates the structure of the double charged layer which consists of several distinct regions. The inner-layer, the closest to the electrode at a distance ( $x$ ), is known as the inner Helmholtz plane (IHP). The IHP contains adsorbed solvent molecules and specifically adsorbed (partly solvated) ions. The closest distance ( $a$ ) a solvated ion can get to the electrode surface represents the edge of the second layer known as the outer Helmholtz plane (OHP). The solvated ions are non-specifically adsorbed and are attracted to the surface by coulombic forces. The outer layer which is beyond the OHP is a three-dimensional region of scattered molecules, and is called the diffuse layer; this layer extends from the OHP to the bulk solution. Such distribution of the ions in this layer is determined by both the electric field which imposes the counterbalance and the random thermal motion (Wang 2006) (P.H. Rieger 1994). The electrostatic forces become weaker with the increasing disorder with the distance from the electrode surface, while the thermal motion becomes predominant. The potential decays within this layer, that is, from the electrode surface to the randomly distributed solvated molecules. Therefore, the potential,  $\phi$ , at any point of the within the double layer can be described by:

$$\phi = \frac{\sigma}{\varepsilon_0 \varepsilon \kappa} e^{\kappa(a-x)} \quad \text{Eq. 2.23}$$

Where  $\sigma$ ,  $\varepsilon_0$ ,  $\varepsilon$  are charge density at the electrode surface, permittivity, and dielectric constant respectively. The constant  $1/\kappa$  or identified as,  $\delta$ , represents the thickness of the diffuse layer.  $x$  and  $a$  represent the distance from the electrode and the position of OHP. When  $x$  approaches  $a$  such that OHP,  $(a - x) \rightarrow 0$ ; under these conditions the potential,  $\phi$ , is designated as,  $\phi_0$ , known as ‘zeta-potential’ equation 2.23 becomes:

$$\phi_0 = \frac{\sigma}{\varepsilon_0 \varepsilon \kappa} = \xi \quad \text{Eq. 2.24}$$

There are effectively two components which describe the potential drop across the interface;  $\phi_0$  across the diffuse layer and  $(\phi - \phi_0)$  across the Helmholtz layer. From the point of view of the external electric circuit, the double layer behaves as a capacitor, serving to store electric charge. The total capacitance,  $C$ , of the double layer is made up of inner adsorption layer capacitance,  $C_H$ , and the diffuse layer capacitance,  $C_D$ ; which are connected in series (Compton Richard G 2010):

$$\frac{1}{C} = \frac{1}{C_H} + \frac{1}{C_D} \quad \text{Eq. 2.25}$$

or

$$C = \frac{C_H C_D}{C_H + C_D} \quad \text{Eq. 2.26}$$

With the capacity,  $C_D$ , of the diffuse layer which is dependent on the electrolyte concentration is given by:

$$C_D = \frac{\sigma}{\xi} = \epsilon_0 \epsilon \kappa \quad \text{Eq. 2.27}$$

For very dilute electrolyte solutions, so that  $C_D \ll C_H$  then  $C \sim C_D$  and the double layer becomes effectively all diffuse (e.g. the diffusive layer can be as thick as 10nm). However, when the solutions are very concentrated the diffuse layer becomes more compact and its capacity becomes very large ( $C_D \gg C_H$  and  $C \sim C_H$ ), the Helmholtz layer contribution dominates. For instance, at electrolyte concentrations of  $>0.1M$  the thickness of the double layer becomes negligible and the potential drop can be treated the same as the Helmholtz potential (Compton Richard G 2010) (Crow 1994) (P.H. Rieger 1994).

### 2.5.1.1 Ionic Activity

The presence of an ion in a given electrolyte is necessarily affected by the surrounding species. Electrostatic interaction is usually expected in solutions except at infinite dilution, thus the concentration of species is an unsatisfactory parameter if the bulk properties of a solution are to be determined. Rather, what is required is a parameter related to the species concentration, such as the number of species present which are available to take part in a chemical reaction (Bates & Vijnh 1973). This number can determine the properties or influence the position of equilibrium. Such parameter is known as the activity,  $a$ , of species,  $i$ , given by:

$$a_i = \gamma_i C_i \quad \text{Eq. 2.28}$$

Where  $\gamma_i$  is the activity coefficient and  $C_i$  is the concentration of species  $i$ . The theoretical model for calculating the activity coefficients is described by the Debye-Hückel equation (Bates & Vijnh 1973):

$$\log \gamma_{\pm} = -\frac{A|z_+ z_-| \sqrt{I}}{1 + B a \sqrt{I}} + bI \quad \text{Eq. 2.29}$$

where  $A$  and  $B$  are constant for a particular solvent at a given temperature and pressure. The term,  $a$ , represents the distance of the closest approach of an ion to another (Figure 2.7), this term was used previously to describe the OHP layer starting position (Figure 2.6).  $I$  is the ionic strength of the electrolyte given by (Compton Richard G 2010):

$$I = \frac{1}{2} \sum c_i z_i^2 \quad \text{Eq. 2.30}$$

where,  $z_i$ , the electronic charge and,  $c_i$ , is the concentration of the electrolyte in mol kg<sup>-1</sup>

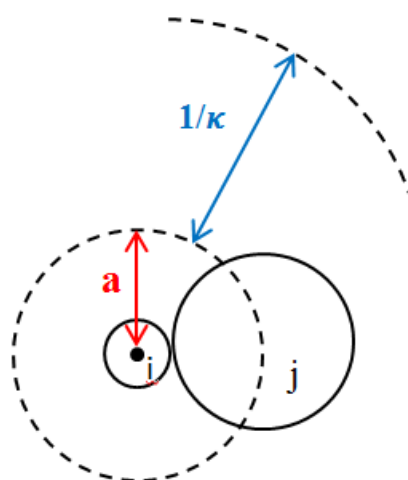


*Figure 2.7 The distance of closest approach,  $a$ , for an ion  $i$  and an atmosphere ion  $j$ , and the Debye length,  $1/\kappa$  radius of the ion atmosphere (Bard & Faulkner 2002).*

In electrochemical studies, the ionic activities for pure solids and liquid solutions are considered equal to unity at any temperature. For electrolytes, the activities are also taken to be unity at any pressure and temperature for infinite dilution of solute. For non-standard state the ionic activities are dependent on the pressure and temperature (Bates & Vijn 1973).

## 2.6 Electrochemical Kinetics

Kinetics is an essential part of electrochemistry concerned with the study of the rate at which an electron, and/or an ion is transferred from the bulk electrolyte to the charged double layer or to the electrode and vice versa. Furthermore, kinetics serves to understand the electrochemical processes and to determine the reactions mechanism. If a unimolecular reaction of species  $A$  and  $B$  is considered (Reaction 2.5):



The forward the backward reaction rates,  $k_f$  and  $k_b$  are written as:

$$v_f = k_f C_A \quad \text{Eq. 2.31}$$

And

$$v_b = k_b C_B \quad \text{Eq. 2.32}$$

Respectively, where the rate constants,  $k_f$  and  $k_b$  have the dimensions of  $s^{-1}$ . The net conversion of  $A$  to  $B$  is:

$$v_{net} = k_f C_A - k_b C_B \quad \text{Eq. 2.33}$$

At equilibrium, the net conversion of  $A$  to  $B$  is written as:

$$\frac{k_f}{k_b} = K = \frac{C_B}{C_A} \quad \text{Eq. 2.34}$$

From a thermodynamic point of view, the equilibrium constant,  $K$ , defined earlier by Eq. 2.1 represents a zero conversion of  $A$  to  $B$ . While in kinetics, equilibrium features a nonzero rate of the conversion, but maintains a constant ratio of those rates. The rate constants are dependent on the temperature ( $T$ ), the relationship was first described by Van't Hoff's equation (Bates & Vijnh 1973):

$$\frac{\partial \ln K}{\partial T} = \frac{\Delta H^\circ}{RT^2} \quad \text{Eq. 2.35}$$

where  $\Delta H^\circ$  is the standard enthalpy change of internal energy of the system.

## 2.6.1 Arrhenius Equation

Arrhenius has expressed the Van't Hoff's relationship of the reaction rate dependence on temperature as follows (Zoski 2007)(Bard & Faulkner 2002):

$$k = A e^{-E_A/RT} \quad \text{Eq. 2.36}$$

where  $E_A$  is the activation energy, the exponential factor indicates the probability to use thermal energy to surmount an energy barrier of height  $E_A$ . The coefficient  $A$  is known as the frequency factor. The Arrhenius equation related the thermodynamics of a reaction to its kinetics (Bard & Faulkner 2002).

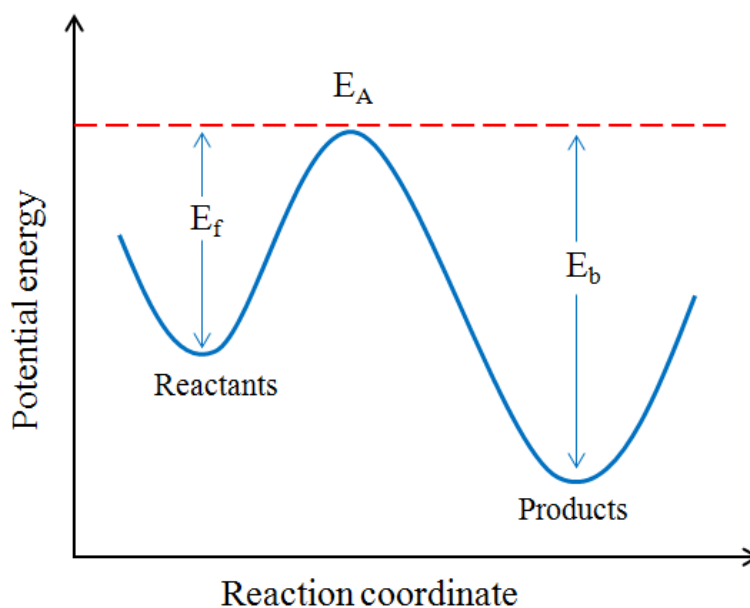


Figure 2.8 Energy potential variation adopted from Bard and Faulkner (Bard & Faulkner 2002)

The transition state theory (Bard & Faulkner 2002) is used to predict the values of  $A$  and  $E_A$  for a specific system in order to determine the factors controlling its reaction rate. Figure 2.8 illustrates the energy change along a reaction coordinate. The reaction coordinate represents the progress of a given reaction along a complex, favoured path to describe the potential energy in the system. The  $E_f$  and  $E_b$  representing the reactants and the products activation energies respectively, occupy minima on the energy surface which indicates that both the reactants and the products are energetically stable. As a reaction takes place, the coordinates change from those of the reactant passing over a maximum, a transition state (or an activated complex) ( $E_A$ ), and then falls in the product zone.

The energy  $E_A$  is usually denoted as  $\Delta E^\ddagger$ , so the enthalpy  $\Delta H^\ddagger$ , becomes  $\Delta E^\ddagger + \Delta PV$ . The variation of the pressure are negligible in a condensed phase, so that  $\Delta H^\ddagger \approx \Delta E^\ddagger$ . Thus, the Arrhenus equation is written as:

$$k = Ae^{-\Delta H^\ddagger/RT} \quad \text{Eq. 2.37}$$

This equation can also be expressed in terms of standard free energy of activation  $\Delta G^\ddagger$  as follows:

$$k = A'e^{-\Delta G^\ddagger/RT} \quad \text{Eq. 2.38}$$

where  $A'$  equals  $e^{\Delta S^\ddagger/R}$ ,  $\Delta S^\ddagger$  denotes the standard entropy and  $R$  is the molar gas constant.

Eq. 2.38 becomes:

$$k = A' e^{-(\Delta H^\ddagger - T\Delta S^\ddagger)/RT} \quad \text{Eq. 2.39}$$

Eq. 2.36 can be also presented by introducing  $k_B$  the Boltzman and  $h$  the Plank constants, so that the rate constant equation becomes:

$$k = \kappa \frac{k_B T}{h} e^{-\Delta G^\ddagger/RT} \quad \text{Eq. 2.40}$$

Eq. 2.40 is the most frequently used for predicting rate constants by the activated complex theory.

## 2.7 Butler-Volmer Model of Electrode Kinetics

Butler-Volmer is one of the theories (Bard & Faulkner 2002) used in electrochemical kinetics that relates the applied potential to the rate of reactions. If the Reaction 2.6 is considered:



and a single electron transfer process is assumed with no preceding or following chemical reactions, the standard free energy variation via a reaction coordinate is illustrated in Figure 2.9.

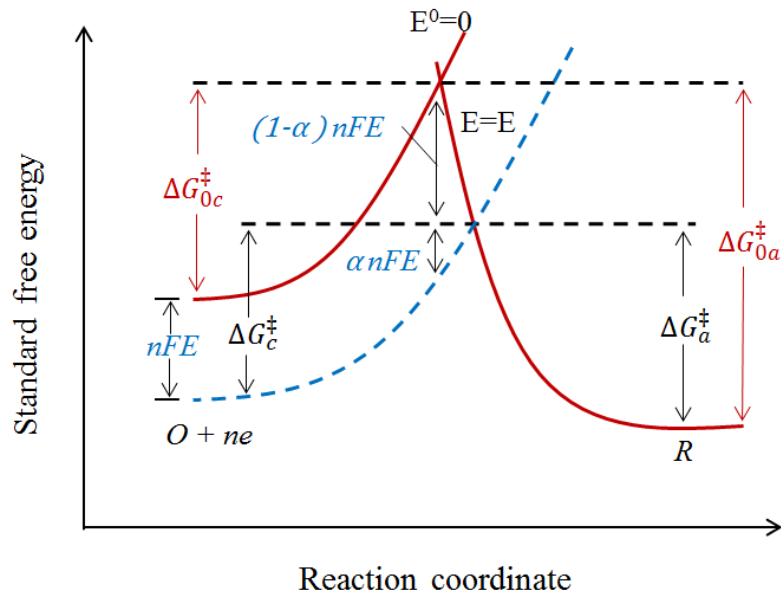


Figure 2.9 Schematic diagram of Butler-Volmer kinetics: a detailed view of the potential effect on free activation energies (Bard & Faulkner 2002)(Wang 2006)

The electrode kinetics is expressed against a point of significance in the chemical system, rather than an arbitrary external reference. The equilibrium potential of the system,  $E$ , and the standard equilibrium of the redox couple under consideration,  $E^0$ , are the two natural points in this instance. Figure 2.9 represents a parabolic profile from reactant to products with the transition state showing the effect of the potential change. At  $E=E^0$ , the activation energy of the cathode is  $\Delta G_{0c}^{\ddagger}$  and the activation energy at the anode is  $\Delta G_{0a}^{\ddagger}$  (solid red curves). If the potential changes by the value  $-nFE$  relevant to the relative electron energy change on the electrode, thus the  $O+ne$  curve moves down by that amount of energy (dashed line). The barrier for oxidation,  $\Delta G_a^{\ddagger}$ , becomes less than  $\Delta G_{0a}^{\ddagger}$  by fraction of change is  $1-\alpha$  where  $\alpha$  is the transfer coefficient, it ranges from 0 to 1. Thus the variation of the free energy can be described as:

$$\Delta G_a^{\ddagger} = \Delta G_{0a}^{\ddagger} + (1 - \alpha)nFE \quad \text{Eq. 2.41}$$

And

$$\Delta G_c^{\ddagger} = \Delta G_{0c}^{\ddagger} + \alpha nFE \quad \text{Eq. 2.42}$$

For oxidation and reduction respectively. If the forward and backward constant rates are assumed to have Arrhenius form:

$$k_f = A_f e^{-\Delta G_c^{\ddagger}/RT} \quad \text{Eq. 2.43}$$

and

$$k_b = A_b e^{-\Delta G_a^\ddagger/RT} \quad \text{Eq. 2.44}$$

By replacing the free energies (Eq. 2.41 and Eq.2.42) in the Arrhenius equation (Eq. 2.26), the rates constant for the forward reaction becomes:

$$k_f = A_f e^{-\Delta G_{oc}^\ddagger/RT} e^{-\alpha n f E} \quad \text{Eq. 2.45}$$

And the backward reaction becomes:

$$k_b = A_b e^{-\Delta G_{oa}^\ddagger/RT} e^{(1-\alpha) n f E} \quad \text{Eq. 2.46}$$

Where  $f=FRT$ . The first two terms in each of these expressions are independent of the potential and equal to the rate constant at  $E=E^0$  then  $A_f e^{-\Delta G_{oc}^\ddagger/RT} = A_b e^{-\Delta G_{oa}^\ddagger/RT}$ . When the interface is in equilibrium with Redox species the concentrations are equal  $C_O^* = C_R^*$ . In this case,  $E=E^0$  and  $k_f C_O^* = k_b C_R^*$  it implies that there is one rate constant named standard rate constant  $k^0$ . The reaction rates at any other potential other than the standard potential are expressed as a function of the standard rate constant,  $k^0$

$$k_f = k^0 e^{-\alpha f (E-E^0)} \quad \text{Eq. 2.47}$$

And

$$k_b = k^0 e^{(1-\alpha) f (E-E^0)} \quad \text{Eq. 2.48}$$

To express the total current as function of the standard rate constant and potential. The forward and backward reaction rates are written as function of the current and expressed as follows:

$$v_f = k_f C_O(0, t) = \frac{i_c}{nFA} \quad \text{Eq. 2.49}$$

and

$$v_b = k_b C_R(0, t) = \frac{i_a}{nFA} \quad \text{Eq. 2.50}$$

where  $i_a$  and  $i_c$  are the anodic and cathodic currents. The overall current becomes:

$$i = i_c - i_a = nFA[k_f C_O(0, t) - k_b C_R(0, t)] \quad \text{Eq. 2.51}$$

The insertion of these relations into the current expression gives

$$i = nFAk^0 [C_O(0, t) e^{-\alpha f (E-E^0)} - C_R(0, t) e^{(1-\alpha) f (E-E^0)}] \quad \text{Eq. 2.52}$$

## 2.8 Electroanalytical Techniques

There are several useful techniques in electrochemical measurement. In this thesis, two of these methods were used: Cyclic Voltammetry (CV) and Potential Step Chronoamperometry (PC). These methods are potential controlled techniques where a desired voltage is applied and the resulting current is monitored.

### 2.8.1 Cyclic Voltammetry (CV)

Cyclic voltammetry (CV) is the most widely used electroanalytical technique for electrochemical reactions studies. Cyclic voltammetry provides qualitative data for a system of interest, including kinetics of heterogeneous electron transfer, thermodynamics of a redox process, of coupled chemical reactions, and of adsorption processes (Bockris et al. 2001). Quantitative data also can be obtained for a single charge transfer reactions (this will be described later in this section). The CV, the potential sweep technique, involves the application of a time-dependent potential at a stationary working electrode resulting in a triangular potential waveform illustrated in Figure 2.10.

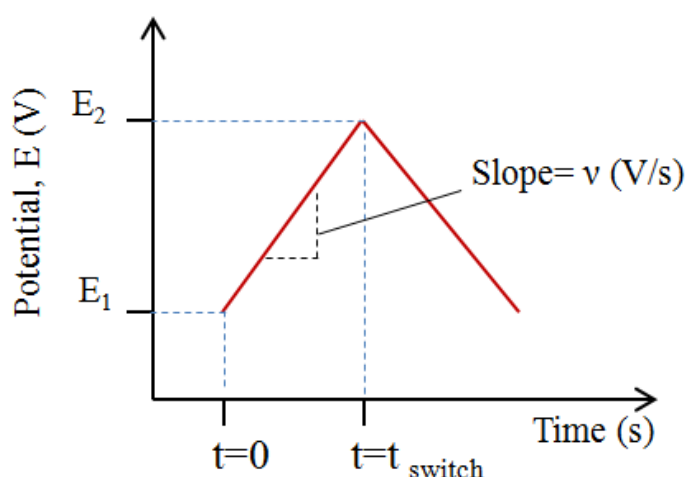


Figure 2.10 Triangular cyclic voltammetric form. The slope designate the scan rate (V/s)(Bockris et al. 2001)

A potential is scanned linearly from  $E_1$  which usually corresponds to negligible current flow at  $t=0$  to a given potential  $E_2$ . The potential is then swept back to the original value  $E_1$ , the time of the reverse scan represents the switching time. The potential difference  $E_2 - E_1$  is usually selected so that it includes the reduction and oxidation of species of

interest. If the redox reaction produces other compounds the potential difference is extended further to allow their characterisation. The resulting current that flows through the working electrode is recorded as a function of the potential applied, and a current-potential plot is constructed, referred to as a voltammogram (Figure 2.11). For a reduction reaction, when the scan starts at a potential well positive than  $E^{0'}$  (Figure 2.11), only non-Faradaic current (capacitive current) flows for some time. When the potential comes closer to  $E^{0'}$ , the reduction begins and the Faradaic current starts to flow. As the potential moves to more negative values the surface concentration of species,  $O$ , starts to drop as it is converted to  $R$ , thus the flux (and the current) increases. When the potential passes,  $E^{0'}$ , the surface concentration drops nearly to zero, the mass transport of  $O$  to the surface reaches a maximum then declines as a result of depletion to form products. The reduced species,  $R$ , follow the same trend as they are re-oxidized upon potential reversal scan, resulting in a similar shape of the forward peak, as shown in Figure 2.11.

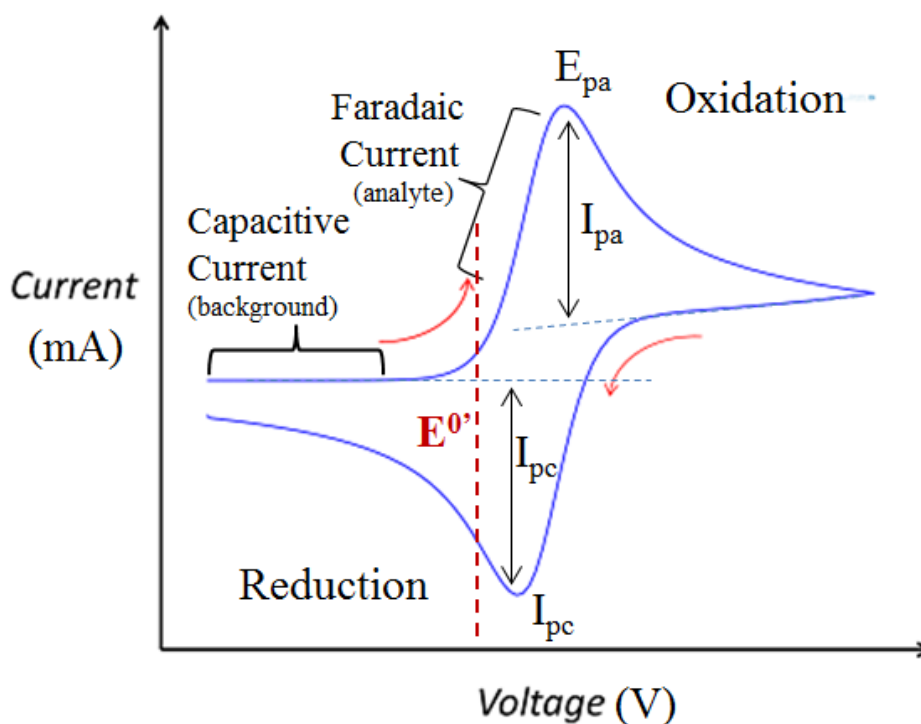


Figure 2.11 A representative cyclic voltammogram

## 2.8.1.1 Theory and Application of Cyclic Voltammetry:

### 2.8.1.1.1. Reversible and Irreversible Behaviour

Based on the different electrode kinetics, the electrochemical reactions can be described as reversible, quasi-reversible, or irreversible. In general, a system is said to be 'reversible' if the charge transfer is faster than the mass transport. On the other hand, if the charge transfer is slower than the mass transport the system is considered irreversible. The rate of an electron transfer reaction is measured by the standard electrochemical rate constant,  $k_s$ , while the mass transport is measured by the mass transport coefficient,  $m_T$ , which is proportional to the diffusion,  $D$ , of the species throughout the electrolyte and inversely proportional to the diffusion layer thickness,  $\delta$ :

$$m_T = \frac{D}{\delta} \quad \text{Eq. 2.53}$$

The diffusion layer thickness,  $\delta$ , depends on time,  $t$ , as  $\delta \sim \sqrt{Dt}$  and the time is given by  $t \sim RT/Fv$ , so the mass transport coefficient is given by Eq. 2.54:

$$m_T \sim \sqrt{\frac{D}{(RT/Fv)}} \quad \text{Eq. 2.54}$$

For a reversible cyclic voltammogram, the standard rate constant,  $k_s$ , is much faster than the mass transport coefficient:  $k_s \gg m_T$ . However, if the CV is irreversible the standard rate constant is much lower than the mass transport coefficient ( $k_s \ll m_T$ ).

#### 2.8.1.1.1.1 Nernstian Reversible System

Reversibility of a given system is determined based on the investigation of different parameters (e.g. current and potential correlation with the scan speed). So if a semi-infinite linear diffusion of a reversible reaction of reactant  $O$  to product  $R$  at a planar electrode is considered,



Applying Fick's second law (Eq. 2.19) along with the boundary conditions for species  $O$  and  $R$  (Eq 2.55-2.59):

$$\frac{\partial C_O(x, t)}{\partial t} = D_O \frac{\partial^2 C_O(x, t)}{\partial x^2} \quad \text{Eq. 2.55}$$

$$\frac{\partial C_R(x, t)}{\partial t} = D_R \frac{\partial^2 C_R(x, t)}{\partial x^2} \quad \text{Eq. 2.56}$$

$$C_O(x, 0) = C_O^*, C_R(x, 0) = 0, \quad \text{Eq. 2.57}$$

$$C_O(0, t) = 0 \quad (\text{for } t > 0) \quad \text{Eq. 2.58}$$

$$\lim_{x \rightarrow \infty} C_O(x, t) = C_O^*, \lim_{x \rightarrow \infty} C_R(x, t) = 0 \quad \text{Eq. 2.59}$$

Then, if the potential is held where no electrode reaction takes place  $E_i$ , the sweep the potential linearly at scan rate  $\nu$  (V/s) the potential as a function of time is expressed as:

$$E(t) = E_i - \nu t \quad \text{Eq. 2.60}$$

If the charge transfer at the electrode is assumed very rapid to keep the transfer in equilibrium, so that the Nernst equation (Eq. 2.4) applies. Rewriting Nernst equation with time-dependent form gives:

$$\frac{C_O(0, t)}{C_R(0, t)} = f(t) = e^{\frac{nF}{RT}(E_i - \nu t - E^0)} \quad \text{Eq. 2.61}$$

Using Laplace transform and integration (shown in Appendix A), the peak current  $i_p$  is given by

$$i_p = 0.4463 \sqrt{F^3/RT} n^{3/2} A D_O^{1/2} C_O^* \nu^{1/2} \quad \text{Eq. 2.62}$$

If  $A$  is in  $\text{cm}^2$ ,  $D_O$  in  $\text{cm}^2/\text{s}$ ,  $C_O^*$  in  $\text{mol}/\text{cm}^3$ , and  $\nu$  in  $\text{V}/\text{s}$  we calculate the second term of equation at  $25^\circ\text{C}$  we obtain the Randles-Sevcik equation (Bard & Faulkner 2002) (Compton Richard G 2010).

$$i_p = (2.69 \times 10^5) n^{3/2} A D_O^{1/2} C_O^* \nu^{1/2} \quad \text{Eq. 2.63}$$

The second characteristic of Nernstian wave is the difference of the peak potential  $E_p$  and the half peak potential  $E_{p/2}$  represented by the potential at  $i_p/2$  (Nicholson & Shain 1964).

$$|E_p - E_{p/2}| = 2.20 \left( \frac{RT}{nF} \right) = \frac{56.5}{n} mV \text{ at } 25^\circ C \quad \text{Eq. 2.64}$$

In a fully reversible system, the peak separation of cathodic to anodic peak potentials is  $56.5/n$  mV (Eq. 2.64). In practical applications, the potential range 60-70mV for a system is considered reversible. The peak potential  $E_p$  in a reversible process is independent of the scan rate as seen in Eq. 2.64, while the peak current,  $i_p$ , is proportional to the scan rate  $\nu^{1/2}$ , this means the system is diffusion controlled (Eq.2.63).

Therefore, diagnostics for a system implies that the,  $i_p$ , is plotted as function of  $\nu^{1/2}$  to determine if the process is diffusion controlled or adsorption dominated or else. The correlation is not always linear as described by theory at non planar electrodes (e.g. hemi-spherical electrode). The spherical correction (diffusion section) is very strong at slow scan rates where it is independent of the scan rate. At higher scan rates, however, the relationship of the current to the square root of the scan rate has a more linear profile.

### 2.8.1.1.2 Nernstian Irreversible System

A typical irreversible cyclic voltammogram is shown in Figure 2.12c. If we consider the irreversible reaction at planar electrode of species  $O$  to  $R$ :



The boundary value problem is similar to the previously described case and the equations also apply to this irreversible case. Eq. 2.60, however, is replaced by:

$$D_O \frac{\partial C_O(0, t)}{\partial x} = k_f(t) C_O(0, t) \quad \text{Eq. 2.65}$$

and the rate constant,  $k_f$ , is defined by:

$$k_f(t) = k^0 e^{-\alpha f(E_i - E^0)} \quad \text{Eq. 2.66}$$

The numerical solution of the integral equation for the irreversible reaction is obtained in a similar manner as described in the Appendix A1; the current  $i$  is given by:

$$i = FAC_O^* D_O^{1/2} \nu^{1/2} (\alpha F / RT)^{1/2} \pi^{1/2} \chi(\alpha f \nu t) \quad \text{Eq. 2.67}$$

Similarly the term  $\chi(\alpha fvt)$  was calculated by Nicholson and Shain (Nicholson & Shain 1964), it attains a maximum of 0.496. The equation becomes:

$$i_p = (2.99 \times 10^5) \alpha^{1/2} A C_0^* D_0^{1/2} \nu^{1/2} \quad \text{Eq. 2.68}$$

Eq. 2.73 still reflects the proportionality of the current with the square root of the scan rate due to the diffusion controlled process. However, the symmetry coefficient of the electron transfer process is included in the equation for irreversible case. If a single electron transfer for irreversible system is considered, unlike the reversible case, the peak separation is dependent on the scan rate is given by:

$$|E_p - E_{p/2}| = 1.857 \left( \frac{RT}{\alpha F} \right) = \frac{47.7}{\alpha} \text{ mV at } 25^\circ\text{C} \quad \text{Eq. 2.69}$$

The peak potential  $E_p$  is function of the scan rate, it shifts to more negative in reduction case by  $30/\alpha$  at  $25^\circ\text{C}$  for each ten-fold increase in  $\nu$ .

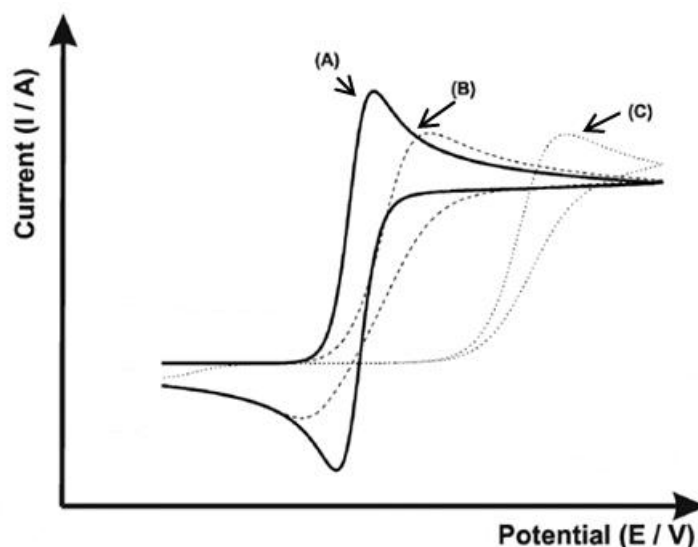


Figure 2.12 Cyclic voltammogram (a) reversible, (b) quasi-reversible, and (c) irreversible system (Zoski 2007)

A system is considered quasi-reversible (Figure 2.12b) if the reaction shows electron-transfer kinetic limitations. A quasi-reversible system exhibits a reversible behaviour at slow scan rate and irreversible at high scan rates.

### 2.8.1.1.2. Voltage Scan Rate and reversibility

When the potential is swept between  $E_1$  and  $E_2$  (Figure 2.11) the thickness of the diffusion layer,  $\delta$ , surrounding the electrode increases. The slower the scan rate the thicker is the diffusion layer. Conversely, the shorter time taken to sweep the voltage the thinner is the diffusion layer. As noted in the previous section, the thickness of the diffusion layer controls the mass transfer. Since the competition between the reversible and irreversible distinction reflects competition between the electrode kinetics and the mass transfer, this means the faster scan rates will encourage greater electrochemical irreversibility (Compton Richard G 2010). Consequently, it is not sensible to refer to a process as reversible or irreversible since all will tend to be irreversible if the voltammetry is taken at sufficiently high scan rates.

### 2.8.1.2 Coupled Chemical Reactions

The electrode reaction pathway can be quite complex, and proceeds in a sequence through multiple steps. The rate of such reactions is determined by the rate of the slowest step in the sequence (Wang 2006). The simplest reaction involves only mass transport of the electroactive species to the electrode surface (E), the electron transfer across the interface, and the transport of products back to the bulk solution (Figure 2.4). More complex reactions involve additional chemical and surface reactions that precede or follow the actual electron transfer. Hence, the current is limited either by the mass transport of the reactant or by the rate of the electron transfer. For complicated electrochemical processes, kinetic analysis involves the validation of the proposed mechanism and the extraction of the kinetic parameters from the experimental data (Zoski 2007).

For an elementary electrode reaction independent or unaffected by any chemical reactions or other processes (e.g. adsorption) can be characterised by specific diagnostic criteria. These include the ratio of the anodic peak current to the cathodic peak current ( $I_p^a/I_p^c$ ), and the peak to peak separation, the evaluation of the anodic to the cathodic peak current ratio and the peak cathodic current variation with the square root of the scan rate ( $I_p^c$  vs  $\sqrt{v}$ ). The latter two were described in the previous sections. If the ratio  $I_p^a/I_p^c$  is independent of the scan rate and equals unity, this indicates the absence or the unimportance of coupled chemical reactions.

The key variable factor determining the mass transfer rate is the scan speed  $v$ . Therefore, kinetic analysis relies on investigations of dependences of the CVs characteristic features on the scan rate. Since these analyses can be complex, depending on several factors that affect the process kinetics (e.g. concentration,  $C$ , diffusion coefficients  $D_0$ , rate constants  $k$ ), the factors are represented in dimensionless kinetic parameters.

Nicholson and Shain developed diagnostic criteria for mechanistic characterization of multi-step reaction systems (Nicholson & Shain 1964). It consists of a numerical method determining the dimensionless kinetic parameters and characteristic voltammograms shape which are specific for each mechanism. The main parameters are shown in Eq 2.70-2.72:

$$a = nFv/RT \quad \text{Eq. 2.70}$$

$$l = k_f + k_b \quad \text{Eq. 2.71}$$

And

$$K = \frac{k_f}{k_b} \quad \text{Eq. 2.72}$$

Where  $F$  is the Faraday constant,  $v$  is the scan rate,  $R$  is the universal gas constant,  $T$  temperature and  $K$  equilibrium constant

This criteria is valid for first-order (or pseudo first order) preceding CE, following EC, or catalytic EC' chemical reactions. Only the latter two reaction mechanisms are considered in this section.

### 2.8.1.2.1. $E_{\text{rev}}C_{\text{rev}}$ Reaction

In this process, a reversible heterogeneous electron transfer process on the electrode surface ( $E_{\text{rev}}$ ) is followed by a reversible homogeneous process ( $C_{\text{rev}}$ ) in the interfacial layer (Reaction 2.10).



The product,  $R$ , is generated by the electrochemical process forms non-electroactive species  $A$ . Three limiting cases exist. First, if the rate of the chemical reaction is fast the system will be in equilibrium at all times, the only effect will be the shift in the reversal anodic peak wave along the potential axis with large  $l/a$  values. Second, if the chemical reaction is very slow ( $l/a$  is small), so that during the experiment no chemical reaction takes place; hence the shape of the voltammogram is seen as a normal reversible shape at its original potential. The third limiting case is when the kinetic parameters  $l/a$  and  $\psi = K\sqrt{a/l}$  are large. In this instance, an irreversible curve is seen (Figure 2.13).

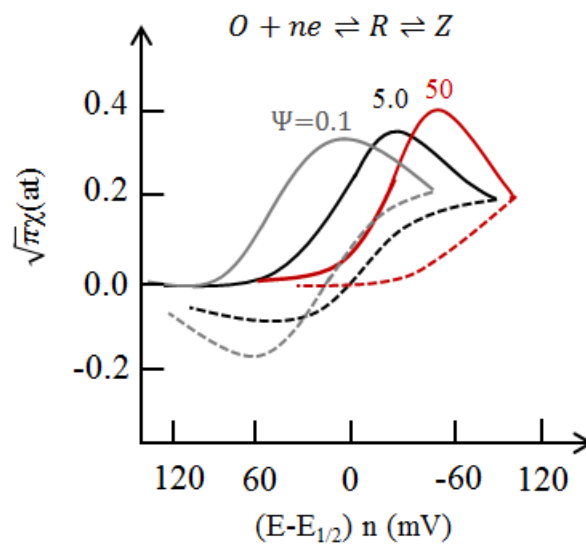


Figure 2.13 Normalised voltammograms for  $E_{rev} C_{rev}$  reaction for different values of kinetic parameter  $\psi$  ( $\psi = K\sqrt{a/l}$ ) (Nicholson & Shain 1964)

These limiting cases lead to the peak potential cathodic shift by about  $60/n$  mV for a ten-fold increase in  $\psi$  (Figure 2.13). The variation of the peak potential with  $\psi$  is a useful for characterizing the kinetic parameters from the cathodic scan. For small values of  $\psi$ , the curves approach reversible behaviour and the potential is independent of this parameter.

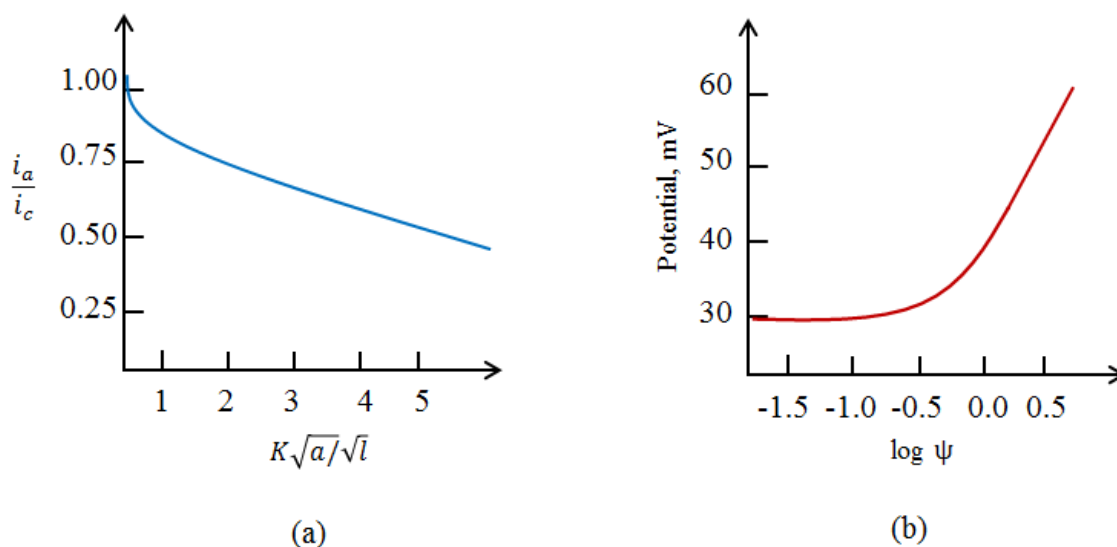


Figure 2.14 Nicholson and Shain criteria for  $E_{rev}C_{rev}$ . (a) Ratio of anodic to cathodic current as function of kinetic parameters. (b) Variation of the peak potential as function of kinetic parameters  $K\sqrt{a}/\sqrt{l}$  and  $\psi = K\sqrt{a}/\sqrt{l}$  (Nicholson & Shain 1964)

While for higher values of  $\psi$ , the peak potential shifts cathodically by about  $60/n$  mV for 10 folds increase in  $\psi$ . For intermediate values of  $\psi$ , a curve can be constructed as illustrated in Figure 2.14b. Both the position and the peak height of the anodic wave of the voltammogram are very sensitive to the kinetic parameter. Nicholson and Shain constructed a curve (Figure 2.14a) of current ratio  $i_p$  (anodic)/  $i_p$  (cathodic) as function of  $K\sqrt{a}/\sqrt{l}$ . The ratio approaches unity at slow scan rates and decreases at higher scan rates, this shows reversible behaviour in the former and irreversible profile in the latter as seen in Figure 2.13.

### 2.8.1.2.2. $E_{rev}C_{irrev}$ Reaction

If the charge transfer is irreversible, the succeeding chemical reaction will have no effect on the voltammogram. But if the equilibrium constant  $K$  is large ( $k_f \gg k_b$ ), the chemical reaction can be considered irreversible ( $E_{rev}C_{irrev}$ ):



This process is similar to the previous one except that the value  $k_f/a$  is small and the chemical reaction has little effect, so a reversible voltammogram is observed at its original potential.

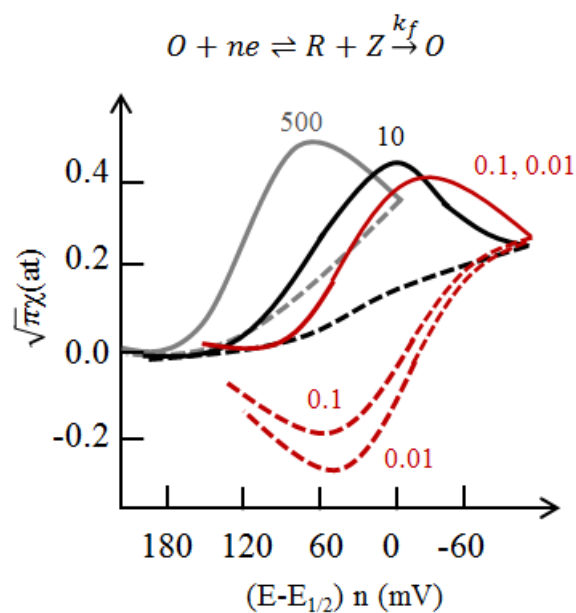


Figure 2.15 Normalised voltammograms for  $E_{rev}C_{irrev}$  reaction for different values of  $k_f/a$  (Nicholson & Shain 1964).

In  $E_{rev}C_{irrev}$  reaction, the potential is independent on  $k_f/a$  for small values of this parameter (Figure 2.15), while for large values, an anodic shift of about  $30/n$  mV is observed for a ten-fold increase in  $k_f/a$ . This case and also that for intermediate values of  $k_f/a$  are included in Figure 2.15.

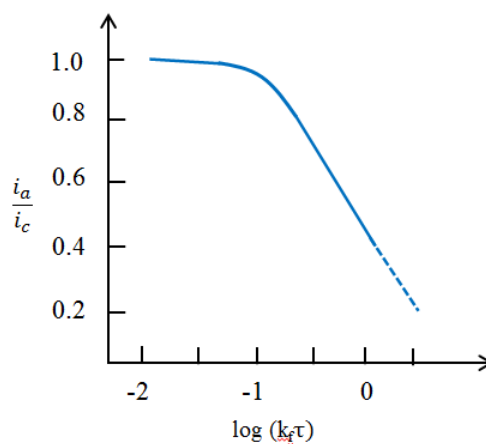


Figure 2.16 Nicholson and Shain criteria for  $E_{rev}C_{irrev}$ . Ratio of anodic to cathodic current as function of the kinetic parameters (Nicholson & Shain 1964).

Varying the  $k_f/a$  and the switching potential,  $E_\lambda$ , and for a constant value of the parameter  $k_f\tau$ , where  $\tau$  is the time in seconds from  $E_{1/2}$  to  $E_\lambda$ , the ratio of the cathodic to the anodic peak is constant (Figure 2.16) as function of  $k_f\tau$ . In this case, if the half-wave potential  $E_{1/2}$  is known, the rate constant can be calculated from the cyclic voltammogram curve.

### 2.8.1.2.3. EC' Catalytic Reaction

The catalytic mechanism is a special case where the electroactive species are regenerated chemically. Analysis of second order reactions is complex, and therefore with such a system we consider  $C_X^\infty \gg C_O^\infty$ . In this case the concentration of X remains constant throughout the experiment and the chemical reaction (Reaction 2.12) can be treated as pseudo first order.



Typical normalised curves are shown in Figure 2.17 for this case. The ratio of the catalytic peak current ( $i_k$ ) to the reversible peak (diffusive) current ( $i_d$ ) is plotted as function of  $(k_f/a)^{1/2}$  illustrated in Figure 2.18a. For values of  $k_f/a > 1$ , the plot is essentially linear. However, for  $k_f/a < 0.06$  the peak ratio  $i_k/i_d$  changes strongly with  $k_f/a$ . For accurate values of the rate constant at small values of  $k_f/a$ , a larger scale plot is needed (this can be obtained from tabulated data of Nicholson and Shain (Nicholson & Shain 1964)). The variation of the peak potential with change of  $k_f/a$  can also be obtained. At lower values of  $k_f/a$ , the peak potential is independent of the rate of the reaction and is constant at  $28.5/n$  mV, while if  $k_f/a$  increases, the peak potential shifts cathodically by about  $60/n$  mV for ten-fold increase in  $k_f/a$ . In the latter case, the peak becomes broader. For  $k_f/a > 1$  no peak is observed.

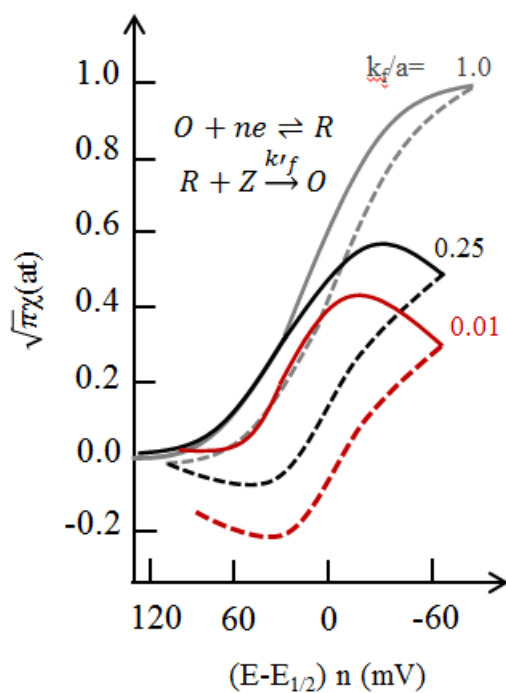


Figure 2.17 Normalised voltammograms to the scan rate for EC' catalytic reaction (Nicholson & Shain 1964)

Therefore, it is more convenient to correlate the half-peak potentials with  $k_f/a$  since it can be extended to a region where no peak is observed. When  $k_f/a$  is larger than about 10, the potential at which the current is equal to half of the limiting current is independent of the rate of the reaction and is equal to  $E_{1/2}$  (Figure 2.18b). If the potential is selected at least  $35/n$  mV cathodic of the peak potential, the anodic curve is the same shape as the cathodic curve, independent of both the switching potential and  $k_f/a$ . The ratio of cathodic current to anodic current is unity, exactly as in the reversible case. At  $k_f/a > 1$  no cathodic peaks or anodic peaks are observed, and on the anodic scan the current simply returns to zero at potentials corresponding to the cathodic wave.

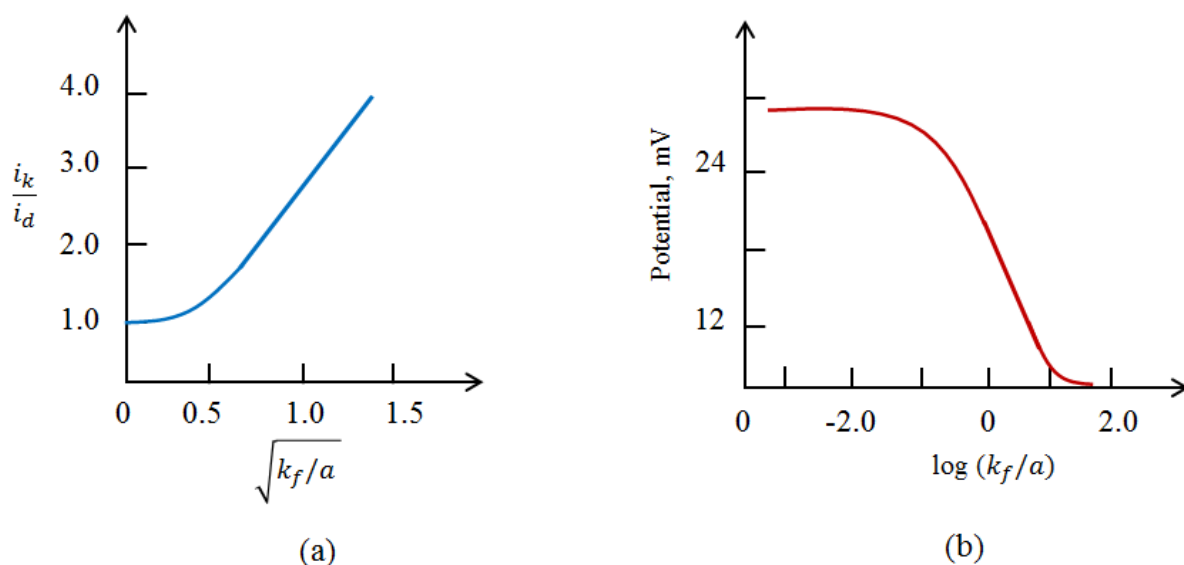


Figure 2.18 Nicholson and Shain criteria for EC' catalytic. (a) Ratio of kinetic to diffusive current as function of kinetic parameters. (b) Variation of the peak potential as function of kinetic parameters (Nicholson & Shain 1964).

Fitting the experimental voltammograms to theoretical curves by digital simulation is a necessary step to confirm the mechanism proposed. CV simulations become particularly important when surface processes prevail in an electrochemical system or higher reactions order (e.g. two-electron processes) are considered. In these cases, the Nicholson and Shain diagnostics are not valid.

## 2.8.2 Potential Step Chronoamperometry (CA)

The potential step chronoamperometry is another controlled potential method where this latter is fixed potential and the current response is monitored as a function of time. The wave-shape and the current-time curve of a potential step chronoamperometry are depicted in Figure 2.19a and Figure 2.19b, respectively. If the electrolysis of  $O$  initially present in the bulk solution precedes *via* a reaction at an electrode area  $A$  with a linear diffusion profile,  $O + ne \rightarrow R$ , is held at a potential  $E_1$  where no electrolysis occurs (Figure 2.19a). The current is given at any time by, Eq. 2.73:

$$i(t) = nF \frac{D_O}{\delta_O} C_O^*(t) \quad \text{Eq. 2.73}$$

At time  $t=0$  the potential is stepped to  $E_2$  value at which the electrolysis of the electroactive species,  $O$ , takes place. The response is observed as current drop as function of time.

The current is detected with large values initially. Since there has been little time before any depletion of the electroactive species, the concentration of these species,  $C_O^*$ , shortly after the applied potential step is very high. Hence, this explains the large values of the current seen at the beginning of the electrolysis. As the depletion takes place the thickness of the diffusion layer,  $\delta_o$ , increases and causes the current to drop during electrolysis (Figure 2.19).

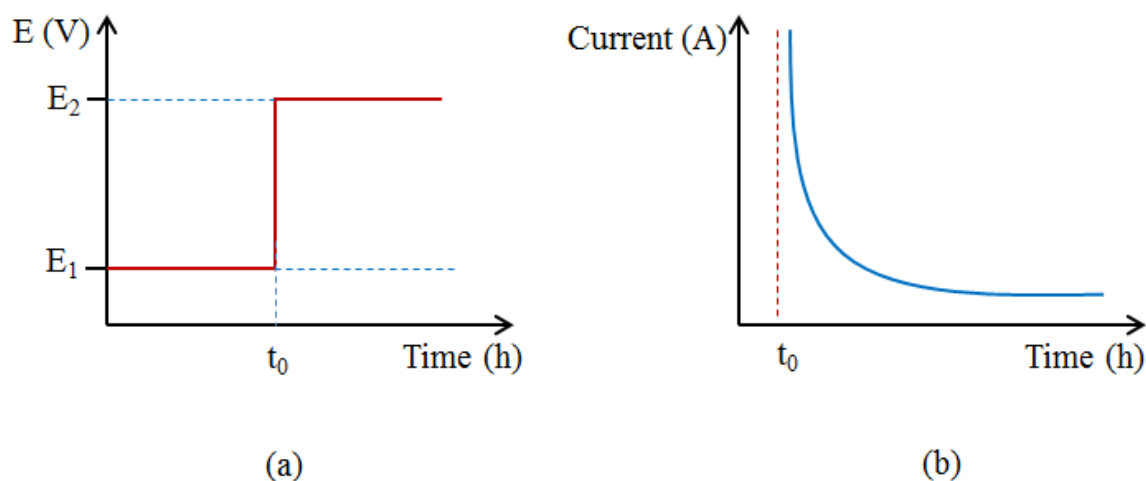


Figure 2.19 Schematic representation of chronoamperometry (a) Potential variation as function of time, (b) current variation as function of time.

### 2.8.3 Gas Chromatography (GC)

Chromatography is a widely used analytical technique for the separation of chemical compounds. It is based on differences in partitioning behaviour between a mobile phase and a stationary phase to separate chemical components in a mixture. In a gas chromatograph, the sample to be analysed is initially injected, where is vaporised in the instrument inlet, then is carried by an inert gas, commonly helium or argon, that acts as carrier (mobile phase). The sample components are carried through a fused silica tube packed with a finely divided solid or coated with a film of a liquid (stationary phase). The components move at velocities that are influenced by the degree of interaction of each constituent with the stationary non-volatile phase. The compounds having the higher interaction with the stationary phase are retained to a greater extent and consequently separate from those with smaller interaction. As the components elute from the column they are quantified by a detector (Fowlis 1995).

Being a simple, sensitive, and effective in separating components of mixtures, gas chromatography is one of the most important tools in various application including: chemical industry, environmental laboratories, forensic science, and pharmaceutical industries among others. It is used for quantitative and qualitative analysis of mixtures, for purity assessment of compounds such as water, food and drugs among other compounds. Gas chromatography is equally important in research laboratories for analysis of chemical products content from synthesis, biosynthesis or electrolysis. (Hübschmann 2009)

## 2.8.4 Mass Spectrometry (MS)

Mass spectrometry characteristics have raised it to distinguishable position among other analytical techniques: unequalled sensitivity, speed, detection limits and diversity of applications. Substances analysed by MS are identified based on their atomic sample composition of the molecules and their charge state (Edmond de Hoffmann 2007). As such, the analysis of unknown samples is possible since the MS does not require detailed pre-knowledge about a given sample composition.

Table 2.1 Cation fragments of methanol (CH<sub>3</sub>OH) detected in MS system

Ions	m/z
$CH_3OH^+$	32
$H_2C = OH^+$	31
$HC = O^+$	29
$H_3C^+$	15

A mass spectrometer creates a gas phase ions of compounds by electron ionisation. Energy imparted by the electron impact and, more importantly, instability in a molecular ion can cause that ion to break into smaller fragments. The molecular ion subsequently undergoes fragmentation. The produced ion fragments are then separated in the mass spectrometer by their mass-to-size ratio and are detected in proportion to their abundance. For instance, methanol (CH<sub>3</sub>OH) ion fragments into cation radicals (Table 2.1) with their corresponding abundance Figure 2.20.

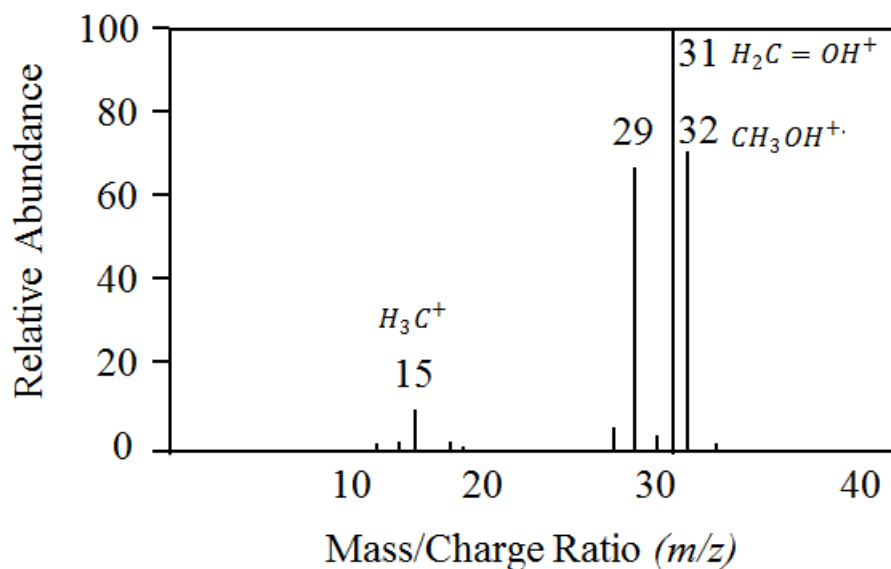


Figure 2.20 Characteristic methanol ( $\text{CH}_3\text{OH}$ ) cations mass spectrum

This section will outline the method development of the high resolution GC separation technique coupled to the powerful MS detection method.

### 2.8.4.1 Selected Ion Monitoring (SIM)

Conventional GCMS employs mass scanning that covers the molecular weight range of the compounds targeted. The mass range starts at the smallest fragmentation to the highest molecular weight of any compound detected. The full mass scan is estimated to be approximately  $1/6^{\text{th}}$  of the retention time width of any chromatographic peak. The scan time is ca. 300 ms (0.3 s) and is selected based on the number of full mass scans of interest for each chromatographic peak, which is a function of the peak width. This scanning type typically averages six mass spectra over the width of the peak to give full mass spectra of the compound peak. The sensitivity of the scan to any ion can be increased by using the scan time for fewer ions. In selected ion monitoring (SIM) mode, individual compound sensitivity may be increased to 10-100 times if fewer ions are selected for scanning. The sensitivity degrades as the number of ions selected for scanning is increased (Low et al. 1985).

The selection of ions in GCMS-SIM is based on the most abundant fragment ions in a given compound spectrum. For instance, ion 31 is the most abundant for methanol ( $\text{CH}_3\text{OH}$ ) (Table 2.1), this ion could be used for estimation of the alcohol amounts. This technique minimise interferences and enhance detection limits of small amounts of

targeted compounds. However, it frequently provides limited qualitative information since the mass spectrum of the target compound is not produced. This limitation becomes secondary if the method aim is the enhancement of the sensitivity in detection which provides more accurate quantification of the analyte to be analysed as is the case in this project (Klicic et al. 2002).

## 2.8.5 Headspace Gas Chromatography (HSGC)

Headspace gas chromatography (HSGC) is the most preferred technique for the analysis of volatiles and semi-volatile organics in liquid samples such as low molecular weight alcohols. HS is based on partitioning behaviour of a substance between the gas and the liquid phase, that contain solute  $i$  and a solvent  $j$ , Henry's constant,  $H_{ij}$ , defined at infinite dilution conditions, as:

$$H_{ij} = \lim_{x_i \rightarrow 0} \frac{f_i}{x_i} \quad \text{Eq. 2.74}$$

Where  $f_i$  is the fugacity of component  $i$  and  $x_i$  is its mole fraction in liquid phase. The primary advantage of HS analysis over direct injection is minimised contamination of the injector and the column with the solvent and other non-volatile substances in the sample to be analysed (Portari et al. 2007). In the HS analysis, the compound is forced into the headspace above a liquid sample in a sealed vial. This is done by heating the vial at typically 40°C to 60°C. The partitioning behaviour is often reported in terms of dimensionless Henry's constant or partition coefficient. This is defined as:

$$H_{ci} = \frac{C_g}{C_l} \quad \text{Eq. 2.75}$$

where  $H_{ci}$  is the dimensionless Henry's constant ( $H_{ci}$ ) or gas/liquid partition coefficient,  $C_g$  the gas phase concentration and  $C_l$  the liquid phase concentration of the species of interest (Teja et al. 2001) (Gupta et al. 2000).

## 2.8.6 GCMS Analysis Method

The accuracy in the identification and quantification of compounds is crucial in GCMS analysis. The assessment criteria of an accurate method include the test the reliability, reproducibility and capabilities of the method. In most regulatory authorities' specifications including International Union of Pure and Applied Chemistry (IUPAC),

International Conference on Harmonisation (ICH) and European Pharmacopoeia (EP), the following quantities are typically determined (Shrivastava & Gupta 2011):

### **2.8.6.1 Specificity**

Specificity describes how well a method discriminates target analytes from potential interferences. The investigation of specificity is usually conducted during the identification of the compounds and the determination of impurities. For chromatographic procedures, some typical chromatograms should be used to demonstrate specificity. The individual components should be appropriately labelled. (ICH CH et al. 1996).

### **2.8.6.2 Repeatability**

The repeatability is the measure of the variation of results between consecutive analyses carried on the same chromatograph by the same operator working in constant conditions. Repeatability should be assessed by: a) a minimum of 9 determinations covering the specified range for the procedure (e.g. three concentrations at three replicates each) or b) a minimum of six determinations. (ICH CH et al. 1996)

### **2.8.6.3 Reproducibility**

Reproducibility of a method measures the closeness of the results produced on different instruments by different operators. This quantity is usually important when the standardization of an analytical procedure is required in order to transfer it between laboratories. Since the method described in next sections is only intended for this work, the reproducibility of this method was not rigorously tested, although good repeatability was achieved between results produced by two operators at the same conditions.

### **2.8.6.4 Precision**

Precision expresses how tightly replicate results match each other; usually includes repeatability and reproducibility. An intermediate precision is reflected if measurements performed by different operators in the same laboratory on the same instrument but and over extended time frame.

## 2.8.6.5 Limit of Detection (LOD)

The limit of detection (LOD) is defined as the lowest measurable peak response of an analyte that is detected above typical system noise under the analysis conditions (ICH Expert Working Group 1996). Noise can be chemical or electronic in origin, but usually the focus is on the higher frequency noise when estimating the LOD.

The most common approach for determining the LOD is based on signal-to-noise ratio (S/N). This is performed by measuring the ratio of peak-to-peak noise around the analyte retention time, and the analyte peak signal. The noise magnitude is either estimated manually on a chromatogram printout, by the auto-integrator of the instrument or any other integration software. A reliable approach in determining the signal-to-noise, a S/N ratio of 3:1 or 2:1 is generally considered acceptable for estimating the detection limit as depicted in Figure 2.21 (ICH Expert Working Group 1996) (Shrivastava & Gupta 2011). The signal-to-noise ratio is calculated using the following equation:

$$S/N = 2H/h \quad \text{Eq. 2.76}$$

where  $h$  is the peak-to-peak background noise in a chromatogram obtained at half-height of the peak in the chromatogram obtained, and  $H$  is the height of the analyte peak, in the chromatogram obtained, and measured from the maximum of the peak to the extrapolated baseline of the signal observed over a distance equal to 20 times the width at half-height  $h$ . It is important that the system is free from significant baseline drift or shift during the estimation of LOD.

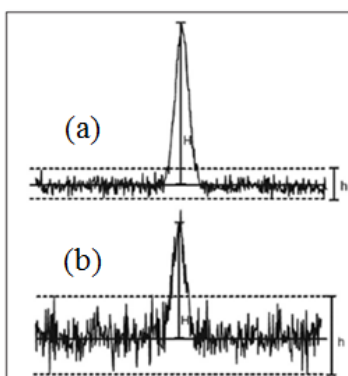


Figure 2.21 Signal-to-noise examples of (a) 10:1 and (b) 3:1 (Shrivastava & Gupta 2011)

## **2.8.6.6 Limit of Quantification (LOQ)**

The LOQ is the lowest analyte concentration that can be identified and quantified with acceptable precision and accuracy, in real samples, under the analysis conditions. The quantification can be performed based on S/N approach described in determination of LOD Section 2.8.6.6. A signal-to-noise ratio of 10:1 is considered acceptable for estimating the LOQ (Figure 2.21).

## **2.8.6.7 Linearity or Calibration**

The concentration range over which the target analyte can be quantified should be determined. The lower range limit should be determined by a standard sample in the range of LOQ. On the other hand, the highest range limit depends on the application and the analyst should be able to determine initially the maximum concentration needed for the calibration procedure.

Linearity is established by confirming that the analytical procedure provides an acceptable degree of repeatability and precision when applied to samples containing amounts of analyte within or at the extremes of the specified range of the analytical procedure. It is evaluated by the correlation coefficient of a plot of response signals as function of standards samples concentration 'calibration graph'.

The concentration of the analyte of interest is then determined from the calibration graph by extrapolation. To obtain a valid comparison for the unknown analyte response to that of the known standard samples, the data must be acquired and processed under identical conditions across the range of the analytical procedure. For the establishment of linearity, a minimum of five concentrations is recommended.

## References of Chapter 2

- Atkins, P. & De Paula, J., 2006. Ch. 13 - Atkins' physical chemistry. *Oxford University Press*.
- Bates, R.G. & Vijh, A.K., 1973. Determination of pH: Theory and Practice. *Journal of The Electrochemical Society*, 120(8), p.263.
- Bard, A. & Faulkner, L., 2002. Allen J. Bard and Larry R. Faulkner, *Electrochemical Methods: Fundamentals and Applications*, New York: Wiley, 2001. *Russian Journal of Electrochemistry*.
- Bockris, J.O., Reddy, A.K.N. & Gamboa-Aldeco, M., 2001. Modern Electrochemistry 2A, Fundamentals of Electrode Processes. *Annals of the New York Academy of Sciences*, 1228, pp.1–817.
- Compton Richard G, C.E.B., 2010. Understanding Voltammetry (2<sup>nd</sup> Edition). *Imperial College Press*.
- Crow, D.R., 1994. Principles and Applications of Electrochemistry, 4<sup>th</sup> Edition.
- Edmond de Hoffmann, V.S., 2007. Wiley: Mass Spectrometry: Principles and Applications, 3<sup>rd</sup> Edition - Edmond de Hoffmann, Vincent Stroobant. , p.502.
- Hübschmann, H.-J., 2009. *Handbook of GC/MS: Fundamentals and Applications*, John Wiley & Sons.
- ICH CH et al., 1996. Validation of Analytical Procedures : Text and Methodology. In pp. 1–11.
- Low, I.A. et al., 1985. Selected ion monitoring mass spectrometry: Parameters affecting quantitative determination. *Biological Mass Spectrometry*, 12(11), pp.633–637
- Nicholson, R.S. & Shain, I., 1964. Theory of Stationary Electrode Polarography. *Analytical chemistry*, 36(4), pp.706–723.
- Rieger, P.H., 1994. *Electrochemistry*, Springer Science & Business Media.
- Scholz, F., 2010. *Electroanalytical Methods* F. Scholz et al., eds., Berlin, Heidelberg: Springer Berlin Heidelberg.
- Shrivastava, A. & Gupta, V., 2011. Methods for the determination of limit of detection and limit of quantitation of the analytical methods. *Chronicles of Young Scientists*, 2(1), p.21.
- Wang, J., 2006. *Analytical Electrochemistry*, Hoboken, NJ, USA: John Wiley & Sons, Inc.
- Zoski, C.G., 2007. *Handbook of Electrochemistry*. In *Handbook of Electrochemistry*. Elsevier.

# Chapter 3 Overview of the Recent Literature

The aim of this Chapter is to provide a context for the present work, which involves the pyridine ( $C_5H_5N$ )/pyridinium assisted reduction of  $CO_2$  to methanol ( $CH_3OH$ ) at platinum (Pt) electrodes. This electrochemical system was originally reported by Bocarsly and co-workers. This Chapter reviews the major recent studies of the electrochemical  $CO_2$  reduction to various products with a focus on methanol ( $CH_3OH$ ) formation on different metals/materials and conditions. The first part outlines the thermodynamic challenge of  $CO_2$  activation and the benefit the electrochemical route can bring in terms of tuning the energy input to drive such reaction. Next, a review is presented of the direct  $CO_2$  reduction at metal electrodes with a catalytic activity toward the formation of products such as carbon monoxide (CO), formate ( $HCOO^-$ ) and formic acid (HCOOH). Mechanisms for the  $CO_2$  reduction mechanism on platinum are reported.  $CO_2$  reduced methanol ( $CH_3OH$ ) is also reviewed with a focus on the reported Faradaic efficiencies. A detailed report on the pyridinium history as a catalyst for  $CO_2$  reduction to methanol ( $CH_3OH$ ) follows. Finally, in view of the importance of the catalyst role in the present study, the early work on the reduction of pyridine ( $C_5H_5N$ ) and derivatives on metals is presented.

## 3.1 Electrochemical $CO_2$ Reduction

Systems for the electrochemical reduction of  $CO_2$  involve the use of active metal or material electrodes capable of converting electrical energy (from a renewable source) to the reduced form of  $CO_2$ . The chemical reactivity of  $CO_2$  is low due to the thermodynamic stability of the molecule being the highest oxidised form of carbon, with a large standard Gibbs free energy of formation ( $\Delta G^0 = -349.67$  kJ/mol) (Green, D.W. ; Perry). Therefore, the activation process of  $CO_2$  requires high energy input. The formation energies of the most common  $CO_2$  reduced products together with the standard and equilibrium potentials (pH 7) are summarized in Table 3.1 ( $E^0$  and  $E_{eq}$  at pH 7 in aqueous solution versus standard hydrogen electrode (SHE),  $25^\circ C$ , 1 atm for gases and 1M for solute) (Qiao et al. 2014) (Augustynski et al. 1996).

Table 3.1 Reduction potential and formation energy for various CO<sub>2</sub> reduced products (Aresta 2003, p. 279)

<b>Reaction</b>	<b>E<sup>0</sup> V vs. SHE</b>	<b>E<sub>eq</sub> V vs. SHE (pH7)</b>	<b>ΔG<sup>0</sup> kJ/mol</b>
$2H^+ + 2e^- \rightleftharpoons H_2$	0	-0.42	0
$CO_2 + 2H^+ + 2e^- \rightleftharpoons CO + H_2O$	-0.103	-0.52	+20
$CO_2 + 2H^+ + 2e^- \rightleftharpoons HCOOH$	-0.199	-0.61	+38
$CO_2 + 4H^+ + 4e^- \rightleftharpoons HCOH + H_2O$	-0.028	-0.45	+10
$CO_2 + 6H^+ + 6e^- \rightleftharpoons CH_3OH + H_2O$	+0.031	-0.38	-18
$CO_2 + 8H^+ + 8e^- \rightleftharpoons CH_4 + 2H_2O$	+0.169	-0.25	-130

The Gibbs energy was calculated using the half standard potential equation:  $E^0 = -\Delta G/nF$ , where n is the number of electrons involved in the reaction and F is the Faraday number (96484.6C/mol).

Among the reactions involving CO<sub>2</sub> reduction (Table 3.1), methanol (CH<sub>3</sub>OH) and methane formation reactions are exothermic. At first glance, they may seem to be spontaneous reactions. Yet, the formation of these fuel products is believed to proceed through 2e<sup>-</sup> (CO) and 4e<sup>-</sup> (formic acid) reductions (Hori 2008). It is clear that the production of these precursor compounds (Table 3.1) involves reactions with a positive free energy of formation ( $\Delta G^0 > 0$ ), and thus are not thermodynamically favoured (endothermic reactions) (Smith 2010). In addition, from an electrochemical perspective, the equilibrium potentials of the CO<sub>2</sub> reduced products (pH 7) are not very positive as compared with the hydrogen (H<sub>2</sub>) reduction equilibrium potential as seen in Table 3.1. Thus, the hydrogen evolution reaction (HER) often competes with the CO<sub>2</sub> reduction (Hori 2008).

Moreover, it is important to note that the  $\Delta G^0$  values represented in Table 3.1 involve the use of hydrogen which is supplied by an external source or via a water splitting reaction. So if the total formation energy involving the reduction of CO<sub>2</sub> and the water splitting is considered; the production of methanol (CH<sub>3</sub>OH), for instance, at standard conditions, simultaneously with the water oxidation, requires the net breaking of C=O bonds and O-H bonds and the net formation of O=O and C-H bonds. This requires a total of +730kJ/mol CO<sub>2</sub>, which is equivalent to -1.26V vs. SHE over a 6 electron process.

Table 3.2 shows the energy stored or potential required for the CO<sub>2</sub> reduced products presented in Table 3.1 simultaneously with the hydrogen formation from water splitting.

Table 3.2 Reduction potential and energy stored per mole of CO<sub>2</sub> for various products and water reduction processes.

Reaction	E <sup>0</sup> V vs. SHE	ΔG <sup>0</sup> kJ/mol
$H_2O \rightleftharpoons H_2 + \frac{1}{2}O_2$	-1.23	+237
$CO_2 \rightleftharpoons CO + \frac{1}{2}O_2$	-1.33	+256
$CO_2 + H_2O \rightleftharpoons HCOOH + \frac{1}{2}O_2$	-1.43	+276
$CO_2 + H_2O \rightleftharpoons HCOH + O_2$	-1.25	+482
$CO_2 + 2H_2O \rightleftharpoons CH_3OH + \frac{3}{2}O_2$	-1.26	+730
$CO_2 + 2H_2O \rightleftharpoons CH_4 + 2O_2$	-1.40	+1080

Given that, the CO<sub>2</sub> reduction combined with the hydrogen generation is energetically an uphill process (Table 3.2), the thermodynamically unfavourable reactions cannot be easily driven chemically at ambient conditions (Jessop et al. 1994). On the other hand, the electrochemical techniques are unique in that the energy input can be controlled by an applied electrode potential, thus driving otherwise thermodynamically unfavourable reactions. The standard potential of reaction,  $E^0$ , determines the thermodynamic lower bound for the applied potential required to form equal concentrations of products and reactants at equilibrium. In order to drive an unfavourable reaction to products formation at a given rate, additional energy is required beyond the standard free energy known as ‘overpotentials’. The energy supplied above the standard potential,  $E^0$ , offers control over the product selectivity and production rate, which are important for both energy storage and industrial process implementation (Ganesh 2011), as well as overcoming the activation barrier for a given reaction.

The product selectivity and production rate are important parameters in the electrochemical CO<sub>2</sub> reduction. These are measured by the Faradaic efficiency (FE) of a system. The FE of a given electrochemically generated product is the ratio of the actual

and the theoretical amounts of a product formed within the same electrolysis time, based on the number of coulombs passed.

$$Efficiency (\%) = Q_{red}/Q_t \quad \text{Eq. 3.1}$$

Where

$$Q_{red} = n_{moles} \times n_e \times F \quad \text{Eq. 3.2}$$

$$Q_t = Ixt \quad \text{Eq. 3.1}$$

And

Where  $Q_{red}$  (in coulombs, C) is the charge involved in the electroreduction of  $CO_2$  to form a particular product,  $Q_t$  (in coulombs, C) is the total (measured) charge passed through the electrolysis cell,  $n_{moles}$  (in moles) is the number of moles of organic molecule produced,  $n_e$  is the number of electrons required for the reduction of  $CO_2$  to form a product,  $F$  is the Faraday constant ( $96484.6 \text{ C mol}^{-1}$ ),  $I$  (in amperes, A) is the electrolysis current and  $t$  (in seconds, s) is the time of electrolysis.

To summarise, an efficient electrochemical system should have:

- High selectivity and Faradaic yield or efficiency toward a chosen product
- Minimum energy input (or low overpotential)
- Current density high enough to ensure commercial application

### 3.1.1 Direct Electrochemical $CO_2$ Reduction

Fundamental studies of the electrochemical reduction of  $CO_2$  started as early as the 19<sup>th</sup> century, and have been further promoted in recent years. In the last two decades, numerous reports on direct  $CO_2$  reduction have been published at various metal electrodes in aqueous electrolytes. The use of aqueous electrolytes represents an attractive option as water is seen as a non-expensive proton source (Hori 2008). Furthermore, electrochemical reduction of  $CO_2$  in aqueous media is much more economic than in organic solvents. However, HER usually competes with  $CO_2$  reduction. Table 3.3 summarizes the  $CO_2$  reduction products at various metal electrodes at ambient pressure and 30 bar of  $CO_2$  adopted from Hori (Hori 2008) presented in the next section.

### 3.1.1.1 Reduction of CO<sub>2</sub> on Metals and Other Material Electrodes to CO, HCOO<sup>-</sup> and HCOOH

One of the first applications of electrochemical reactions yielding chemical products was the reduction of CO<sub>2</sub> in aqueous sodium bicarbonate to HCOOH (Beck et al. 2010). Since then, the electrochemical reduction of carbon dioxide has been directed toward the study of the effect of the electrode materials and the electrolyte media on the nature of the products (Hori 2008). The electrode material in the direct reduction plays a catalytic role to electrochemically reduce CO<sub>2</sub>; the product selectivity of CO<sub>2</sub> electroreduction depends on the electroactivity of a particular electrode material and the nature of the electrolyte used in the reduction process (Sánchez-Sánchez et al. 2001) (Jitaru et al. 1997). The products seen most often for metal electrodes are CO, formate and formic acid (Hori 2008).

Reduction of CO<sub>2</sub> at metal surfaces has generally occurred at high overpotentials, often with large competing hydrogen evolution rates especially in aqueous solutions. Therefore, many studies were carried out in aqueous solutions at metal electrodes with high hydrogen overvoltage such as mercury (Hg) and lead electrodes. One of the successful CO<sub>2</sub> reductions was reported by Eyring, where formate was produced with 100% Faradaic efficiency on a mercury (Hg) electrode (Beck et al. 2010). Later, transition metals were extensively studied as electrode materials. CO<sub>2</sub> reduction was studied at Zn, Sn, In, Cd, and Pd electrodes in hydrogen carbonate electrolytes with various alkali metal cations. Ito et al have reported the exclusive production of formic acid on these metal electrodes. The highest Faradaic efficiency (92%) was achieved at 3.9 mA cm<sup>-2</sup> at around -1.4V vs. SHE in 0.2M LiHCO<sub>3</sub> at In electrode. Hori and co-workers reported the reduction at 5 mA/cm<sup>2</sup> in aqueous KHCO<sub>3</sub>, CO, CH<sub>4</sub>, formic acid and hydrocarbons at ambient temperature and pressure. This group performed full chemical analysis and studied the Faradaic balance; the product selectivity was found to be dependent on the electrode metal (Hori et al. 1985).

Transition metals for CO<sub>2</sub> reduction fall into two groups, illustrated in Table 3.3 (Hori 2008) for the electrolyses performed at a current density of 5 mA/cm<sup>2</sup> and at ambient pressure. The first group (Au, Ag, Zn, Pd, and Ga) are those metals that form CO as the major product at generally relatively low overpotentials (ca. -1.2V to -1.5V vs. SHE).

Table 3.3 Metal electrode reductions of CO<sub>2</sub> in aqueous electrolyte, grouped by reduction product (Adapted from Hori, et al).

Electrode Material	Product	Potential (V) vs. SHE	Current density (mA/cm <sup>2</sup> )	Faradaic efficiency (%)	Other products
CO as the main product					
Au	CO	-1.14	5.0/1.0a	87.1/93.4a	HCOOH(0.7), H <sub>2</sub>
Ag	CO	-1.37	5.0	81.5	HCOOH(0.8), H <sub>2</sub>
Zn	CO, HCOO <sup>-</sup>	-1.54	5.0	79.4,6.1	H <sub>2</sub>
Pd	CO	-1.20	5.0	28.3	H <sub>2</sub> ,CH <sub>4</sub> , HCOO <sup>-</sup>
Ga	CO	-1.24	5.0	23.2	H <sub>2</sub>
HCOO <sup>-</sup> as the main product					
Hg	HCOO <sup>-</sup>	-1.51	0.5	99.5	H <sub>2</sub>
Pb	HCOO <sup>-</sup>	-1.63	5.0	97.4	H <sub>2</sub>
Tl	HCOO <sup>-</sup>	-1.60	5.0	95.1	H <sub>2</sub>
In	HCOO <sup>-</sup>	-1.55	5.0	94.9	H <sub>2</sub> , CO
Sn	HCOO <sup>-</sup> , CO	-1.48	5.0	88.4,7.1	H <sub>2</sub>
Cd	HCOO <sup>-</sup> , CO	-1.63	5.0	78.4,13.9	H <sub>2</sub> , CH <sub>4</sub>
Bi	HCOO <sup>-</sup>	-1.56	1.2	77.0	H <sub>2</sub>
Electrochemical reduction of CO <sub>2</sub> under pressure of 30 bar					
HCOOH as the main product					
Pb	HCOOH	-1.35	163	95.5	H <sub>2</sub> ,CH <sub>4</sub> ,C <sub>2</sub> H <sub>6</sub>
Sn	HCOOH	-1.39	163	92.3	H <sub>2</sub> ,CO, CH <sub>4</sub>
In	HCOOH	-1.55	200	90.1	H <sub>2</sub> ,CO, CH <sub>4</sub>
Bi	HCOOH	-1.42	150	82.7	H <sub>2</sub> ,CO, CH <sub>4</sub>
Cu	HCOOH	-1.64	163	53.7	H <sub>2</sub> ,CO, CH <sub>4</sub> , H <sub>2</sub> ,C <sub>2</sub> H <sub>6</sub>
Pt	HCOOH	-1.48	163	50.4	H <sub>2</sub> ,CO, CH <sub>4</sub>
Pd	HCOOH	-1.76	500	44.0	H <sub>2</sub> ,CH <sub>4</sub>
W	HCOOH	-1.61	163	31.9	H <sub>2</sub> ,CO
Fe	HCOOH	-1.63	163	28.6	H <sub>2</sub> ,CO, CH <sub>4</sub>
Co	HCOOH,CO	-1.54	163	21.9,15.8	H <sub>2</sub> ,CH <sub>4</sub>
Mo	HCOOH	-1.34	163	6.5	H <sub>2</sub> ,CH <sub>4</sub>
CO as the main product					
Au	CO	-1.30	163	64.7	H <sub>2</sub> ,HCOOH(12%),CH <sub>4</sub>
Ag	CO	-1.48	163	75.6	H <sub>2</sub> ,HCOOH(17%),
Rh	CO	-1.41	163	61.0	CH <sub>4</sub>
Zn	CO,HCOOH	-1.70	163	48.7,40.5	H <sub>2</sub> ,HCOOH, H <sub>2</sub> ,CH <sub>4</sub>
Pd	CO,HCOOH	-1.56	163	46.1,35.6	H <sub>2</sub> ,CH <sub>4</sub>
C	CO,HCOOH	-1.68	50	44.0,30.2	H <sub>2</sub> ,CH <sub>4</sub>
Ni	CO,HCCOH	-1.59	163	33.5,31.3	H <sub>2</sub> ,CH <sub>4</sub>
Cr	CO	-1.49	163	11.8	HCOOH, CH <sub>4</sub>

Au and Ag proved to be very good catalysts toward CO selective production with Faradaic efficiencies of 87-93.4% and 81.5%, respectively (Table 3.3), followed by Zn which produced CO at a Faradaic yield of 79.4% and formate at 6.1%. Pd and Ga also produce CO with Faradaic efficiencies of 28.3% and 23.2%, respectively. The second group of metals are those that form formate, generally at higher overpotentials

including: Pb, Hg, In, Sn, Cd, Ti and Bi which form formate ions as the main product at higher overpotentials with Faradaic efficiencies ranging between 77-99.5%.

Other workers also achieved high Faradaic yields of formate formation by reducing CO<sub>2</sub> on Cu and Zn cathodes. Udupa et al reduced CO<sub>2</sub> to formic acid with Faradaic efficiency of 81% and a maximum concentration of 200 g l<sup>-1</sup> at a cell potential of -3.5V and a current density of 20mA cm<sup>-2</sup>. The reduction was achieved on a rotating amalgamated Cu cathode in 10% sodium sulphate with CO<sub>2</sub> separated by a cation-exchange membrane from a lead electrode in the anodic compartment (Udupa et al. 1971). Using Zn amalgam electrodes Coehn and Jahn were able to reduce aqueous CO<sub>2</sub> with 89% Faradaic yield of formic acid (Vassiliev et al. 1985). Ehrenfield, however, enhanced the Faradaic yield further to 95% using the same electrode in ammonium carbonate electrolyte (Vassiliev et al. 1985). Another highly efficient CO<sub>2</sub> reduction by Rabinowitsch and Maschoertz who used sodium amalgam cathodes with 2% CO<sub>2</sub> saturated aqueous NaHCO<sub>3</sub>, at a current density of 16 to 25 mA cm<sup>-2</sup>, the Faradaic yield of formic acid reached 86-97% (Vassiliev et al. 1985). The metal group Ni, Fe, Pt, and Ti does not give a product from CO<sub>2</sub> reduction continuously, due to HER competition prevailing at such surfaces.

In addition to the products reported in Table 3.3 other products were also produced such as malate, carboxylic acids, and glycolate. Bewick and Greener reported the production of malate at Hg electrodes and glycolate at Pb electrodes in high yield in aqueous tertaalkyl ammonium solutions (Bewick & Greener 1970); these results were then investigated by Kaizer and Heitz but were not reproduced. No formation of oxalic acid was seen in aqueous solutions. These authors have shown the reduction of oxalic acid to glyoxylic and maleic acids at Ni, Al, Pb and Hg electrodes in the presence of quarternary ammonium salts (Noda et al. 1989). On the other hand, some other studies confirmed the oxalic acid formation in basic aqueous solutions of tertamethylammonium chloride and tertamethylammonium hydroxide at Hg in addition to glyoxylic acid and formate (Noda et al. 1989). From these series of experiments in aprotic electrolytes and mixtures of aqueous and aprotic electrolytes, it was concluded that the activity of Pt and Ni under elevated CO<sub>2</sub> pressure proceeds in a similar way to the case in aprotic solvents since the solubility of CO<sub>2</sub> is enhanced in both cases.

In an attempt to enhance the CO<sub>2</sub> concentration in the electrolyte and to increase the transport rate, the reduction of CO<sub>2</sub> was investigated at elevated pressures. Hara et al have reported the reduction of CO<sub>2</sub> at 30bar at metal electrodes, some of which have higher activity at elevated pressures. The metal electrodes are divided into two groups forming CO and HCOOH (Table 3.3). The metal electrodes Sn and Bi have the preferential formation of formic acid as seen at atmospheric pressure with high FE of 88.4% and 77%, respectively. These FE increase by 5% and 7% respectively, at 30bar with relatively low overpotentials. Pt and Ni did not yield products continuously in CO<sub>2</sub> reduction in aqueous solutions at ambient pressures according to Hori and co-workers. At these electrodes, CO is a strongly adsorbed which totally covers these surfaces, preventing further reduction of CO<sub>2</sub>. The adsorption of CO on Pt is discussed in the results section.

The hydrogen evolution reaction, however, is favoured in this case in aqueous solutions and ambient pressure. At 30bar of CO<sub>2</sub> and current density of 163mA/cm<sup>2</sup>, these electrodes can reduce CO<sub>2</sub> in aqueous KHCO<sub>3</sub> yielding HCOOH at 50% and CO at 33% Faradaic efficiencies at Pt and Ni respectively (Hara et al. 1995). Moreover, Kedzierzawski and Augustynski achieved 93% of CO Faradaic efficiency at Au electrode at -0.95 vs. SHE (Augustynski et al. 1996). Similar FE of 92% for CO production were also achieved by Dufek and co-workers at 20 bar and 350mA/cm<sup>2</sup> (Dufek et al. 2012). The apparent increase of the catalytic activity is believed to derive from the CO<sub>2</sub> concentration increase in the electrolyte. Moreover, the enhancement of the reduction rate is accompanied by the possibility of controlling the product selectivity by elevating the pressure. For instance, a Pd electrode which forms CO at 1 atm, yields HCOOH at 30 bar and 1mA cm<sup>-2</sup> in 0.5M KHCO<sub>3</sub>.

Hara et al reported the reduction of CO<sub>2</sub> on Pt to HCOOH and CO with Faradaic efficiencies of 50.4% and 6.1% respectively at 30 bar with a current density of 163mA/cm<sup>2</sup>. CO was detected as the major reduction product on Ag and Au electrodes, even at 30 bar, with FE of 76% and 65% respectively (Hara et al. 1995). These results show that the product selectivity of predominant CO formation on these electrodes remains unchanged at higher pressure. However, the Faradaic efficiencies for the formation of formic acid on Ag and Au cathodes at constant current density of 5 mA/cm<sup>-2</sup> and CO<sub>2</sub> pressure of 1 bar are very small (e.g. 1.6% and 0.4%, respectively) (Hori et al. 1985). Hara and co-worker detected formic acid with 17% and 12%

Faradaic efficiencies at 30 bar on Ag and Au electrodes respectively, indicating the favourable formation of formic acid at high pressures. Overall, the reduction of CO<sub>2</sub> at elevated pressure seems encouraging in terms of increasing the Faradaic efficiencies of the products. Therefore, this technique was used in attempts to increase the Faradaic efficiencies of methanol (CH<sub>3</sub>OH) in this thesis. However, the nature of the electrochemical interaction of CO<sub>2</sub> with metals is not completely clear; some mechanistic insights on Pt are reported herein.

### **3.1.1.1.1. Mechanistic Aspects of the Direct CO<sub>2</sub> Reduction on Pt**

The reduction of CO<sub>2</sub> at Pt electrodes has long been studied. Platinum is well known for its effective catalytic activity toward HER. This has been rationalized by the low energy for both adsorption and desorption of protons and molecular hydrogen through Pt-hydrogen hydrides on the cathode surface, resulting in low free energy changes and facilitating the formation of intermediates. Moreover, Pt cathodes have low kinetic barriers for surface hydride formation due to the low barriers for the activation of these intermediates (Markovic 2002). Unlike many other materials, Pt preferentially forms molecular hydrogen in aqueous solutions rather than carbon-based products. For this reason, Hori et al have focused on materials with low HER rates such as Hg, In and Pb for CO<sub>2</sub> reduction studies at 1bar in order to suppress HER (Hori 2008).

On the other hand, at elevated pressures of CO<sub>2</sub>, carbon-based reduction products are observed for platinum electrodes as reported earlier (Table 3.3). Similarly, when the ratio of H<sub>2</sub>O and CO<sub>2</sub> was modulated in a mixed acetonitrile and water system, it was found that the formate production rate was greater than H<sub>2</sub> formation rate at CO<sub>2</sub> to H<sub>2</sub>O molecular ratios between 0.1 and 1 (Tomita et al. 2000). However, this was achieved at lower Faradaic yields (65%) and higher overpotentials at Pt in comparison to other transition metals. At other electrode metals, product distributions also changed upon pressure increases; however the effect was particularly prominent on Pt indicating that these surfaces are good catalysts for CO<sub>2</sub> reduction at conditions where HER is minimal. Surprisingly, Pt surfaces were reported to favour methanol (CH<sub>3</sub>OH) production by pyridinium assisted CO<sub>2</sub> reduction as this is discussed in the next sections.

### 3.1.2 Catalytic Electrochemical Reduction of CO<sub>2</sub>

To be economically viable the electrochemical reduction of CO<sub>2</sub> should be energetically efficient with a high reaction rate. Although not often discussed in the literature, the energetic efficiency is a critical parameter as it measures the recovery of the energy used in product formation; hence it determines its energy cost. High energetic efficiency is achieved through high Faradaic efficiency and low overpotentials (Figure 3.1).

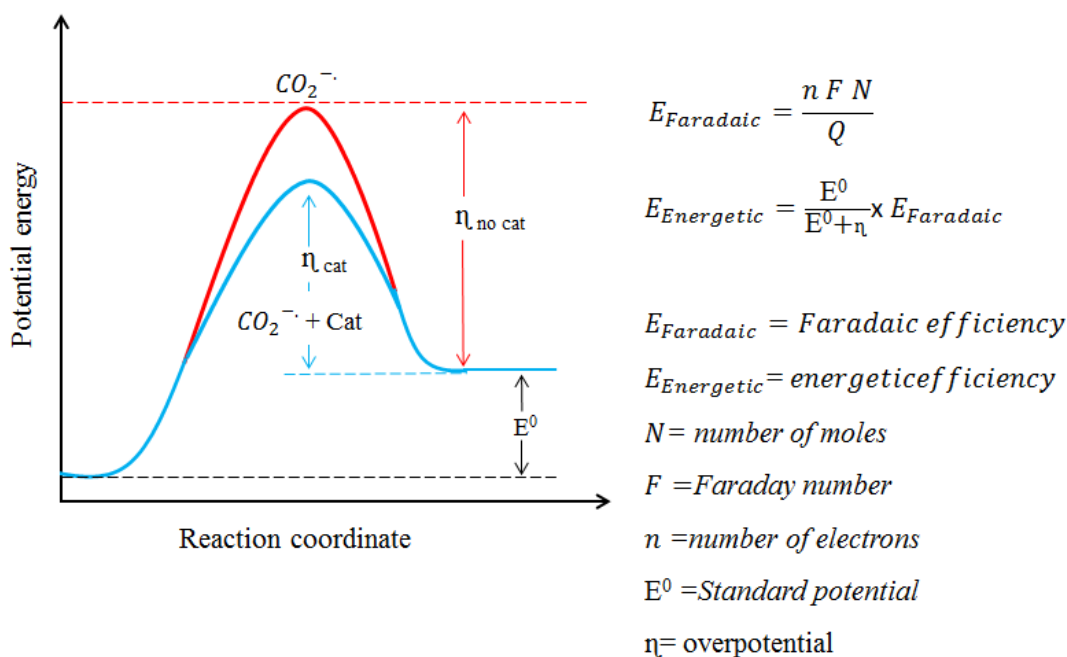


Figure 3.1 Qualitative reaction scheme for CO<sub>2</sub> conversion. Catalysts and electrolytes acting as co-catalysts can lower the energy of the intermediate and thus improve the energetic efficiency of the conversion. (Redrawn from Whipple and Kenis review)(Whipple & Kenis 2010)

For instance, although high Faradaic efficiencies have been reported, with >90% for formate and CO and ca. 70% for hydrocarbons such as methane, the high overpotentials at which these products were formed presents a real obstacle to enhancing the energy efficiency (Whipple & Kenis 2010). The direct electrochemical reduction of CO<sub>2</sub> (of the processes reported earlier) by one electron to the radical anion CO<sub>2</sub><sup>•-</sup> requires a highly negative potential -1.9V vs. SHE (pH 7) in aqueous solutions (Schwartz 1993) and -1.97 V vs. SHE in dimethylformamide (DMF) (Lamy et al. 1977). To avoid the highly energetic CO<sub>2</sub><sup>•-</sup> radical anion intermediary, catalytic approaches are sought to form high Faradaic efficiency carbon-based products from the electrochemical reduction of CO<sub>2</sub> while reducing the overpotentials Figure 3.1).

In general, the electrochemical reduction of CO<sub>2</sub> to hydrogenated organic products in aqueous solution is believed to proceed by the indirect chemical interaction of CO<sub>2</sub> with adsorbed hydrogen atoms produced by the electrochemical reduction of protons (Whipple & Kenis 2010). Thus, the efficient, reduction of CO<sub>2</sub> necessitates designing a system wherein a specific poisoning of the electrode material toward hydrogen generation is coupled with the catalytic reduction of the CO<sub>2</sub>.

### **3.1.2.1 Methanol Economy**

The challenges of efficiently storing energy using CO<sub>2</sub> as an abundant feedstock in chemical bonds are high, but the potential rewards are very promising. Considering that this alcohol is the primary building block for many organic compounds and various chemicals (e.g. paint, plastics), the electrochemical reduction of CO<sub>2</sub> into methanol is an interesting route. Currently, methanol (CH<sub>3</sub>OH) is used in the Direct Methanol Fuel Cell, an electrochemical device that directly converts chemical energy of fuels into electrical energy (Olah et al. 2009).

Most importantly, in its liquid form, methanol (CH<sub>3</sub>OH) presents an ideal fuel for combustion and an excellent way to store energy conveniently and safely. Due to the issues related to the production of 6e<sup>-</sup> or above products discussed earlier, very few works on the production of methanol *via* the electrochemical CO<sub>2</sub> reduction route were reported until recently. This will be discussed in the next sections. However, the 2e<sup>-</sup> and 4e<sup>-</sup> CO<sub>2</sub> reduced products such as carbon monoxide and formic acid were extensively studied and successfully produced with interesting Faradaic efficiencies and current densities on several metals as reported in the next section. The success of these processes has led to the Mantra Energy project which is in the development stage towards an industrial scale power plant for formic and formate salt production technology by electroreduction of carbon dioxide (ERC) (Li & Oloman 2005)(Li & Oloman 2007).

### **3.1.2.2 Reduction on Metal and other Material Electrodes to Methanol and Other Hydrocarbons**

Considering the enormous benefits that can be gained from methanol (CH<sub>3</sub>OH) production outlined earlier, many researchers have focused their studies on metals and materials which favour methanol (CH<sub>3</sub>OH) production by direct CO<sub>2</sub> reduction. In 1983,

Halmann et al studied the reduction of aqueous CO<sub>2</sub> on p-GaP and p-GaAs photocathodes. Methanol showed the highest Faradaic yield of the reduction products at 80% on p-GaP, with a relatively low energy input (-1V vs. saturated silver electrode) alongside formic acid and formaldehyde formation. This interesting results has encouraged workers in the field to investigate methanol production via both electrochemical and photoelectrochemical CO<sub>2</sub> reduction routes.

Five years later, Ayers and Farlay reported CO<sub>2</sub> reduction to methanol on a hydrogenated palladium electrode at low electrolytic current densities. Other workers also reported the formation of methanol on different electrodes, but according to Hori et al the extremely low concentrations of the alcohol reported is of little interest since no higher current densities of methanol (CH<sub>3</sub>OH) formation were reported (Hori 2008). In addition, methanol formation from CO<sub>2</sub> reduction at metal surfaces has been observed on Mo, Ru and RuO<sub>2</sub>. However, the Mo system was not durable as the electrode corroded during the formation of methanol (Summers et al. 1986).

Table 3.4 shows the most successful methanol systems formation by reduction of CO<sub>2</sub> on metals and other material. Efficiencies of up to ca. 38%, 2% and 10% of ethanol (C<sub>2</sub>H<sub>6</sub>O), methanol and propanol were achieved respectively, at transition-metal based oxide with the composition La<sub>1.8</sub>Sr<sub>0.2</sub>CuO<sub>4</sub> gas diffusion electrode (GDE) at a high overvoltage of >-1.86V (ca. 120mA/cm<sup>2</sup>) vs. SHE. Only methanol is shown in Table 3.4 since it is the product of interest (Schwartz 1993). However, Le et al reported a better methanol (CH<sub>3</sub>OH) Faradaic efficiency of 38% on copper oxide electrodes. The process occurred at relatively high overpotentials of -1.31V vs. SHE (Le et al. 2011). Similar methanol Faradaic efficiency of 40% was achieved (Table 3.4) at 9mA/cm<sup>2</sup> and -0.88V vs. SHE on Cu cathode at high pressure in a CO<sub>2</sub>-ethanol/water LiCl system (Li & Prentice 1997).

Table 3.4 Summary of methanol production by electrochemical or photoelectrochemical reduction of CO<sub>2</sub> on several metals and materials

Electrode Material	Potential (V) vs. SHE	Current density (mA/cm <sup>2</sup> )	Faradaic efficiency (%)	Reference
p-GaP	-0.08	0.005	99.00	(Barton et al. 2008)
Ru <sup>a</sup>	-0.70	0.20 (37.40)	99.00	(Arai et al.2010)
Ru/Cu	-0.56	0.005	41.30	(Popic et al. 1997)
Ru/Cd	-0.56	0.005	38.20	(Popic et al. 1997)
RuO <sub>2</sub>	-0.56	-	60.50	(Qu et al. 2005)
Mo	-0.56	0.12	84.00	(Summers et al. 1986)
Cu <sup>b</sup>	-0.88	9.00	40.00	(Li & Prentice 1997)
La <sub>1.8</sub> Sr <sub>0.2</sub> CuO <sub>4</sub> GDE	-1.86	120.00	02.00	(Schwartz 1993)
Cu/Zn/Al	-0.02-0.1	2.00	01.00	(Kobayashi & Takahashi 2004)
CuO <sub>4</sub>	-1.96	180.00	30.70	(Schwartz 1993)
Cu <sub>2</sub> O	-1.31	15.00	38.00	(Le et al. 2011)
Pd	-0.36	0.005	30.00	(Morris et al. 2011)

a Glassy carbon/Ru poly- quinone

b under 60bar

GDE: gas diffusion electrode

Mo and Ru (Table 3.4) were reported to reduce CO<sub>2</sub> to methanol (CH<sub>3</sub>OH) or methane (Summers et al. 1986). Methanol was produced with 84% Faradaic efficiency at -0.56V vs. SHE but these results were not reproducible (Hara et al. 1995). Popic et al reported the CO<sub>2</sub> reduction to methanol on RuO and related oxides deposited on a Ti substrate, at -0.56V vs. SHE. The yield increased with electrolysis time (Popic et al. 1997). In addition, Qu et al used carbon nanotubes as the substrate of a RuO<sub>2</sub>/TiO<sub>2</sub> coated electrode to reduce CO<sub>2</sub> to methanol at Faradaic efficiency of 60% with a current density 6.5mA cm<sup>-2</sup> (Qu et al. 2005). Low methanol yields of 0.84-0.97% were reported by Kobayashi and Takahashi on Cu/Zn/Al at 2mA/cm<sup>2</sup> and -0.02-0.1V vs. SHE (Kobayashi & Takahashi 2004). Bandi was able to reduce CO<sub>2</sub> on RuO<sub>2</sub> +TiO<sub>2</sub> coated on a Ti substrate electrode and reported methanol production with 24% Faradaic efficiency at 0.52mA/cm<sup>2</sup> and 900mV vs. Hg/Hg<sub>2</sub>SO<sub>4</sub> in 0.05M H<sub>2</sub>SO<sub>4</sub>. Higher methanol Faradaic efficiency processes are reported below.

Arai et al were able to reduce CO<sub>2</sub> on ruthenium modified polymers electro-polymerized on glassy carbon electrodes, obtaining up to 99% methanol (CH<sub>3</sub>OH) Faradaic efficiency at 0.2mA/cm<sup>2</sup> (Arai et al. n.d.). Moreover, ruthenium and ruthenium oxide electrodes were suggested to operate at low overpotentials of -0.5 to -0.7V vs. SCE and Faradaic efficiencies of 30-100%, possibly through the formation of adsorbed

carboxylate species, which are then hydrogenated to methanol (Halmann 1978). Bocarsly and co-workers also were able to reduce CO<sub>2</sub> to methanol (CH<sub>3</sub>OH) on both metallic (30% Faradaic efficiency) and semiconductor materials (99% Faradaic efficiency); this process will be discussed in detail later in the CO<sub>2</sub> reduction assisted by pyridinium to methanol section.

### **3.1.2.2.1. Reduction of CO<sub>2</sub> on Copper Electrodes**

Copper electrodes were extensively used as catalysts for the electrochemical reduction of CO<sub>2</sub>. The reason being that, in addition to their low price, these catalysts were the first to show a significant amount of hydrocarbons at high reaction rates and over a sustained period of time (Kuhl et al. 2012). However, overpotentials of higher than 1V are required and a fairly broad-mix of major and minor hydrocarbons are produced including hydrogen, ethylene and methane. Interestingly, these metal catalysts also produced amounts of alcohols such as methanol (CH<sub>3</sub>OH) and ethanol (C<sub>2</sub>H<sub>6</sub>O). The current review aims at covering the most recent work on copper cathodes for a reference to the work reported in this thesis in terms of amounts of products formed, reaction rate, and the electrolysis time.

In 2002, Yano et al reported the electrochemical conversion of CO<sub>2</sub> to CO, C<sub>2</sub>H<sub>4</sub>, and CH<sub>4</sub> at the three-phase interface on a copper net electrode in acidic solution (electrolyte, 0.5MKCl). Products detected with high yield at -1.2V are (acetone, 66 μM), (lactic acid, 56 μM), (EtOH, 27μM) and (MeOH, 20μM) among other products (Yano et al. 2002). Kuhl et al. also reported the electro-reduction of CO<sub>2</sub> on copper surfaces across a range of potentials (-0.6V to -1.2V) and observed a total of 16 different CO<sub>2</sub> reduction products (Kuhl et al. 2012). Methane was produced with the highest Faradaic efficiency 40% (52ppm) and methanol with less than 0.2% (0.34ppm) Faradaic efficiency (Jessop et al. 1994). Reduction of CO<sub>2</sub> was carried out on nanocluster Cu/ZnO at -0.1V vs. Ag/AgCl. Ethylene (10.1%, 2.65x10<sup>-4</sup>mmol/cm<sup>2</sup>/h), ethanol (C<sub>2</sub>H<sub>6</sub>O) (10.2%, 2.7x 10<sup>-3</sup>mmol/cm<sup>2</sup>/h), methane (1.8%, 7.8x 10<sup>-3</sup>mmol/cm<sup>2</sup>/h) and methanol (2.8%, 1.53x 10<sup>-3</sup>mmol/cm<sup>2</sup>/h) were among other products formed in the 0.1M aqueous KHCO<sub>3</sub> solution (Andrews et al. 2013). The electro-catalytic reduction of CO<sub>2</sub> was investigated on Cu-Au alloys in an aqueous 0.5 M KHCO<sub>3</sub> solution.

Ohta used copper tubes for methanol (CH<sub>3</sub>OH) and formic acid production under atmospheric pressure of CO<sub>2</sub> with FEs of 2.6% and 0.84%, respectively. The detected

concentration corresponding to these FEs is 2ppm of each product (Ohta 1995). Another study of methanol formation by electrochemical reduction of carbon dioxide on electrodeposited copper oxide thin film resulted in the highest methanol yield, which was near  $43 \mu\text{mole hr}^{-1}$  with a Faradaic efficiency of 38%. Moreover,  $\text{CO}_2$  was reduced on nanotube copper electrodes, Faradaic efficiencies for alcohols were reported to vary depending on the composition of the nanostructures with the best efficiencies: methanol 17% and ethanol ( $\text{C}_2\text{H}_6\text{O}$ ) 12% (Jia et al. 2014). A photoelectrochemical  $\text{CO}_2$  reduction in aqueous 5M sodium hydroxide solution to methanol ( $\text{CH}_3\text{OH}$ ) with 11% Faradaic yield ( $2.5 \times 10^{-8} \text{ moles cm}^{-2} \text{ s}^{-1}$ ) was reported using Cu gauze as dark electrode. The amount of methanol produced increased two fold in the presence of methanol (0.5mM) serving as as an auto-catalyst. The photo anode, carbon modified titanium oxide ( $0.65\text{cm}^2$ ), was illuminated with light intensity of  $100\text{mW cm}^{-2}$  with a solar simulator (Palanichamy et al. 2013). A high photochemical conversion of  $\text{CO}_2$  of 97% Faradaic efficiency was reported on  $\text{TiO}_2$  supported on  $\text{Al}_2\text{O}_3$  representing mainly methanol (14% vol) (Nazimek & Czech 2011). Ramaroson et al have reported 7.2% Faradaic efficiency of production methanol at 120bar and  $350^\circ\text{C}$  on supported palladium electrodes  $\text{LiPd/SiO}_2$  (Ramaroson et al. 1982).

Although, some efforts (reported earlier) on the production of methanol ( $\text{CH}_3\text{OH}$ ) from reduction of  $\text{CO}_2$  at Cu electrodes and other materials, the amounts of the alcohol produced are extremely low and no increase was shown at higher overpotentials. Hori and co-workers have carefully examined the  $\text{CO}_2$  reduction on copper electrodes. This group and others reported the deactivation of the metal electrodes as a persistent defect irrespective of the potential applied in the  $\text{CO}_2$  reduction (Hori 2008). For instance, Augustynski reported the formation of methane and ethylene on Cu. The electrolysis current decays rapidly in ~30 minutes after the start of the experiment and HER takes place. The decay of the current and the cessation of the production of the hydrocarbons were attributed to the deactivation of the electrode (Augustynski et al. 1996).

Different aspects related to the deactivation of the copper cathodes were reported. The deactivation of Cu was reported in the form of blackening of the electrode surface after electrolysis. Analyses of the surface were conducted using X-ray photoelectron spectroscopy (XPS); the contamination of the surface with a carbon-containing substance was reported. The carbonaceous substance was believed to form during the  $\text{CO}_2$  reduction and poisons the reaction (Hori 2008). Jermann and Augustynski have

attempted the activation of copper electrodes for long term electrolysis to reduce CO<sub>2</sub> reduction. A periodic anodic activation of the cathode resulted in not only maintaining the electrolysing current stable but the efficiencies of CH<sub>4</sub> and C<sub>2</sub>H<sub>4</sub> at 55% and 45% Faradaic efficiencies respectively over 50 hours (Jermann & Augustynski 1994).

The activation of a Cu electrode following electrolytic deactivation was shown to be recovered by periodic anodic polarisation of the electrode (Hori 2008). Periodic anodic pulses are effective at maintain the electrolysing current stability and the activity of the electrode for prolonged times. Hori et al have shown the deactivation of Cu was due to the surface coverage with cathodically reduced heavy metal impurities from the electrolyte solutions used in the reaction. Therefore, they pointed out the importance of the use of pure metal electrodes as well as high purity reagents in the electrolyte, in addition to a pre-electrolysis for further purification. Frese et al also referred to the heavy metal impurities such as Fe and Zn on Cu electrode detected by XPS (Summers et al. 1986).

Hori et al have investigated the deactivation of the electrode by using reagents from different sources. The electrolysing current dropped rapidly and the catalytic activity for methane production was lost within ca.100min. The activity was temporarily recovered by anodic stripping voltammetry, followed by an anodic polarization at -0.05V; the activity of the electrode deteriorates again after a short period. The same experiments were conducted by deliberately introducing impurities in the electrolyte. The same behaviour of the electrode was observed; this led the authors to the conclusion that the heavy metal ions were responsible for the deactivation of the electrode (Hori et al. 1985). These electrode activation methods and techniques were adopted in Chapter 7.

Most of the work reported above on different metals and other materials, whether leading to hydrocarbons, alcohols or other organic chemicals, uses high overvoltages of typically >-1V. This is mainly due to the first step of the reduction to CO<sub>2</sub><sup>-</sup> radical which occurs at -1.9V vs. SHE (pH7). Although the theoretical reduction potentials for multiple electron reductions of CO<sub>2</sub> are much less negative (Table 3.1) (e.g. -0.38V for 6 electron reduction to methanol) any outer-sphere electron transfer (i.e. uncatalyzed) must initially proceed through this difficult reduction. This illustrates the need for electrocatalysts that allow multi-electron reduction (Hori 2008). It is clear from these reports that the methanol (CH<sub>3</sub>OH) formation process is challenging in view of the low Faradaic yields achieved, high reported overpotentials and/or non-repeatability of the

results. Although, some of the reports of nearly 100% methanol Faradaic efficiencies are achieved there is still need to validate these results and further studies aiming at understanding the mechanism of such processes is needed.

### **3.1.2.3 CO<sub>2</sub> Reduction Assisted by Pyridinium to Methanol**

Although electrochemical systems have been developed to reduce CO<sub>2</sub> to methanol or methane with good product yields, high electrode overpotentials are required to drive these processes. This leads to highly energy inefficient processes which offer little or no benefit since the quantity of fuel consumed during the synthesis of the products far exceeds the fuel value of these products.

In 1994, Bocarsly and co-workers have reported a pyridinium catalysed CO<sub>2</sub> reduction to methanol (CH<sub>3</sub>OH) on a hydrogenated palladium electrode. The CO<sub>2</sub> reduction, performed in aqueous acidic solutions (0.5M NaClO<sub>4</sub>) at pH close to pK<sub>a</sub> of pyridine (C<sub>5</sub>H<sub>5</sub>N) (pH 5.4), was achieved with 30% Faradaic yield at low overpotentials of -0.55V vs. SCE (Seshadri et al. 1994). Pyridine (C<sub>5</sub>H<sub>5</sub>N) was not consumed or degraded during a 19h run. The redox potential of CO<sub>2</sub> reduction at pH 5.4 was reported to be at -0.57V vs. SCE, which is close to the thermodynamic potential for the reduction to methanol (Barton et al. 2008).

In 2010, detailed kinetic and mechanistic studies of the pyridinium-CO<sub>2</sub> reduction to methanol were reported on Pt electrodes. Methanol (CH<sub>3</sub>OH) production was initially suggested to proceed through 6-electron multi-step process mediated by pyridine (C<sub>5</sub>H<sub>5</sub>N) and some of its derivatives such as 4-tert-butylpyridine (Ohta 1995). The reduction goes through 2e<sup>-</sup> and 4e<sup>-</sup> reduced intermediates formic acid and formaldehyde respectively. The homogeneous process was believed to be initiated by pyridine (C<sub>5</sub>H<sub>5</sub>N) protonation in acidic media (pH5.2 to pH5.5) to form a pyridinium cation (PyH<sup>+</sup>) (Reaction 1, Figure 3.2). This is followed by pyridinium radical (Pyridinyl, PyH<sup>\*</sup>) formation at -0.58V vs. SCE on Pt (Reaction 2, Figure 3.2). A series of experimental, digital simulation and computational investigations have proved that the first step toward the production of methanol (CH<sub>3</sub>OH) proceeds through the interaction of the pyridinium radical with the substrate leading to CO<sub>2</sub>-pyridinium complex formation (Reaction 4, Figure 3.2). Concurrently, the charge transfer was believed to be coupled to pyridinyl radical dimerization reaction (Reaction 3, Figure 3.2) leading to

HER. Several routes have been explored for the zwitterionic complex transformation to products (Barton Cole et al. 2010).

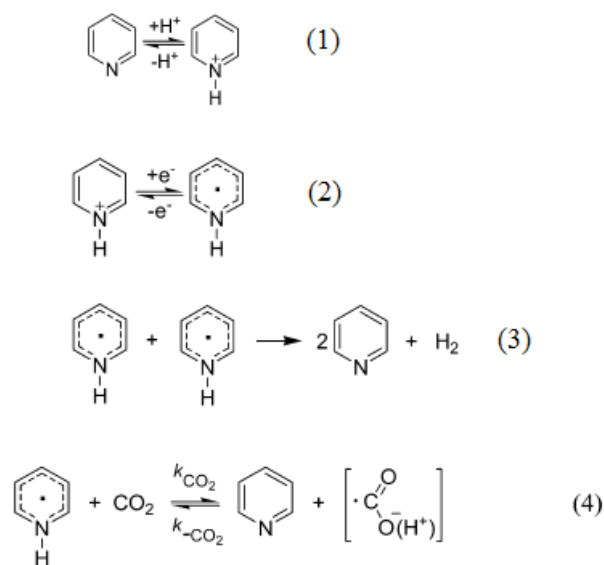


Figure 3.2 Bocarsly initial mechanism of CO<sub>2</sub> reduction to methanol via pyridinyl formation (Barton et al. 2008)

This mechanism was proposed based on the cyclic voltammetry response showing a first order dependence of the current on concentrations of both pyridinium and CO<sub>2</sub>. Further evidence was gained by digital CV simulations and theoretical calculations (Barton Cole et al. 2010)(Morris et al. 2011)(Barton et al. 2008). In addition, a vibrational spectrum indicative of carbamate formation has been observed in the gas phase upon reaction of CO<sub>2</sub><sup>•-</sup> with pyridine (C<sub>5</sub>H<sub>5</sub>N) (Barton Cole et al. 2010).

Methanol (CH<sub>3</sub>OH) was not produced when the pyridinium ion was replaced by N-methyl pyridinium ions, indicating that the N-H hydrogen atom of the pyridinium ion was required for the reduction CO<sub>2</sub> (Barton et al. 2008)(Morris et al. 2011)(Barton Cole et al. 2010). This system was exported to photoelectrochemically reduce of CO<sub>2</sub> on p-GaP to produce methanol (CH<sub>3</sub>OH). Faradaic efficiencies of ~96% were achieved with the CO<sub>2</sub>-pyridinium system at underpotentials of ~200mV (Barton et al. 2008). In view of the high FEs and low overpotentials reported, if higher current densities could be achieved in such a system, this could open up a new horizon in the carbon capture and utilisation sector, since this process has the potential to contribute greatly to CO<sub>2</sub> emission reductions (Keets et al. 2012).

This system involving the use of p-GaP as photocathode for the reduction of CO<sub>2</sub> catalyzed by pyridine (C<sub>5</sub>H<sub>5</sub>N) (Barton et al. 2008), was explored for imidazole (Bocarsly et al. 2012) as an electrocatalyst on iron pyrites. The products yielded from the reduction are the same as the ones involving pyridine (C<sub>5</sub>H<sub>5</sub>N), but the mechanism is suggested to differ from the latter.

Recently Boston, et al were able to produce formate and methanol at an illuminated ruthenium chromophore, [Ru(phen)<sub>3</sub>]<sup>2+</sup>, in acidic aqueous solution (pH5) containing pyridinium ion as the CO<sub>2</sub> reduction catalyst and ascorbic acid as a sacrificial agent. Formate and methanol were produced with quantum yields of 0.025 and 1.1 x 10<sup>-4</sup> respectively. Beyond simply providing a conductive medium, the use of KCl salt an electrolyte increased significantly the formate yield (x8) and doubled methanol yield. While, the role of this salt is not completely understood, it was suggested the presence of the potassium cation (K<sup>+</sup>) may contribute to the stabilization of the Py-CO<sub>2</sub> complex via ion-pairing, thus improving the reaction yield. The process reduction path was proposed to proceed by either a reductive quenching of the photo-excited complex by ascorbate followed by electron transfer to pyridinium ions, or by an oxidative quenching by the pyridinium ions followed by reduction of the ruthenium complex by ascorbate. It was demonstrated in this study that metal surfaces are not necessary for methanol formation (Boston et al. 2013).

Quantum chemical calculations were employed to investigate the mechanism of electrochemical reduction of CO<sub>2</sub> at illuminated p-GaP in the presence of pyridinium ions. The reduction process is believed to initiate by the protonation of pyridine (C<sub>5</sub>H<sub>5</sub>N); the pyridinium ion formed then is reduced to a pyridyl radical. The radical formed then reduces CO<sub>2</sub> by one electron transfer through nucleophilic attack of the N lone pair on the C of CO<sub>2</sub>. Finally proton transfer from the pyridyl radical to CO<sub>2</sub> produces PyCOOH\*. This pathway suggests that pyridine (C<sub>5</sub>H<sub>5</sub>N) catalyses the formation of formic acid and formaldehyde en route to formation of methanol (Lim et al. 2013).

Barista and co-workers reported a theoretical work on the CO<sub>2</sub> reduction to formic acid on single crystal Pt electrodes. They suggested that CO<sub>2</sub> is reduced by binding of hydrogen atoms to the Pt surface that are transferred as hybrids to CO<sub>2</sub> in proton coupled hybrid transfer (PCHT) activated by pyridinium. The reduction proceeds by one-electron reduction of pyridinium on Pt to form hydrogen atoms adsorbed on Pt (Pt-

H hybrid) and regenerate pyridine ( $C_5H_5N$ ) at a pH independent potential in acidic solution, where pyridinium concentration is higher than the proton concentration. The hydrogen adsorbate is then electrophilically attacked by  $CO_2$  in a two-electron PCHT reaction, that is first order both in  $CO_2$  and pyridinium (Ertem et al. 2013).

Given the near 100% Faradaic efficiencies achieved on p-GaP (Barton et al. 2008) and ca. 20% on Pt cathodes (Morris et al. 2011) at low overpotentials, the highly efficient and selective reduction of  $CO_2$  to methanol catalysed by pyridinium cation has enticed many researchers into this field, shortly after the  $CO_2$ -pyridinium system was reported. However, discrepancies of the coupled reaction rate constant were reported. Tossel et al have calculated the redox potential of pyridinium radical at -1.44V vs. SCE, which is nearly 1V more negative than the experimentally observed redox potential (-0.58V) of what is believed to be the same process. Similarly Keith and co-workers reported the calculated homogeneous redox potential as -1.45V, very close to the redox potential reported by Tossel (-1.44V) (Tossell 2011). These high overpotentials are most probably related to the pyridine ( $C_5H_5N$ ) reduction, which is reported in the next section. The discrepancy of the rate constant ruled out the possibility of pyridinyl formation in homogeneous solutions at such low overpotential (J. a Keith & Carter 2013).

Moreover, the voltametrically evidenced pyridinium radical formation proved contentious due to the electrode surface role in the reaction. The pyridinium cation was experimentally observed to discriminate cathode interfaces, since the glassy carbon was reported to be inert toward this ion (Barton et al. 2008)(Costentin et al. 2013), while the voltammetric wave of the predicted radical was observed on some electrode interfaces including Pd (Seshadri et al. 1994), Pt (Morris et al. 2011), p-GaP (Barton et al. 2008), Pt/C-TiO<sub>2</sub> (de Tacconi et al. 2012) and iron pyrites (Bocarsly et al. 2012). This has invoked several computational calculations reported earlier. Although discrepancies in the theoretical pyridinium reduction potential were reported, it is well agreed that the reduction of the ion occurs at least -0.6V more negative than experimentally observed (Keith & Carter 2012)(Lim et al. 2013). This fact has made the mechanism proposed improbable, which stimulated further investigations aimed at uncovering the underlying mechanism.

Discrepancies were observed in the optimized rate constant for the coupled reaction leading to molecular hydrogen which was used to estimate pyridinium concentrations at

the interface. Eight orders of magnitude difference was reported by Keith and co-workers in the rate constant estimated for the HER reaction. While Bocarsly reported a rate constant of  $k=2.7\text{M}^{-1}\text{s}^{-1}$ , a time-resolved electron spin-resonance (ESR) spectroscopy study during UV photolysis of pyridine ( $\text{C}_5\text{H}_5\text{N}$ ) revealed a rate constant of  $k=7 \times 10^8\text{M}^{-1}\text{s}^{-1}$  for the same reaction (J. a. Keith & Carter 2013). This has questioned the experimentally observed potential at  $-0.58\text{V}$  vs. SCE on Pt electrode which was previously believed to be the potential of one electron charge transfer to the pyridinyl radical. Quantum chemistry studies revealed that the reaction proceeds via two electron charge transfer to ortho or para dihydropyridine as the active co-catalyst in the  $\text{CO}_2$  rather than pyridinyl radical proposed previously by Bocarsly and co-workers (Keith & Carter 2012).

Moreover, the number of electrons transferred in the electrochemical reduction of pyridinium-acid system was controversial in the literature. Bocarsly and co-workers reported a one-electron pyridinium reduction. The quantum chemistry calculations have predicted two-electron reductions of pyridine ( $\text{C}_5\text{H}_5\text{N}$ ),  $\text{Py} + 2\text{H}^+ + 2\text{e}^- \rightarrow \text{DHP}$ , as a possible mechanism to form 1,4-dihydropyridine (DHP) at low overpotentials ( $-0.72 \pm 0.30\text{V}$  vs. SCE), since the DHP has shown thermodynamic stability at the experimentally observed potential and pH used (Keith et al). However, Bocarsly et al showed that the formation of the intermediate, 4,4'-bipyridine (bpy), requires a rapid cleavage of the C-C bond of DHP to regenerate pyridinium, is energetically unfavourable process. In addition, these authors reported the difficulty of the proton exchange to the para position for pyridinium in bulk deuterium electrolysis, this rules out the possibility of two-electron transfer reaction (Barton Cole et al. 2010).

A recent voltammetric study of acids on Pt electrode has revealed some of the features related to pyridinium cation behaviour in the absence and the presence of  $\text{CO}_2$ . The cation is believed to behave as any weak acid in aqueous solutions on Pt interfaces leading exclusively to hydrogen generation reaction. According to Costentin et al the peak current observed under argon (Seshadri et al. 1994) (Morris et al. 2011)(Costentin et al. 2013) is merely the reduction of diffused hydrated protons to the electrode surface. The protons are released by the acid, pyridinium, as part of the fast cation deprotonation equilibrium. This group argues that the mechanism leading to the catalytic current observed under  $\text{CO}_2$  does not differ much from the current resulting under an inert gas; the enhancement of the former is due to increased proton concentration, resulting from

both the deprotonation of pyridinium seen in the latter case and from carbonic acid dissociation. This interpretation together with NMR analysis, which showed no sign of methanol, explicitly rules out the catalytic role of pyridinium towards methanol production.

Electrochemical reduction of pyridinium was studied at Pt electrodes in acidic acetonitrile solutions on Pt electrode. The potential of pyridinium reduction was observed at -0.75V vs. Ag/AgCl, the peak current of the observed wave increased with the addition of protons to the system to a certain limit after which a second wave at -0.35V was observed. The latter wave was believed to be the reduction of free protons. Thus, the diffusion controlled reduction of pyridinium ion was suggested to lead to HER and regeneration of pyridine ( $C_5H_5N$ ) (Tomita 2000).

The mechanism of the  $CO_2$  electrochemical reduction assisted by pyridine ( $C_5H_5N$ ) is debatable to date. The intermediates in this process have not been well characterized and may differ under the various photochemical, photoelectrochemical and electrochemical conditions employed. The reduction of heterocyclic compounds containing nitrogen has been studied by polarography, chemical and radiolytic reductions at metal electrodes and this provides some insights into the mechanism and the likely intermediates for pyridinium-mediated  $CO_2$  reduction.

### **3.1.3 Reduction of Nitrogen-Heterocycles: Pyridine and Derivatives**

The chemical reduction of nitrogen-bearing heterocycles has been studied in homogeneous solutions using active metals in aqueous solutions by high energy activation routes such as gamma ray irradiation and electron pulse radiolysis. Both methods produce pyridinyl radicals which are unstable and tend to dimerize or disproportionate. The reduction of pyridine ( $C_5H_5N$ ) with sodium metal was shown to form dimers and other polymeric species, this is indicative of radical intermediate formation. The reduction of pyridine derivatives such as ortho- and para-dimethylpyridine species by sodium metal formed the dihydropyridine derivatives; this route inevitably goes through pyridine derivative radicals (Watt 1949). Similarly, pyridine radicals have been seen by the electron spin resonance (ESR) technique upon reaction with potassium metal in aprotic solvent. The unstable product was 4,4'-bipyridyl (Ward 1961).

The formation of dihydropyridines was detected by several workers upon the reduction of pyridine ( $C_5H_5N$ ) derivatives with lithium (Tanner & Yang 1993), magnesium and zinc (Lansbury & Peterson 1961) (Kedzierzawski 1994). Moreover, transient intermediates were detected by gamma ray irradiation and pulse radiolysis to form dihydropyridines by pyridine derivative reduction (David et al. 1966). Solar, et al. found that pyridinium was much more easily reduced to the radical form than pyridine. Derivatives of pyridine were also examined using pulse radiolysis and were found to produce similar products (Talcott & Myers 1967)(Grover et al. 2003).

### **3.1.3.1 Electrochemical reduction of N-heterocycles at Metal Electrodes**

The reduction of nitrogen bearing heterocycles such as pyridine and pyridinium derivatives has been extensively investigated at several metal electrodes as early as the 19<sup>th</sup> century. Cathode materials with high overvoltage for HER (such as lead and mercury (Hg)) were examined to diminish the HER. Pyridine ( $C_5H_5N$ ) and its derivatives were reduced in several aprotic solvents yielding different compounds via the formation of radicals at exceptionally high overvoltage. In non-aqueous dimethylformamide (DMF) solution at a dropping mercury (Hg) electrode, pyridine was reported to reduce by two electrons at -2.01 V versus a mercury pool electrode (Given 1964). Similarly, Tabner and co-workers reported the reduction of pyridine at -2.76 V vs. Ag/AgCl (Tabner & Yandle 1968). This was confirmed later by Stradyn and co-workers; the unprotonated form of pyridine formed a 2-electron wave to dihydropyridine at potentials above -2V (Stradyn et al. 1975).

Pyridinium derivatives were also reduced on metals via radical formation. For instance, the electrochemical reduction of alkyl-pyridinium cation was achieved in pyridinium chloride ( $Cl^-$ ) ionic liquid at -0.95V vs. SCE on glassy carbon and tungsten (Gale 1980). The reduction resulted in 45% yield of the relatively unstable primary pyridinyl radical, 4,4'-tetrahydrobipyridine, at a reduction potential of -0.81V vs. SCE, which rapidly dissociated to form a more stable and active 1,1'-dibutyl-4,4'-bipyridinium radical. Furthermore, the reduction of 1-methylpyridinium was reported to proceed through radical generation at -1.28V vs. SCE on Hg in acetonitrile (Shikata & Tachi

1926). Derivatives that are electron accepting, but have an electrochemically inactive substituent attached to the ring, give a 2-electron wave resulting from the electroreduction of the pyridine ( $C_5H_5N$ ) ring and also a catalytic hydrogen wave (Given 1964).

In most cases, the one-electron reduced pyridinyl intermediate has been proposed as the initial reduction product, which is then quickly consumed by subsequent chemical or electrochemical steps to produce bipyridines and dihydropyridines. Under certain circumstances it was possible to detect the one-electron reduced pyridinyl radical before coupling or secondary reduction events occur. Similar high overpotential reduction processes of pyridine and pyridinium derivatives via radical formation were observed when aqueous solutions were used. Shikata et al have reported the reduction of pyridine to piperidine at 65-95% with other by-products in aqueous solutions at lead and mercury electrodes; the reduction was achieved at high overpotentials ( $>-1.7V$  vs. SCE) (Shikata & Tachi 1926). Moreover, in ammonium chloride ( $Cl^-$ ) aqueous solution at a mercury (Hg) electrode, pyridine was reduced at  $-1.67 V$  vs. SCE (Shikata & Tachi 1926).

In general, when reduction potentials of greater than  $-1.5 V$  vs. SCE were employed, the most common reduction products of pyridine or pyridinium derivatives reported were the dimerization products (e.g. 4,4'-bipyridines or 1,4-dihydropyridine). In aqueous solutions, hydrogen generation was reported by some workers to dominate over the formation of the dimerization products upon the reduction of pyridine (Stradyn et al. 1975) (Mairanovskii 1963). Opinions as to whether pyridine, in protogenic solvent, gives in addition to the hydrogen wave, the reduction wave of the pyridine-ring itself are contradictory. Some authors suppose that pyridine gives two, one-electron reduction waves at  $-1.5 V$  and  $-1.8V$  corresponding to pyridinyl radicals, which undergo parallel dimerization adding a second electron to form dihydropyridine (Stradyn et al. 1975). However, Stradyn has observed that under the conditions of classical polarography at a mercury (Hg) electrode and in aqueous solutions of pyridinium, these cations only catalyze the liberation of hydrogen ions and pyridine ( $C_5H_5N$ ) is not reduced at all in the unprotonated form. These observations are consistent with the work of Mairanovovskii, who has reported the exclusive evolution of molecular hydrogen upon the polarographic reduction of N-heterocycles in aqueous solutions. Nitrogen bearing heterocycles such as pyridine contribute to formation of molecular hydrogen on the cathode in aqueous solutions without being reduced themselves.

The catalytic hydrogen wave usually appears at more positive potentials than the hydrogen reduction potential in the same solution. This gives the catalyst the property of accelerating HER at underpotentials. In this process the lower overvoltage is driven by the regeneration of the cationic active form to the catalyst (Mairanovskii 1963). However, Kolthoff and Lingane believe that the polarographic behaviour of N-heterocyclic compounds is reflected in the reduction of the aromatic compound wave in addition to catalytic hydrogen wave (Kolthoff & Lingane 1955).

Such controversy has led Shikata and Tachi to investigate pyridine ( $C_5H_5N$ ) behaviour further in acidic solutions on DME. Two waves were observed at -1.5V and -1.7V vs. SCE corresponding to pyridinium ion reduction and the reduction of the undissociated molecule respectively (Shikata & Tachi 1926). These observations were confirmed by Tompkins, P.C; Schmidt. However, the first wave seen at -1.5V vs. SCE was believed to be proton reduction to hydrogen rather than pyridinium reduction, since the current of the direct reduction by transfer of electrons from the cathode to pyridine is controlled solely by the diffusion of the latter. On the other hand, the catalysis of protons to form hydrogen is dependent on both pH and the concentration of pyridine (Tompkins, P.C; Schmidt 1942). The process leading to the formation of a hydrogen wave on a mercury (Hg) drop electrode (MDE) was shown to proceed via adsorption followed by a set of reactions, which result in the generation of a hydrogen molecule in an aqueous medium. Based on detailed analysis of this process, a mechanism was proposed for the formation of hydrogen, catalysed by pyridinium.

### **3.1.4 Summary**

The electrochemical  $CO_2$  reduction to valuable products has been extensively studied over the past few years. Although, high Faradaic efficiencies of carbon monoxide and formate were reported by the direct  $CO_2$  reduction at different metals and other material electrodes, the process usually requires high overvoltages of  $>-1V$  as outlined in the present Chapter. The high energy input of these electrochemical systems renders the reduction process less efficient. Thus, the catalytic  $CO_2$  reduction approach is becoming more popular. In particular, the catalytic reduction of  $CO_2$  to methanol has recently attracted the researchers' attention due to the value and the numerous advantages the alcohol can offer. However, methanol production through the electrochemical  $CO_2$  reduction has only been reported by a limited number of literature works. Despite, the

good methanol yields/Faradaic efficiencies achieved in some of these reports, high electrode overpotentials were used to drive the reactions. The high electrode overpotential remains the main issue in most systems.

The recently high efficient electrochemical CO<sub>2</sub> reduction to methanol assisted by pyridinium has attracted considerable attention. The unprecedented system used a simple organic molecule as a catalyst to drive the CO<sub>2</sub> reduction at low overpotentials (~100-200mV) resulting in high methanol Faradaic efficiencies of nearly 100%. However, the CO<sub>2</sub>-pyridinium system was reported only at low current densities (~50μA cm<sup>2</sup>). In addition, the initially proposed mechanism based on the pyridinyl radical intermediate as a first step toward the production of methanol was disproved by theoretical calculations.

Subsequently, alternative mechanisms for the CO<sub>2</sub>-pyridinium reduction system were suggested by independent groups. However, the suggested reactions pathways are controversial in terms of the catalytic role of pyridinium. Some of these investigations believe the aromatic amine catalyses the CO<sub>2</sub> reduction by binding of hydrogen atoms to the Pt surface creating Pt-H hybrid that are transferred to CO<sub>2</sub> to produce formic acid as a first step toward the methanol formation (Ertem et al. 2013) (Liao et al. 2015), whereas, another group of workers demonstrated that pyridinium merely catalyses HER (Costentin et al. 2013). Moreover, the CO<sub>2</sub>-pyridinium reduction system was exported to other material electrodes. Some of these reports confirmed the production of methanol (Boston et al. 2013) (de Tacconi et al. 2012) (Zeng et al. 2014), while others could not detect the alcohol or any other carbon based products (Costentin et al. 2013)(Lucio & Shaw 2015).

In view of the controversy surrounding the reduction of pyridinium discussed above and considering that the pyridinium-based electrochemistry for CO<sub>2</sub> reduction at a platinum electrode in aqueous solutions process is still unclear. The mechanism and products of pyridinium reduction on platinum are investigated in the following chapters. First, the role of pyridinium in the electrochemical CO<sub>2</sub> reduction was investigated. This was based on analysis of the experimentally-derived mechanisms (Barton Cole et al. 2010) (Costentin et al. 2013), high pressure voltametric study, numerical simulation and Nicholson based diagnostics.

A high pressure electrolytic study was also conducted under various conditions aimed at increasing the methanol yields and enhancing the current densities of the electrochemical reduction of CO<sub>2</sub>. The concentration of CO<sub>2</sub> can be enhanced by increasing its pressure. The abundance of this reactant near the electrode surface is expected to maximise the current contributing to CO<sub>2</sub> reduction to methanol. Hence, the electrochemical reduction in the CO<sub>2</sub>-pyridinium system was extended to high CO<sub>2</sub> pressure (50-55bar) at Pt electrodes.

## References of Chapter 3

- Andrews, E. et al., 2013. Electrochemical Reduction of CO<sub>2</sub> at Cu Nanocluster / (100) ZnO Electrodes. *Journal of the Electrochemical Society*, 160(11), pp.H841–H846.
- Appel, A.M. et al., 2013. Frontiers, opportunities, and challenges in biochemical and chemical catalysis of CO<sub>2</sub> fixation. *Chemical Reviews*, 113(8), pp.6621–6658.
- Arai, G., Harashina, T. & Yasumori, I., Selective electrocatalytic reduction of carbon dioxide to methanol on Ru-modified electrode. *Chemistry Letters*, (7), pp.1215–1218.
- Aresta, M., 2010. *Carbon Dioxide as Chemical Feedstock* M. Aresta, ed., Weinheim, Germany: Wiley-VCH Verlag GmbH & Co. KGaA.
- Aresta, M. ed., 2003. *Carbon Dioxide Recovery and Utilization*, Dordrecht: Springer Netherlands.
- Augustynski, J., Jermann, B. & Kedzierzawski, P., 1996. Electroreduction of Carbon Dioxide in Aqueous Solutions at Metal Electrodes. *American Chemical Society Division Fuel Chemistry*, 41, pp.1420–1424.
- Barton Cole, E. et al., 2010. Using a one-electron shuttle for the multielectron reduction of CO<sub>2</sub> to methanol: Kinetic, mechanistic, and structural insights. *Journal of the American Chemical Society*, 132(33), pp.11539–11551.
- Barton, E.E., Rampulla, D.M. & Bocarsly, A.B., 2008. Selective solar-driven reduction of CO<sub>2</sub> to methanol using a catalyzed p-GaP based photoelectrochemical cell. *Journal of the American Chemical Society*, 130(20), pp.6342–6344.
- Bewick, A. & Greener, G.P., 1970. The electroreduction of CO<sub>2</sub> to glycolate on a lead cathode. *Tetrahedron Letters*, 11(5), pp.391–394.
- Bocarsly, A.B. et al., 2012. Comparative study of imidazole and pyridine catalyzed reduction of carbon dioxide at illuminated iron pyrite electrodes. *ACS Catalysis*, 2(8), pp.1684–1692.
- Boston, D.J. et al., 2013. Photochemical reduction of carbon dioxide to methanol and formate in a homogeneous system with pyridinium catalysts. *Journal of the American Chemical Society*, 135(44), pp.16252–5.
- Costentin, C. et al., 2013. Electrochemistry of acids on platinum. Application to the reduction of carbon dioxide in the presence of pyridinium ion in water. *Journal of the American Chemical Society*, 135(47), pp.17671–4.
- David, C. et al., 1966. E.S.R. study of gamma irradiated binary mixtures of pyridine and methanol. *Molecular Physics*, 11(6), pp.599–600.

- Department of Energy and Climate Change (DECC) & National Statistics, 2014. Uk Energy in Brief, p.48.
- Dufek, E.J. et al., 2012. Operation of a Pressurized System for Continuous Reduction of CO<sub>2</sub>. *Journal of the Electrochemical Society*, 159(9), pp.F514–F517.
- Ertem, M.Z. et al., 2013. Functional Role of Pyridinium during Aqueous Electrochemical Reduction of CO<sub>2</sub> on Pt(111). *The Journal of Physical Chemistry Letters*, 4(5), pp.745–748.
- Ganesh, I., 2014. Conversion of carbon dioxide into methanol – a potential liquid fuel: Fundamental challenges and opportunities (a review). *Renewable and Sustainable Energy Reviews*, 31, pp.221–257.
- Ganesh, I., 2011. Conversion of Carbon Dioxide to Methanol Using Solar Energy - A Brief Review. *Materials Sciences and Applications*, 02(10), pp.1407–1415.
- Given, B.P.H., 1964. Given : Polarography. , (2684), pp.1954–1957.
- Green, D.W. ; Perry, R., Perry's Chemical Engineers' Handbook, Eighth Edition - Access Engineering from McGraw-Hill.
- Grover, R. et al., 2003. Kinetics and spectral properties of electron and •OH adducts of dimethylpyridines: a pulse radiolysis study. *Research on Chemical Intermediates*, 29(2), pp.157–168.
- Halmann, M., 1978. Photoelectrochemical reduction of aqueous carbon dioxide on p-type gallium phosphide in liquid junction solar cells. *Nature*, 275(5676), pp.115–116.
- Hara, K., Kudo, A. & Sakata, T., 1995. Electrochemical reduction of carbon dioxide under high pressure on various electrodes in an aqueous electrolyte. *Journal of Electroanalytical Chemistry*, 391(1-2), pp.141–147.
- Haynes, L. V. & Sawyer, D.T., 1967. Electrochemistry of carbon dioxide in dimethyl sulfoxide at gold and mercury electrodes. *Analytical Chemistry*, 39(3), pp.332–338.
- Hirota, K. et al., 1998. Photoelectrochemical Reduction of CO<sub>2</sub> at High Current Densities at p-InP Electrodes. *Journal of the Electrochemical Society*, 145, pp.L82–L84.
- Hori, Y., Murata, A. & Yoshinami, Y., 1991. Adsorption of CO, intermediately formed in electrochemical reduction of CO<sub>2</sub>, at a copper electrode. *Journal of the Chemical Society, Faraday Transactions*, 87(1), p.125.
- Hori, Y. et al., 2005. “Deactivation of copper electrode” in electrochemical reduction of CO<sub>2</sub>. *Electrochimica Acta*, 50(27), pp.5354–5369.
- Hori, Y., 2008. Electrochemical CO<sub>2</sub> Reduction on Metal Electrodes. In *Modern Aspects of Electrochemistry*. pp. 89–189.

- Hori, Y., Kikuchi, K. & Suzuki, S., 1985a. Production of CO and CH<sub>4</sub> in electrochemical reduction of CO<sub>2</sub> at metal electrodes in aqueous hydrogencarbonate solution. *Chemistry Letters*, (11), pp.1695–1698.
- Hori, Y. & Suzuki, S., 1983. Cathodic reduction of carbon dioxide for energy storage. *J. Res. Inst. Catal., Hokkaido Univ.*, 30(Copyright (C) 2011 American Chemical Society (ACS). All Rights Reserved.), pp.81–88.
- Hori, Y.; Takahashi, R.; Yoshinami, Y.; Murata, A., 1992. Electrochemical reduction of CO<sub>2</sub> at Cu + Au electrodes. *J. Electrochem. Soc.*, 328(97), pp.233–243.
- IPCC, 2014. *Climate Change 2013 - The Physical Science Basis* Intergovernmental Panel on Climate Change, ed., Cambridge: Cambridge University Press.
- Jermann, B. & Augustynski, J., 1994. Long-term activation of the copper cathode in the course of CO<sub>2</sub> reduction. *Electrochimica Acta*, 39(11-12), pp.1891–1896.
- Jessop, P. et al., 1994. Catalytic production of dimethylformamide from supercritical carbon dioxide. *Journal of the American Chemical Society*, 116(8), pp.8851–8852.
- Jitaru, M., 2007. Electrochemical Carbon Dioxide Reduction - Fundamental and Applied Topics. *Journal of Chemical Technology and Metallurgy*, 42, pp.333–344.
- Jitaru, M. et al., 1997. Electrochemical reduction of carbon dioxide on flat metallic cathodes. *Journal of Applied Electrochemistry*, 27(8), pp.875–889.
- Keets, K. a. et al., 2012. Analysis of pyridinium catalyzed electrochemical and photoelectrochemical reduction of CO<sub>2</sub>: Chemistry and economic impact. *Indian Journal of Chemistry - Section A Inorganic, Physical, Theoretical and Analytical Chemistry*, 51(9-10), pp.1284–1297.
- Keith, J. a & Carter, E. a, 2012. Theoretical insights into pyridinium-based photoelectrocatalytic reduction of CO<sub>2</sub>. *Journal of the American Chemical Society*, 134(18), pp.7580–3.
- Keith, J. a. & Carter, E. a., 2013. Electrochemical reactivities of pyridinium in solution: consequences for CO<sub>2</sub> reduction mechanisms. *Chemical Science*, 4(4), p.1490.
- Kobayashi, T. & Takahashi, H., 2004. Novel CO<sub>2</sub> Electrochemical Reduction to Methanol for H<sub>2</sub> Storage. *Energy & Fuels*, 18(1), pp.285–286.
- Kolthoff, I.M. & Lingane, J.J., 1955. *Polarography*, Interscience Publishers.
- Kuhl, K.P. et al., 2012. New insights into the electrochemical reduction of carbon dioxide on metallic copper surfaces. *Energy & Environmental Science*, 5(5), p.7050.
- Lansbury, P.T. & Peterson, J.O., 1961. Lithium N-Dihydropyridyl Aluminum Hydride-A Selective Reducing Agent for Highly Electrophilic Carbonyl Compounds. *Journal of the American Chemical Society*, 83(16), pp.3537–3538.

- Le, M. et al., 2011. Electrochemical Reduction of CO<sub>2</sub> to CH<sub>3</sub>OH at Copper Oxide Surfaces. *Journal of The Electrochemical Society*, 158(5), p.E45.
- Li, H. & Oloman, C., 2007. Development of a continuous reactor for the electro-reduction of carbon dioxide to formate - Part 2: Scale-up. *Journal of Applied Electrochemistry*, 37(10), pp.1107–1117.
- Li, H. & Oloman, C., 2005. The electro-reduction of carbon dioxide in a continuous reactor. *Journal of Applied Electrochemistry*, 35(10), pp.955–965.
- Li, J.W. & Prentice, G., 1997. Electrochemical synthesis of methanol from CO<sub>2</sub> in high-pressure electrolyte. *Journal of the Electrochemical Society*, 144, pp.4284–4288.
- Lim, C.-H., Holder, A.M. & Musgrave, C.B., 2013. Mechanism of homogeneous reduction of CO<sub>2</sub> by pyridine: proton relay in aqueous solvent and aromatic stabilization. *Journal of the American Chemical Society*, 135(1), pp.142–54.
- Mairanovskii, S.G., 1963. The theory of catalytic hydrogen waves in organic polarography. *Journal of Electroanalytical Chemistry*, 6(2), pp.77–118.
- Morris, A.J., McGibbon, R.T. & Bocarsly, A.B., 2011. Electrocatalytic carbon dioxide activation: The rate-determining step of pyridinium-catalyzed CO<sub>2</sub> reduction. *ChemSusChem*, 4(2), pp.191–196.
- Nazimek, D. & Czech, B., 2011. Towards Methanol. *IOP Conference Series: Materials Science and Engineering*, 19, p.012010.
- Noda, H. et al., 1989. Potential dependencies of the products on electrochemical reduction of carbon dioxide at a copper electrode. *Chemistry Letters*, 85(2), pp.289–292.
- Ohta, K., 1995. Electrochemical Reduction of Carbon Dioxide. , 36(6), pp.625–628.
- Olah, G. a., Goepfert, A. & Prakash, G.K.S., 2009. Chemical recycling of carbon dioxide to methanol and dimethyl ether: From greenhouse gas to renewable, environmentally carbon neutral fuels and synthetic hydrocarbons. *Journal of Organic Chemistry*, 74(2), pp.487–498.
- Paik, W., Andersen, T.N. & Eyring, H., 1969. Kinetic studies of the electrolytic reduction of carbon dioxide on the mercury electrode. *Electrochimica Acta*, 14(12), pp.1217–1232.
- Peter Styring, D.J., 2011. *Carbon Capture and Utilisation in the green economy*, The Centre for Low Carbon Futures 2011 and CO<sub>2</sub>Chem Publishing 2012.
- Polievktov, M. K; Mairanovskii, S.G., 1965. Influence Of The Concentration And Nature Of The Cation Of Indifferent Electrolytes On The Polarographic Catalytic Waves Of Hydrogen Induced By Pyridine In Unbuffered Solutions. *Journal of the Academy of Sciences*, pp.400–405.

- Qiao, J. et al., 2014. A review of catalysts for the electroreduction of carbon dioxide to produce low-carbon fuels. *Chem. Soc. Rev.*, 43(2), pp.631–675.
- Qu, J. et al., 2005. Electrochemical reduction of CO<sub>2</sub> on RuO<sub>2</sub>/TiO<sub>2</sub> nanotubes composite modified Pt electrode. *Electrochimica Acta*, 50(16-17), pp.3576–3580.
- Ramaroson, E., Kieffer, R. & Kiennemann, A., 1982. Reaction of carbon dioxide and hydrogen on supported palladium catalysts. *Journal of the Chemical Society, Chemical Communications*, (12), p.645
- Sánchez-Sánchez, C.M. et al., 2001. Electrochemical approaches to alleviation of the problem of carbon dioxide accumulation. *Pure and Applied Chemistry*, 73(12), pp.1917–1927.
- Schwartz, M., 1993. Carbon Dioxide Reduction to Alcohols using Perovskite-Type Electrocatalysts. *Journal of The Electrochemical Society*, 140(3), p.614.
- Seshadri, G., Lin, C. & Bocarsly, A.B., 1994. A new homogeneous electrocatalyst for the reduction of carbon dioxide to methanol at low overpotential. *Journal of Electroanalytical Chemistry*, 372(1-2), pp.145–150.
- Shine, K.P. et al., 1990. Radiative Forcing of Climate. In *Climate Change: The IPCC Scientific Assessment. Report prepared for Intergovernmental Panel on Climate Change by Working Group I*.
- Smith, Y., 2010. *Photo-electrochemical and Photo-catalytic Conversion of Carbon Dioxide*, Photo-Electrochemistry & Photo-Biology for the Sustainability.
- Stradyn, Y.P., Kadysh, V.P. & Giller, S.A., 1975. Polarography of heterocyclic compounds - I. Miscellaneous data on the polarographic behavior of heterocycles and electrochemical reduction of heteroaromatic compounds (review). *Chemistry of Heterocyclic Compounds*, 9(12), pp.1435–1448.
- Suleimenov, O.M., 2004. Simple, compact, flow-through, high temperature high pressure cell for UV-Vis spectrophotometry. *Review of Scientific Instruments*, 75(10), pp.3363–3364.
- Summers, D.P., Leach, S. & Frese, K.W., 1986. The electrochemical reduction of aqueous carbon dioxide to methanol at molybdenum electrodes with low overpotentials. *Journal of Electroanalytical Chemistry and Interfacial Electrochemistry*, 205(1-2), pp.219–232.
- Tabner, B.J. & Yandle, J.R., 1968. A correlation of half-wave reduction potentials with theoretical calculations for some nitrogen-containing heteromolecules in dimethylformamide. *Journal of the Chemical Society A: Inorganic, Physical, Theoretical*, p.381.
- De Tacconi, N.R. et al., 2012. Electrocatalytic Reduction of Carbon Dioxide Using Pt/C-TiO<sub>2</sub> Nanocomposite Cathode. *Electrochemical and Solid-State Letters*, 15(1), p.B5.

- Talcott, C.L. & Myers, R.J., 1967. Electron spin resonance spectra of the radical anions of pyridine and related nitrogen heterocyclics. *Molecular Physics*, 12(6), pp.549–567.
- Tanner, D.D. & Yang, C.M., 1993. On the Structure and Mechanism of Formation of the Lansbury Reagent, Lithium Tetrakis(N-Dihydropyridyl)Aluminate. *Journal of Organic Chemistry*, 58(7), pp.1840–1846.
- Tomita, Y. et al., 2000. Electrochemical Reduction of Carbon Dioxide at a Platinum Electrode in Acetonitrile-Water Mixtures. *Journal of The Electrochemical Society*, 147(11), p.4164.
- Tompkins, P.C; Schmidt, C.A., 1942. Polarographic Characterisation of Nicotinic Acid and Related Compounds. *J. Biol. Chem.*, 143, pp.643–653.
- Tossell, J. a., 2011. Calculation of the properties of molecules in the pyridine catalyst system for the photochemical conversion of CO<sub>2</sub> to methanol. *Computational and Theoretical Chemistry*, 977(1-3), pp.123–127.
- Vassiliev, Y.B. et al., 1985. Electroreduction of carbon dioxide. *Journal of Electroanalytical Chemistry and Interfacial Electrochemistry*, 189(2), pp.271–294.
- Ward, R.L., 1961. An Electron Spin Resonance Study of the Reaction of Pyridine with Potassium : The Formation of Bipyridyl Negative Ion. *Journal of the American Chemical Society*, 83(17), pp.3623–3626.
- Watt, G.W., 1949. Reactions of Inorganic Substances with Solutions of Metals in Liquid Ammonia. , (410), pp.289–315.
- Yan, Y. et al., 2013. Electrochemistry of aqueous pyridinium: exploration of a key aspect of electrocatalytic reduction of CO<sub>2</sub> to methanol. *Journal of the American Chemical Society*, 135(38), pp.14020–3.
- Yano, H. et al., 2002. Efficient electrochemical conversion of CO<sub>2</sub> to CO, C<sub>2</sub>H<sub>4</sub> and CH<sub>4</sub> at a three-phase interface on a Cu net electrode in acidic solution. *Journal of Electroanalytical Chemistry*, 519(1-2), pp.93–100.
- Yasukouchi, K. et al., 1979. Cathodic reduction of pyridinium ion in acetonitrile. *Journal of Electroanalytical Chemistry and Interfacial Electrochemistry*, 105(2), pp.403–408.

# Chapter 4 Experimental Methods and Techniques

The first part of this Chapter describes the high pressure set up used in both the voltammetric and the bulk electrolysis measurements. The second part outlines the electrolysis products analysis by gas chromatography mass spectrometry (GCMS).

## 4.1 High Pressure Experimental Setup

The high pressure set up used in both the voltammetric and the bulk electrolysis measurements is illustrated in Figure 4.1. It consists of a CO<sub>2</sub> cylinder, JASCO<sup>®</sup> CO<sub>2</sub> delivery pump (Section 4.1.2.1), JASCO<sup>®</sup> backpressure regulator (BRP) (Section 4.1.2.2), a high pressure vessel (Section 4.1.1.2), JULABO<sup>®</sup> water circulator and Metrohm<sup>®</sup> Autolab potentiostat connected to a computer equipped with Nova<sup>®</sup> software.

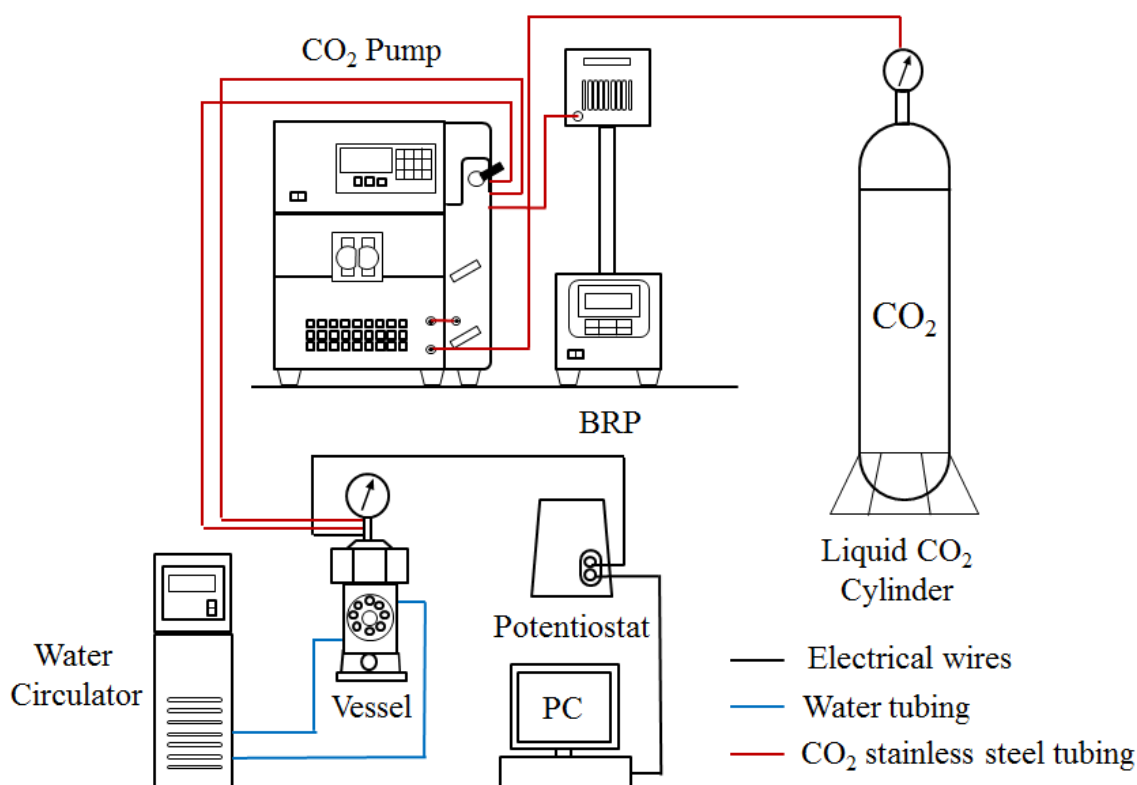


Figure 4.1 Schematic diagram of the high pressure set up

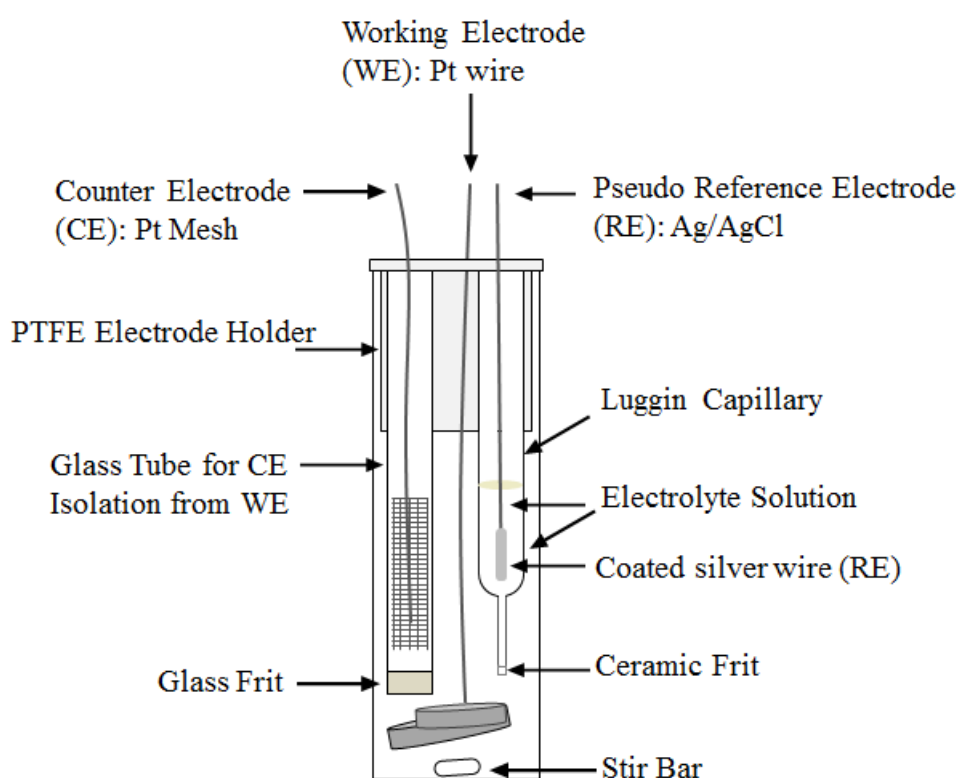
The CO<sub>2</sub> delivery pump, the BRP, and the high pressure vessel are connected using 1/16" 316 HPLC stainless steel capillary tubing. Liquid CO<sub>2</sub> is supplied via the cylinder equipped with a dip tube for liquid use and fed directly into JASCO<sup>®</sup> CO<sub>2</sub> pump via the inlet port (Figure 4.6) as seen in Figure 4.1; this is controlled by valve 1 (Figure 4.6). Then CO<sub>2</sub> circulates *via* the outlet port which is connected to a Rheodyne valve (Figure 4.6). The Rheodyne valve has two positions, by-pass position and vessel position which has another control valve 2 in (Figure 4.6). The pump has an in-built pressure sensor which is connected to a trip circuit. If a blockage occurs then the pump would register an over-pressure and stop pumping CO<sub>2</sub>. The pump requires restart even if the blockage is solved and system pressure dropped to normal. The BRP is connected to the pump and the reaction vessel as a second measure of pressure control in case the pump sensor fails. The JASCO<sup>®</sup> pump head is chilled to maintain a constant temperature (-10°C). The nozzle of the BPR can be heated to ~40 °C to avoid freezing of the pipe work upon expansion of the CO<sub>2</sub>. Liquid/gaseous CO<sub>2</sub> is then fed into the reaction vessel. The vessel temperature is maintained at 20°C or 25°C using a water circulator (JULABO<sup>®</sup>) (Figure 4.1). The electrodes fitted in the vessel top are connected to the potentiostat for cyclic voltammetric experiments and electrolysis measurements, and this latter is controlled by a computer/software.

## 4.1.1 High Pressure Vessel

### 4.1.1.1 Experimental Specification and Conditions

Both the voltammetric measurements and the bulk electrolysis at high pressure CO<sub>2</sub> were undertaken in the glass liner which is inserted into the Parr<sup>®</sup> stainless steel vessel (Section 4.1.1.2). Aqueous electrolytes of 0.5MKCl were used in all experiments (10-25ml volume range). A three electrode arrangement was employed (Figure 4.2). All high pressure experiments were referenced against the home-made pseudo Ag/AgCl electrode (RE) (Section 4.3.3.3). A platinum mesh (Section 4.3.2) (ca. 20 cm<sup>2</sup>) was used as a counter electrode (CE) for these series of experiments. The CE was isolated from the other electrodes in a separate tube as illustrated in Figure 4.2. The isolation arrangement is to prevent/minimise the interference of the counter electrode/anode products (CE) with the products of electrolysis of interest in the working electrode (WE) containing electrolyte. Platinum electrode wires of 0.3mm or 0.5mm diameter (area 0.07cm<sup>2</sup> and 0.6cm<sup>2</sup> respectively) or Pt discs (100μm, ~7.85x10<sup>-5</sup>cm<sup>2</sup>) and

( $300\ \mu\text{m}$ ,  $\sim 7.06 \times 10^{-4}\ \text{cm}^2$ ) were used as working electrodes (WEs) in the voltammetric measurements. Higher area Pt electrode (Pt foil  $\sim 3.8\ \text{cm}^2$ ) was used for the bulk electrolysis experiments (Section 4.3.1). The temperature was maintained at  $20^\circ\text{C}$  or  $25^\circ\text{C}$  using the water circulator. The aqueous electrolytes were purged with  $\text{CO}_2$  for  $\sim 1\ \text{h}$  for all pyridine concentrations used.  $\text{CO}_2$  saturation at low atmospheric pressure (1bar) with bubbling mean results in the evaporation of pyridine, however, gas chromatography mass spectrometry (GCMS) analysis showed that pyridine is lost with approximately 5%, this is considered acceptable and does not affect the results.



Schematic Diagram of the High Pressure Reactor  
The three-electrode arrangement

*Figure 4.2 Schematic diagram of the glass liner (inserted in the high pressure vessel) with the three electrode arrangement*

#### 4.1.1.1.1. High Pressure Vessel Design Considerations

The experiments at elevated pressure had to be carried out in a specific high pressure cell. The design of such a part should correspond to the specification needed to perform the electrochemical reduction of carbon dioxide at high pressure and mild heating. The

vessel should withstand up to 350 bar and a maximum of 150°C, thus the most suitable material selected for the vessel construction was stainless steel (SS-316), which exhibits good mechanical strength and relative inertness toward many corrosive solutions. The vessel should comprise two main parts: the vessel body and the vessel cap (Appendix B, Figure B1). The vessel body is the lower part where the electrochemical reactions take place and the vessel cap is the top part which holds the sealed electrodes fittings.

Performing electrochemical reactions implies working in insulated space with no conducting intruder of any kind, so the vessel body needed to be either coated with non-conductive material such as PTFE or a glass liner should be inserted into this part. Considering that this part contains two windows and given the high weight of the vessel, the latter option is more practical in terms of better cleaning of the inner walls of the cell following each use. The glass liner was chosen as a reaction container in the current work. For safety purposes, the volume of the vessel was restricted to no more than 100ml and a minimum of 15mm was used as the thickness of the vessel body walls.

The vessel body should hold two cylindrical windows, for watching/recording the reactions. The windows incorporated into the cell should be designed to withstand the maximum pressure and temperature which the vessel can tolerate. Sapphire is the material satisfying these requirements and is readily used in high pressure spectroscopic systems (Suleimenov 2004). For high reliability of the vessel performance and durability of the windows seals, some sealing systems based on the unsupported area principle were examined (Brunner et al. 1984)(Suleimenov 2004)(Hara & Morishima 1988)(Gorbaty et al. 2003). The unsupported area principle is based on exerting a pressure on the seal for a higher contact force between the sealing element and the moving part. Hence, the sealing becomes more effective as the pressure increases. The upper pressure limit is set by the deformation of the seal where the unsupported area disappears (Brunner et al. 1984).

The closest design which satisfied the needs of the project and was initially considered with some modification was the sealing system by Brunner and co-workers (Brunner et al. 1984). In this design the cylindrical sapphire disk is pressed against the polished surface of the pressure distributing ring; this renders the vessel self-sealing when the pressure is applied (Appendix B, Figure B1). The vessel cap should hold the sealed electrodes and the CO<sub>2</sub> input and output tubing. The sealing of cell cap is equally

important and should be carefully designed. A reliable sealing technique was inspired from the instrument company Parr<sup>®</sup>. It consists of a flat PTFE gasket that is sealed in a screw cap. The cap is then clamped to the cell body by split-ring with cap screws (Appendix B, Figure B1).

Another important factor which had to be taken into consideration when constructing the vessel cap was the stability of the electrode sealing. Hence, various electrode sealing methods were examined. First, Vici<sup>®</sup> fitting by Valco<sup>®</sup> Instruments Co. Inc., used to seal wires and optical fibres individually, was inspected. This sealing technique relies on compression fittings, in which a ferrule is compressed onto a tube as a nut is tightened. Considering that three electrodes are needed in the vessel, Vici<sup>®</sup> fitting was not convenient since each wire has to be sealed individually. This requires a larger diameter of the area to be inserted into the vessel body; hence the volume of the vessel should be increased which reduces its safety. A more satisfactory option was Conax<sup>®</sup> sealing by Conax<sup>®</sup> Technologies (Appendix B, Figure B3). Conax<sup>®</sup> sealing is based on axial follower force, applied on the cap and translated by the torque, which compresses or crushes the sealant that is contained within the body thus creating a seal on the element. Tension in the body acts like a spring to maintain compression, friction between the sealant and restrains the element from moving under pressure. In addition, Conax<sup>®</sup> Technologies offer a multi-sealing system (Appendix B, Figure B1). The PTFE was the best sealant holding up to four wires of 1mm diameter with a gland mounting thread (NPT)1/2” which could be used up to 345bar and 232°C and thus satisfies this project/application requirements. The electrodes inside the vessel are insulated with Kapton<sup>®</sup>, a polyimide film with fluoropolymer resin (FEP) binder that is hermetically wrapped on wires and has excellent dielectric and insulation properties (DuPond, 2015).

#### **4.1.1.2 Parr<sup>®</sup> High Pressure Vessel**

The vessel was custom designed and constructed by Parr<sup>®</sup> as shown in Figure 4.3 to the specifications described in Section 4.1.1.1.1 with some modifications. The Parr<sup>®</sup> vessel body comprises two windows, colourless synthetic sapphire with 16mm thickness and 35mm diameter (Figure 4.3, dark grey), polished faces mounted plane-parallel and 30mm distant to each other by means of a supporting screw. The window sealing adopted by Parr<sup>®</sup> is slightly different from the sealing system initially considered in Section 4.1.1.1.1. It consists of an O-ring and a pressure distributing ring. To facilitate

sealing a thin Teflon film (1mm) is placed between the supporting ring and the flat surface of the window. The cap sealing designed by Parr<sup>®</sup> consists of a flat PTFE gasket (Figure 4.3, dark red) which seals tightly between the vessel body and the cap once clamped using the split-ring (Figure 4.4, grey). This clamping system adds greatly to the convenience of the equipment and ease of handling so the head with all of its fittings can be lifted from the cylinder without disrupting any attached fittings.

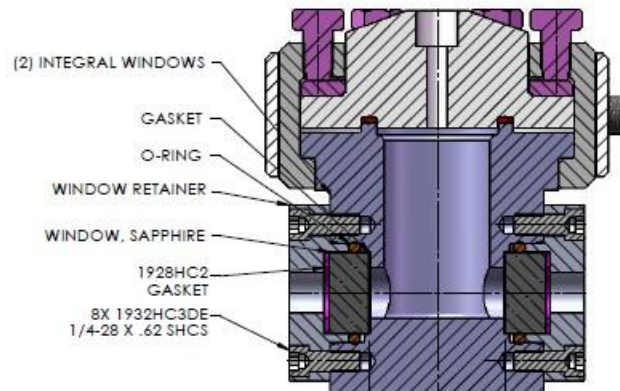


*Figure 4.3 Section view 2D drawing of the high pressure vessel (design by Parr<sup>®</sup>)*

The cap screws can be tightened or loosened, but they are never completely removed from the split ring. This saves time in opening and closing the vessel and looking for lost parts.

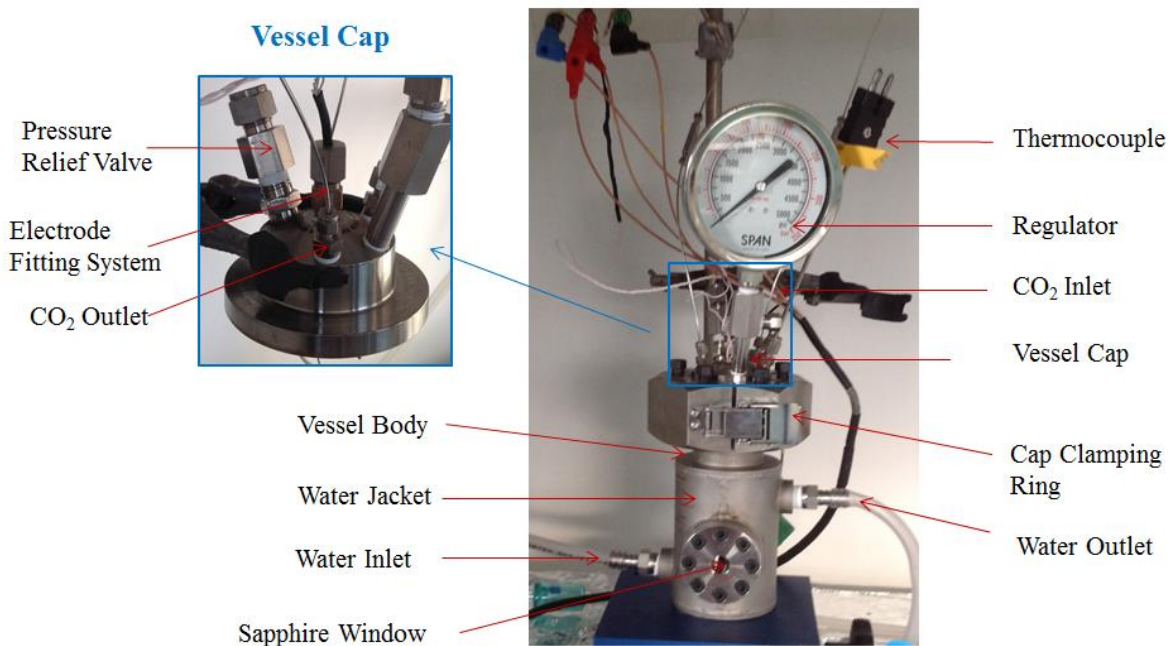


*Figure 4.4 Parr® high pressure vessel, left close view of the vessel cap*

The vessel was constructed with an outer wall jacket for heating purposes. In addition, the vessel cap contains a safety pressure relief valve, thermocouple, and a pressure regulator (Figure 4.4). The reaction container consists of a glass liner of 100ml which fits into the stainless steel vessel (Figure 4.5). A PTFE holder was machined to fit inside the glass liner to hold the electrodes in place.

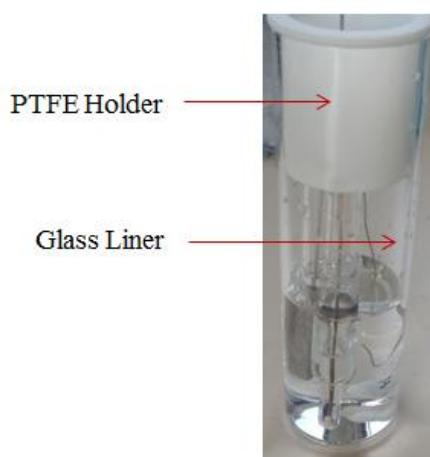


*Figure 4.5 PTFE electrode holder inserted in the glass liner(100ml)*

The glass reaction cell is heated by means of thermal transfer from the inner walls of the stainless steel vessel. This latter is heated by water circulating in the outer heating jacket

(Figure 4.4). The water temperature is controlled ( $\pm 0.1\text{C}$ ) using the JULABO<sup>®</sup> circulator shown in the diagram (Figure 4.2) in section 4.1.

## 4.1.2 CO<sub>2</sub> Pump and Back Pressure Regulator (BRP)

### 4.1.2.1 CO<sub>2</sub> Delivery Pump

High pressure experiments were carried out using JASCO<sup>®</sup> liquid CO<sub>2</sub> delivery pump (PU-2080-CO<sub>2</sub>). The CO<sub>2</sub> is supplied in liquid form to the pump from a CO<sub>2</sub> cylinder equipped with a dip tube. The liquid CO<sub>2</sub> delivery pump consists of the pump, head cooling unit, and controller, all integrally housed for convenience of operation (Figure 4.6). The pump employs a Slow Suction-Quick Delivery (SSQD) method to enable a stable transfer for up to 500 bar and has an in-built pressure sensor. The maximum recommended pressure is 300 bar with an accuracy of  $\pm 1\text{bar}$ . Figure 4.6 shows the main parts of the CO<sub>2</sub> delivery pump. The CO<sub>2</sub> pump instrument is equipped with an electronic cooling unit (lower part of the instrument, Figure 4.6) which maintains the temperature of the pump heads below -4 up to -10°C.

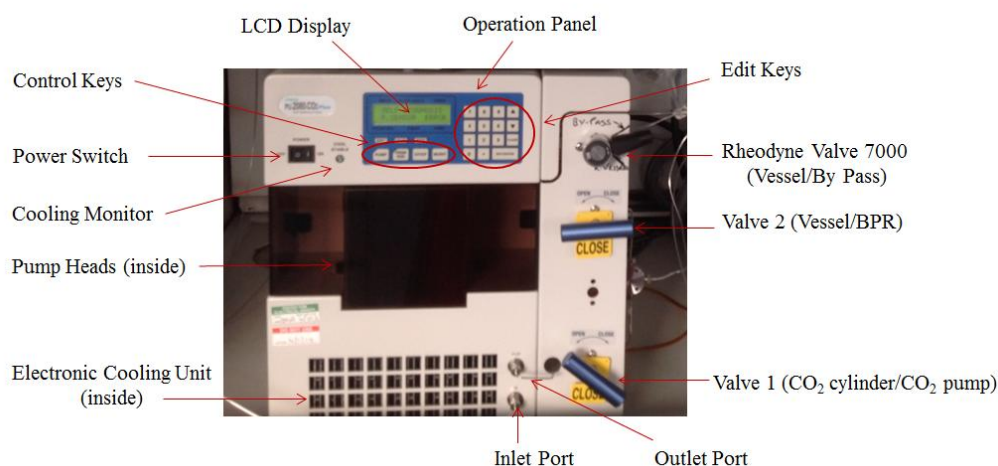


*Figure 4.6 CO<sub>2</sub> Liquid Delivery Pump JASCO<sup>®</sup> (PU-2080-CO<sub>2</sub>)*

The operation panel (at the top of the instrument, Figure 4.6) consists of edit keys, LCD display, and control keys. The control and the edit keys are used to monitor the pump operations, including the flow stat/stop and time program stat/stop. On the right, are shown the valves which control the CO<sub>2</sub> stream in and out. Valve1 controls the inlet port for liquid CO<sub>2</sub>, valve 2 links the vessel to the BRP and the Rheodyne valve supplies CO<sub>2</sub> to the vessel.

The pump operates at two optional delivery modes, constant flow or constant pressure. The constant flow rate can be set in the flow range 0 to 10ml/min with a minimum increment of 0.001ml/min. The recommended flow rate range is 0.5 to 5.0 ml/min with an accuracy of  $\pm 2\%$  or 2 $\mu$ l/min whichever is larger; the flow rate precision is 0.1%. The pressure control mode is settable in the range of 30 to 300 bar with 1 bar increment. The pressure accuracy in this mode is  $\pm 10\%$  of the setting value or  $\pm 10$ bar whichever is larger. The constant flow and the constant pressure options are used in the normal operation mode. The pump could also be operated in a program mode. In program mode, a gradient delivery, time programs for the flow rate and the pressure selection can be set.

A self-diagnostic test is done automatically when the pump is turned on. It checks the memories RAM and ROM, direct current (DC) power supply, and the pressure sensor. A leak test was performed prior the first operation. The leak test was carried out to check leaks in the high pressure including, the pump, BRP, tubing and the vessel described in the next section.

#### **4.1.2.2 Back Pressure Regulator (BRP)**

A programmable back-pressure regulator (JASCO<sup>®</sup> BP- 2080 BPR) was used to control the pressure of the system (Figure 4.7). BRP BP-2080 is a control device for supercritical fluid chromatographs, for small supercritical fluid extraction equipment, and for the CO<sub>2</sub> delivery pump.

The BRP consists of a valve unit attached to heater jacket. The pressure control mode works by opening /closing a variable stroke needle valve. The pressure setting ranges between 0 and 500 bar with 1 bar increment. The precision of the pressure control is  $\pm 1\%$  of the setting value or  $\pm 1$  bar. The operating flow range for the BRP is 0.1 to 120ml/min. Figure 4.7 shows the back-pressure regulator main parts. The operating panel consists of an LCD display and control keys. The BRP is operated on a time program, where the pressure, temperature, and the fluid flow rate can be set using the control keys. The heating unit (Figure 4.7) operates at a temperature setting range of 30°C (or the room temperature plus 10°C) to 80°C.

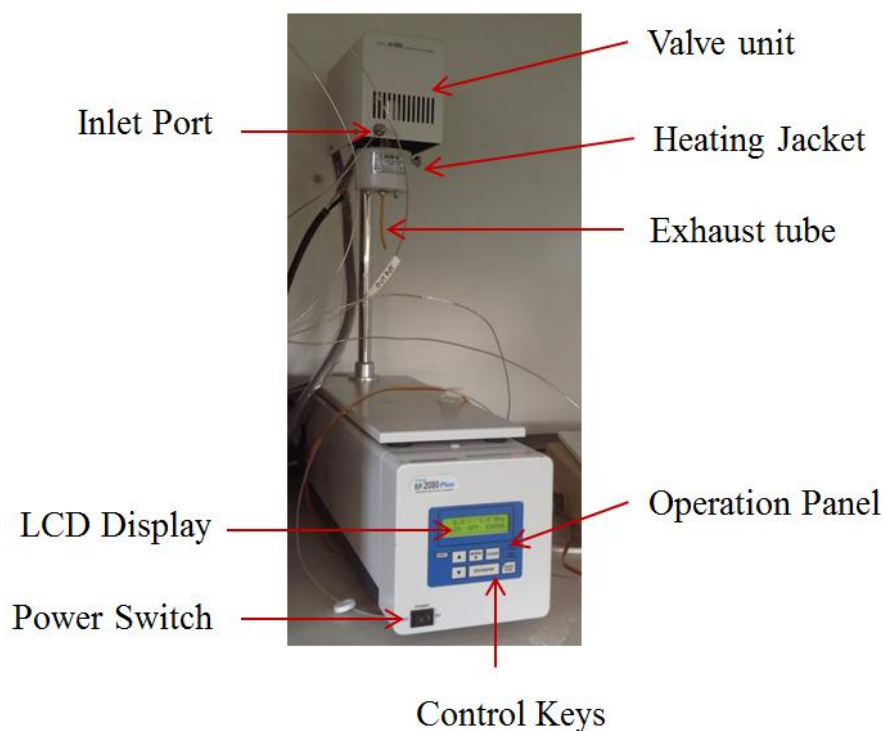


*Figure 4.7 Back Pressure Regulator JASCO® (PB-2080)*

The BRP performs a self-diagnostic test automatically similar to the pump ‘switching on’ mode. The BRP checks the same components listed above in addition to the stroke valve check.

### **4.1.3 Potentiostat**

All electrochemical measurements were performed on a Metrohm® Autolab PGSTAT101 potentiostat/galvanostat controlled by an Intel® Core™ 2 processor computer using Windows® 7 as the operating system. Nova 10.1 software, written by Metrohm®, was used to control the Autolab system.

## **4.2 Reaction Cells for Ambient Pressure**

### **4.2.1 Experimental Specification and Conditions**

Both the voltammetric measurements and the bulk electrolysis at 1bar of CO<sub>2</sub> or N<sub>2</sub> were undertaken in a Metrohm® cell of conical shape of 50ml volume or a cylindrical 500ml volume glass cell (Figure 4.8a, b). Aqueous electrolytes of 0.5 MKCl were used

in all experiments of volume 25ml-30ml range for Metrohm® cell or 250ml for the cylindrical shape cell. Both cells use the same fittings on their caps: A gas bubbler for either CO<sub>2</sub> or N<sub>2</sub> introduction in the system and a three-electrode system as shown in Figure 4.8. The experiments in either cell were referenced against the Metrohm® Ag/AgCl reference electrode (RE) (Section 4.3.3.3) or saturated calomel electrode (SCE) (Section 4.3.3.2).

A Metrohm® glassy carbon or Pt foil was used as a counter electrode (CE). The CE was isolated from the other electrodes in a separate tube as illustrated in Figure 4.2. Metrohm® Pt disc (3mm diameter, 0.07cm<sup>2</sup> area), Pt electrode wires of 0.3mm or 0.5mm diameter (area 0.07cm<sup>2</sup>, and 0.6cm<sup>2</sup> respectively) or Pt discs (100µm, ~7.85x10<sup>-5</sup>cm<sup>2</sup>) and (300µm, ~7.06x10<sup>-4</sup>cm<sup>2</sup>) were used as working electrodes (WEs) in the voltammetric measurements. Higher area Pt electrodes (Pt foil ~3.8 cm<sup>2</sup> and Pd wire ~2.56 cm<sup>2</sup>) were used for the bulk electrolysis experiments. The temperature was maintained at 20°C or 25°C using the water circulator.

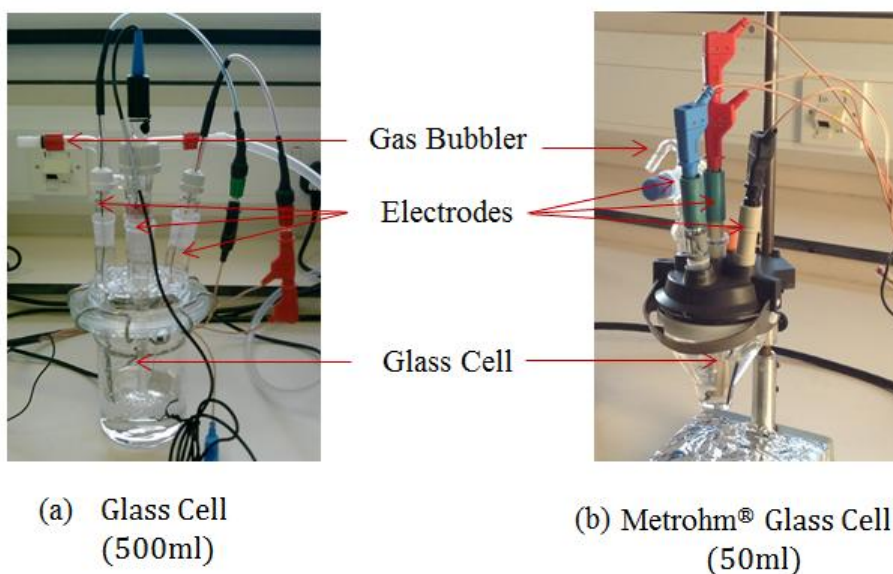


Figure 4.8 Glass reaction cells used in the ambient pressure experiments

## 4.3 Electrodes

A standard three-electrode arrangement was used in all experiments. Electrodes from Metrohm® and Russell® were used in the ambient pressure experiments. Other homemade working electrodes, counter electrodes and some reference electrodes were

prepared and used for convenience and to fit the experimental cell shown in Figure 4.4 and Figure 4.8.

### 4.3.1 Working Electrodes (WE)

A range of working electrodes of different size and shape were used for a specific experiment need or to fit in the different electrochemical cells (Figure 4.4 and Figure 4.8). Three types of electrodes were employed:

**Metrohm® Pt disc electrode** (Figure 4.9) (3mm diameter, 0.07cm<sup>2</sup> area) was used in the Metrohm® cell (Figure 4.4).

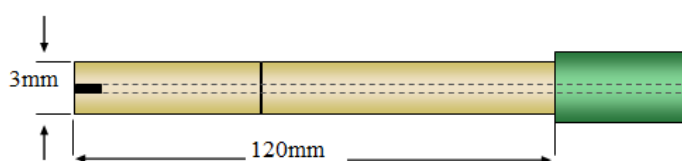


*Figure 4.9 Schematic diagram of macro-electrode Metrohm® Pt disk*

For bulk electrolysis experiments, a larger area than the Metrohm® Pt electrode was employed. Furthermore, the Metrohm® electrodes would not fit into the larger cylindrical shape cell (Figure 4.8a), hence other electrodes were constructed. First, a large area macro-electrode, a flag electrode, was constructed in the following manner. A bare Pt wire of 99.9% purity was welded to a ~3cm<sup>2</sup> area Pt foil; the foil was then folded around the wire. The welding point was covered with non-conductive epoxy to avoid any contamination and/or interference of the welding material with the reaction of interest on Pt. A Pt wire electrode with flattened end (~3cm<sup>2</sup>) was also used in the bulk electrolysis.

**Medium area macro-electrodes** were constructed for the high pressure experiments. Platinum wire of 99.99% purity and 0.3mm or 0.5mm diameter (area 0.07cm<sup>2</sup>, and 0.6cm<sup>2</sup> respectively) was soldered to a conducting wire and the latter was soldered to a gold coated pin (Figure 4.10) for convenient connection to the potentiostat electric attachment. The Pt wire was then cleaned and inserted in a glass tube. The desired area of Pt electrode was left out of the glass tube. The end part of the tube was then melted using a gas torch around the Pt wire, so that the exposed area, which determines the area of the working electrode, is insulated from the soldered point.

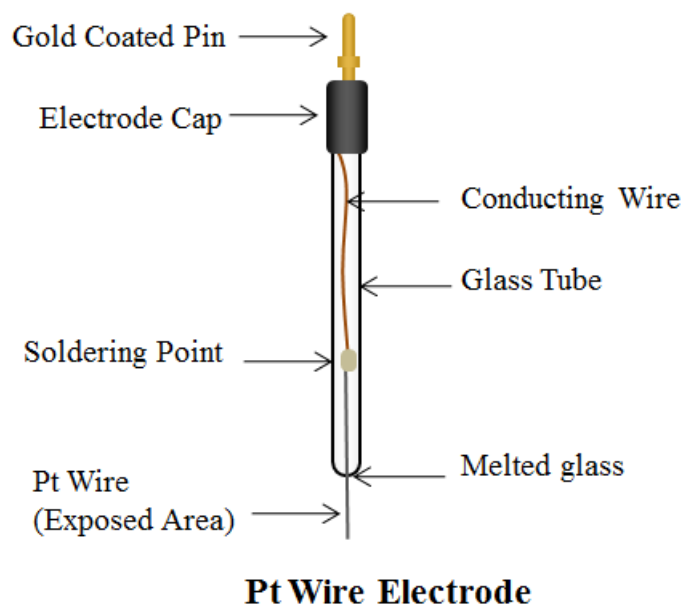
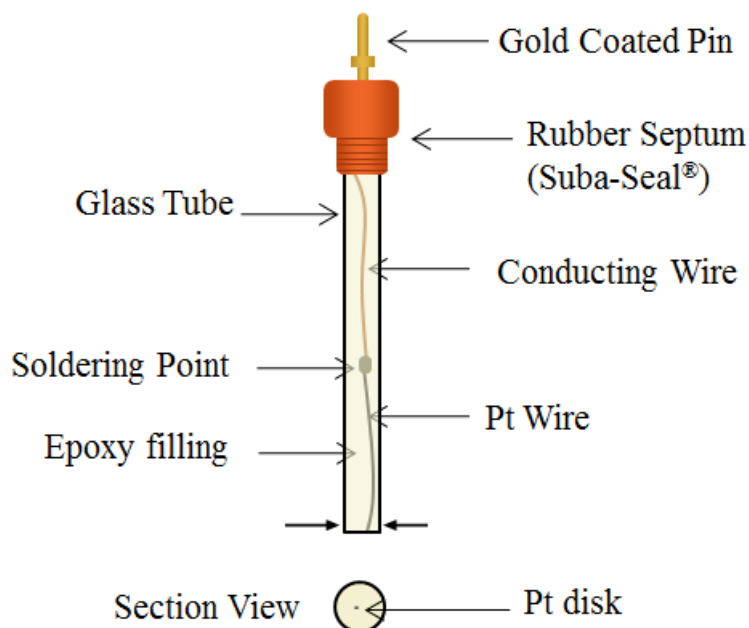


*Figure 4.10 Schematic diagram of the home-made working electrode: Pt wire electrode.*

**A third type electrode, a near micro-size working electrode,** was also made. A platinum wire of 99.9% purity and 100 $\mu\text{m}$  or 300 $\mu\text{m}$  diameter was soldered to a conducting wire then to a gold coated pin (Figure 4.11). This was then inserted in a glass tube and filled with a non-conductive epoxy then left to dry overnight. Once the epoxy was set, the glass tube end was polished with silicon carbide grinding papers from Buehler-Met<sup>®</sup> with successively smaller particle size (15 $\mu\text{m}$ , 6 $\mu\text{m}$ , 3 $\mu\text{m}$  and 1 $\mu\text{m}$ ) until a mirror-like finish was obtained; it was, then washed with ethanol ( $\text{C}_2\text{H}_6\text{O}$ ) to remove traces of the polishing material. The glass tubes were fitted into the Metrohm<sup>®</sup> cell through a rubber septa seal (Suba-Seal<sup>®</sup>) or connected directly to the electrode fittings of the Parr<sup>®</sup> vessel. Palladium wire (99.99%, 2.56 $\text{cm}^2$ ) was also used as a working electrode.



### Pt Microelectrode Electrode

Figure 4.11 Schematic diagram of a near micro- size electrode

Prior to experiments the Pt working flag and wires were flamed with a gas torch, then immersed in concentrated hydrochloric acid then peroxide, finally, washed with deionised water. The Pt disks were polished with aluminium oxide (0.3 $\mu$ m particles size) Metrohm<sup>®</sup> polishing kit then rinsed thoroughly with deionised water.

### 4.3.2 Counter Electrodes (CE)

Different counter electrodes were used in this project to fit in the different cells (Figure 4.8). Metrohm<sup>®</sup> glassy carbon electrode (Figure 4.12) was used a counter electrode in the Metrohm<sup>®</sup> cell. For the cylindrical shape cell (Figure 4.8a), a Pt flag electrode was constructed by the same technique as described in the previous section (Section 4.3.1). For the high pressure experiments, a Pt mesh of 99.9% purity (ca. 20 cm<sup>2</sup>) was used instead of Pt foil.

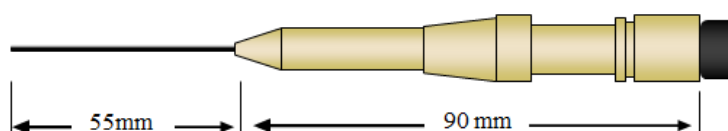


Figure 4.12 Schematic diagram of Metrohm<sup>®</sup> glassy carbon electrode (2D drawing)

All Pt CE used in the bulk electrolysis were isolated in a separate compartment (glass tube) ending in a fine glass frit. The glass frit was attached to the tube using PTFE heat shrink.

### 4.3.3 Reference Electrodes (RE)

Two different reference electrodes were used in the experiments: a saturated calomel ( $Hg/Hg_2Cl_2$ ) electrode (SCE) and a silver/silver chloride (Ag/AgCl) electrode. These electrodes, often used in practical measurements, are considered secondary type reference electrodes which are conventionally referenced against a primary electrode (standard hydrogen electrode SHE).

#### 4.3.3.1 Standard Hydrogen Electrode (SHE)

The standard hydrogen electrode (SHE) is a primary electrode against which relative half-cell potentials are conventionally reported. The SHE consists of a platinised platinum electrode (platinum black) immersed in a proton rich solution (1M). Hydrogen gas, at a pressure of 1 atm, is bubbled over the platinum electrode and the following potential equilibrium is established:

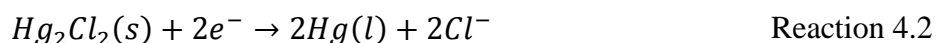


It is important to note that although the SHE is the universal reference standard, it exists only as a theoretical electrode used as an arbitrary reference with a temperature independent, half-cell potential of 0 volt. The zero potential convention was based on the assumption that protons are at unit activity. However, in practice a unit activity of protons is not physically attainable under such conditions (1M concentration) (Sawyer & Roberts 1994)(P. H. Rieger 1994).

For practical measurements, secondary reference electrodes are used. A practical secondary reference electrode should be easily and reproducibly prepared. It should also be relatively inexpensive, and stable over time. Two electrodes, saturated calomel electrode (SCE) and silver/silver chloride (Ag/AgCl) electrode, meet these requirements and are used in this work.

### 4.3.3.2 .Saturated Calomel ( $Hg/Hg_2Cl_2$ ) Electrode (SCE)

Figure 4.13 illustrates SCE electrode, constructed by Russel<sup>®</sup>, used in the atmospheric (1bar) experiments. The SCE is based on the interaction of elemental mercury (Hg) and mercury I chloride in saturated potassium chloride ( $Cl^-$ ) solution:



The SCE potential is +0.242V vs. standard hydrogen electrode (SHE) at 25°C. This standard potential refers to unit activity for all species including chloride ( $Cl^-$ ) ion. In practice, it is often convenient to use a saturated KCl solution as a filling with a few crystals of solid KCl present in the electrode to maintain saturation, so that, the chloride ( $Cl^-$ ) ion concentration is held constant ( P. H. Rieger 1994).

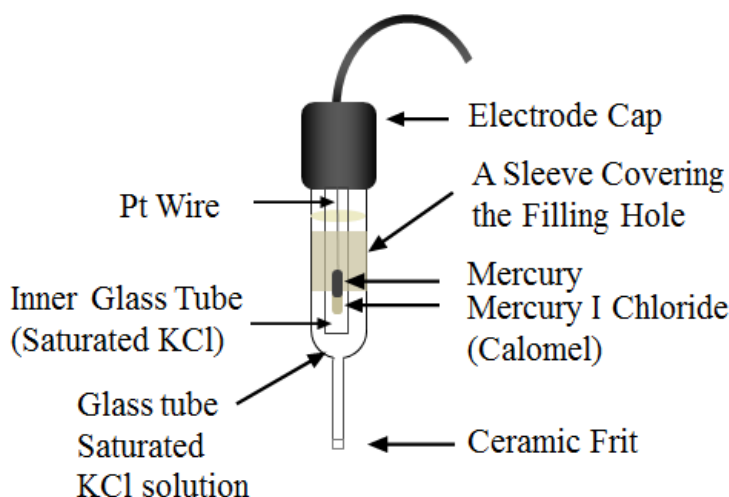


Figure 4.13 Schematic diagram of Russel<sup>®</sup> saturated calomel electrode (SCE)

### 4.3.3.3 Silver/Silver Chloride ( $Ag/AgCl$ ) Electrode

Figure 4.14 depicts a schematic diagram of the Metrohm<sup>®</sup> Ag/AgCl reference electrode used in the atmospheric pressure (1bar) experiments. The Silver/Silver chloride ( $Ag/AgCl$ ), is one of the most reproducible and reliable reference electrodes and most regularly used for the simplicity of its design, convenience of use, and nontoxic components (Zoski 2007).

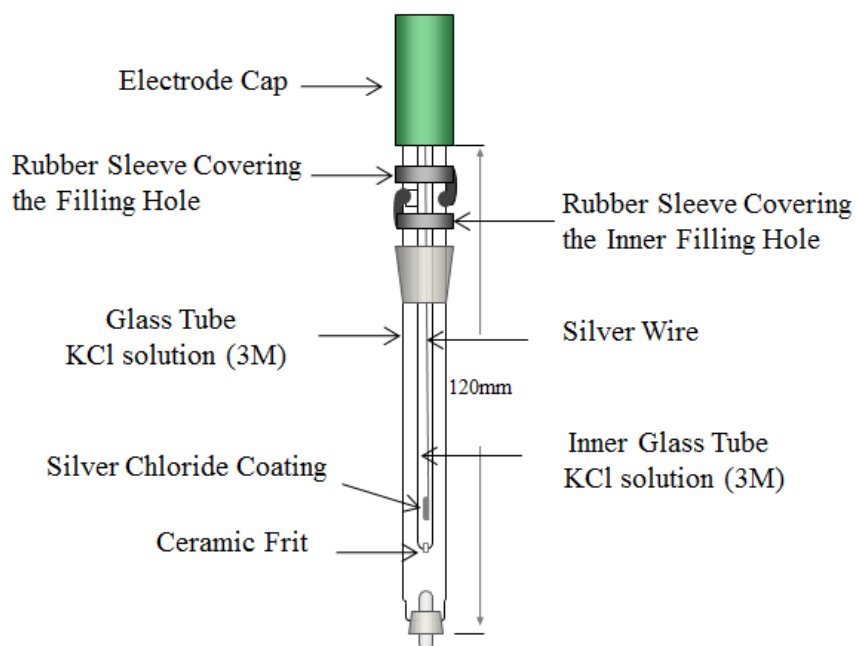


Figure 4.14 Schematic diagram of Metrohm<sup>®</sup> Silver/Silver Chloride electrode (2D drawn)

The electrode is made by chlorinating, a process whereby silver wire, immersed in aqueous potassium chloride solution, is electrochemically coated with a thin layer of silver chloride (P. H. Rieger 1994). The potential of Ag/AgCl, equipped with 3M potassium chloride solution, is +0.222V vs. SHE (298K) (Inamdar et al. 2009).



The potential is calculated by the Nernst equation (Eq. 4.1):

$$E_{\text{Ag}/\text{AgCl}} = E_{\text{Ag}/\text{AgCl}}^0 - \frac{RT}{F} \ln a_{\text{Cl}^-} \quad \text{Eq. 4.1}$$

The potential of Ag/AgCl is a function of the chloride ions  $\text{Cl}^-$  activity (this is related to the concentration of these ions). Thus, the voltage of the electrode varies with KCl solution concentration (e.g. the Ag/AgCl potential is ~10mV more negative in saturated KCl than in 3M KCl).

The commercial SCE and Ag/AgCl electrodes are not suitable for high pressure measurements. Thus, it was necessary to fabricate **a pseudo Ag/AgCl reference electrode** for this purpose. A pseudo reference electrode is usually a wire immersed in a sample solution. This type of electrode provides a constant potential; however, the reference potential is unknown since it is dependent on the solution composition. As

described above this type of electrode is usually constructed by electrochemical chlorination. Among the various chlorination techniques, electroplating was chosen for simplicity and availability of the materials. The Ag/AgCl electrode is prepared by electrolytic hydrolysis coating of a silver wire. According to Ives et al, the process requires the immersion of a silver wire in a dilute hydrochloric acid solution (0.1 M) and a platinum wire is used as a cathode. Upon the passage of an electrical current, through the two wires, at a rate of 10mA/cm<sup>2</sup> anodic biasing for half an hour, the silver wire should turn light grey, then to a dark grey signifying a successful coating process. The newly coated electrode is then rinsed with deionized water and left to soak in a 3 M KCl solution overnight to allow the potential to stabilize (Ives 1961).

The electrode was prepared by the above described procedure. For that, a 1mm diameter silver wire was cleaned with 1200 grit silicon carbide grinding papers from Buehler-Met<sup>®</sup>, then wiped with ethanol (C<sub>2</sub>H<sub>6</sub>O) to remove any oxide layers on the surface followed by ample rinsing with deionised water. The silver wire was then positioned carefully to have a length of 30 mm immersed into the acid solution. This gives ca. 0.95 cm<sup>2</sup> area, hence the silver wires would require 9.5 mA current source. Finally, the silver wire was coated using a 0.1M HCl solution. A short lived purplish grey colour was formed which then turned into light grey. The wire was rinsed with deionised water and inserted into 3M KCl solution. The potential of the prepared pseudo Ag/AgCl electrode was tested against the commercial Russel<sup>®</sup> SCE (which is kept for calibration purposes). The two electrodes were immersed in 3M KCl solution and a potential difference of 42.5 ±0.1mV was measured by a voltmeter. The measured voltage deviates (from the literature potentials reported above) by 22.5±0.1mV. This is considered within acceptable range (Sawyer & Roberts 1994). Silver salts are photo-sensitive so light inevitably has an effect on the reference potential (Ives 1961). Hence, the pseudo reference electrode was stored in AMBER glass vials. The effect of ionic species contamination from this electrode into the electrolyte of interest is reported in Chapter 7. The pH meter used to adjust the acidity of the electrolytes has an accuracy of ±0.01.

## 4.4 Reagents

All the chemicals used in this project were purchased from Sigma-Aldrich unless otherwise mentioned. Electrolyte solutions of 0.5M potassium chloride KCl (Sigma Aldrich,

>99.99%) and pyridine (C<sub>5</sub>H<sub>5</sub>N) (Sigma Aldrich, >99.9%) were purged for 10-45min with N<sub>2</sub> (Energas, 99.99%) or CO<sub>2</sub> (Energas, 99.9%). The pH of the solution was adjusted using HCl (Sigma Aldrich, >99.99%). Deionized water (18.2 MΩ cm) was used for the aqueous electrolyte solutions preparation. The electrolyte consisted of a solution containing pyridine (C<sub>5</sub>H<sub>5</sub>N) in aqueous 0.5M KCl as the supporting electrolyte. For the effect of pH study, adjustment of the pH was performed by the addition of 0.1M hydrochloric acid.

## **4.5 Product Analysis by Gas Chromatography-Mass Spectrometry (GCMS) in Selected Ion Monitoring (SIM) Mode**

The products of the bulk electrolysis were analysed for the alcohol content including methanol (CH<sub>4</sub>O), ethanol (C<sub>2</sub>H<sub>6</sub>O), isopropanol (C<sub>3</sub>H<sub>8</sub>O) and butanol (C<sub>4</sub>H<sub>10</sub>O). Calibration samples were prepared in aqueous pyridine-containing solutions and analysed by a Hewlett-Packard<sup>®</sup> gas chromatograph HP-6890 connected to a Hewlett-Packard<sup>®</sup> mass spectrometer HP-5973. Helium (99.999%) was used as the carrier gas.

### **4.5.1 Method Development**

#### **4.5.1.1 Column Selection**

The primary goal of column selection was to detect and quantify semi-volatile substances such as methanol in aqueous solvent. Sensitivity, selectivity, and high resolution separation and quantification of analytes were sought.

Wall-coated capillary columns of different brands with a variety of phases and dimensions were initially considered. A Porous Layer Open Tubular PLOT (Agilent<sup>®</sup> HP-PLOT-U, 30 m × 0.32 mm, 20μm) column was initially selected and used for the head space gas chromatography (HSGC) analysis described in Section 4.5.1.4.1.

The Agilent<sup>®</sup> HP-PLOT-U column consists of bonded divinylbenzene/ethylene glycol dimethacrylate coated onto a fused silica capillary. Due to the high molecular weight of the stationary phase particles (130 gmol<sup>-1</sup>/198 gmol<sup>-1</sup>) and the relatively large film

coating thickness, the particles dislodge from the column and flow downstream; this may result in flow restriction and detector contamination. Headspace gas chromatography (HSGC) analysis on this column caused the interference of “ghost” peaks with the target analytes. Thus, the identification and quantification of the alcohol was hindered although the precise reason for this issue is unclear.

Thus, the Agilent® HP-PLOT-U column was replaced by a Restek® (Rt®-Q-Bond, 30m ×0.25mm, 8µm) with similar stationary phase but a thinner coating film. Rt®-Q-Bond column proved to be the best column that could fulfil all the needs of the method, i.e., higher sensitivity, shorter runtime and higher resolution between analytes without the “ghost” peaks.

### 4.5.1.2 Standard Sample Preparation

The standard samples were prepared in aqueous 0.5M KCl solutions using deionised water resistivity of 18.2 MΩ cm and containing (0.791g/l, 10mM) pyridine (C<sub>5</sub>H<sub>5</sub>N). Stock solutions of 5000µg of alcohol/l were prepared at room temperature; the standard calibration concentrations are shown for each set of analysis (Figure 4.26). The standard solutions were transferred in 4ml vials and sealed with Teflon-coated septum caps. For liquid injections the vials were filled to ~4ml. However, for the headspace analysis the vials were filled to 3.5ml. This volume represents the optimum liquid volume at which the concentration of the alcohol in the headspace is at maximum as shown below by calculations of the partitioning of the analyte between these two phases. The partitioning behaviour is often reported in terms of dimensionless Henry’s constant or partition coefficient. This is defined as:

$$H_{ci} = \frac{C_g}{C_l} \quad \text{Eq. 4.2}$$

where  $H_{ci}$  is the dimensionless Henry’s constant or gas/liquid partition coefficient,  $C_g$  the gas phase concentration,  $C_l$  the liquid phase concentration (Teja et al. 2001) (Gupta et al. 2000)

Calculation of analyte concentration in the headspace and in liquid phases was performed using Eq.4.2. The partitioning behaviour of methanol in aqueous solutions is an important factor for estimating its concentration in the headspace for the present analysis. Henry’s constant of methanol was calculated at different temperatures as part

of headspace gas chromatographic analysis (Teja et al. 2001) (Gupta et al. 2000). The equilibrium temperature for HS analysis of low molecular weight alcohols ranges between 40°C and 60°C (Teja et al. 2001). Equilibrium tests of identical vials content have shown that an optimum of 60°C at minimum of 20min is required. At 60°C, dimensionless Henry's constant,  $H_{ci}$ , was reported at  $10^{-3}$  (Teja et al. 2001). At equilibrium the mass balance is written as:

$$M = C_l^0 V_l = C_l V_l + C_g V_g \quad \text{Eq. 4.3}$$

where  $C_l^0$  is the initial concentration of methanol,  $V_l$  is the initial volume of methanol in the liquid phase,  $C_l$  is the equilibrium concentration of methanol in the liquid phase,  $C_g$  is the equilibrium concentration of methanol in the gas phase (headspace) after equilibrium is attained, and the  $V_g$  is the volume of the headspace. The concentration of methanol in a standard sample of  $C_l^0 = 200\mu\text{g}/\text{l}$  is considered for illustration purpose. The equations Eq.4.2 and Eq. 4.3 are solved for  $C_g$  (Eq.4.4) and potted in Figure 4.15.

$$C_g = 200V_l/(1000V_l + V_g) \quad \text{Eq. 4.4}$$

The volume of the liquid phase was taken as 3.5ml (Figure 4.15). The concentration of methanol in the headspace is 99.98% of the total concentration at 3.5ml. Higher volume proved impractical for HS sampling as liquid contamination was an issue.

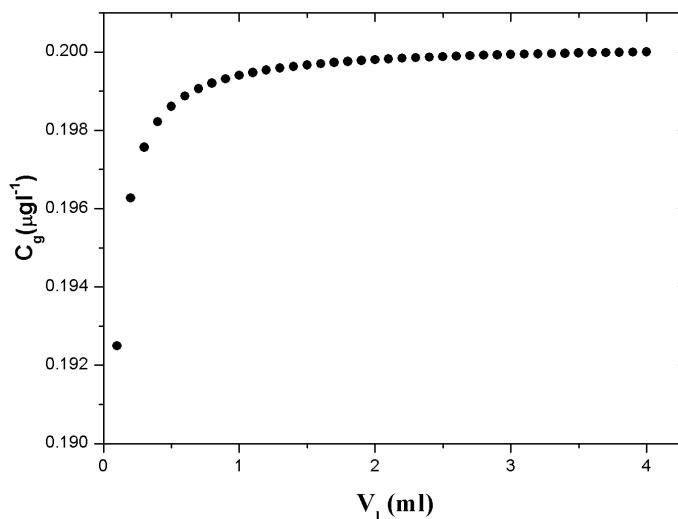


Figure 4.15 Equilibrium concentrations of methanol in the headspace as function of the initial liquid samples volume

### 4.5.1.3 Identification of the Target Compounds

Qualitative identification of each analyte was performed on full scanning mode so as to obtain the mass spectrum corresponding to each analyte. The identification of each alcohol was based upon the characteristic mass spectrum of the peak of interest compared with the mass spectrum of an authentic compound. The mass spectrum of isopropanol ( $\text{C}_3\text{H}_8\text{O}$ ) is given as an example (Figure 4.16); all other mass spectra are given in the Appendix D4.

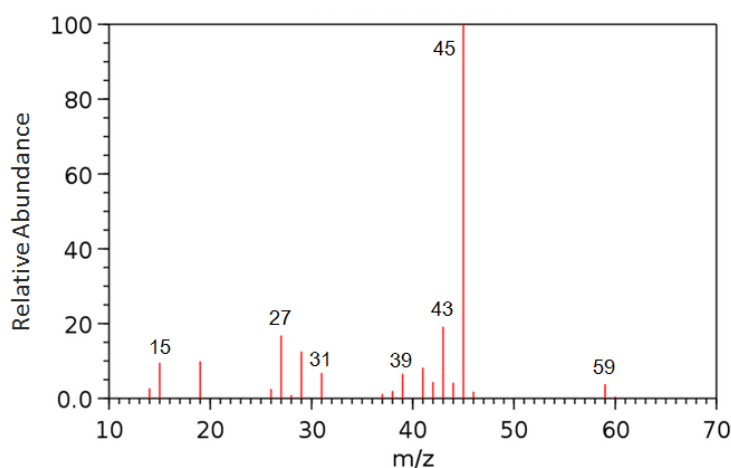


Figure 4.16 Mass spectrum of isopropanol ( $\text{C}_3\text{H}_8\text{O}$ )

The characteristic ions selected for SIM scanning mode was based on the most abundant fragment ion of each compound (Table 4.1). The ions 31, 56, 45 and 79 were selected for methanol, butanol (C<sub>4</sub>H<sub>10</sub>O), and pyridine (C<sub>5</sub>H<sub>5</sub>N) respectively. Since the selected 31 ion, is the most abundant fragment ion for both methanol and ethanol (C<sub>2</sub>H<sub>6</sub>O) and the ion 45 represents an ion fragment of both ethanol (C<sub>2</sub>H<sub>6</sub>O) and isopropanol (C<sub>3</sub>H<sub>8</sub>O), the latter ion (45) was selected for both alcohols. The elution time for each the compound was also determined as illustrated in the chromatogram Figure 4.17.

Table 4.1 Compounds with their most abundant ions

Compound	Most Abundant Ions	Selected Ions for SIM Analysis
Methanol (CH <sub>3</sub> OH)	31	31
Ethanol (C <sub>2</sub> H <sub>6</sub> O)	31	45
Isopropanol (C <sub>3</sub> H <sub>8</sub> O)	45	45
Butanol (C <sub>4</sub> H <sub>10</sub> O)	56	56
Pyridine (C <sub>5</sub> H <sub>5</sub> N)	79	79

Errors were minimised throughout the entire procedure by rigorous cleaning of the syringes used for injection, and the column was flushed out before any measurements (blank run were performed prior injections).

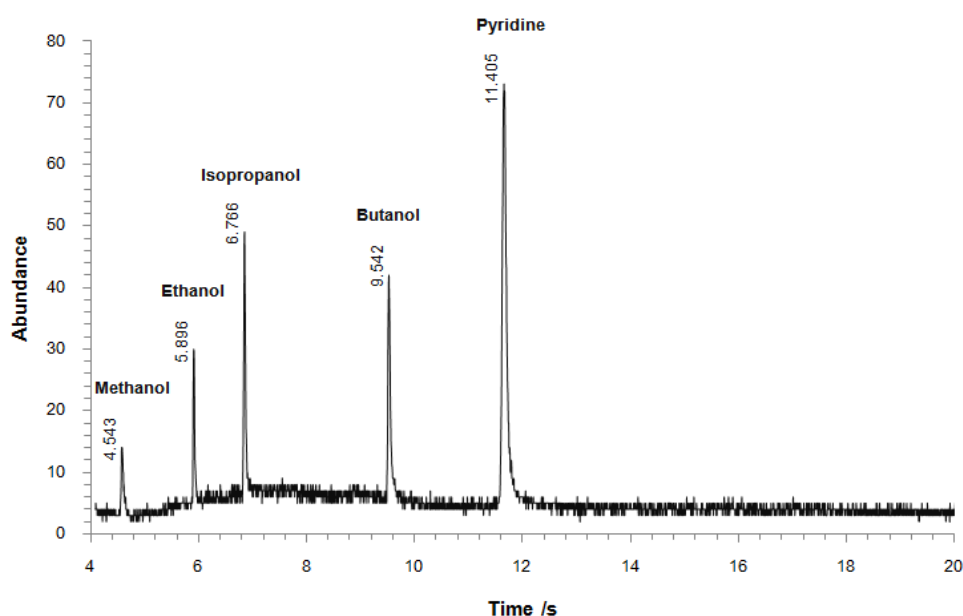


Figure 4.17 Chromatogram of methanol, ethanol, isopropanol, butanol, and pyridine peaks and their corresponding elution time

### 4.5.1.4 Optimisation of the SIM GCMS Operating Conditions

Selected Ion Monitoring (SIM) provides specific compound detection, by selecting the characteristic ion as described in the previous section, with very high sensitivity. The thermal gradient mode of operation enhanced the signal-to-noise ratio and allowed better analysis.

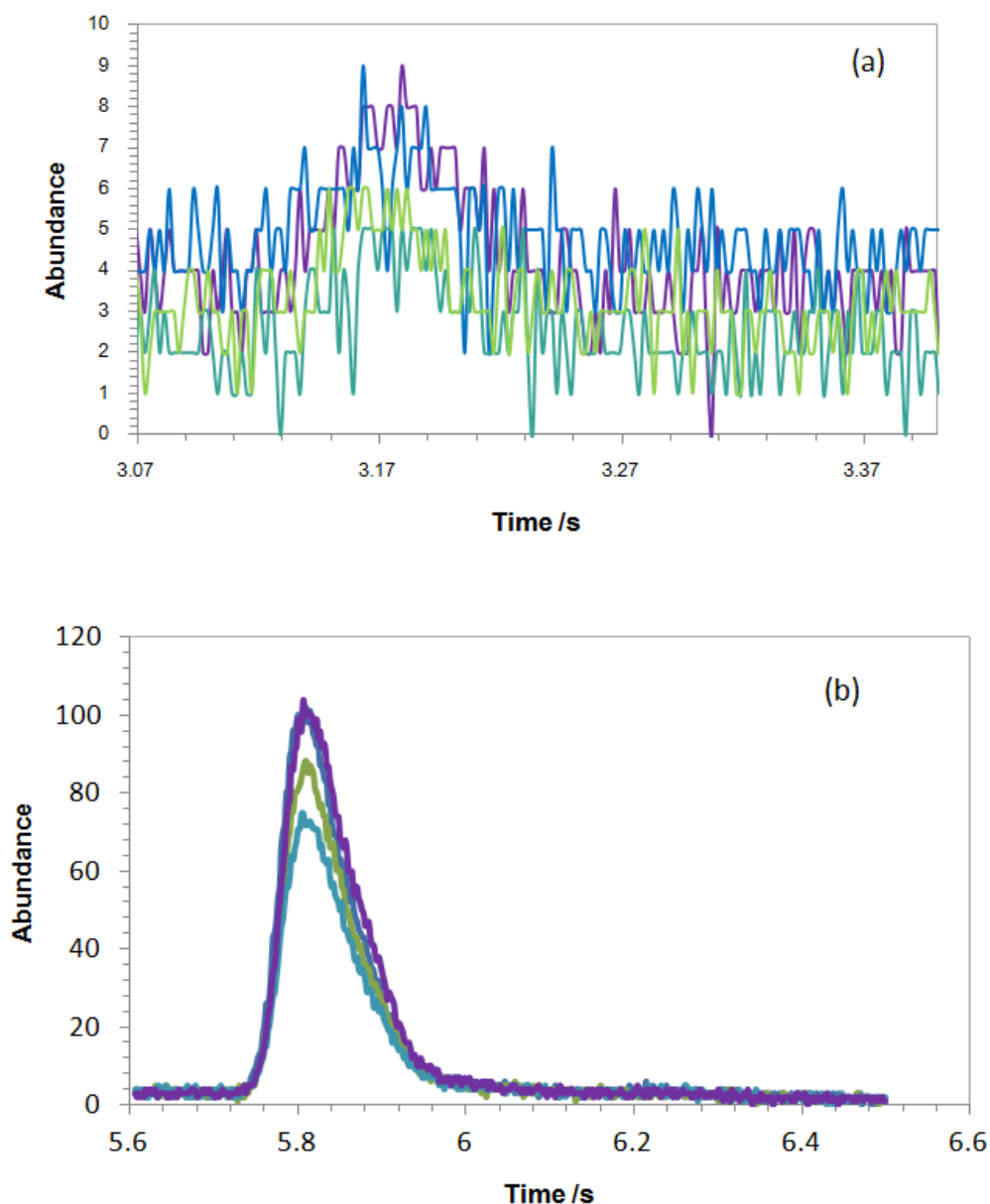


Figure 4.18 Chromatograms of methanol (500  $\mu$ g/l, 5ppm) run on (a) method 1 and (b) method 3 described in Table 4.3.

The methods in Table 4.3 were tested with standard samples containing methanol in aqueous solution prepared as described in section 4.5.1.2 (samples preparation). The chromatograms of four methanol samples were run with method 1 and method 3, for which the operating conditions are summarised in Table 4.3 and plotted in Figure 4.18a and b respectively. In method 1, the temperature was fixed at 130°C, while in method 3 a thermal program was employed. The thermal gradient method (method 3) clearly showed better sensitivity than the method 1. This is demonstrated by the peak heights/area difference of nearly one order of magnitude for the same sample (Figure 4.18). However, method 3 results in considerable peak tailing which affects the quantification of the target compounds.

Table 4.2 Headspace (HS) selected ion monitoring gas chromatography (SIM GC) initial conditions for the method development

<b>Sample Number</b>	<b>Thermal Gradient °C/Min</b>	<b>Pressure psi</b>	<b>Initial Temp °C</b>	<b>Temp holding time /Min</b>	<b>Solvent Time Delay /Min</b>
302	20	4	40	0.5	0.5
304	20	4	50	0.5	0.5
308	20	2	40	1.5	1.5
310	30	2	40	1.5	1.5
318	20	2	50	1.0	1.0

In the SIM method, each of the GCMS parameters affects the elution time, shape of the peak, and the signal-to-noise ratio. Therefore, the method development necessitates optimisation of these parameters. For instance, the pressure of the carrier gas affects the height and the retention time of the peak. Samples-304 and 318 containing methanol and ethanol (C<sub>2</sub>H<sub>6</sub>O) were run at 4psi and 2psi respectively (Table 4.2).

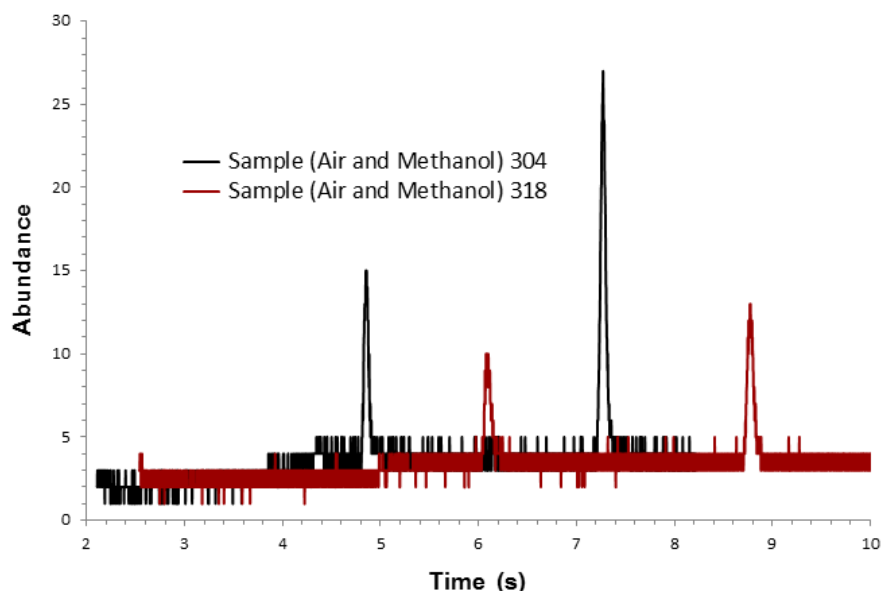


*Figure 4.19 Effect of pressure on the peak height and retention time of air (first peak) and methanol (second peak)*

Increasing the pressure by a factor of 2 increases the peak height approximately two times as well (Figure 4.19). Moreover, the initial temperature applied to the column affects the GC response; the peak height of sample-302 is enhanced at 40°C and retained longer (0.5seconds) compared to the sample-304 peak height, which was run at 50°C (Figure 4.20) but otherwise under the same conditions (Table4.2). However, sample-302, run at the lower initial temperature resulted in a slight peak tailing.

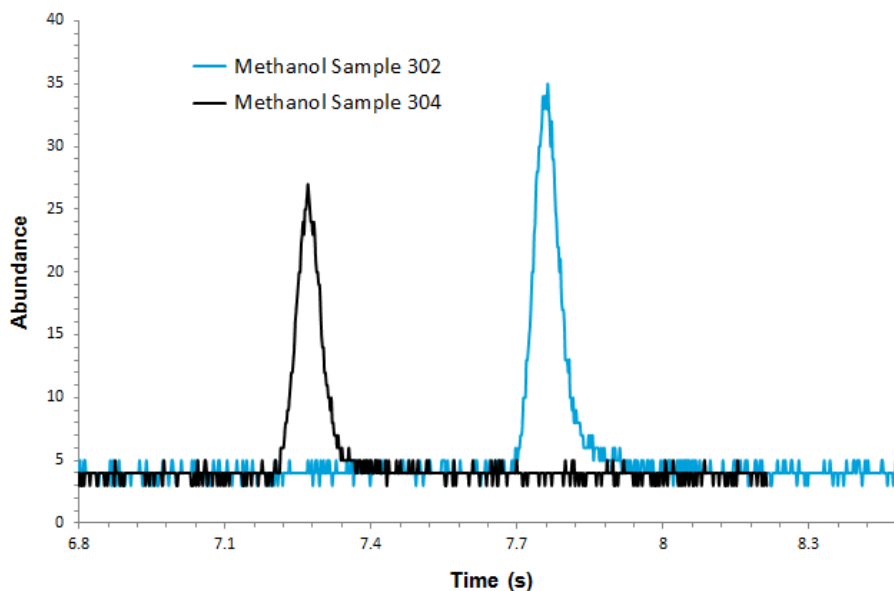


*Figure 4.20 Effect of initial column temperature on peak height and retention time of methanol*

The heating increment also affects the peaks shapes. Samples 308 and 310 were run at identical conditions with the exception of the initial column temperature. Sample-308 was run at 20°C/min and sample-310 at 30°C/min (Figure 4.21).

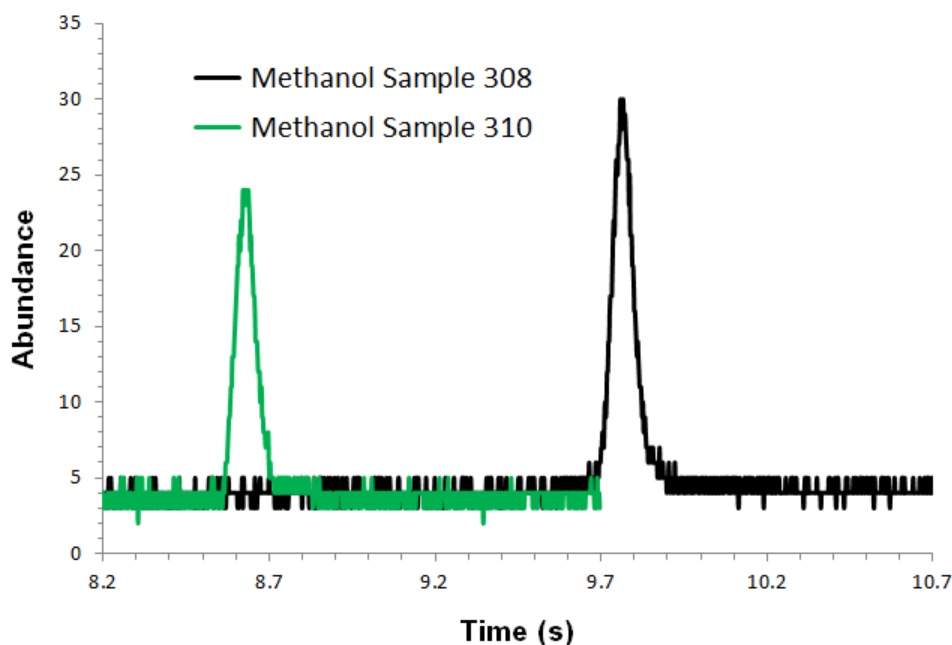


*Figure 4.21 Effect of the initial column temperature on methanol peak shape*

At the latter condition, 30°C/min heating increment, the resulting peak has no tailing as compared to 20°C/min; the peak in this case is also 1.5times narrower. The GC conditions investigated in the method development and are illustrated in Appendix D5, Table D1.

All the samples to be analysed contain the aromatic amine, pyridine ( $C_5H_5N$ ), which has a long elution time of  $11.4\pm 1.1$  s comparing to the target analytes: methanol, ethanol ( $C_2H_6O$ ), isopropanol ( $C_3H_8O$ ), and butanol (Table 4.6). The high concentration of such compounds (0.791g/l) was accumulated in the capillary column when low initial temperature was set at 40°C; this caused an overload of the column. Hence, the column was freed from the amine which caused an interference with the subsequent injection. The carryover was eliminated by extending the total time beyond pyridine ( $C_5H_5N$ ) elution time to 30min.

Table 4.3 GCMS Manual Headspace Methods

METHOD NUMBER	OVEN RAMP TEMP PRGM			INLET TEMP (°C)	AUX TEMP (°C)	PRESSURE (Psi)	SPLIT/SPLITLESS MODES	SOLVENT DELAY (min)	RUN TIME (min)
	HEAT GRADIENT	TEMP	HOLD TIME						
Method 1	HEAT GRADIENT	TEMP	HOLD TIME	150	150	2	SPLIT	2.0	5
	-	130°C	5.0						
	-	-	-						
Method 2	HEAT GRADIENT	TEMP	HOLD TIME	170	170	4	SPLITLESS	4.0	11
	-	50°C	1.5						
	30°C/min	140°C	7.0						
Method 3	HEAT GRADIENT	TEMP	HOLD TIME	170	170	2	SPLITLESS	4.5	21
	-	40°C	1.50						
	30°C/min	140°C	2.00						
	30°C/min	170°C	13.0						

INLET TEMP: Inlet temperature

AUX TEMP: Auxiliary temperature

OVEN RAMP TEMP PRGM: Column ramping mode temperature program

#### 4.5.1.4.1. Headspace (HS) Method: Optimisation

The manual headspace method was optimized in such a way that maximum amount possible of the analyte present in the liquid sample gets into the headspace for the detection. For this the standard sample vials and the manual gas tight syringes were heated at 40–60°C for 25–60 min. A combination of sample vial heating at 60°C for at least 25 min in order to reach equilibrium was found to be suitable for getting a good response. The heating was limited to 60°C as this was the temperature limit the manual syringes can withstand. Errors were minimised by the use of the same manual gas syringe of 20µl for the HS injections. Care was taken to consistently repeat the injection procedure. The vials were filled to the same liquid volume (this was described in Section 4.5.1.2). The syringe was heated to the same temperature as the vials (60°C) and was cleaned regularly to remove any compound residue. Method 3 described earlier in the method development section was optimised, since the target analyte peaks in Figure 4.18b needed width reduction and tailing minimisation. The optimised GCMS parameters are summarised in Table 4.4.

Table 4.4 HS SIM GCMS operating conditions

<b>Operating Conditions of HS GCMS</b>	
Oven temperature program	-
Initial temperature	40°C
Hold time	1.5min
Thermal gradient	20°C/min
Final temperature	120°C
Total time	30min
Inlet temperature	150°C
Inlet	Splitless
MS Source temperature	230°C
MS Quad temperature	150°C
Aux temperature	177°C
Column flow	0.5ml/min
Column type	HP-Plot -U

HS SIM analyses were performed in the following sequence:

1. First the blank run (air) is performed in SIM mode (monitoring fragment ion(s) characteristic of the target analyte to be detected)
2. Then the sample to be analysed is injected in a minimum of three replicas

3. Virtual run (no injections) is frequently performed to allow any compounds remaining in the column to elute

4. Then calibration samples are injected in a minimum of three replicas

During the HS GCMS method development and early analysis, continual dislodging of the column particles and their flow downstream to the MS detector was found to have contaminated the MS. This may have caused interferences in the detector leading to spikes. This is reflected in the appearance of ghost peaks. The presence of the ghost peaks presents two main issues. First, the appearance of these peaks affected the repeatability of the injections. Second, the ghost peaks were observed at the methanol elution time; this rendered the analysis difficult and lowered the accuracy of the quantification.

The procedure of the HS method reliability assessment and the presence of ghost peaks investigation are as follows: HS injections in the full scan mode of 20 $\mu$ l air, which is in this case the blank sample, sampled with a Hamilton<sup>®</sup> gas tight syringe. The injections are performed on the same run for a convenient assessment of repeatability. The same procedure is performed with a calibration sample containing the target analyte. When reasonable repeatability of the both the blank and the calibration sample are obtained, both samples are then injected in SIM mode monitoring the ion fragment 31 on individual runs. The injection of the blank run on SIM mode usually confirms presence/absence of the ghost peaks. The persistent interference of the ghost peaks rendered the HS method unreliable and the conditions uncontrollable, hence the direct liquid injection method was considered.

#### **4.5.1.4.2. Direct (liquid) injection GCMS Method**

The method involved direct 3 $\mu$ l liquid injections sampled using Agilent<sup>®</sup> 10 $\mu$ l liquid syringes for the analysis of alcohols in aqueous pyridine-containing solutions. The detection of alcohols was carried out in SIM mode. A thermal gradient was chosen considering the higher sensitivity seen for this program during HS method development. An initial hold of 2 min at 40 $^{\circ}$ C and a linear thermal gradient to 200 $^{\circ}$ C at 30 $^{\circ}$ C/min was found to result in the best peak shape and retention without affecting the resolution. The operating conditions are listed in Table 4.5. The method accuracy assessment, parameters such as repeatability, precision, specificity, linearity, limit of detection and limit of quantification were evaluated as indicated by the International Conference on

Harmonisation (ICH) guideline (ICH CH et al. 1996). The ICH of technical requirements for methods validation for registration of pharmaceuticals was chosen in view of the rigorousness of the limits set for assessing the accuracy of an analytical method and estimation of errors.

Table 4.5 SIM GCMS operating conditions for liquid injections

<b>Operational conditions of GC-MS</b>	
Oven temperature program	-
Initial temperature	80°C
Hold time	2min
Thermal gradient	30°C/min
Final temperature	200°C
Total time	30min
Inlet temperature	200°C
Inlet	Splitless
MS Source temperature	230°C
MS Quad temperature	150°C
Aux temperature	200°C
Pressure	0.7ml/min
Column flow	7.93psi
Column type	Rt-Q Bond

#### 4.5.1.4.2.1 System Specificity

Samples were prepared with concentrations above the limit of detection (LOD) (described in Chapter 2 Section 2.8.6.5 and estimated in the next section) of methanol, ethanol (C<sub>2</sub>H<sub>6</sub>O), isopropanol (C<sub>3</sub>H<sub>8</sub>O), butanol and pyridine (C<sub>5</sub>H<sub>5</sub>N) in aqueous solution (NB. for analysis of trace compounds lower range calibration curve were constructed). The sample was chromatographed to examine the interference, if any, of the analytes peaks. The selectivity was assessed based on the resolution of compounds and their corresponding retention time (Figure 4.17). The retention time of all alcohols indicate that they were well resolved from each other and no interferences were observed (Table 4.6).

Table 4.6 Retention time of the target compounds

<b>Target Compound</b>	<b>Retention Time (min)</b>
Methanol (CH <sub>3</sub> OH)	4.5±0.45
Ethanol (C <sub>2</sub> H <sub>6</sub> O)	5.9±0.59
Isopropanol (C <sub>3</sub> H <sub>8</sub> O)	6.8±0.68
Butanol (C <sub>4</sub> H <sub>10</sub> O)	9.5±0.95
Pyridine (C <sub>5</sub> H <sub>5</sub> N)	11.4±0.11

#### 4.5.1.4.2.2 System Precision and Repeatability

Three standard solutions containing methanol at different concentrations of 500 µg/l (0.5ppm), 2000 µg/l (2ppm), and 5000 µg/l (5ppm), were prepared and chromatographed in three replicas as shown in Figure 4.22.

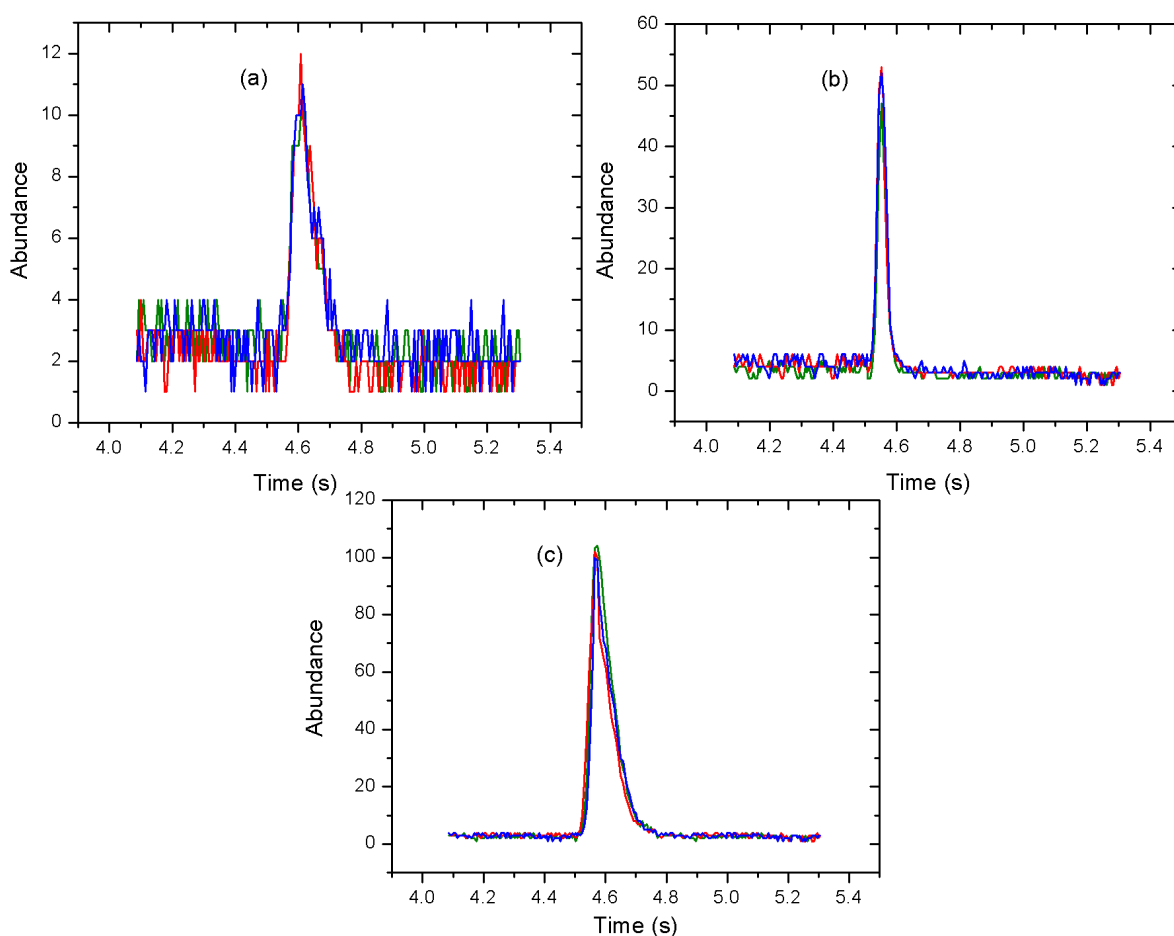


Figure 4.22 Repeatability of three injection replicas of three different methanol concentrations (a) 500 µg/l (0.5ppm), (b) 2000 µg/l (2ppm), and (c) 5000 µg/l (5ppm)

The area of each replica of the three GC peaks was calculated to assess the system repeatability. The integration of area under peak was performed using Origin<sup>®</sup> 8. The calculated areas are represented in Table 4.7. The consecutive injections of each sample indicate an acceptable level of repeatability for the analytical system. The variation of <10% demonstrates an acceptable repeatability of the analyses.

Table 4.7 Calculated GC peak areas of standard methanol concentrations

Standard concentration (µg/l)	GC peak Area	Mean	Variation
300	0.51	0.52	±0.04
	0.56		
	0.49		
500	0.87	0.89	±0.02
	0.90		
	0.92		
2000	1.84	2.06	±0.19
	2.15		
	2.21		
5000	6.99	6.50	±0.42
	6.27		
	6.25		

#### 4.5.1.4.2.3 Limit of Detection (LOD) and Limit of Quantification (LOQ)

The LODs and the LOQs of the alcohols prepared in aqueous solutions were determined based on the signal-to-noise ratio as defined by ICH (refer to Chapter 2, Section 2.8.6.5 and 2.8.6.6). The signal-to-noise ratio is calculated using Eq.2.76 (Chapter 2, Section 2.8.6.5).

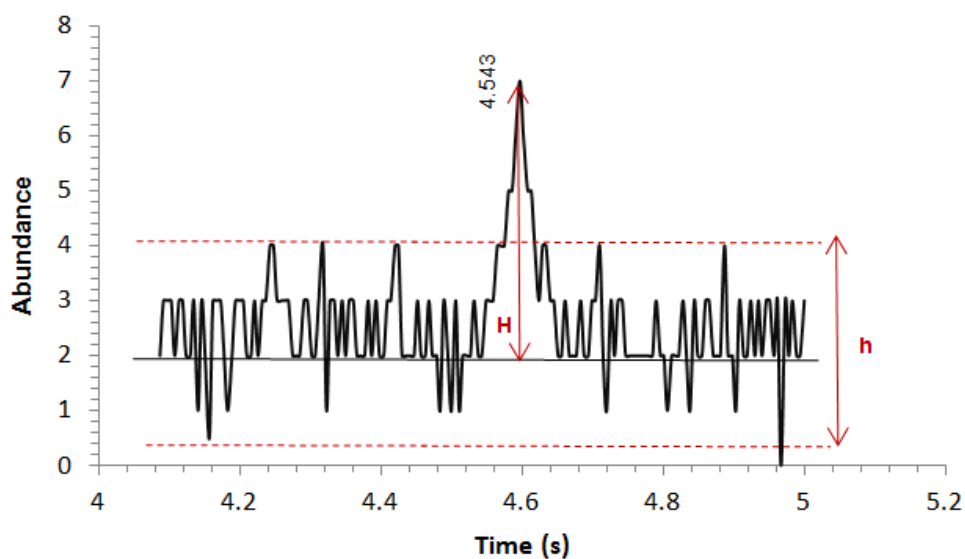
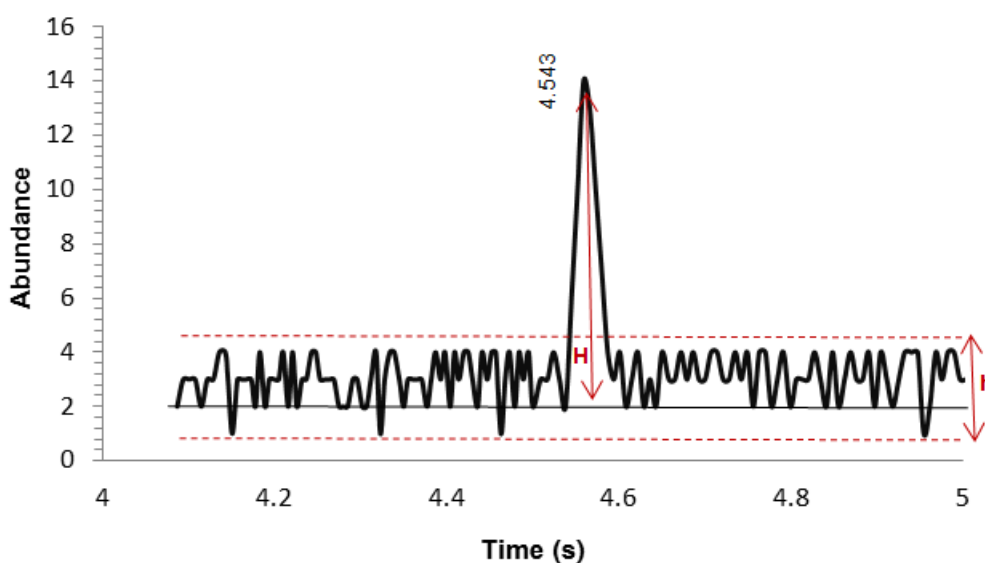


Figure 4.23 Methanol Limit of Detection (LOD)

Figure 4.23 and 4.24 illustrate methanol peak at LOD and LOQ respectively. The height of the analyte peak of the chromatogram obtained was estimated at  $H=5$  and  $H=12$  for the LOD and LOQ respectively. The measure of the peak-to-peak background noise in the chromatogram obtained at half-height of the peak,  $h$ , was performed based on the signal observed over a distance of 20 times the width at half-height,  $h=4$  for LOD and  $h=3$  for LOQ. The LOD and LOQ are computed to a signal-to-noise of  $> 1:2$  and  $1:8$  which is within acceptable limit for estimating the detection limit.



*Figure 4.24 Methanol Limit of Quantification*

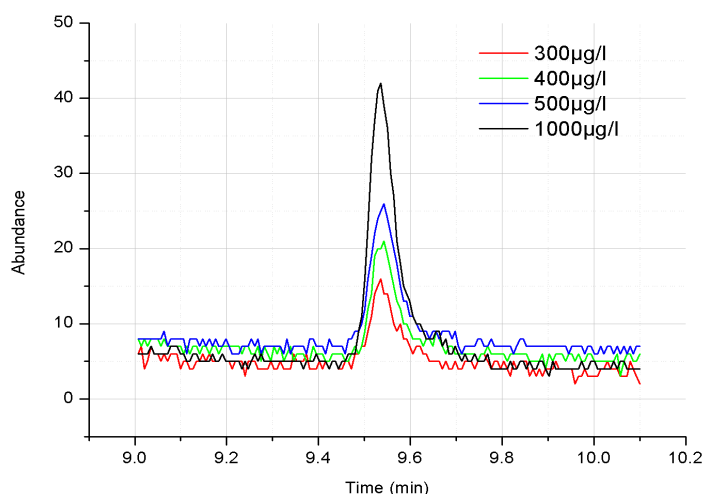
The LOD and LOQ were estimated in the same manner as described earlier for all the target analytes and are summarised in Table 4.8. The limit of detection was estimated at 1:2 ratios for all target analytes, while the limit of quantification was estimated at 1:8 ratio for methanol and ethanol ( $C_2H_6O$ ) and at 1:9 and 1:10 ratios for isopropanol ( $C_3H_8O$ ) and butanol respectively.

Table 4.8 LOD and LOQ concentrations for target analytes

<b>Analyte</b>	<b>LOD Concentration (<math>\mu</math>g/l)</b>	<b>LOQ Concentration (<math>\mu</math>g/l)</b>
Methanol ( $CH_3OH$ )	100	200
Ethanol ( $C_2H_6O$ )	100	200
Isopropanol ( $C_3H_8O$ )	100	200
Butanol ( $C_4H_{10}O$ )	100	200

#### 4.5.1.4.2.4 System Linearity: Standards Calibration

The linearity of the method was determined by constructing a calibration graph of standard samples for each alcohol. The sample preparation, injections, and analysis were acquired and processed under identical conditions as described in above. Pyridine ( $C_5H_5N$ ) was added ( $0.79g/l/10mM$ ) for each standard sample as a reference compound. The GC response of this reference has the purpose of compensating the loss of the standard sample amounts during the preparation and injection. Injections of each standard sample over the range of limit of quantification of the standards concentrations were performed in three replicas and minimum of 5 concentrations. Typical butanol chromatographs of standard samples concentrations are shown in Figure 4.25.



*Figure 4.25 Chromatograms of butanol standard samples at 300, 400, 500 and 1000 µg/l*

Figure 4.26 shows the calibration graphs of the alcohols standard samples. The corrected GC peak area represents the ratio of the alcohol peak area to the reference peak area (pyridine ( $C_5H_5N$ )). The error bar were estimated from the average GC peak area of three injections replica for each concentration. The GC response is linear over the concentration range analysed for each alcohol as indicated by the correlation coefficient ( $R^2$ ) values ( $>0.999$ ) (Figure 4.26). The concentration of the unknown alcohol (produced by electrolysis) was then determined from the linear regression equations in Figure 4.26 for each alcohol. This method has been successfully applied for the identification and quantification of methanol amounts and other alcohols in the electrolysis samples (Chapter 7).

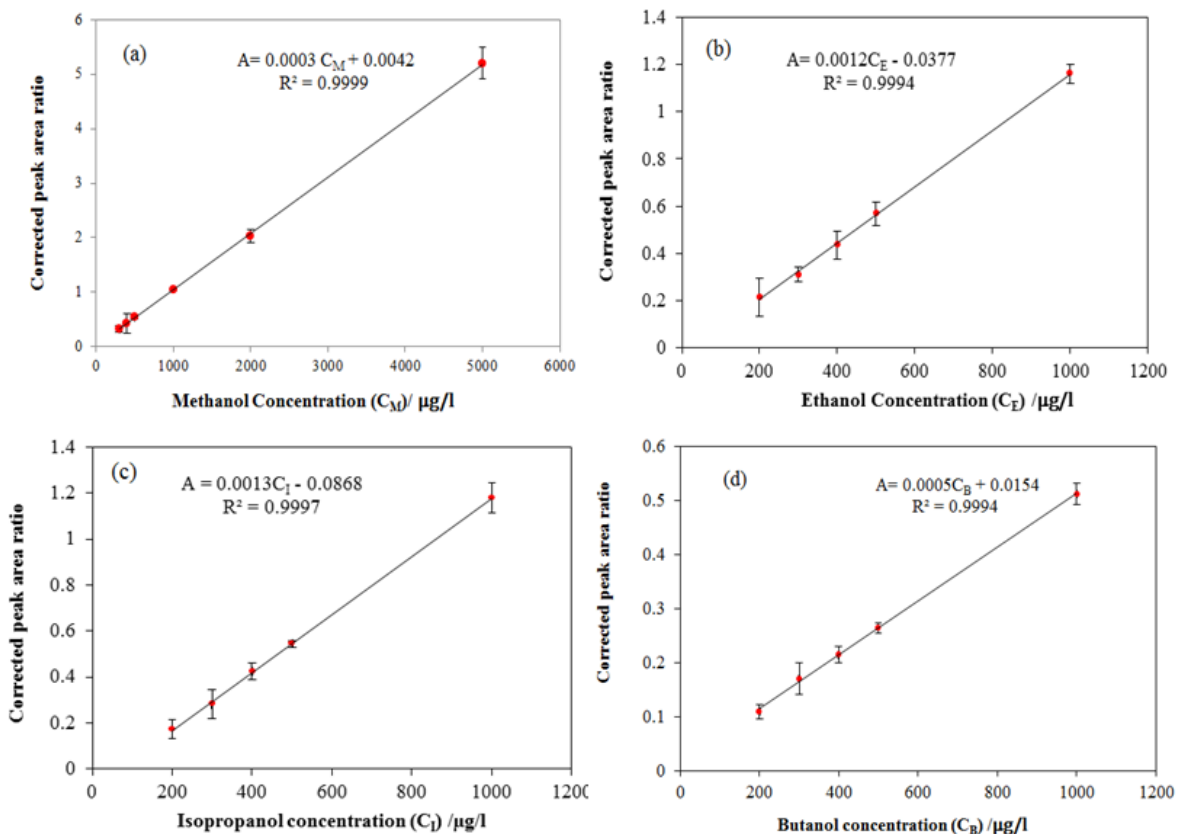


Figure 4.26 Calibration graphs of the alcohols: (a) methanol, (b) ethanol, (c) Isopropanol and (d) butanol. A: is the corrected area of the relevant alcohol to pyridine area ratio. Error bars were estimated from repeatability of three injections replica for each concentration within each alcohol

## 4.6 Numerical Simulations of Cyclic Voltammograms

Cyclic voltametric simulations were performed using DigiSim<sup>®</sup> 4.0 and DigiElch<sup>®</sup> 7.0 software written by GAMRY<sup>®</sup> Instruments. The software used incorporated diffusion, charge balance, coupled chemical reactions and electron transfer thermodynamics and kinetics. The coupled chemical reactions were characterised by their equilibrium constant and the forward rate constant. For the electrochemical process, the Butler-Volmer kinetics model was used with an apparent reduction potential,  $E^0$ , transfer coefficient,  $\alpha$ , and heterogeneous electron transfer rate constant,  $k_s$  as the model parameters. The equilibrium concentrations were calculated by the software according to the equilibrium constants and initial concentrations entered. The results of simulations and their discussion are presented in Chapter 6.

## References of Chapter 4

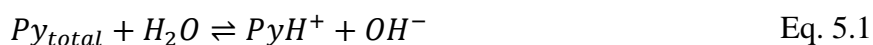
- Brunner, E., Maier, S. & Windhaber, K., 1984. Three high-pressure optical cells for phase equilibrium investigations. *Journal of Physics E: Scientific*, 44.
- Dupont. 2015 Extreme Versatility and Thermal Performance Dupont™, Kapton®. <http://www.dupont.com/products-and-services/membranes-films/polyimide-films/brands/kapton-polyimide-film/products/kapton-hn.html>.
- Gorbaty, Y.E. et al., 2003. High-temperature and high-pressure cell for kinetic measurements of supercritical fluids reactions with the use of ultraviolet-visible spectroscopy. *Review of Scientific Instruments*, 74(6), p.3073.
- Hara, K. & Morishima, I., 1988. High-pressure cell and its inner capsule for optical studies of liquids. *Review of Scientific Instruments*, 59(11), p.2397.
- ICH CH et al., 1996. Validation of Analytical Procedures : Text and Methodology. In pp. 1–11.
- Inamdar, S.N., Bhat, M. a. & Haram, S.K., 2009. Construction of Ag/AgCl reference electrode from used felt-tipped pen barrel for undergraduate laboratory. *Journal of Chemical Education*, 86(3), pp.355–356.
- Ives, D., 1961. *Reference electrodes, theory and practice*, New York: Academic Press.
- Licence, P. et al., 2004. Large-aperture variable-volume view cell for the determination of phase-equilibria in high pressure systems and supercritical fluids. *Review of Scientific Instruments*, 75(10), pp.3233–3236.
- Rieger, P.H., 1994. *Electrochemistry*, Dordrecht: Springer Netherlands.
- Sawyer, D.T.T.A.M.U. & Roberts, J.L.J.U.O.R., 1994. *Electrochemistry for Chemists Second Edition*. John Wiley Sons Inc, p.133.
- Shrivastava, A. & Gupta, V., 2011. Methods for the determination of limit of detection and limit of quantitation of the analytical methods. *Chronicles of Young Scientists*, 2(1), p.21.
- Suleimenov, O.M., 2004. Simple, compact, flow-through, high temperature high pressure cell for UV-Vis spectrophotometry. *Review of Scientific Instruments*, 75(10), pp.3363–3364.
- Zoski, C.G., 2007. *Handbook of Electrochemistry*. In *Handbook of Electrochemistry*. Elsevier.

# Chapter 5 Ionic Equilibria of Pyridine-CO<sub>2</sub> System

The recent interest in pyridine (C<sub>5</sub>H<sub>5</sub>N) as an electrocatalyst for CO<sub>2</sub> reduction has extended to its mechanism investigation. An important step of the process study is the determination of the ionic species concentrations in the system. As such, the calculations of these concentrations as function of pH and CO<sub>2</sub> pressure of the system become necessary. In this Chapter, the interaction of pyridine (C<sub>5</sub>H<sub>5</sub>N) with CO<sub>2</sub> is reported along with the calculated concentrations of the ionic species in this system at different conditions. The theoretical principles governing reactions at equilibrium in acid-base systems reported in (Butler 1991), (Bates & Vijnh 1973) and (Hunter 1998) along with the CO<sub>2</sub> equilibria studied by Lower, Wang and co-workers (Lower 1999) and (Wang et al. 2010) are applied to determine the pyridine CO<sub>2</sub> equilibria in aqueous systems. The ionic species concentrations of pyridine-strong acid and pyridine-CO<sub>2</sub> systems were numerically estimated using the equations determined for each system and solved using Matlab. These calculations are used in the voltammetric analysis and simulations described in the results Chapter 6 and for CO<sub>2</sub> concentrations in Chapter 7.

## 5.1 Calculation of Ionic Species Concentrations in Aqueous Pyridine Solution

Pyridine (C<sub>5</sub>H<sub>5</sub>N) is a heterocyclic aromatic amine. Its nitrogen atom has a lone pair of electrons which are not part of the aromatic ring. When pyridine is dissolved in water, the nitrogen lone pair abstracts a proton from a water molecule; forming pyridinium, PyH<sup>+</sup>, and hydroxyl ions. This makes pyridine (C<sub>5</sub>H<sub>5</sub>N) a weak base with a pK<sub>b</sub> of 8.55 at 20°C (Polievktov, M. K; Mairanovskii 1965).



To calculate the ionic species concentrations in this system, the dissociation equilibria of the base (Eq.5.2) and water (Eq.5.3) must be taken in consideration:

$$[OH^-][PyH^+] = K_b[Py] \quad \text{Eq. 5.2}$$

$$[OH^-][H^+] = K_w \quad \text{Eq. 5.3}$$

Where  $[PyH^+]$  is the conjugate acid (pyridinium concentration), and  $[Py]$  is the non-protonated pyridine concentration. If  $C_1$  is considered the total concentration of pyridine initially added to the system, e.g. total moles of the base per litre of solution, the mass balance is:

$$[Py] + [PyH^+] = C_1 \quad \text{Eq. 5.4}$$

And the charge balance of pyridine ( $C_5H_5N$ ) in water is

$$[H^+] + [PyH^+] = [OH^-] \quad \text{Eq. 5.5}$$

The equations (Eq.5.2) to (Eq.5.5) with four unknowns are simplified and rearranged in a polynomial form as shown below. The pyridinium  $[PyH^+]$  ion in equation (Eq.5.4) is replaced in equation (Eq. 5.2) and solved for its concentration:

$$[PyH^+] = \frac{K_b C_1}{K_b + [OH^-]} \quad \text{Eq. 5.6}$$

Solving equation (Eq.5.3) for hydroxyl anion and substituting together with (Eq. 5.6) in the charge balance equation (Eq.5.5) gives:

$$\frac{K_w}{[OH^-]} + \frac{K_b C_1}{K_b + [OH^-]} = [OH^-] \quad \text{Eq. 5.7}$$

Rearranging (Eq.5.7) gives the following cubic equation:

$$-[OH^-]^3 - K_b[OH^-]^2 + (K_w + C_1 K_b)[OH^-] + K_w K_b = 0 \quad \text{Eq. 5.8}$$

Eq.5.8 allows the hydroxyl ion concentration to be calculated at any given pyridine ( $C_5H_5N$ ) concentration. Thus, the proton concentration present in this system can be estimated.

## 5.2 Calculation of Ionic Species in the Pyridine-Acid System

### 5.2.1 Concentration of Pyridine Species in the Presence of a Strong Acid

The addition of hydrochloric acid to pyridine ( $C_5H_5N$ ) alters the charge balance equation (Eq.5.5); since the chloride concentration represents the total analytical concentration of the strong acid as result of the complete dissociation of the latter. Taking in account the added acid, the equation (Eq.5.5) becomes:

$$[H^+] + [PyH^+] = [OH^-] + [Cl^-] \quad \text{Eq. 5.9}$$

where  $[Cl^-]$  is the concentration of the chloride. Since pyridine ( $C_5H_5N$ ) protonation is reversible, it can be considered either as described above or as an acid ( $K_a=3.55 \times 10^{-6}$  at  $25^\circ C$ ) (Polievktov, M. K; Mairanovskii 1965) with an equilibrium equation:

$$[H^+][py] = K_a[PyH^+] \quad \text{Eq. 5.10}$$

Solving Eq.5.10 for pyridinium  $[PyH^+]$  concentration and replacing in the charge balance Eq.5.9 gives:

$$\frac{K_a[PyH^+]}{C_1 - [PyH^+]} + [PyH^+] = \frac{K_w}{[H^+]} + [Cl^-] \quad \text{Eq. 5.11}$$

Simplifying Eq.5.11 and solving for  $[Cl^-]$  gives:

$$[HCl] = [Cl^-] = \frac{[H^+]^3 + (K_a + C_1)[H^+]^2 - K_w K_a - K_w [H^+]}{K_a [H^+] + [H^+]^2} \quad \text{Eq. 5.12}$$

The concentration of the added acid can be determined for any pyridine ( $C_5H_5N$ ) concentration at a given acidity of the system using Eq.5.12. The combination of the acid amount added to the system with the pH of the solution at specific concentration of pyridine allows the ionic species concentration calculations. Solving Eq.5.10 for protons:

$$[H^+] = \frac{K_a [pyH^+]}{C_1 - [PyH^+]} \quad \text{Eq. 5.13}$$

Substituting  $[H^+]$  in the charge balance Eq.5.9

, together with hydroxide from Eq.5.3 gives:

$$\frac{K_a[PyH^+]}{C_1 - [PyH^+]} + [PyH^+] = \frac{K_w}{[H^+]} + [Cl^-] \quad \text{Eq. 5.14}$$

Simplifying Eq.5.14 gives:

$$-[H^+][PyH^+]^2 + [(K_a + C_1 + [Cl^-])[H^+] + K_w][PyH^+] - C_1(K_w + [Cl^-][H^+]) = 0 \quad \text{Eq. 5.15}$$

The addition of a strong acid such as hydrochloric acid to pyridine ( $C_5H_5N$ ) disturbs the equilibria described above (pyridine in water). It not only increases the acidity of the system but also alters the cation to anion ratio. Eq.5.15 can be used to construct Pourbaix diagram at any pyridine concentrations. In this section, the Pourbaix diagram is constructed (using the Matlab<sup>®</sup> script presented in Appendix C) for 10mM of total pyridine since this amount represents the most used concentration in this work. Moreover, equilibrium concentrations of all ionic species present in pyridine-strong acid system are calculated at the analytical pyridine ( $C_5H_5N$ ) concentration range used in the experimental and simulation data in Chapter 6.

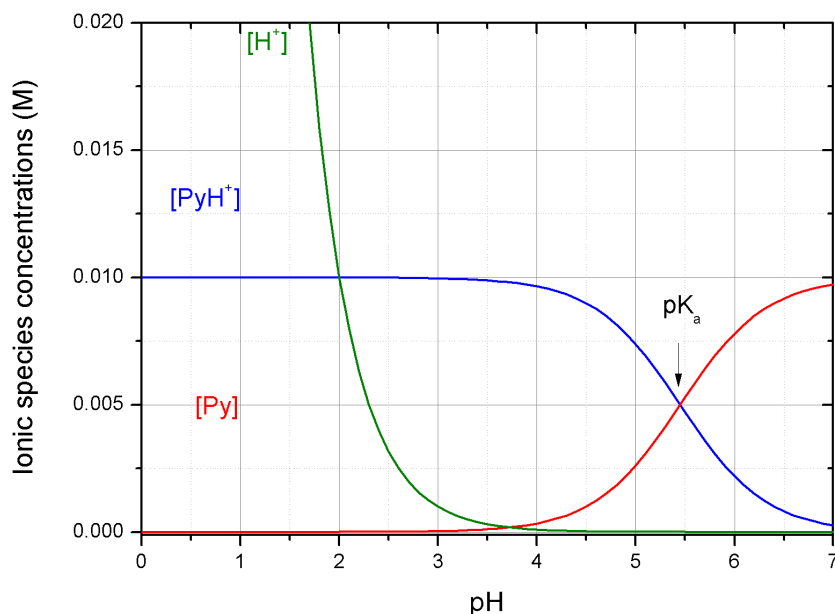


Figure 5.1 Ionic species equilibrium concentrations of protons and pyridine/pyridinium in 10mM of total pyridine concentration as function of pH in the range 0-7 (calculated data)

The concentrations of pyridinium  $[PyH^+]$  and the non-protonated pyridine  $[Py]$  are equal at  $pH=pK_a=5.45$  at  $25^\circ C$  (Figure 5.1). The pyridinium cations concentration becomes larger than the protons and non-protonated fraction at  $pH < pK_a$  at pH range 2-5.45; equating to the hydrated protons at pH 2 and levelling up to total concentration of the pyridine. In this range pyridine is nearly fully protonated. As the pH becomes more alkaline pyridinium deprotonates and regenerates the non-protonated fraction of the pyridine.

In Chapter 6 (section 6.2.1), as part of the pyridinium voltammetric behaviour investigations, pyridine ( $C_5H_5N$ ) prepared in aqueous electrolyte was titrated using hydrochloric acid to pH5.5. Hence, pyridinium concentrations at the analytical pyridine concentration range studied are tabulated herein (Table 5.1). At the 5 to 200mM analytical concentration range, pyridine can be considered half protonated at pH5.5 since this is close to the  $pK_a$  value as shown in Figure 5.1.

Table 5.1 Pyridinium and non-protonated pyridine ( $C_5H_5N$ ) concentrations at pH5.5 for pyridine range 5-200mM of concentration (C) (calculated data)

Concentration $C_1$ (mM)	Pyridinium [PyH <sup>+</sup> ] (mM)	Pyridine [Py] (mM)
05	2.4	2.6
10	4.7	5.3
50	23.6	26.4
100	47.1	52.9
200	94.2	105.8

Section 6.2.2 of Chapter 6 investigates the voltammetric pyridine ( $C_5H_5N$ ) behaviour at different pH. The concentrations of pyridine/pyridinium species at total concentration of 10mM are calculated at pH range 1 to 7 and tabulated (Table 5.2). At pH 2, pyridine is almost completely protonated, while, at pH8 the protonated pyridine fraction is negligible compared to the non-protonated fraction.

Table 5.2 Pyridinium [PyH<sup>+</sup>] and non-protonated pyridine [Py] concentrations in 0-7 pH range in 10mM total pyridine ( $C_5H_5N$ ) concentration (calculated data)

pH	[PyH <sup>+</sup> ] (mM)	[Py] (mM)
1	10.00	0
2	9.996	0.004
3	9.965	0.035
4	9.657	0.343
5	7.380	2.620
6	2.219	7.260
7	0.274	7.802
8	0.028	9.972

## 5.2.2 Concentration of Pyridine and CO<sub>2</sub> Species at elevated CO<sub>2</sub> pressure

Pyridinium behaviour was also investigated in the presence of CO<sub>2</sub> at 1bar and elevated pressure and this discussed in Chapter 6. Hence, the concentrations of the ionic species are calculated in this section as function of CO<sub>2</sub> pressure and the analytical pyridine ( $C_5H_5N$ ) range used in the next Chapter.

### 5.2.2.1 Hydration

Dissolving CO<sub>2</sub> in water forms carbonic acid H<sub>2</sub>CO<sub>3</sub> by hydration reaction (Eq. 5.16):



This step is slower than the ionisation of CO<sub>2</sub>. Carbonic acid is not taken into consideration in the acid-base equilibrium, since it is a neutral molecule. Thus, the acid concentration is not taken into account in the ionisation equation (Butler 1991) (Wang et al. 2010).

### 5.2.2.2 Dissociation

Carbonic acid is ionised to release bicarbonate ions HCO<sub>3</sub><sup>-</sup> and protons H<sup>+</sup>:



Since H<sub>2</sub>CO<sub>3</sub> accounts for a small fraction of CO<sub>2</sub>, independent of concentration and pH, it is usually neglected in calculations; the ionisation reaction is written as follows:



The equilibrium constant of the first dissociation of carbonic acid/aqueous CO<sub>2</sub> is:

$$K_{a1} = \frac{[HCO_3^-][H^+]}{[CO_2]} \quad \text{Eq. 5.19}$$

The second dissociation of bicarbonate ions ionise to give carbonate ion CO<sub>3</sub><sup>2-</sup> at basic pH as illustrated in Pourbaix diagram (Figure 5.)



The equilibrium constant of the second dissociation of bicarbonate to carbonate ion CO<sub>3</sub><sup>2-</sup>

$$K_{a2} = \frac{[CO_3^{2-}][H^+]}{[HCO_3^-]} \quad \text{Eq. 5.21}$$

The dissolution of CO<sub>2</sub> in water depends on its partial pressure; this is expressed by Henry's law:

$$[CO_2] = K_H P_{CO_2} \quad \text{Eq. 5.22}$$

Where  $K_H$  is Henry's constant,  $[CO_2]$  is in moles per litre, and  $P_{CO_2}$  in atmospheres. This is applicable on the assumption that the activity coefficient of dissolved  $CO_2$  (in water) is unity.

Table 5.3 Carbon dioxide constants at 20°C and 25°C (1 bar) (Butler 1991)

Temperature (°C)	$pK_H$ (mol/L.atm)	$pK_{a1}$ (mol/L)	$pK_{a2}$ (mol/L)	$pK_w$ (mol/L)
20	1.410	6.381	10.377	14.161
25	1.470	6.352	10.329	13.999

The interaction of pyridine ( $C_5H_5N$ ) with carbon dioxide is a weak acid-weak base reaction. The first dissociation of carbon dioxide, described above, gives bicarbonate ions and protons; this results in the protonation of pyridine ( $C_5H_5N$ ). The charge balance of this weak acid-weak base system is:

$$[PyH^+] + [H^+] = [HCO_3^-] + [OH^-] + 2[CO_3^{2-}] \quad \text{Eq. 5.23}$$

In this work, only the first  $CO_2$  dissociation is taken in consideration since the pH range studied is less than 6. Thus the concentration of  $[CO_3^{2-}]$  is negligible and not taken into consideration in these calculations. Eq.5.19 is solved for bicarbonate ions

$$[HCO_3^-] = \frac{K_{a1}[CO_2]}{[H^+]} \quad \text{Eq. 5.24}$$

Eq.5.10 solved for  $PyH^+$  as function of protons

$$[PyH^+] = \frac{C_1[H^+]}{K_a + [H^+]} \quad \text{Eq. 5.25}$$

Replacing Eq.5.24 and Eq.5.25 in the charge balance Eq.5.23 with the assumption of negligible carbonate ions gives:

$$\frac{C_1[H^+]}{K_a + [H^+]} + [H^+] = \frac{K_{a1}[CO_2]}{[H^+]} + \frac{k_w}{[H^+]} \quad \text{Eq. 5.26}$$

Simplifying and rearranging Eq.5.26 gives

$$-[H^+]^3 - (K_a + C_1)[H^+]^2 + (K_{a1}[CO_2] + K_w)[H^+] + K_{a1}K_a[CO_2] + K_wK_a = 0 \quad \text{Eq. 5.27}$$

The resulting equation allows the calculation of the proton concentration (pH) of the system at any given concentration of pyridine (C<sub>5</sub>H<sub>5</sub>N) and calculated CO<sub>2</sub> concentration. In these equilibria equations, Henry's law is not directly used since this law is not applicable at the conditions studied herein. Diamond and his co-worker have found that the assumption of the aqueous CO<sub>2</sub> activity coefficient equal to unity (widely assumed in the literature) is only applicable at a solubility of around 2mol% (Diamond & Akinfiev 2003). These authors found that the activity coefficient and hence the solubility of aqueous CO<sub>2</sub> is affected by the temperature and the pressure of the system. Correspondingly, a model was developed by these workers based on Henry's law and thermodynamic considerations. The model was used herein in the calculations of CO<sub>2</sub> concentrations at 20°C and 25°C and various CO<sub>2</sub> pressure and available at <http://www.geo.unibe.ch/diamond/publications.php>. The calculated CO<sub>2</sub> concentrations are summarised in Table 5.4. These values were used in Eq.27 to calculate the acidity of the medium and the ionic species concentrations at different CO<sub>2</sub> pressure (using the Matlab<sup>®</sup> script presented in Appendix C).

Table 5.4 CO<sub>2</sub> concentrations (M) at different pressure at 20°C and 25°C (calculated using Diamond program)

Temperature (°C)	Pressure (bar)					
	1	6	10	45	50	55
20	0.034 M	0.202 M	0.329 M	1.145 M	1.218 M	1.281 M
25	0.029 M	0.176M	0.288 M	1.025 M	1.095 M	1.156 M

The effect of CO<sub>2</sub> (1.28M) introduction into an aqueous system containing pyridine is illustrated in Figure 5.2. The proton concentration increases as the total pyridine amount is decreased from 1M to 1mM (Figure 5.2). This decreases the acidity of the system by approximately 2.5pH units (from pH 5.76 at 1M pyridine to pH3.39 at 1mM). The proton amount decreases further by ~0.3pH unit at 10<sup>-2</sup>M reaching pH3.12.

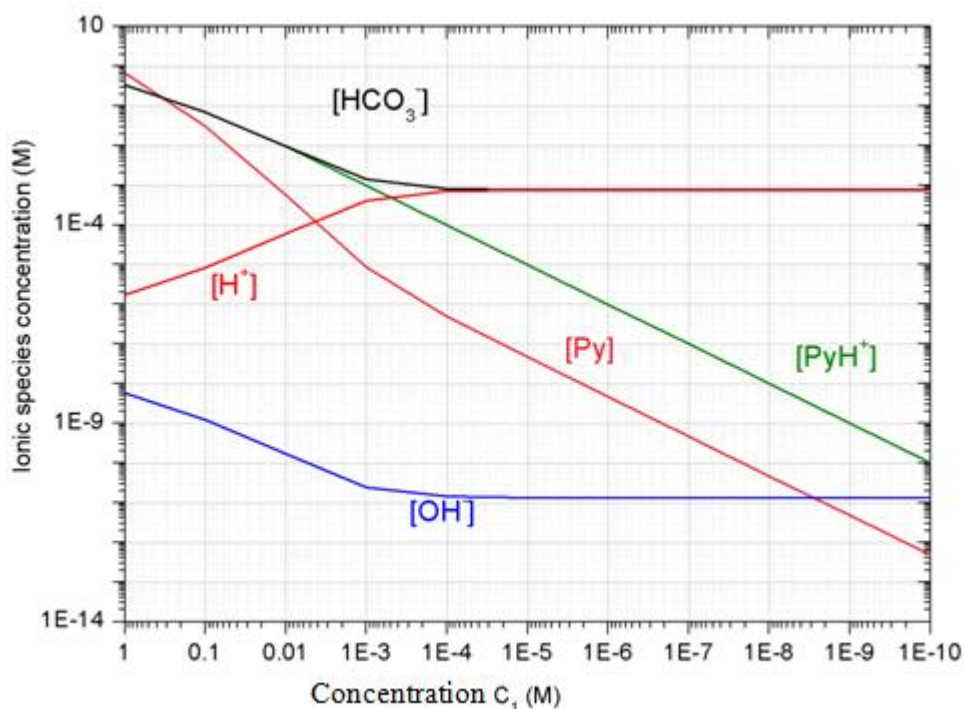


Figure 5.2 Ionic species equilibrium concentrations of protons, pyridine species and carbonic acid in pyridine ( $10^{-10}$ -1M) aqueous solutions at 20°C and 55bar of  $CO_2$

Lower than this concentration ( $C_1 < 10^{-3}$  M), the proton concentration (the pH) levels up. In the presence of high pyridine ( $C_3H_5N$ ) concentrations  $CO_2$  dissolves more rapidly as the former plays the role of a base, stimulating the proton abstraction from dissolved  $CO_2$ /carbonic acid to form pyridinium. At total pyridine concentrations lower than  $10^{-3}$  M, pyridine can no longer cope with the buffering effect of  $CO_2$  since the protons released by the latter exceeds the total concentration of pyridine added to the system. Hence, the total pyridine concentration of 1mM seems critical in that the pH of the acidity of the system is significantly altered in the presence of excess  $CO_2$ . The electrochemical behaviour of pyridine at these conditions also differs depending on the concentration of this molecule in the system as will be discussed in Chapter 6.

Table 5.5 illustrates the calculated ionic species concentrations using the thermodynamic model by Diamond and Akinfiev with  $>2\%$  (standard deviation) (Diamond & Akinfiev 2003). The pyridine and  $CO_2$  interaction described herein together with the calculated concentrations in Table 5.5 are used to explain pyridine electrochemical behaviour in the presence of  $CO_2$  in Chapter 6.

Table 5.5 Species concentrations in 10mM of pyridine containing solutions saturated with CO<sub>2</sub> at different pressure (1-55bar)

<b>Pressure (bar)</b>	<b>pH</b>	<b>HCO<sub>3</sub><sup>-</sup> (mM)</b>	<b>PyH<sup>+</sup> (mM)</b>	<b>Py (mM)</b>
1	5.50	4.73	4.73	5.27
6	4.93	7.68	7.67	2.32
10	4.75	8.33	8.32	1.68
45	4.27	9.44	9.38	0.62
50	4.24	9.47	9.42	0.58
55	4.22	9.50	9.44	0.56

## Reference of Chapter 5

- Bates, R.G. & Vihj, A.K., 1973. Determination of pH: Theory and Practice. *Journal of The Electrochemical Society*, 120(8), p.263C.
- Butler, J.N., 1991. Carbon Dioxide Equilibria and Their Applications - CRC Press Book. *CRC Press*, p.272.
- Diamond, L.W. & Akinfiyev, N.N., 2003. Solubility of CO<sub>2</sub> in water from -1.5 to 100 °C and from 0.1 to 100 MPa: evaluation of literature data and thermodynamic modelling. *Fluid Phase Equilibria*, 208(1-2), pp.265-290.
- Hunter, K. a, 1998. Acid-base Chemistry of Aquatic Systems. , pp.1-10.
- Lower, S.S.K., 1999. Carbonate equilibria in natural waters. *Simon Fraser University*, Chem 1(Environmental Chemistry), pp.1-26.
- Polievktov, M. K; Mairanovskii, S.G., 1965. Influence Of The Concentration And Nature Of The Cation Of Indifferent Electrolytes On The Polarographic Catalytic Waves Of Hydrogen Induced By Pyridine In Unbuffered Solutions. *Journal of the Academy of Sciences*, pp.400-405.
- Wang, X. et al., 2010. Comprehensive Study of the Hydration and Dehydration Reactions of Carbon Dioxide in Aqueous Solution. *The Journal of Physical Chemistry A*, 114(4), pp.1734-1740.

# Chapter 6 Pyridinium Behaviour at Platinum Electrode in the Absence and the Presence of CO<sub>2</sub>

## 6.1 Introduction

The controversy over the protonated pyridine (pyridinium, PyH<sup>+</sup>) role in the CO<sub>2</sub>-pyridine system calls for further investigation. In this Chapter, the outcome of the PyH<sup>+</sup> behaviour both in an inert atmosphere (N<sub>2</sub>) and in the presence of CO<sub>2</sub> is reported at atmospheric and elevated CO<sub>2</sub> pressure. All voltammetric measurements herein were conducted at 20°C referenced against a Ag/AgCl electrode for the atmospheric pressure experiments and against a pseudo Ag/AgCl electrode for high pressure measurements (the reference electrodes specification/preparation is detailed in Chapter 4, Section 4.3).

### 6.1.1 Review of the CO<sub>2</sub>-Pyridine Mechanistic Picture

As explained in Chapter 3 Section 3.1.2.3, pyridinium was reported to have an electrocatalytic activity for CO<sub>2</sub> reduction on a platinum electrode leading to methanol formation (The system history is reported in the Literature Review Chapter 3, Section 3.1.2.3) (Morris et al. 2011). The methanol production was initially suggested to proceed via a multi-step process characterised by an EC' catalytic type mechanism as illustrated in Figure 6.1 (EC' catalytic type mechanism: E is the electron transfer reaction and C' is the catalytic chemical reaction) (Barton Cole et al. 2010). The key step in the mechanism proposed involves a rapid pyridine (Py) protonation in acidic media (Reaction 1, C'), to generate the electro-active species, PyH<sup>+</sup>, which are one-electron reduced on the electrode surface for subsequent formation of pyridinyl radical (PyH<sup>\*</sup>) (Reaction 2, E). The charge transfer step has been suggested to proceed reversibly toward the electron/proton transfer agent formation, PyH<sup>\*</sup>, which upon oxidation regenerates PyH<sup>+</sup> cation. This step leads to the *redox wave* observed at -0.58V vs. SCE. Upon the introduction of CO<sub>2</sub> into the system, the same steps 1, 2 and 3 (Figure 6.1) take place with an additional reaction (Reaction 4) coupled to Reaction 2. It

was suggested that in the CO<sub>2</sub> presence, the PyH<sup>\*</sup> radical formed in Reaction 2 interacts with CO<sub>2</sub> to generate a complex ‘CO<sub>2</sub>-bound carbamate’ intermediate (Reaction 4) ultimately leading to the alcohol formation. A current enhancement of the *redox wave* has been observed under CO<sub>2</sub> as compared to under the inert atmosphere on Pt and Pd cathodes (Seshadri et al. 1994) (Barton Cole et al. 2010) (Morris et al. 2011). This observation was interpreted as an evidence of the CO<sub>2</sub> activity.

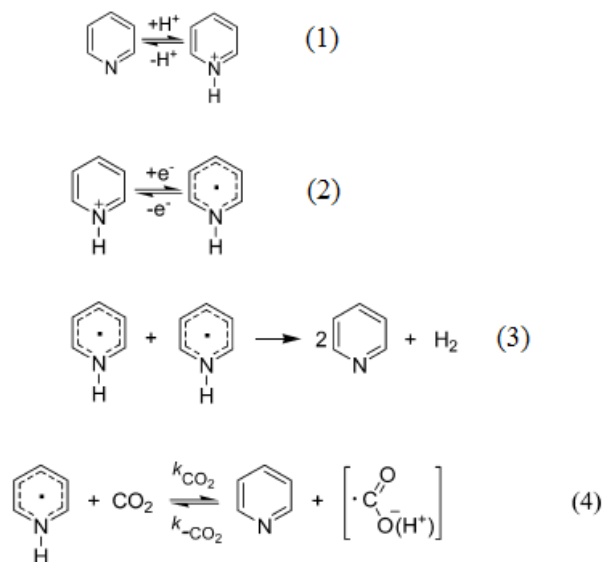
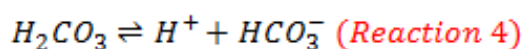
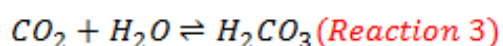
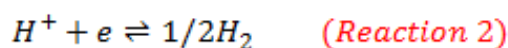


Figure 6.1 Bocarsly's Model: Scheme of the initially proposed mechanism of pyridinium assisted CO<sub>2</sub> reduction to methanol on Pt electrode. The key step of this mechanism is the radical formation (Reaction 2). (Barton Cole et al. 2010)

The *redox wave* reflecting the single-electron charge transfer in pyridine-containing electrolyte has been observed on some other electrodes including Pd (Seshadri et al. 1994), p-GaP (Barton et al. 2008), Pt/C-TiO<sub>2</sub> (de Tacconi et al. 2012) and iron pyrites (Bocarsly et al. 2012). These reports have experimentally confirmed the electroactivity of pyridinium cation based on the redox wave seen. However, the cation was observed to discriminate cathode interfaces, since the glassy carbon electrode was reported to be inert toward pyridinium (Barton Cole et al. 2010). Consequently, the electrode surface role involvement in the reaction was suspected; this fact has stimulated several theoretical investigations which focused on the reduction potential calculations of the pyridinyl (PyH<sup>\*</sup>) radical formed in Reaction 2 (Figure 6.1). The suggested PyH<sup>\*</sup> radical intermediate was found unlikely to form at the experimentally observed reduction potential (-0.58V vs. SCE) as confirmed by the density functional theory (DFT) calculations (Keith & Carter 2012). The radical production was reported to occur at

least -0.6V vs. SCE more negative than experimentally observed on Pt cathode and at the conditions explored. Therefore, the calculations have ruled out the key step, radical formation, of the mechanism proposed. Further investigations aimed at understanding the underlying mechanism of such process followed. A theoretically derived mechanism for this system was presented by Barista and co-workers (Ertem et al. 2013). In addition to the catalytic activity of PyH<sup>+</sup> cation, this route takes in consideration the catalytic role of platinum surface in the CO<sub>2</sub>-pyridinium reduction process. Pyridinium, formed by the protonation of pyridine (Reaction 1, Figure 6.1), in conjunction with platinum surface reduces by a single electron transfer to form a hydrogen-platinum hybrid (Pt-H). The Pt-H hybrid combines with CO<sub>2</sub> in the presence of pyridinium and reduces to formic acid as follows: Pt-H + CO<sub>2</sub> + PyH<sup>+</sup> + e = Py + Pt + HCOOH.



*Figure 6.2 Savéant's Model: Scheme of the mechanism proposed of pyridinium catalytic role for HER in the presence of CO<sub>2</sub> on Pt electrode. HA: acid (Costentin et al. 2013)*

A recent experimental study of PyH<sup>+</sup> cation on a Pt cathode revealed some features similar to the weak acid behaviour on metal electrodes (Costentin et al. 2013). The PyH<sup>+</sup> cation was reported to behave as any weak acid in aqueous solutions on Pt surfaces leading exclusively to hydrogen evolution reaction (HER). According to Costentin et al, the redox wave observed in acidified electrolyte under the inert atmosphere (Seshadri et al. 1994) (Morris et al. 2011) (Costentin et al. 2013) is merely the reduction of hydrated protons (H<sub>3</sub>O<sup>+</sup>) upon their diffusion to the electrode surface (Costentin et al. 2013) (NB in this Chapter, the hydrated protons (H<sub>3</sub>O<sup>+</sup>) are referred to as protons (H<sup>+</sup>) for simplification purposes). These authors have suggested an alternative EC' mechanism (Figure 6.2) which according to them does not involve the reduction of CO<sub>2</sub> at least at the cathodic potential reported. In such process, the protons (H<sup>+</sup>) are released by the acid, pyridinium in this case, as part of the fast PyH<sup>+</sup> cation

deprotonation equilibrium in Reaction 1, Figure 6.2. The released  $H^+$  ions are then reduced to form molecular hydrogen (Reaction 2, Figure 6.2).

Thus, the coupled reactions give rise to the redox wave observed. The enhancement of the amplitude of this wave under  $CO_2$  reported by the Bocarsly group (Barton Cole et al. 2010) was also observed by Costentin et al, but was explained by the latter authors as simply the increase of protons concentration as result of carbonic acid ( $H_2CO_3$ ) formation (Reaction 3, Figure 6.2) and its subsequent dissociation (Reaction 4, Figure 6.2). This interpretation together with NMR analysis of the  $CO_2$ -pyridinium reduction products, which showed no sign of methanol, explicitly ruled out the catalytic role of pyridinium toward methanol production (Costentin et al. 2013).

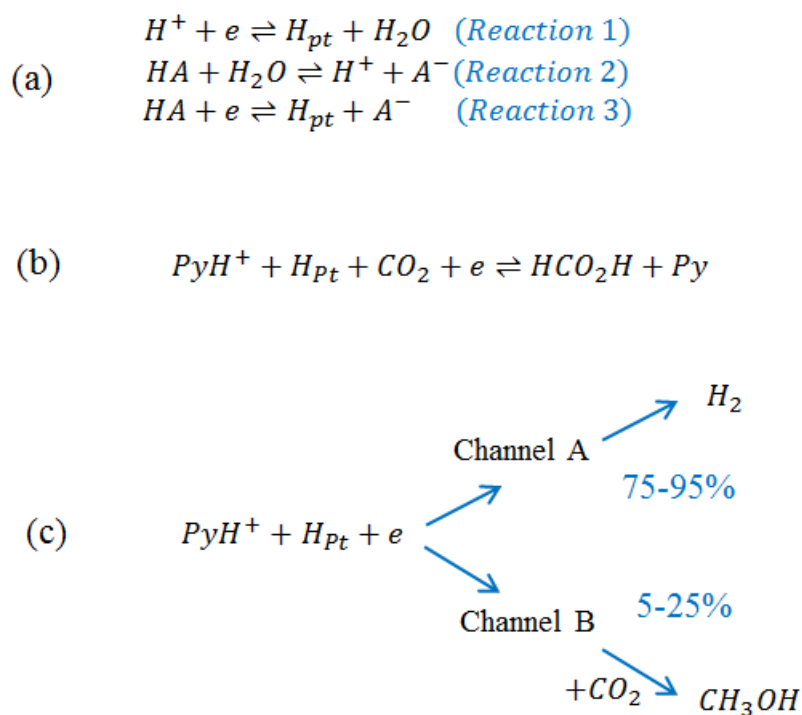


Figure 6.3 Bocarsly-Barista Model: Scheme of the newly proposed reaction pathways for the  $CO_2$ -pyridinium reduction system on Pt electrode. HA: acid (Barton Cole et al. 2014)

More recently, the first group, the ‘Bocarsly group’ who originally reported the pyridinium-assisted  $CO_2$  reduction in collaboration with the ‘Batista group’ presented a new mechanism for methanol formation on Pt electrode. Based on the experimentally observed surface dependencies of  $PyH^+$  by the Bocarsly group and the theoretical work of the Batista group, the Pt electrode surface was suggested to play a key role in a

multistep CO<sub>2</sub> reduction to methanol. The reaction step (a) in Figure 6.3 involving the Pt-H hybrid reaction with CO<sub>2</sub>-pyridinium reduction to formic acid, replaces the radical formation step (Reaction 2, Figure 6.1) in the old mechanism. In the new mechanism (Figure 6.3), the reduction of the CO<sub>2</sub>-pyridinium system was proposed to form methanol with 5-25% of the cathodic current contribution, while the remaining 75-95% goes toward the competing HER.

The two mechanisms presented in Figure 6.2 and Figure 6.3 (Barton Cole et al. 2014) (Costentin et al. 2013), which reached divergent conclusions, are among the few experimental studies attempting to elucidate the mechanism of the CO<sub>2</sub>-pyridinium reduction system. Most other investigations were attempting the methanol production on different electrode materials (Boston et al. 2013) (de Tacconi et al. 2012) (Portenkirchner et al. 2014), (Zeng et al. 2014), Au (Lebègue et al. 2014) (Lucio & Shaw 2015)). Some of these have confirmed the methanol production and others were not able to detect any CO<sub>2</sub> based products. In this work, the cyclic voltammetry (CV) studies were conducted for extended range of pyridinium and high CO<sub>2</sub> concentration aiming at resolving the mechanistic picture.

## 6.2 CV Studies in the Absence of CO<sub>2</sub>

### 6.2.1 Cyclic Voltammetry of Pyridinium at Platinum Electrodes

The role of PyH<sup>+</sup> in the CO<sub>2</sub> reduction process is of a critical importance in the mechanism investigation of such system; as it involves the interaction of both PyH<sup>+</sup> and CO<sub>2</sub> species. The latter induce some complexity to the system. Hence an electrochemical behaviour study of the PyH<sup>+</sup> cation in the absence of CO<sub>2</sub> becomes necessary.

In the absence of CO<sub>2</sub>, the Bocarsly group suggested that the observed *redox wave* at a Pt electrode is due to the PyH<sup>+</sup> reduction reaction (Reaction a3, Figure 6.3), coupled to the pyridine (C<sub>5</sub>H<sub>5</sub>N) protonation equilibrium (Reaction a2, Figure 6.3). While Savéant's group have proposed, the H<sup>+</sup> reduction as the electrode reaction (Reaction 2, Figure 6.2) coupled to the fast pyridine deprotonation reaction which is responsible for

the *redox wave* observed (Reaction 1, Figure 6.2). However, these latter authors also did not exclude a concerted electron proton transfer involving the reduction of  $\text{PyH}^+$  cation. Both groups, who studied the system for one pyridine concentration, agree that the process represents a diffusion controlled single electron transfer electrode reaction, where the pyridinium is the rate-limiting diffusing species.

In order to investigate the mechanism pathways proposed by the two groups, CVs of pyridinium-containing electrolytes were collected under  $\text{N}_2$  atmosphere for various pyridine ( $\text{C}_5\text{H}_5\text{N}$ ) concentrations (10-200mM) at scan rates ranging between 10mV/s and 2000mV/s (Figure 6.4). The pH was adjusted to pH5.5 by hydrochloric acid addition. For reference, the pH was chosen to be close to the pyridine pKa (5.45 at  $20^\circ\text{C}$ ), the relationship between pH and pKa is illustrated in Figure 6.12.

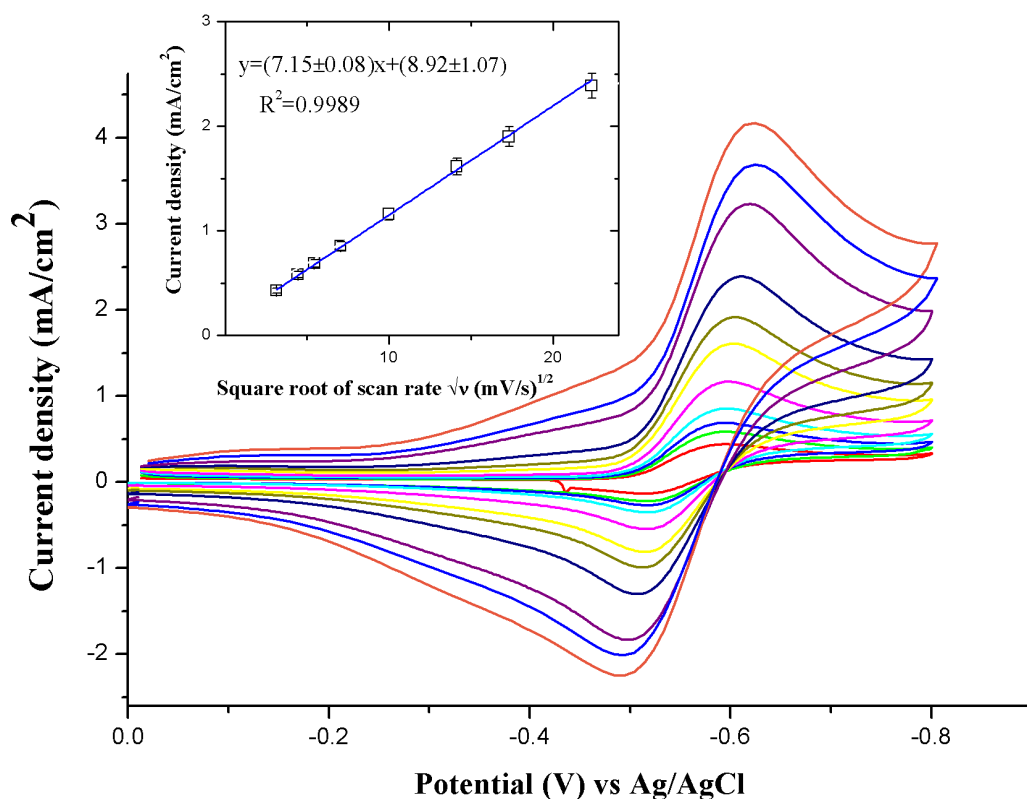
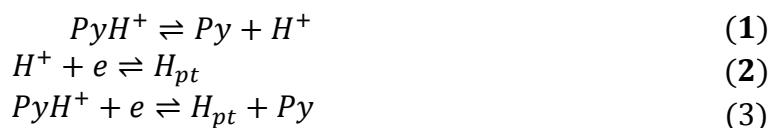


Figure 6.4 Scan rate dependence CVs of 10mM pyridine in 0.5M KCl (at pH 5.5) on Pt electrode ( $0.07\text{cm}^2$ ) at 10-2000 mV/s. Inset: Cathodic current as function of the square root of the scan rate (10-500mV/s).

Figure 6.4 illustrates the CVs of 10mM pyridine obtained at different scan rates 10-2000mV/s under  $\text{N}_2$  (other concentrations investigated in this work are presented in the Appendix D, Figure D1-4). Based on the analysis of the CVs conducted herein and by taking in consideration both electrode reactions in Bocarsly (Reaction a3, Figure 6.3)

and Savéant (Reaction 2, Figure 6.2) models, a set of reactions is proposed in this work (Scheme 6.1). Analysis of the dataset in Figure 6.4 and the datasets for other pyridine concentrations (Appendix D, Figure D1-4), was undertaken according to the diagnostic criteria which are outlined in Chapter 2 Section 2.8.1.2. These include the estimation of the redox potential ( $E_{1/2}$ ), the peak to peak separation, the evaluation of the anodic to the cathodic peak current ratio ( $I_p^a/I_p^c$ ) and the peak cathodic current variation with the square root of the scan rate ( $I_p^c$  vs  $\sqrt{v}$ ). These criteria can only be assessed for an elementary electrode reaction independent or unaffected by any chemical reactions. Hence, the criteria can be applied for the current system provided the set of the reactions proposed in Scheme 6.1 would satisfy this condition. In other words, the chemical reaction (Reaction 1, Scheme 6.1) would have no effect on the electrode reactions. This is discussed further in the next sections.

*Scheme 6.1 Set of reactions proposed in acidic solutions under  $N_2$*



**The redox potential ( $E_{1/2}$ )** of the CV wave, obtained at half value of the cathodic peak current ( $E_{p/2}$ ) with  $n=1$  (Eq.6.1), was examined at pyridine ( $C_5H_5N$ ) concentrations (10mM, 50mM, 100mM and 200mM) and different scan rates (10-2000mV/s). At concentrations <50mM and scan rates <500mV/s the peak to peak separation is less than 70mV, which indicates the system reversibility. Hence, an average redox potential was estimated at  $-0.56 \pm 0.01V$  at these conditions ( $[Py] < 50mM$  and  $v < 500mV/s$ ). For all pyridine concentrations studied at scan rates above 500mV/s; the peak separation becomes higher than 100mV with stronger distortion observed for the larger concentrations (e.g. >150mV for 100mM pyridine, see Appendix D, Figures D1-4). This increase of the peak separation reflects the quasi-reversibility of the system at higher scan rates. The high peak to peak separation could be due to faster scan rates as compared to the pyridinium deprotonation equilibrium. At the most studied pyridine concentration in the literature (10mM), the redox potential of  $-0.56 \pm 0.01V$  was determined at peak separation of less than 70mV at <500mV/s. Higher than this scan rate results in an increased peak separation. These observations agree well with the

previous work at -0.58V (Barton Cole et al. 2010) and -0.57V (Costentin et al. 2013) for the redox potentials.

$$E_{p/2} = E_{1/2} + 28.0n \text{ mV at } 25^{\circ}\text{C} \quad \text{Eq. 6.1}$$

Where  $E_{p/2}$  is the peak potential at half cathodic current value,  $E_{1/2}$  is the redox potential and  $n$  is the number of electron transferred.

**The anodic peak current to the cathodic peak current ( $I_p^a/I_p^c$ ) ratio** was plotted as function of the scan rate (Figure 6.5). In the case of a reversible redox reaction, not coupled to any chemical reaction, the ratio  $I_p^a/I_p^c$  is supposed to be independent of the scan rate and approximately unity. Figure 6.5 suggests that this criterion is well satisfied at scan rates below ~250 mV/s. However, a gradual deviation from one is observed for higher scan rates. This could be due to the pyridinium deprotonation reaction effect on the electrode reaction. The symmetry of the anodic peak current to the cathodic peak current clearly indicates that the electrode reaction is independent and/or unaffected by any coupled chemical reactions or other processes below ~250 mV/s scan rates. This means that the deprotonation of  $\text{PyH}^+$  (Reaction 1, Scheme 6.1), coupled to Reaction 2 in Scheme 6.1, is considered fast enough to remain at equilibrium and has no effect on the electrode kinetics (this is valid for the scan rates  $\sim < 250 \text{ mV/s}$ ). This deduction is in line with the Savéant group's analysis. As for the electrochemical electrode reaction (Reaction 3, Scheme 6.1), this can effectively be considered to have a minor effect on the protonation reaction (reverse of Reaction 1, Scheme 6.1) under the conditions explored in this work. This is also proposed by the Bocarsly group for the reason that  $\text{PyH}^+$  cations are the dominating species at pH 5.5 (Yan et al. 2014). Indeed, at such acidity,  $[\text{PyH}^+] \gg [\text{H}^+]$  (e.g. At the lowest  $[\text{Py}] = 5 \text{ mM}$ ,  $[\text{PyH}^+] = 2.4 \text{ mM}$  while  $[\text{H}^+] = 3.16 \mu\text{M}$ ), thus the pyridine reprotonation by  $\text{H}^+$  has only a minor effect on the electrode Reaction 3 in Scheme 6.1.

Further analyses are depicted in Figure 6.4 inset. Figure 6.4 inset shows the cathodic peak current ( $I_p^c$ ) vs. the square root of the scan rate ( $\sqrt{v}$ ) for 10-500 mV/s range. The linear dependence of **the reduction peak current  $I_p^c$  on the square root of the scan rate ( $\sqrt{v}$ ) following from Eq. 6.1**, indicates a diffusion controlled electrochemical reduction. This linearity diagnostic is demonstrated for 10 mM pyridine ( $\text{C}_5\text{H}_5\text{N}$ ) concentration. Other concentrations investigated in this work display good linearity

(refer to Appendix D, Figure D1-4) as reflected in the correlation coefficient ( $R^2$ ) which is close to unity (Table 6.1).

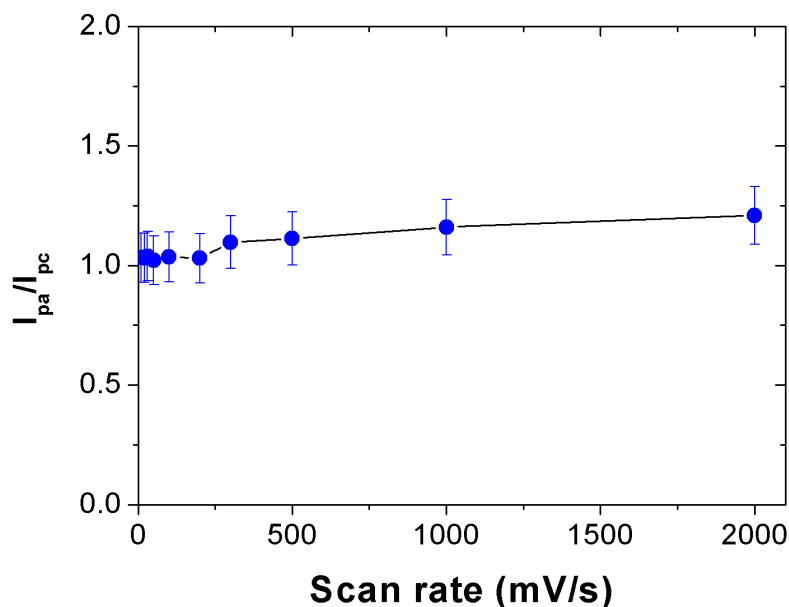


Figure 6.5 The ratio of the anodic peak current to the cathodic peak current ( $I_p^a/I_p^c$ ) as function of the scan rate (mV/s) for the 10mM pyridine dataset under  $N_2$

The Randles-Sevcik/Nicholson equation (Eq. 6.2 and theory Section 2.8.1.1.1) assumes a reversible charge transfer (Bard & Faulkner 2002). This can be applied at the scan rate range  $<500\text{mV/s}$  and at pyridine ( $C_5H_5N$ ) concentrations  $\leq 50\text{mM}$ , where the system behaves reversibly (as characterised above in  $E_{1/2}$  section).

$$i_p(\text{plane}) = (2.69 \times 10^5) n^{3/2} A D_O^{1/2} C_O^* \nu^{1/2} \quad \text{Eq. 6.2}$$

Where  $i_p$  is the current in amperes,  $n$  is the number of electrons,  $A$  is the area in  $\text{cm}^2$ ,  $D_O$  is the diffusion coefficient in  $\text{cm}^2/\text{s}$ ,  $C_O^* = [\text{PyH}^+]$  is the concentration of pyridinium in  $\text{mol}/\text{cm}^3$  and  $\nu$  is the scan rate in  $\text{V/s}$

**The diffusion coefficient ( $D_O$ )** of pyridinium to the electrode was estimated by two alternative approaches, both involving the Randles-Sevcik equation (Eq. 6.2) for assessment of the data obtained; these values were then compared with theory and with literature values. In the first approach, the value of the linear gradient of the cathodic current  $I_p^c$  vs.  $\sqrt{\nu}$  for a particular concentration (e.g. Figure 6.4 inset for 10mM pyridine) of the electroactive species,  $C_O^* = [\text{PyH}^+]$  was used for the estimation of  $D_O$ .

The gradients,  $R^2$  and the calculated diffusion coefficient  $D_O$  of the  $\text{PyH}^+$  species are summarised in Table 6.1 for three pyridine concentrations. In the second approach, the peak current was analysed as function of the species concentration for a fixed scan rate (current  $I_p^c$  vs.  $C_0^* = [\text{PyH}^+]$  plot). The values of  $D_O$  extracted from the related linear gradient coefficient are presented in Table 6.2 for several scan rates.

Table 6.1 Diffusion coefficient calculated at scan rates  $\leq 500\text{mV/s}$  obtained from the plot of the cathodic peak current as a function of the square root of the scan rate ( $I_p$  vs.  $\sqrt{v}$ )

Total Pyridine [Py] (mM)	[PyH <sup>+</sup> ] (mM)	R <sup>2</sup>	Gradient ((mol. cm)/s <sup>1/2</sup> )	Diffusion Coefficient D <sub>O</sub> (cm <sup>2</sup> /s)
5	2.4	0.996	(1.29±0.03) x10 <sup>-5</sup>	(9.09±0.03)x10 <sup>-6</sup>
10	4.7	0.999	(7.15±0.08) x10 <sup>-6</sup>	(1.00±0.08)x10 <sup>-5</sup>
50	23.6	0.997	(0.99±0.05) x10 <sup>-5</sup>	(9.99±0.05)x10 <sup>-6</sup>
Average				(9.97±0.06)x10 <sup>-6</sup>

[PyH<sup>+</sup>] (Calculated in Chapter 5 CO<sub>2</sub> pyridinium equilibria) were estimated from the pK<sub>a</sub> (5.45 at 20°C) at pH5.5. The equilibrium constant was potentiometrically determined by the titration of 50mM pyridine in 0.5MKCl with 50mM HCl in the same salt (Polievktov, M. K; Mairanovskii 1965).

Strictly speaking, the applicability of Eq. 6.2 is limited to a linear diffusion on plane electrode. However, all the measurements presented in the present work were recorded on a cylindrical shape electrode (Pt wire, diameter=0.3mm, length 7 mm). For large enough diffusion time (or low scan speed), this geometry should be considered as a finite size electrode with a substantial convergent diffusion component, with an approximately a hemispherical shaped diffusion layer rather than a linear one (refer to Section 2.4.2, Chapter 2). In this case, the Eq. 6.2 requires correction for the spherical diffusion, which is accounted for by the second term of Eq. 6.3. The  $I_p^c$  vs.  $C_0^*$  plot equation is now effectively represented by Eq. 6.3 where the gradient (Table 6.2) of the plot has an extra contribution from the second term of Eq. 6.3.

$$i = i_p(\text{plane}) + \frac{nFAD_0C_0^*\phi[(nF/RT)vt]}{r_0} \quad \text{Eq. 6.3}$$

Where F is Faraday constant (96,484.6 C mol<sup>-1</sup>),  $r_0$  is an apparent electrode radius (of a value between the cylinder radius and height)

It is important to note that for the purpose of diffusion coefficient extraction, this correction applies only to the  $I_p^c$  vs.  $C_0^*$  plot (the second estimation approach). On the other hand, the estimation of the diffusion coefficient from the  $I_p^c$  vs.  $\sqrt{v}$  (the first estimation method) does not require correction since the correction term (second term) in Eq. 6.3 is independent of  $\sqrt{v}$  and it characterises the intercept value of the related linear dependence. Hence, for the latter case  $D_O$  was determined from Eq. 6.2 and the gradients are summarised in Table 6.1. An average diffusion coefficient of pyridinium to the electrode from this set is  $(9.97 \pm 0.06) \times 10^{-6} \text{ cm}^2/\text{s}$ .

Table 6.2 Diffusion coefficient calculated at different pyridine concentration obtained from the plot of the cathodic current as a function of pyridinium concentration ( $I_p$  vs  $[PyH^+]$ )

Scan rate (mV/s)	$R^2$	Gradient ( $\times 10^{-2}$ )	Intercept (A)	Diffusion coefficient $D_O$ ( $\text{cm}^2/\text{s}$ )
20	0.995	$1.20 \pm 0.08$	$(3.04 \pm 0.08) \times 10^{-6}$	$(9.12 \pm 0.08) \times 10^{-6}$
30	0.993	$1.41 \pm 0.06$	$(1.67 \pm 0.07) \times 10^{-5}$	$(1.07 \pm 0.06) \times 10^{-5}$
50	0.998	$1.60 \pm 0.05$	$(3.21 \pm 0.05) \times 10^{-5}$	$(1.11 \pm 0.05) \times 10^{-5}$
100	0.992	$2.50 \pm 0.03$	$(1.74 \pm 0.06) \times 10^{-4}$	$(1.25 \pm 0.03) \times 10^{-5}$
300	0.997	$3.10 \pm 0.08$	$(4.00 \pm 0.08) \times 10^{-4}$	$(1.09 \pm 0.08) \times 10^{-5}$
Average				$(1.09 \pm 0.15) \times 10^{-5}$

*Errors were estimated from the error in the gradient of the best straight line through the extracted peak current data points*

The alternative estimate for (an average) pyridinium diffusion coefficient of  $D_O = (1.09 \pm 0.15) \times 10^{-5} \text{ cm}^2/\text{s}$  was obtained from Eq. 6.3 and the gradient of  $I_p^c$  vs.  $C_0^*$  plot summarised in Table 6.2. The average value corresponds to the concentration range  $\leq 50 \text{ mM}$  of total pyridine concentrations and for the scan rates range  $\leq 500 \text{ mV/s}$ . The values estimated using the different approaches are close enough to each other. Moreover, the average values reported above agree well with the literature diffusion coefficient values ( $1 \times 10^{-5} \text{ cm}^2/\text{s}$ ) (Costentin et al. 2013) and ( $1.05 \times 10^{-5}$ ) (Mairanovskii 1963) for  $PyH^+$  species. This confirms the diffusion controlled system of the species  $PyH^+$  to the electrode, which fits well with the peak current symmetry determined above at scan rates  $< 500 \text{ mV/s}$ .

**The number of electrons, n, transferred for a reactant** can be evaluated by cyclic voltammetry provided the diffusion coefficient of the electroactive species is known.

For the calculation of  $n$  in Eq. 6.2, a  $\text{PyH}^+$  diffusion coefficient value of  $1 \times 10^{-5} \text{ cm}^2/\text{s}$  was taken (from Costentin et al. 2013 reference). The number of electrons,  $n$ , transferred in the charge transfer reaction of  $[\text{PyH}^+]$  was determined to be  $0.79 \pm 0.09$ . This is in line with the electron value  $n=0.8$  of (Yan et al. 2014). The calculated value  $n=0.79 \pm 0.09$ , indicates a single-electron transfer electrochemical reduction. This value is (unexpectedly) less than 1 which is probably due to the reduced diffusional peak current. The decrease in the diffusive peak current seems to be caused by the pre-peak feature observed in the CVs (Yan et al. 2013). The pre-peaks appear as shoulder preceding the pyridine usual wave these are more prominent at higher scan rates as illustrated in Appendix D, Figure D1. More importantly, these calculations further exclude the two-electron reduction of pyridine to DHP reported in the literature (refer to Chapter 3 Section 3.1.2.3).

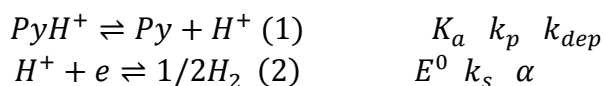
### **6.2.1.1 Summary of the CVs Analysis**

The criteria assessed herein were found to be applicable at limited scan rate and pyridine concentration ranges in acidic media under  $\text{N}_2$ . Under these conditions, the observed redox wave was confirmed to be a one-electron reduction at redox potential of  $-0.56 \pm 0.01 \text{ V}$ , controlled by pyridinium diffusion. The data obtained is in good agreement with literature reports. The above analyses do not allow differentiation between the electrode Reactions 2 and 3 in Scheme 6.1. Indeed, the electrode reduction appears to be unaffected by the coupled  $\text{PyH}^+$  deprotonation, i.e. chemical Reaction 1 in Scheme 6.1, which can be interpreted as evidence of either the high deprotonation rate or of a dominant contribution of pyridinium. CVs simulation described in the next section, are expected to explain the data at the entire scan rate and pyridine concentration ranges.

### **6.2.1.2 CVs Simulation: Model Under $\text{N}_2$**

The CV curves were simulated assuming Butler-Volmer kinetics (see theory and methods Sections 2.7 and 4.6). Numerical CV simulation was initially conducted considering the simplest CE model (Scheme 6.2) (Costentin et al. 2013).

*Scheme 6. 2 Model suggested by Constantin et al*



where  $E^0$  is the standard hydrogen potential,  $k_s$  is the standard heterogeneous rate constant,  $\alpha$  transfer coefficient (see Butler-Volmer kinetics, Chapter 2, Section 2.7),  $K_a$  is the equilibrium constant of pyridine,  $k_p$  is the rate constant of protonation ( $\text{g mol}^{-1} \text{s}^{-1}$ ), and  $k_{dep}$  is the rate constant of deprotonation ( $\text{s}^{-1}$ ).

The proton reduction (E) was simulated as a single apparent electrode reaction coupled to the deprotonation equilibrium of pyridine (C) (Scheme 6.2). Fitting the experimental CVs, using the CE model assumed above, resulted in a significant underestimation of the cathodic peak current ( $\sim >30\%$ ). The underestimation of the simulated current was more prominent at high scan rates and high pyridine concentrations. This current limit is set by the fundamental upper limit of deprotonation, given by the pyridinium rate constant ( $k_{dep}$  in Reaction 1, Scheme 6.2), which is the product of the fastest protonation rate of  $10^{10} \text{ s}^{-1}\text{M}^{-1}$  and the known equilibrium constant  $K_a = 3.5 \times 10^{-6}$  (Mairanovskii 1963).

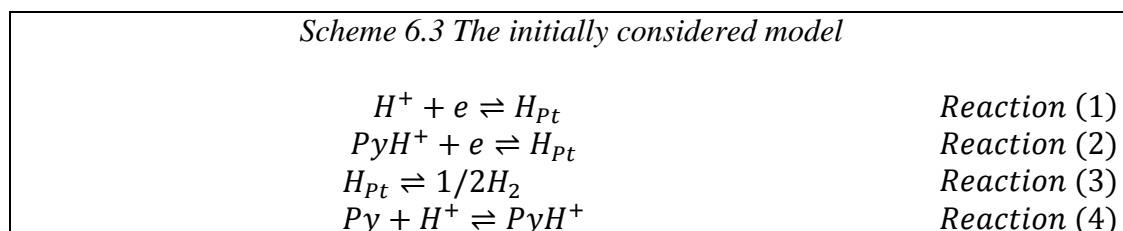
Therefore, an alternative reduction process had to be taken into account to overcome this limit and to fit the experimental CV data. Direct reduction of  $\text{PyH}^+$  cations was added to the reaction in Scheme 6.3 as a second electrode reaction. This electrode reaction was considered as a concerted electron proton transfer (CPET). The redox potential of the two electrode reactions are related by Eq. 6.4 (Reaction 1 and 2, Scheme 6.3). Eq. 6.4 was derived (Appendix A3) according to the Nernst equation (Yan et al. 2013).

$$E_{\text{PyH}^+/\text{H}_{\text{Pt}}}^{0 \text{ app}} = E_{\text{H}^+/\text{H}_{\text{Pt}}}^{0 \text{ app}} - RT/F \quad pK_a \quad \text{Eq. 6.4}$$

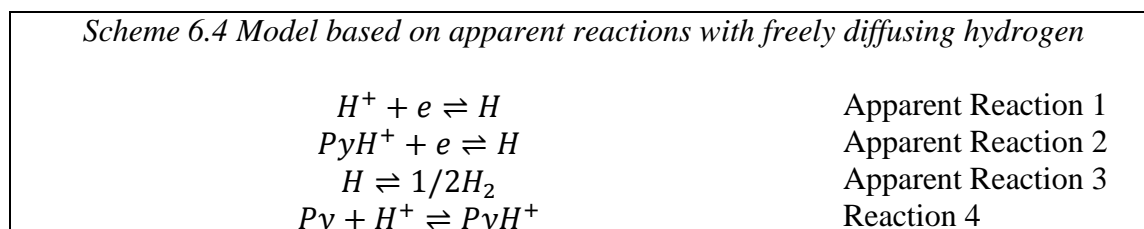
where  $E_{\text{PyH}^+/\text{H}_{\text{Pt}}}^{0 \text{ app}}$  is the apparent standard potential of Reaction 2 Scheme 6.3 and  $E_{\text{H}^+/\text{H}_{\text{Pt}}}^{0 \text{ app}}$  is the apparent standard potential of Reaction 1, Scheme 6.3

Such electrode transfer reactions (Reaction 1 and 2, Scheme 6.3) are expected to reproduce the peak current of the experimental data. The individual contribution of each of the parallel reduction routes should be affected by the total pyridine content and the acidity of the medium. In this model, HER is represented by the dimerization of

adsorbed hydrogen on Pt surface leading to dihydrogen formation (Reaction 3, Scheme 6.3). The set of reactions, best describing the process, are presented in Scheme 6.3:

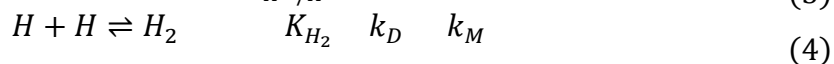
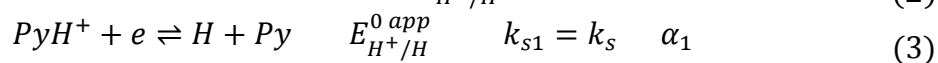
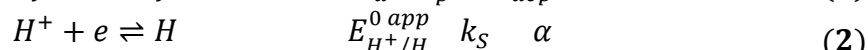
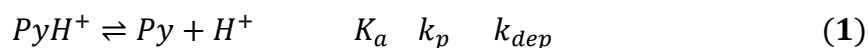


The Reactions 1, 2, and 3 (Scheme 6.3) all involve atomic hydrogen which is adsorbed on platinum electrode. However, due to the complexity of the adsorption process these surface reactions were simulated with freely diffusing atomic hydrogen as shown in Scheme 6.4.



Hence, all simulation parameters for freely diffusing hydrogen atoms are purely fictitious and serve the purpose of hydrogen accumulation imitation and its transport away from the electrode (Scheme 6.4). The simulation of the true surface reactions (Reactions 1, 2 and 3 in Scheme 6.3) still does not provide an adequate model which reflects the real process. Indeed, under the experimental conditions of pyridine concentration and pH investigated, the reactions presented in Scheme 6.3 result in an excessive accumulation of molecular hydrogen in the vicinity the electrode surface, which far exceeds the hydrogen solubility limit (15mg per kg of water). In reality, this excess is balanced by H<sub>2</sub> gas bubble generation. This nontrivial process would have to be also included in any realistic simulation.

Scheme 6.5 Model used for simulating the experimental CV data under  $N_2$



The apparent model parameters were obtained by fitting the same experimental CV dataset presented in last section obtained for 10 mM pyridine (at different scan rates) prepared in acidic electrolyte at pH =5.5 (HCl adjusted), purged with  $N_2$ . The equilibrium constants for the bulk chemical reactions and the kinetic parameters for the surface reactions used in the simulation are presented in Table 6.3.

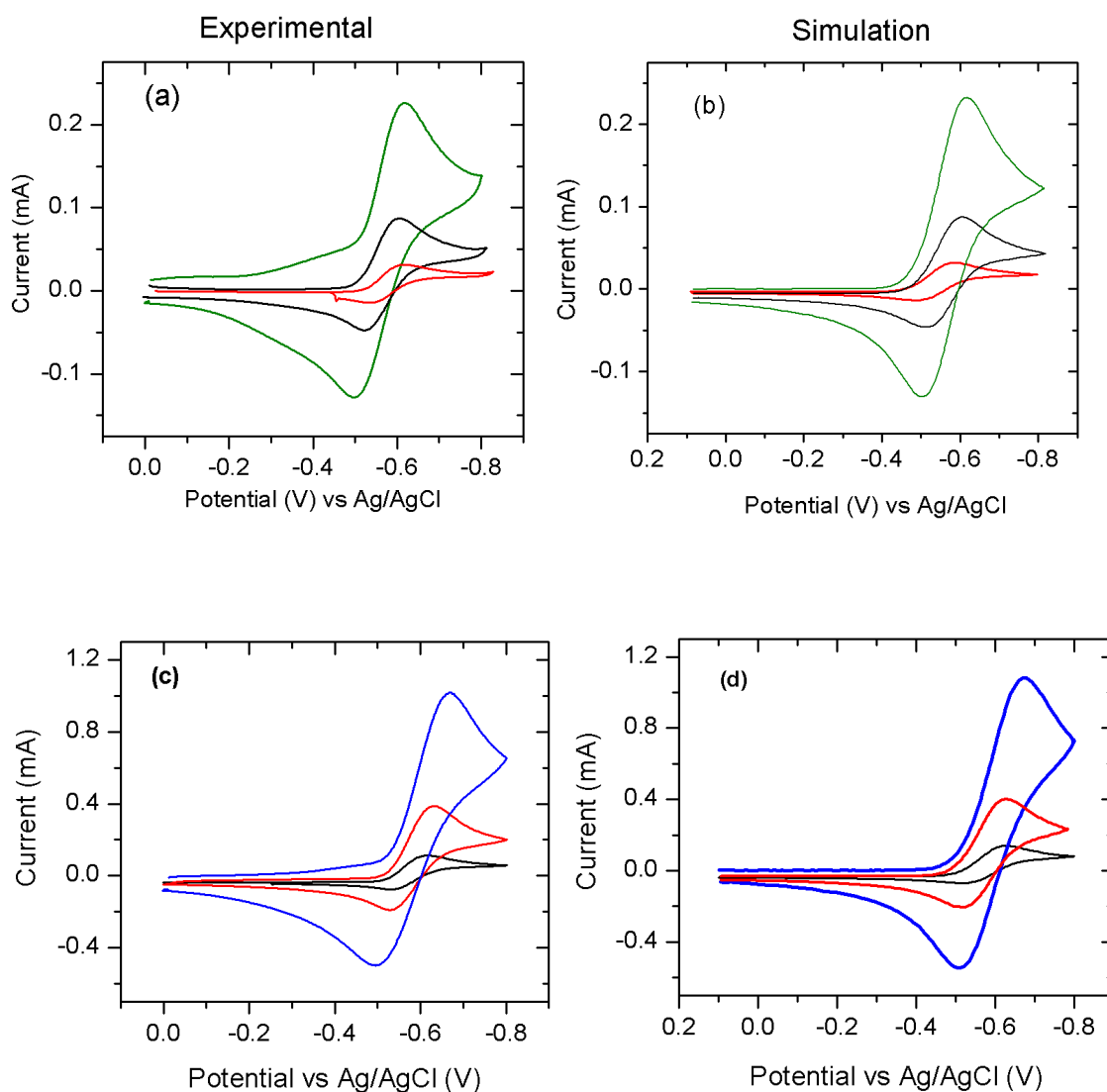


Figure 6.6 CV of Pyridine in 0.5 KCl solution at pH = 5.5. (top) 10mM, (bottom) 50mM at 10, 100, and 1000mV/s. Experiment (a and c), simulation (b and d) (Model of Scheme 6.5)

The simulation was undertaken according to Scheme 6.5. The standard redox potentials of the electrode reactions (Reaction 1 and 2, Scheme 6.5) are interrelated by Eq. 6.4. Figure 6.6 compares the simulated to experimental CVs of 10mM and 50mM pyridine. The simulated model (Scheme 6.5) fitted the experimental CV shapes reasonably well by reproducing the cathodic peak potentials (deviation of  $\sim <15\%$ ).

Table 6.3 Apparent chemical and kinetic parameters used in the CV simulations

	<b>Electrode reactions</b> $E_{H^+/H}^{0app}, E_{H^+/H}^{0app}, k_s,$ $\alpha, \alpha_1, k_{s1}$	<b>Coupled chemical reactions</b>	<b>Scan rates (mV/s)</b>	<b>Pyridine concentrations (mM)</b>
Scheme 6.5	$E_{H^+/H}^{0app}$ and $E_{PyH^+/H}^{0app}$ are related by Eq. 6.4 $\alpha = \alpha_1 = 0.5$ $k_s = k_{s1} = 0.3$	$K_a = 3.5 \times 10^{-6}$ $k_p = 10^{10} \text{ cm s}^{-1}$	10mV/s- 2000mV/s	5mM-200mM
Scheme 6.7	$E_{H^+/H}^{0app}$ and $E_{PyH^+/H}^{0app}$ are reported in Table 6.6 $\alpha = \alpha_1 = 0.5$ $k_s = k_{s1} = 0.3$	$K_a = 3.5 \times 10^{-6}$ $k_p = 10^{10} \text{ cm s}^{-1}$ $K_{H_2} = 10$ $k_{hydr} = 3 \times 10^{-2} \text{ s}^{-1}$ $K_{hydr} = 1.7 \times 10^{-3}$	10mV/s- 5000mV/s	1mM-200mM

a: literature value

Figure 6.7 depicts the experimentally acquired and the simulated cathodic peak current as a function of the pyridine concentration range investigated in this study. The simulation model fitted well the experimental data at pyridine concentration 5-200mM and in the scan rate range investigated (Figure 6.7). The simulated cathodic peak current deviated by a maximum of 15% as compared to the experimentally observed cathodic peak current. This is fairly acceptable considering the reproducibility of the experimental CV data is  $\sim 10\%$ .

The simulation does not reproduce a characteristic feature of background current observed at high scan rate (1000mV/s) in experimental CVs (Figure 6.6). This feature was previously observed for weak acids and was associated with a hydrogen adsorption pre-wave (Yan et al. 2013). This background current was not reproduced in simulated

CVs, which is not surprising since the adsorption process was not included in the model.

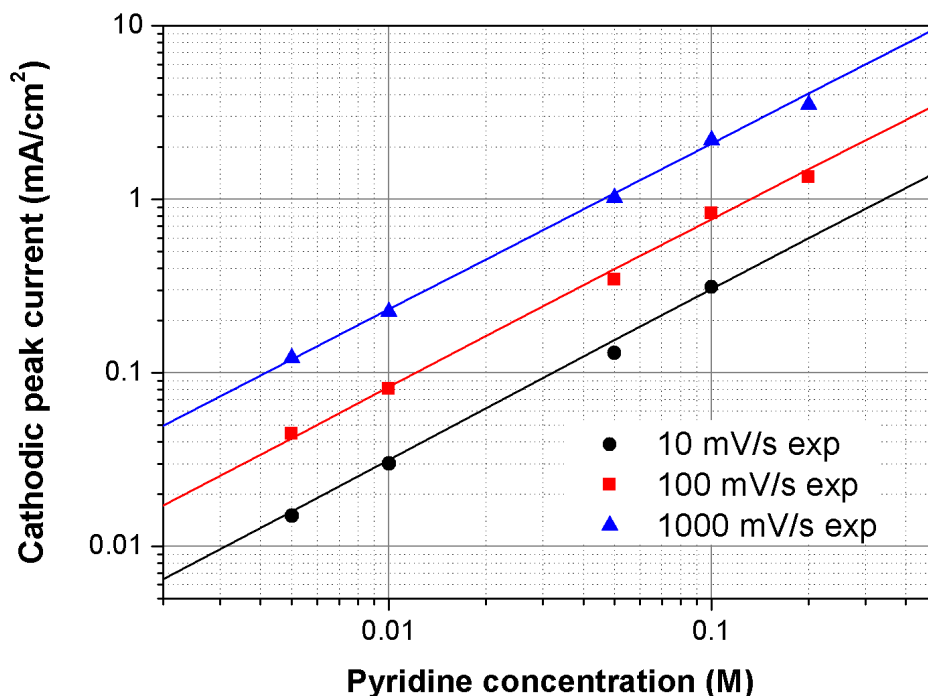


Figure 6.7 Cathodic peak current of CVs at different pyridine concentrations and scan rates in 0.5M KCl solution at pH = 5.5. Under N<sub>2</sub>. Circles - experiment, lines - simulation.

### 6.2.1.3 Summary of the CVs Simulation Analysis

To summarise, the analysis of the CVs data under N<sub>2</sub> in acid-adjusted electrolytes on Pt electrode showed that the observed voltametric response can be well reproduced by simulation using the Scheme 6.5 model for the entire range of pyridine (C<sub>5</sub>H<sub>5</sub>N) concentrations and scan rates. The dependence of the voltametric wave on the acidity of the electrolyte is presented in the next section.

### 6.2.2 pH Dependence Study of the Pyridinium System

Further investigation of the pyridinium cation behaviour in acidic solutions was carried out with the aim of assessing the applicability of the model proposed in the last section (Scheme 6.5) to low pH range. Analysis of the CV waves revealed that pyridinium

behaves distinctively depending on the acidity of the medium. Three regions can be observed:

**(1) At a basic pH ( $\text{pH} \geq 6$ ),** pyridinium gives rise to a diminished CV wave ( $\text{pH} \sim 6$ ) due to the low concentration of the cation (calculated in Chapter 2, Section 5.2.1) confirming the previously reported observations (Yan et al. 2013). As the pH is increased further the CV wave amplitude start weakening ( $\sim \text{pH} 7$ ) until it is not observed at all (refer to Appendix D, Figure D5).

**(2) At proton concentration  $[\text{H}^+]$  lower than 1mM ( $3 < \text{pH} \leq 5.5$ ),** the voltammetric response is observed as a redox wave at  $-0.56 \pm 0.01 \text{V}$  (See Figure 6.4 and Figure 6.8). The latter Figure 6.8 shows experimental and simulated CVs of pyridine (10mM) at a Pt cathode between pH 5.3 and pH 2.0 adjusted using hydrochloric acid. The appearance of the redox wave at  $-0.56 \pm 0.01 \text{V}$  applies to the conditions ( $[\text{H}^+] = 0.01 \text{mM}$  at  $\text{pH} 5.5$ ) at which all the previous experiments/simulations were undertaken (in section 6.2.1). In this case, the Randle-Sevick analysis together with the model proposed in Scheme 6.5 confirmed the diffusion controlled  $\text{PyH}^+$  reduction masking the  $\text{H}^+$  reduction reaction which coupled to the protonation reaction.

**(3) As the  $[\text{H}^+]$  concentration is increased beyond 1mM ( $\text{pH} \leq 3$ ),** a new wave appears (experimentally) at more positive potential  $-0.43 \pm 0.01 \text{V}$  (Figure 6.8a, line: black ( $[\text{H}^+] \sim 10 \text{mM}$  to violet ( $[\text{H}^+] \sim 1 \text{mM}$ )) alongside the usual wave at  $-0.56 \pm 0.01 \text{V}$ . The amplitude of the preceding wave observed at  $-0.43 \pm 0.01 \text{V}$  is inversely proportional to the pH of the medium (i.e. it increases with concentration of  $\text{H}^+$ ). This proportionality is clearly seen in Figure 6.9a inset where the experimental peak current  $I_p$  (anodic and cathodic) of the wave appearing at low pH ( $-0.43 \pm 0.01 \text{V}$ ,  $\text{pH} < 3$ ) is plotted as function of the proton concentration  $[\text{H}^+]$ . Figure 6.9 shows  $I_p$  of the two waves observed in Figure 6.8 vs.  $[\text{H}^+]$ . The subsequent wave ( $-0.56 \pm 0.01 \text{V}$ ) peak current does not seem proportional to the pH variation on both cathodic and anodic peaks (Figure 6.9a) and is in fact independent of  $[\text{H}^+]$  over the pH range 3-5.5. Instead, the cathodic current of this wave is linear with  $[\text{PyH}^+]$  concentration (Figure 6.10). Hence, the voltammetric behaviour points to the newly arising wave being due to  $\text{H}^+$  reduction (Yan et al. 2014) (Costentin et al. 2013) and the subsequent wave to the  $\text{PyH}^+$  reduction.

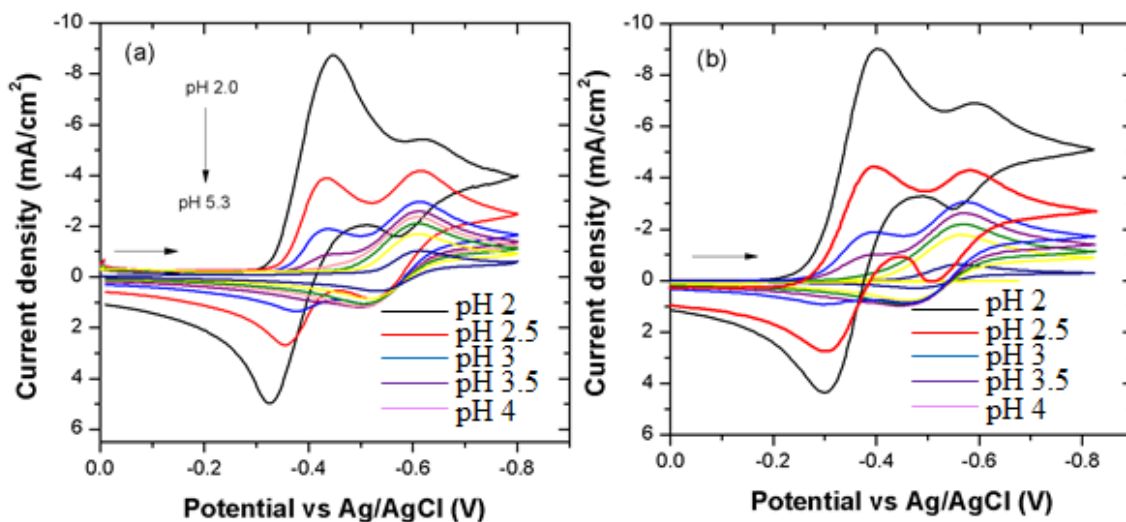


Figure 6.8 Cyclic voltammograms of 10mM pyridine in 0.5M KCl under  $N_2$  at 100mV/s. The acidity varies between pH 2.0-5.3. (a) experiment, (b) simulation. Horizontal arrows- scanning direction, vertical arrow- pH increment

These observations indicate that the electrode reactions proposed (Reactions 2 and 3 Scheme 6.5) are both contributing to the observed redox waves. In this case the  $H^+$  reduction (Reaction 2, Scheme 6.5) is more prominent at high protons concentrations (1-10mM) as compared with the weakly acid electrolytes ( $3\mu\text{M}$ , pH5.5 in the previous Section 6.2.1).

The system at such low pH is characterised by the diffusion of both species [ $H^+$ ] and [ $\text{PyH}^+$ ] to the electrode, which are also coupled by equilibrium Eq. 6.4. Therefore, the quantification of the diffusion coefficient parameter is complex since the previous Randle Sevcik/Nicholson analyses do not apply under such conditions. The alternative approach is analysis using numerical simulation which is described in the next section.

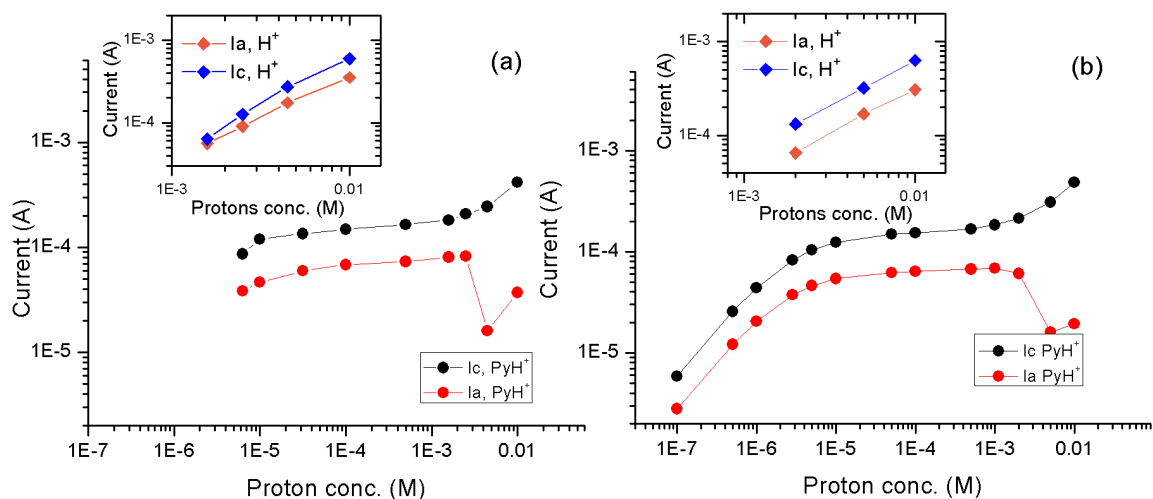


Figure 6.9 Peak current of 10mM pyridine in 0.5MKCl at 100mV/s as function of protons concentration (a) experimental, (b) simulation. Inset: Peak current of protons as function of the proton concentration

## 6.2.2.1 CVs Simulation

The experimental data presented in Figure 6.8a and Figure 6.9a were numerically simulated (Scheme 6.5 model) at an extended pH range as shown in Figure 6.8b and Figure 6.9b respectively. The model in Scheme 6.5 has reproduced the CVs shape (Figure 6.8) and the current (Figure 6.9) within ~15% deviation. The new wave, observed in the high acidic electrolyte, was also reproduced starting from pH < 3. This outcome together with the observations discussed above further confirms the model proposed (Scheme 6.5).

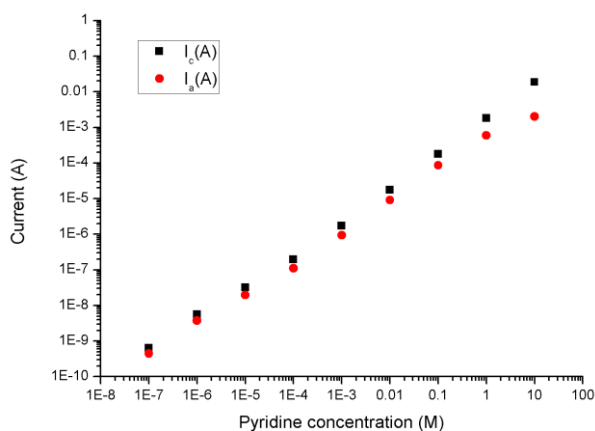


Figure 6.10 Simulated peak current as function of pyridine concentration at pH 1-7

Interestingly, the wave assigned to the proton reduction can only be observed in the presence of pyridinium. For instance, the CV of pyridinium-free acidic (HCl) solution did not display a proper redox wave. However, ambiguously, the proton reduction (in a supposedly pyridinium-free medium) was presented as a distinctive reversible voltammetric wave at pH 5.5 (Costentin et al. 2013) and at pH 2.3 (Supplement data Yan et al., 2013) very similar to the wave obtained in the present work at  $\sim 10\mu\text{M}$  pyridine CV wave in Figure 6.11. The voltammetric measurements on Pt in acidic media showed that the proton electrochemical response does not show a well-defined reversible wave (Zhan et al. 2009) (Pletcher & Sotiropoulos 1994) (Priyantha & Malavipathirana 1996) which contradicts the former studies (Costentin et al. 2013) (Yan et al. 2013). Instead, the CV of protons shows broad features associated with hydrogen adsorption/desorption (Figure 6.11b) on a Pt surface. Thus, the  $-0.43\text{V}$  wave arising in the low pH region seems to be assisted by pyridine/pyridinium species. This can be well explained by the formation of Pt-H hybrid via the electro-desorption of pyridinium from the Pt surface:  $\text{PyH}^+(\text{ad}) + \text{Pt} + e \rightarrow \text{Pt} - \text{H} + \text{Pt}$  (Ertem et al. 2013).

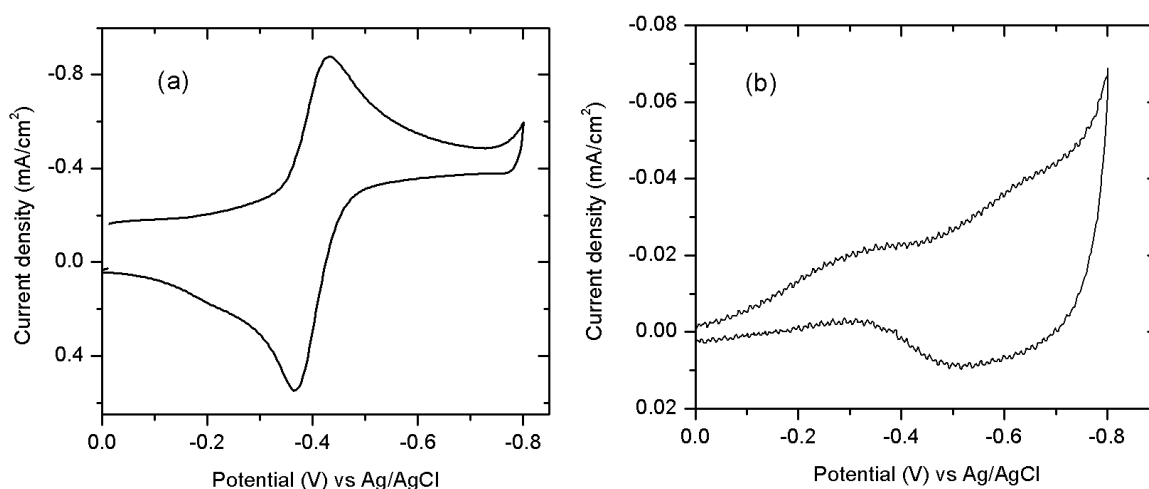


Figure 6.11 CVs under  $\text{N}_2$  hydrochloric acid (HCl) adjusted pH at  $100\text{mV/s}$ : (a) CV of  $\sim 10\mu\text{M}$  pyridine at pH 3, (b) CV with no pyridine at pH 5

The behaviour of pyridinium in low pH media can be further rationalised in terms of the Pourbaix diagram (Figure 6.12) (species concentrations are calculated in Chapter 5, Table 5.4). As can be seen in Figure 6.12, in the low pH region ( $< \text{pH} 3$ ) where the new wave ( $-0.43\text{V}$ ) is seen, the concentration of pyridinium does not vary significantly. A considerable shift of the dissociation equilibrium (Reaction 1, Scheme 6.5) to regenerate

the protons occurs once the proton concentration close to the electrode is small. This behaviour is attributed to the proton reduction coupled to their rapid regeneration upon the dissociation of pyridinium (Costentin et al. 2013). The emergence of the new wave (-0.43V) is associated with the large equilibrium concentration of protons since the increase of the protons resulted in the build-up of this wave. Correspondingly, the  $\text{PyH}^+$  cation reduction wave (-0.56V) emerges through the proton reduction once these cations are consumed at the level of the first wave. The set of reactions in Scheme 6.5 fits well the voltammetric observations obtained herein and this was further confirmed by the numerical simulations. The behaviour of pyridinium outcome is well in line with the literature. However, the emergence of CV wave in the absence of pyridinium reported by Savéant and Bocarsly groups is questionable. Contrary to what has been reported, the -0.43V of the waves assigned to proton reduction is only observed when pyridine/pyridinium is present. This observation indicates that the wave arising at -0.43V, assigned to the proton reduction, is assisted by pyridinium and cannot possibly emerge independently. This suggestion is in line with the pyridinium assisted H-Pt hybrid formation (Ertem et al. 2013)

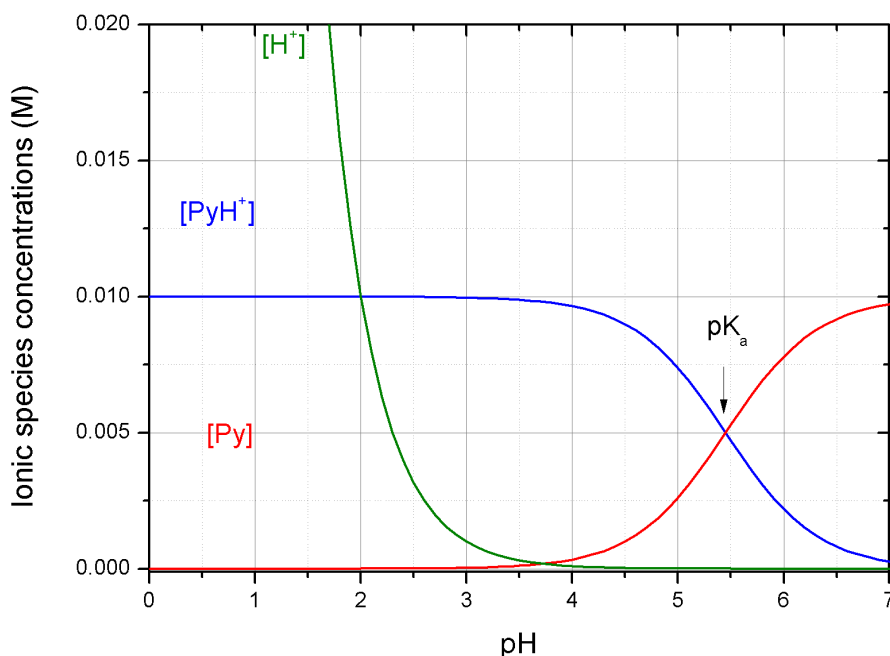


Figure 6.12 Pourbaix diagram for 10mM analytical pyridine concentration

## 6.2.2.2 Summary of CV Studies at Low pH

To summarise, the pyridinium system displays three distinctive electrochemical characteristics (1, 2 and 3) which are dependent on the acidity of the medium. At pH higher than ~6, very weak waves are observed then disappear at ~pH 8. At such conditions, the concentrations of both cations are very low (e.g. at pH7  $[H^+] = 0.1\mu M$  and  $[PyH^+] = 0.2mM$ ). This further confirms that these cations are giving rise to the CV waves in the potential range studied. At  $3 < pH < 5.5$  (the most studied acidity range for this system in the literature), a CV wave at  $-0.56 \pm 0.01V$  is observed (characterised in the previous Section 6.2.1). At this range, the pyridinium concentration ranges between 9.96mM and 7.38mM which is 9 to ~700 times higher than the proton concentration. This leads to assigning this wave to pyridinium reduction (Reaction 3, Scheme 6.5). However, at  $pH \leq 3$  region, two CV waves are observed. These voltammetric responses are unambiguously explained by proton reduction (Reaction 2, Scheme 6.5) coupled to the deprotonation of  $PyH^+$  reaction (Reaction 1, Scheme 6.5) responsible for the first wave and pyridinium reduction (Reaction 3, Scheme 6.5) for the second. This was further confirmed by the numerical simulations.

## 6.3 CV Studies in the Presence of CO<sub>2</sub>

### 6.3.1 Current Enhancement at Atmospheric Pressure (1 bar of CO<sub>2</sub>)

As described previously in the mechanisms summary Section (6.1.1), the introduction of CO<sub>2</sub> to pyridine-containing electrolytes, results in an enhancement of the *redox wave* amplitude as compared to the same wave observed in the inert atmosphere (N<sub>2</sub>) (refer to the mechanisms summary Section 6.1.1). The current enhancement observed under CO<sub>2</sub> was interpreted differently by Bocarsly and Savéant groups. In Bocarsly's initial mechanism (Figure 6.1), the current enhancement was explained by the interaction of pyridinyl radical (Reaction 2, Figure 6.1) with CO<sub>2</sub> (Reaction 4, Figure 6.1). This pathway was disproved by the theoretical calculations as discussed earlier. An alternative catalytic pathway based purely on the observed Faradaic yields of the products was subsequently suggested by Bocarsly group. The process according to these workers involves two pathways in which 5-25% of the current contributing to methanol

production, proceeds through the interaction of H-Pt hybrid surface with  $\text{CO}_2$ - $\text{PyH}^+$  in a reduction reaction (Reaction b, Figure 6.3) to produce formate. This reaction is considered a first step toward methanol formation. The remaining 75-95% of the current is believed to be directed toward the competing HER. On the other hand, Savéant's group propose that the current enhancement is merely the contribution of protons released by  $\text{CO}_2$  dissociation resulting solely in the production of molecular hydrogen (Reaction 3 and 4, Figure 6.2). Although, both routes consider a catalytic mechanism, these pathways lead to different products where HER competes with methanol formation in the former, while HER takes place exclusively in the latter. Therefore, further investigation to understand the  $\text{CO}_2$  effect on the voltammetric  $\text{PyH}^+$  behaviour was undertaken at atmospheric  $\text{CO}_2$  pressure (1bar  $\text{CO}_2$ ) in the present study and is reported herein.

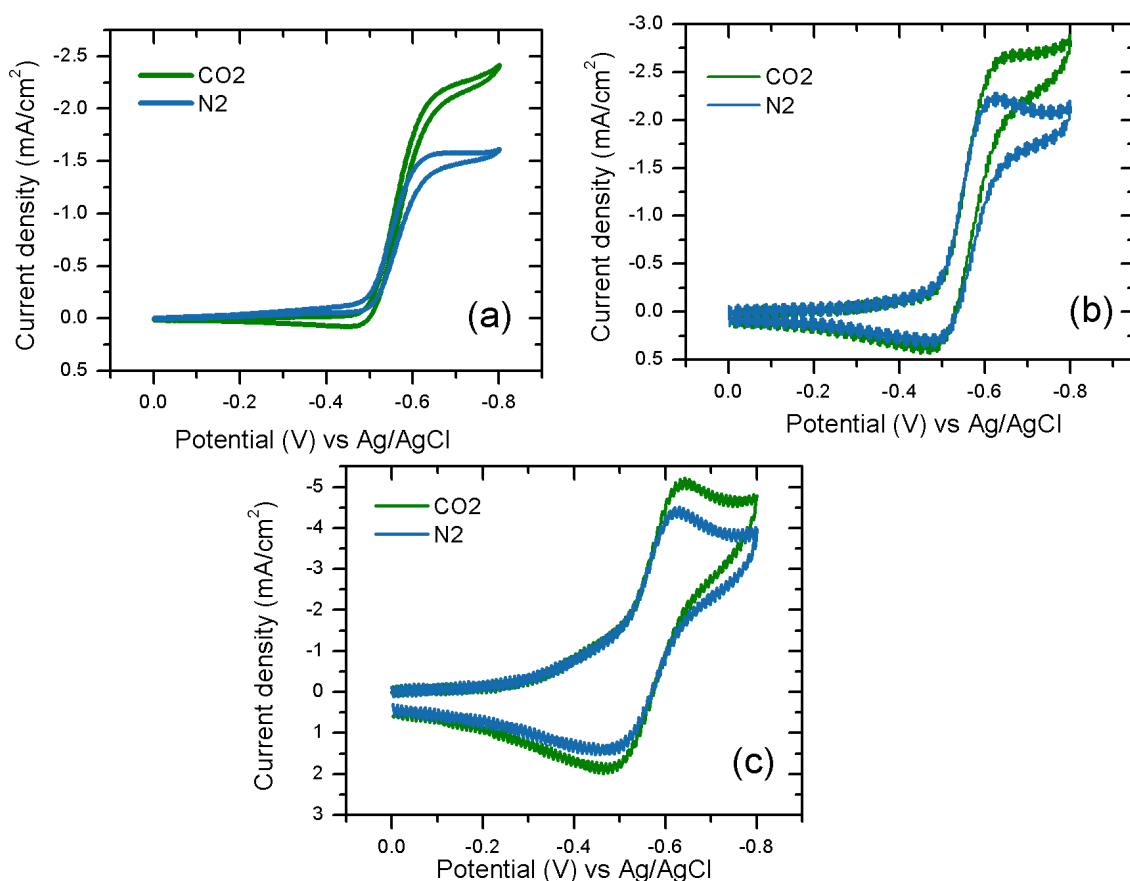


Figure 6.13 CVs of 10mM pyridine in 0.5MKCl at atmospheric pressure 1bar and 20°C (blue) under  $\text{N}_2$ , (green) under  $\text{CO}_2$  at (a) 5mV/s, (b) 50mV/s and (c) 500mV/s on Pt disk (100 $\mu\text{m}$  diameter).

Figure 6.13 illustrates CVs collected in pyridine-containing (10mM) aqueous electrolyte at Pt cathode under an inert gas ( $N_2$ ) and at atmospheric  $CO_2$  (1bar) at 5mV/s, 50mV/s and 500mV/s. The  $CO_2$ -buffered electrolyte reaches  $\sim$ pH5.3 in the presence of 10mM pyridine. Thus, the pH was adjusted (to pH5.3) with hydrochloric acid for the inert atmosphere experiment to match the  $CO_2$ -buffered electrolyte. Under  $CO_2$ , the strongest enhancement of the cathodic peak current ( $\sim$ 2-fold) is observed at the lowest scan rate (5mV/s) as depicted in Figure 6.13. As the scan rate is increased the current difference between the  $CO_2$  saturated medium and under  $N_2$  becomes smaller.

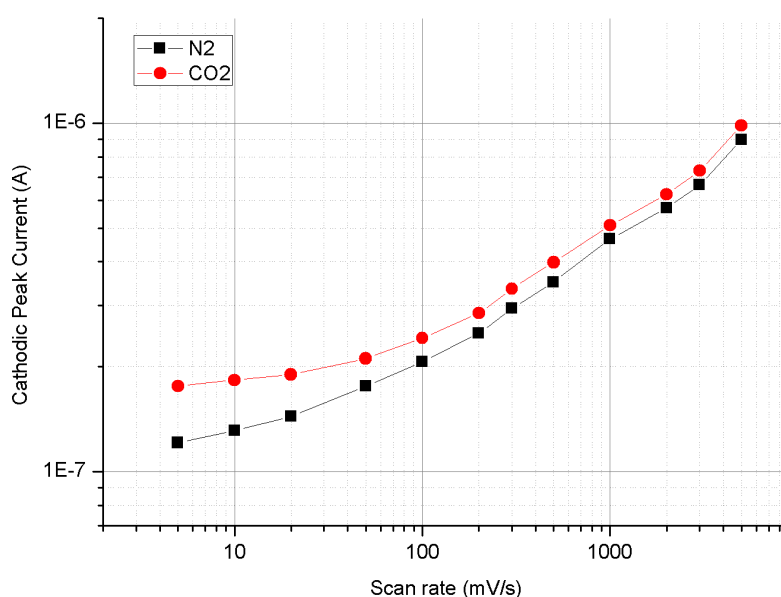


Figure 6.14 Plot of the cathodic peak current under  $CO_2$  and under  $N_2$  at 100mM pyridine and Pt disk (100 $\mu$ m diameter)

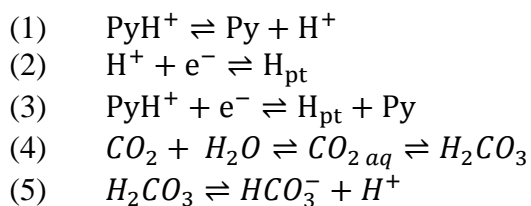
The current enhancement under  $CO_2$  was also observed at other pyridine concentrations as depicted in Figure 6.14 for 100mM pyridine. The enhancement of the current is clearly dependent on the scan rate. Although comparable enhancement of the pyridinium related peak current under  $CO_2$  was reported at similar conditions by the Bocarsly group (Morris et al. 2011), these workers presented the current enhancement at the lowest scan rates and excluded its variation at higher scan speeds. Hence, the catalytic mechanism proposed by this group did not account for any scan speed dependence. Instead, the catalytic characteristic ‘S-shape’ was only reported to appear at a very low scan rate (1mV/s) (Cole et al. 2010). Furthermore, the current attributed to

CO<sub>2</sub> reduction should represent 100% response which did not reflect the product Faradaic yields of only ~20%. Hence, the direct contribution of CO<sub>2</sub> to the voltametric wave observed seems unlikely and the electron transfer reaction involved in the system should be independent of CO<sub>2</sub>.

The charge transfer process under CO<sub>2</sub> proposed herein proceeds through Reactions 2 and 3 in Scheme 6.5. As for the chemical reaction, the dependence of the current enhancement on the scan rate (Figure 6.13 and Figure 6.14) suggests that the electrochemical process involves a slow chemical reaction coupled to the electrode reaction (Costentin et al. 2013). In the inert atmosphere, according to Scheme 6.5 the only chemical reaction identified is the deprotonation of pyridinium which is known to be a fast equilibrium reaction. On the other hand, in the presence of CO<sub>2</sub>, two chemical reactions namely CO<sub>2</sub> hydration and dissociation take place. The set of reactions best describing this system are suggested in Scheme 6.6.

In Scheme 6.6, the Reactions 4 and 5 simply represent a reprotonation source for pyridine via the reverse of Reaction (1) which is coupled to Reaction 3 in an EC' mechanism and/ or coupled to Reaction 2 in a CE mechanism depending on the concentration of pyridine and the acidity of the medium. The dissociation Reaction (5) is well-known to be a fast equilibrium reaction as it involves a proton transfer from an oxygen acid, while the hydration reaction is much slower since it involves a high activation energy for the molecular reorganization due to adjustment of the bonds length and angles (Costentin et al. 2013). Thus, the electrode Reactions 2 and 3 are affected by the hydration reaction (Reaction 4) kinetics. Hence, the enhancement of the current at slow scan rates is most likely due to the slow chemical step (Reaction 4, Scheme 6.6). At fast scan rates (>100mV/s in Figure 6.14) a negligible difference of the reduction current is observed, which indicates the slow release of the protons needed in the reprotonation of pyridine (reverse of Reaction 1). These observations further confirm that the hydration step is the rate limiting chemical reaction coupled to the electron transfer reaction.

*Scheme 6.6 Set of reactions describing the process under CO<sub>2</sub>*



This mechanism (Scheme 6.6) agrees well with Savéant group who explained the voltammetric wave, under CO<sub>2</sub>, as merely the supply of protons to the electrode reaction by the added contribution from the dissociation of PyH<sup>+</sup> (Reaction 1, Scheme 6.6) and the dissociation of CO<sub>2</sub> (Reaction 4 and 5, Scheme 6.6) (Costentin et al. 2013). As part of attempting to justify the contribution of the current from both PyH<sup>+</sup> deprotonation and H<sub>2</sub>CO<sub>3</sub> dissociation, Costentin et al have presented the current of the pyridinium-CO<sub>2</sub> CV waves as the superimposition of the current from CO<sub>2</sub> alone and pyridinium alone. In these authors work, the pyridinium-CO<sub>2</sub> medium was auto-buffered to pH 5.15, the pyridinium alone was adjusted to pH 5.15, while CO<sub>2</sub>-saturated electrolyte has reached pH 4.5. Two peculiar features are noticed from this group's work. First, the acidity of the three media is not matched (pH 4.5 and 5.15). At these differently buffered electrolytes the species concentrations vary as shown in Table 6.4. Consequently, the current arising from CO<sub>2</sub> at such pH (4.5) where protons are higher (~5 times) than in the PyH<sup>+</sup> alone medium (pH 5.15) may overestimate the current resulting from this CV. Due to this inconsistency similar experiments to those of the Savéant group's work were undertaken in the present study.

Table 6.4 Species concentrations in 3mM pyridine-CO<sub>2</sub> system

	pH	[PyH <sup>+</sup> ] (mM)	[H <sup>+</sup> ] (mM)	[CO <sub>2</sub> ] (M)	[HCO <sub>3</sub> <sup>-</sup> ] (mM)
<b>CO<sub>2</sub> Alone</b>	4.5 <sup>a</sup>	-	0.032	0.0383	0.043
<b>PyH<sup>+</sup> + CO<sub>2</sub> (calculated in this work)</b>	5.15 <sup>a</sup> 5.09 <sup>b</sup>	2.089	0.008	0.0383	2.096
<b>PyH<sup>+</sup> Alone</b>	5.15 <sup>a</sup>	1.997	0.007	-	-

a reported value (Costentin et al. 2013)

b calculated in this work

CVs were recorded at 5mV/s and 500mV/s in pyridine-containing electrolyte (10mM) (a) under N<sub>2</sub> with the medium adjusted to pH 5.3; (b) in pyridine-containing electrolyte which is buffered by CO<sub>2</sub> to pH 5.3 and (c) of CO<sub>2</sub> saturated electrolyte (PyH<sup>+</sup> free medium) naturally buffered to ~pH 4 (Figure 6.15). Although, the protons are ~20 times higher in the case of electrolyte containing CO<sub>2</sub> alone (pH 4.5) as compared to the pH5.3 media, the cathodic current of CO<sub>2</sub> alone (in pyridinium-free medium) is much lower. On the other hand, a significant enhancement is observed between the current of pyridinium under N<sub>2</sub> (absence of CO<sub>2</sub>) and the current of this cation in the presence of CO<sub>2</sub> as illustrated in Figure 6.15. The addition of the currents measured under CO<sub>2</sub> alone and in the presence of pyridine under N<sub>2</sub> does not explain the current observed under the combined CO<sub>2</sub>-pyridine system. On the contrary, Figure 6.15 indicates that the waves arising in the two pyridinium containing electrolytes, under CO<sub>2</sub> and under N<sub>2</sub>, both proceed through the electrode Reaction 3 in Scheme 6.6; this was not explicitly considered in Savéant mechanism.

Comparing these conditions, when pyridinium is present, the concentration is ~250 times higher than the protons (Table 6.4). Hence, the pyridinium reduction (Reaction 3 in Scheme 6.6) dominates. While, in the case of CO<sub>2</sub> alone in the medium, the protons are the only electroactive species present and these reduce *via* Reaction 2 in Scheme 6.6. Considering the low protons concentration in this case (Table 6.4) the weak wave observed in CO<sub>2</sub> alone is expected.

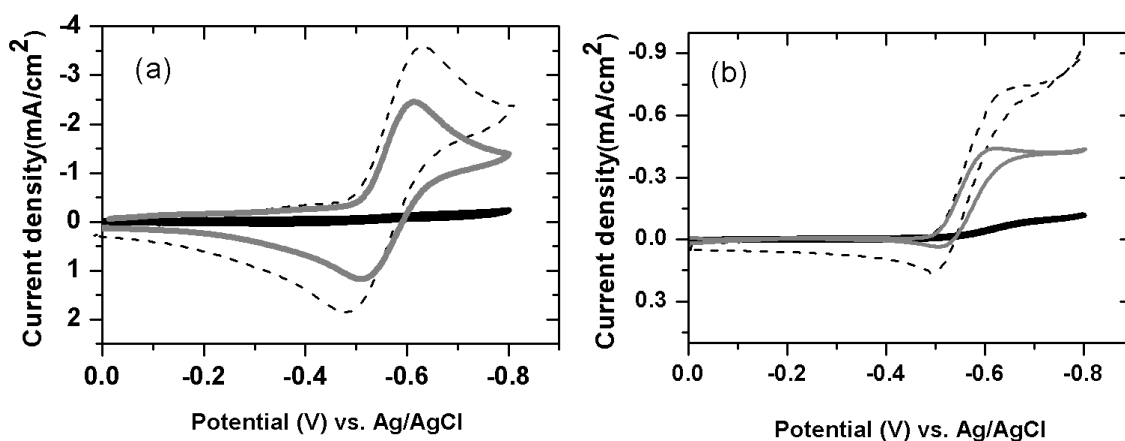


Figure 6.15 Cyclic voltammograms of: 10mM pyridine under CO<sub>2</sub> pH5.3 (dashed line), 10mM pyridine under N<sub>2</sub> adjusted using HCl to pH5.3 (grey), CO<sub>2</sub> in the absence of pyridine pH 4 (black) (a) 500mV/s, and (b) 5mV/s collected on Pt (0.07cm<sup>2</sup>).

Moreover, the wave resulting from CO<sub>2</sub> alone in Savéant's reported work casts some doubt on their proposed mechanism since the well-defined wave shape presented for these conditions in Costentin et al., 2013 is not expected. In this work, the voltametric features for CO<sub>2</sub> alone (in the absence of pyridine) does not show a well-distinguished wave (Figure 6.15). The redox wave presented by Costentin et al, 2013 is likely to be due to adsorbed pyridinium at micromole level which is similar to the CV wave obtained at ~10 $\mu$ M pyridine (Figure 6.16). In an electrolyte containing CO<sub>2</sub> alone, the CO<sub>2</sub> indirect contribution via Reactions 4 and 5 in Scheme 6.6 coupled to Reaction 2, explained earlier, is effectively not different from the proton reduction in a pyridinium-free medium seen in Figure 6.11b. The present observations confirm that the role of CO<sub>2</sub> in the presence of pyridinium consists of the cyclic protonation of pyridine (Reaction 1, Scheme 6.6) by the protons released from H<sub>2</sub>CO<sub>3</sub> dissociation (Reactions 4 and 5, Scheme 6.6).

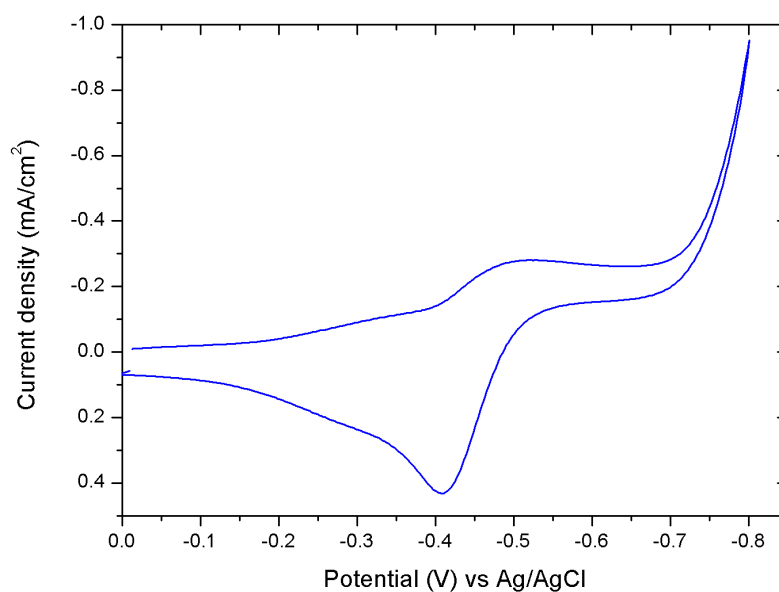


Figure 6.16 CV of  $\sim 10\mu\text{M}$  pyridine in  $0.5\text{M}$  KCl aqueous electrolyte in the presence of  $\text{CO}_2$  at  $55\text{bar}$  and  $10\text{mV/s}$

## 6.3.2 Effect of High Pressure $\text{CO}_2$ on Pyridinium Voltammetric Behaviour at Platinum

In an attempt to further elucidate the interaction of  $\text{CO}_2$  with  $\text{PyH}^+$  cation, which ultimately leads to understanding the voltammetric behaviour of such system, a large excess of  $\text{CO}_2$  (up to  $\sim 1.2\text{M}$ ) was introduced to the system using high pressure. For comparison, this is much greater than the maximum analytical pyridine concentration of  $200\text{mM}$ . This system is investigated both experimentally and using simulation of the CV curves.

### 6.3.2.1 $\text{CO}_2$ Pressure Dependence

Figure 6.17 shows CVs of  $10\text{mM}$  pyridine in aqueous electrolyte which were collected in  $\text{CO}_2$  saturated solutions at  $1\text{-}55\text{bar}$ . The  $\text{CO}_2$  concentration reaches  $\sim 1.2\text{M}$  at  $50\text{bar}$  and  $20^\circ\text{C}$  calculated in Chapter 5, Table 5.4. The cathodic peak current shows a steady increase with  $\text{CO}_2$  pressure, is in agreement with the current enhancement reported by Bocarsly group at elevated  $\text{CO}_2$  pressures up to  $6\text{bar}$  (Morris et al. 2011). If it is assumed that  $\text{CO}_2$  is directly involved in the electrode reaction as was proposed by Bocarsly group, the current is expected to increase proportionally with the  $\text{CO}_2$  amount

present in the electrolyte. In contrast to this assumption, the cathodic current increases only ~7-fold compared to more than ~35 times increase in CO<sub>2</sub> concentration at 55bar (~1.3M). The current then reaches saturation above ~50 bar (Figure 6.17, inset). It is important to note that at the above conditions the concentration of all species including [CO<sub>2</sub>], [PyH<sup>+</sup>] and [H<sup>+</sup>] are varying with CO<sub>2</sub> pressure as summarised in Table 6.5. This fact complicates the interpretation of the current enhancement. Moreover, the current enhancement shown in Figure 6.17 is significant only at slow scan rate and this represents a specific case in which current plateau (S-shape) is observed, so no analysis should be based upon data acquired at low scan rates solely (as was the case in the reference (Barton Cole et al. 2010)). Herein, the current increase (Figure 6.17) is investigated further by CVs simulations and Nicholson diagnostic technique at elevated pressure conditions.

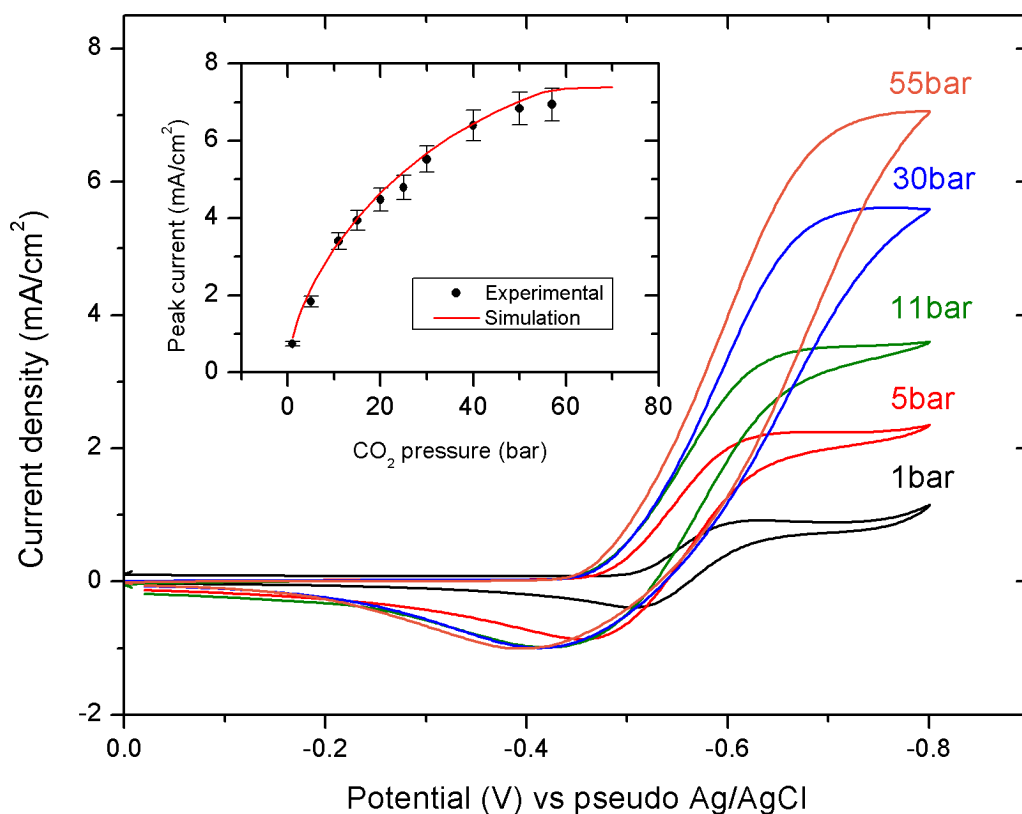


Figure 6.17 CV waves of 10mM pyridine in 0.5M KCl at 5mV/s at CO<sub>2</sub> saturated electrolyte (1-55 bar range). Inset: reduction peak/limiting current versus CO<sub>2</sub> pressure (for the same data series as shown on the main graph). Line-simulation, dots-cathodic peak current. Positive values represent the reduction in this case.

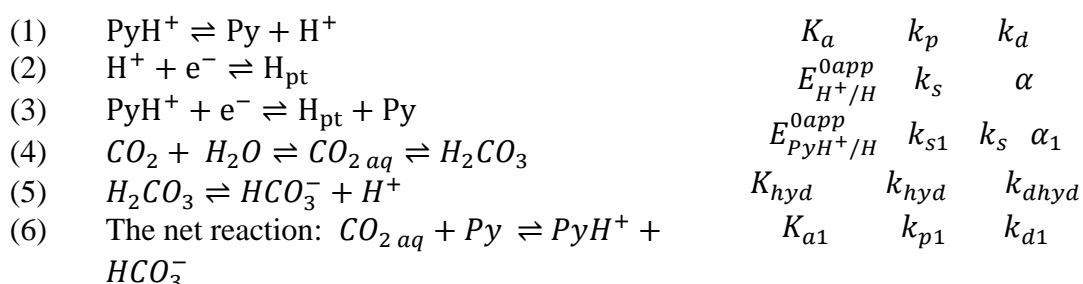
Table 6.5 Pyridinium and CO<sub>2</sub> concentrations in 10mM pyridine-containing aqueous solution at 20°C and varying pressure

Pressure (bar)	pH	[PyH <sup>+</sup> ] (mM)	[CO <sub>2</sub> ] (M)
1	5.50	4.7	0.0339
6	4.93	7.7	0.2016
10	4.75	8.3	0.3286
50	4.24	9.4	1.218

### 6.3.2.2 Numerical Simulation of CV curves for Pyridinium at Pt Cathode Under High CO<sub>2</sub> Pressure

The model suggested in Scheme 6.5 and discussed in Section 6.2 for an inert atmosphere (N<sub>2</sub> gas) explained well the behaviour of PyH<sup>+</sup> in acidic solutions and reproduced the CV data with good agreement. This is expected to hold upon the introduction of excess CO<sub>2</sub> into the system. Hence the same set of reactions used in the previous section is used for the present simulations (Scheme 6.7).

*Scheme 6.7 Model used in simulation of experimental CV data under CO<sub>2</sub>*



In this scheme, the presence of CO<sub>2</sub> is believed to simply represent a hydrated proton replenishment source for the reprotonation of pyridine as described in the previous Section (6.3.1). Hence, in this instance, CO<sub>2</sub> is effectively replacing the acid role in the inert gas case. The CO<sub>2</sub> effect, reflected in Reactions 4 and 5 in Scheme 6.7, can be either considered as a preceding chemical reaction (CE) to the hydrated protons reduction (Reaction 2), or a subsequent catalytic reprotonation of pyridine (EC') of the pyridinium electrode reaction (Reaction 3). These routes are constantly engaged and

both make a contribution to the system depending on the pyridine concentration and the acidity of the medium. In the catalytic EC' mechanism (Reaction 3, Scheme 6.7), the CO<sub>2</sub> hydration (Reaction 4) and H<sub>2</sub>CO<sub>3</sub> acid dissociation (Reaction 5) represent a proton source for the pyridine protonation (reverse of Reaction 1). These chemical Reactions 1, 4 and 5 are coupled to the pyridinium reduction Reaction (3), whereas, in the CE pathway, the CO<sub>2</sub> equilibrium Reactions (4 and 5, Scheme 6.7) are coupled to the proton reduction (2). CV data obtained at high CO<sub>2</sub> pressure was simulated according to the model in Scheme 6.7 and using simulation parameters obtained by fitting of the CV data under N<sub>2</sub>, summarised in Table 6.4.

Table 6.6 Simulation parameter ( $E^{0\text{ app}}_{\text{H}^+/\text{H}}$ ,  $k_s=0.3$ ,  $\alpha=0.5$ ) for CV data at 55 bar of CO<sub>2</sub> and different analytical concentrations of pyridine.

<b>Py (mM)</b>	<b>10</b>	<b>50</b>	<b>100</b>	<b>200</b>
<b><math>E^{0\text{ app}}_{\text{H}^+/\text{H}}</math> (V)</b>	-0.790	-0.775	-0.715	-0.715
<b>H<sup>+</sup> (μM)</b>	40.00	9.70	5.65	3.46

A noteworthy exception to the the inert atmosphere parameters set is that the apparent standard redox potential of protons (Reaction 2, Scheme 6.7),  $E^{0\text{ app}}_{\text{H}^+/\text{H}}$ , required consistent/deliberate adjustment for reproduction of the experimental CV wave positions. A possible reason for the redox potential adjustment could be the variation of the acidity of the medium (Table 6.6). The simulated cathodic peak current is compared to the experimental values with varying total pyridine concentration at 55 bar CO<sub>2</sub> in Figure 6.18. The deviation of the cathodic peak current values for the simulated and experimental data for 10-200mM pyridine concentration range (Figure 6.18a) is not more than ~15%; this is comparable to the ~10% reproducibility of the experimental data obtained.

However, on the lower region of the pyridine concentrations investigated ( $\leq 1\text{mM}$ ) (Figure 6.18b) the simulation model consistently overestimated the current by about a factor of 2. In this region, the proton reduction (Reaction 2, Scheme 6.7) dominates. The deviation of the current which is more prominent at high scan rates ( $>1000\text{mV/s}$ ) and low pyridine ( $\leq 1\text{mM}$ ) concentrations can be rationalised in terms of an incomplete CO<sub>2</sub> saturation at such low pyridine concentrations (the aqueous electrolytes were purged with CO<sub>2</sub> for ~1h for all pyridine concentrations used, the time was determined from pre-experimental study presented in Appendix D, Figure D16). In the presence of high pyridine concentrations CO<sub>2</sub> dissolves more rapidly as the former plays the role of a

base, stimulating the protons abstraction from  $\text{CO}_2$ . On the other hand, at low pyridine concentrations a lack of the protons consumption effect is reflected in much slower  $\text{CO}_2$  dissolution than in the former case.

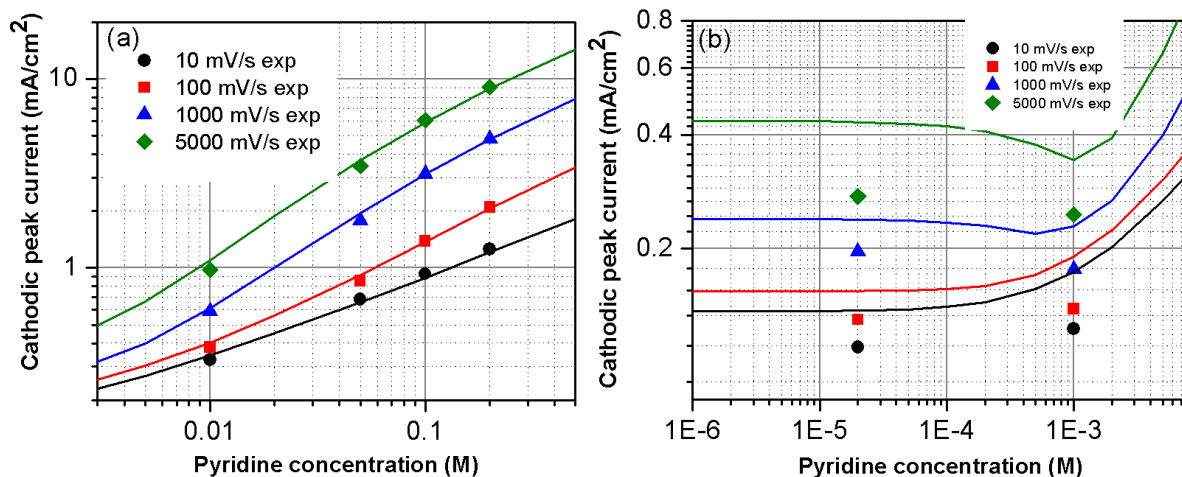


Figure 6.18 Cathodic peak current as function of pyridine total concentration for CVs at 55 bar  $\text{CO}_2$ . Dots - experiment, lines - simulation

An alternative explanation is that the diminished current is observed when the pre-peak features (Figure 6.19) appear on the experimental waves at  $-0.32 \pm 0.02\text{V}$ . The pre-wave, which reflects adsorbed product co-existing with the diffusion limiting pyridinium peak, is proportional to the scan rate (Figure 6.19, inset). The prefeatures are stronger at high scan rates  $>1000\text{mV/s}$ , which interfere with usual pyridinium CV wave and could affect the current (cause the diminished current observed). Indeed, at  $5000\text{mV/s}$  the pre-waves start exceeding the amplitude of the original wave. This confirms the adsorption prefeatures behaviour reported in the literature (Yan et al. 2013). The adsorption prefeatures were not included in the simulation model as explained in the CV simulations in the inert atmosphere Section 6.2.1.2. Considering that the pre-peak waves were assigned to hydrogen adsorption and that this effect occurs at concentration range where surface effects prevail (Yan et al. 2013), this process is expected to affect the observed cathodic current in the low pyridine region, resulting in the diminished current observed experimentally.

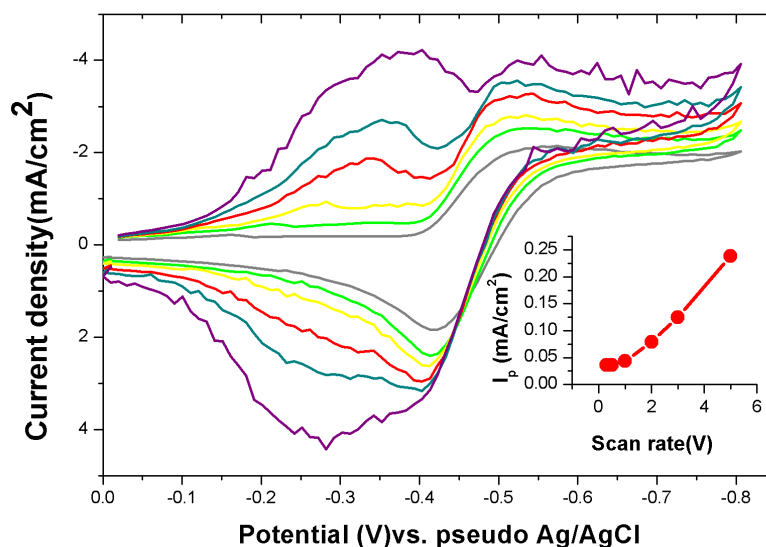


Figure 6.19 CVs of  $\sim 10\mu\text{M}$  pyridine at 55bar of  $\text{CO}_2$  on  $\text{Pt } 0.07\text{cm}^2$  at 300-5000mV/s scan rates. Pre-peaks preceding the usual CV wave are observed at  $-0.32\pm 0.02\text{V}$

Illustrated in Figure 6.20 are experimental and simulated cyclic voltammograms of pyridine at 10 and 100mM pyridine (other concentrations are presented in the Appendix D, Figure D7-10) at 55 bar of  $\text{CO}_2$  and 10,100, and 1000mV/s scan rates. The model in Scheme 6.7 reproduced well the experimental CV data within  $\sim <15\%$  as described above.

### 6.3.2.3 Nicholson Diagnostics Applied to High $\text{CO}_2$ Pressure CV Data

The CV waves under elevated  $\text{CO}_2$  pressure display characteristic features of coupled catalytic chemical reaction (EC'). The catalytic EC' mechanism can be further illustrated using Nicholson diagnostic criteria. The criteria can be applied in this instance as the forward part of the summary Reaction 6 in Scheme 6.7 can be considered as pseudo-1<sup>st</sup> order. This approximation is valid at  $>50\text{bar}$  experiments where the presence of  $\text{CO}_2$  is in large excess in respect to pyridine concentration and hence can be considered constant. This can be further observed in Scheme 6.7, where the equilibrium of carbonic acid dissociation (Reaction 5) reaction is much faster than the hydration step (Reaction 4); the carbonic acid released from this reaction is consumed at a faster rate than its decomposition to regenerate  $\text{CO}_2$ . Thus, at high  $\text{CO}_2$

pressure, Reaction (6) can be treated as a pseudo-1<sup>st</sup> order irreversible coupled reaction and Nicholson criteria can be applied qualitatively.

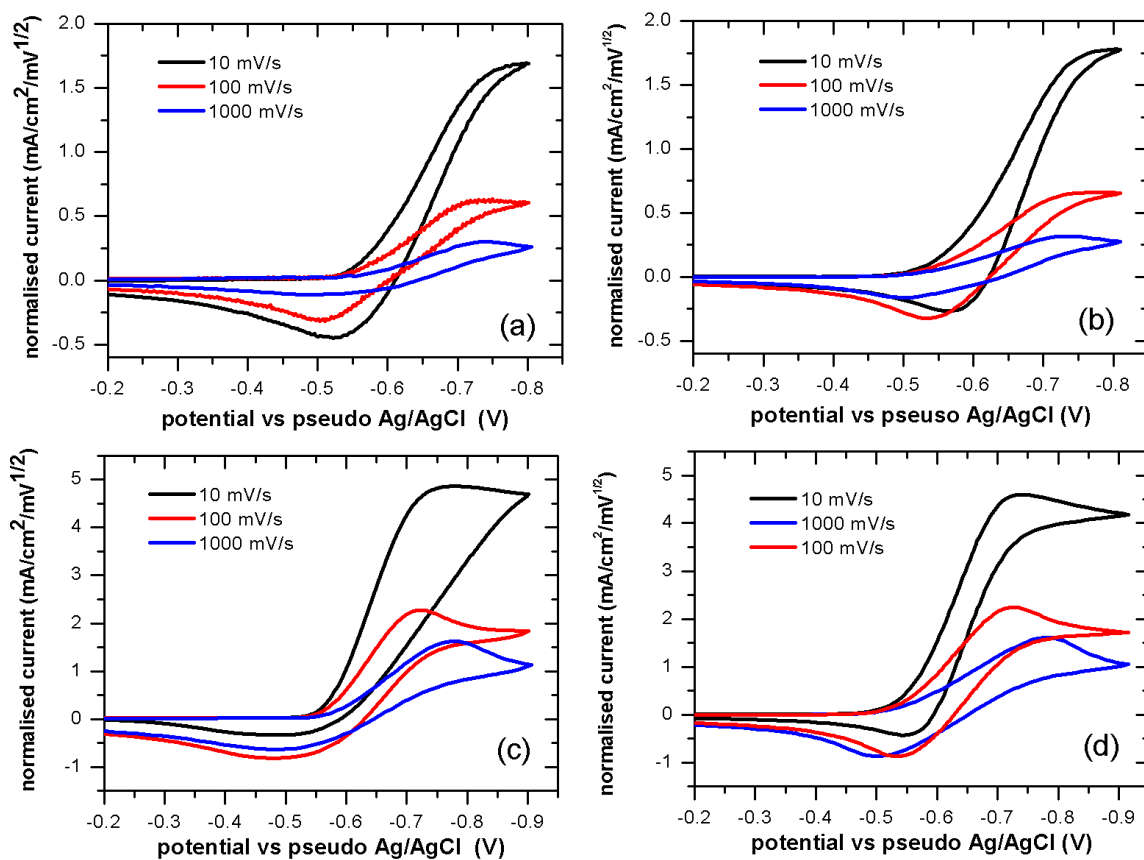


Figure 6.20 Normalised cyclic voltammograms by the square root of the scan rate on Pt 0.07cm<sup>2</sup> at 55 bar CO<sub>2</sub> of (a and b) 10mM pyridine, (c and d) 100mM pyridine at 1000mV/s (blue), 100mV/s (red), and 10mV/s (black). Left images - experiment, right - simulation. Positive values of the current represent reduction in this case.

The CVs of 10mM pyridine under 55 bar CO<sub>2</sub> are normalised (Figure 6.20) to the square root of the scan rate, the current is represented as  $I_p^C/\nu^{1/2}$ . This ratio gives a time independent current value, free from the obscuring effects of the diffusion time of the reactant to the electrode surface, as described by the Nicholson-Shain diagnostic technique (refer to Chapter 2, Section 2.8.1.2). The CVs display features characteristic for the coupled catalytic chemical reaction (EC'). That is if no coupled chemical reaction was detected the cathodic current would be independent of the scan rate and as a result the CVs at different scan rates would merge.

The Reactions 4, 5 in the catalytic EC' mechanism (Scheme 6.7), represent a reprotonation source for pyridine via the reverse of Reaction (1). These Reactions (1, 4 and 5) are coupled to the pyridinium reduction (electrode Reaction 3) which is affected

by the rate limiting step (hydration Reaction 4). This effect is observed as a steady state current, which is significant at slow scan rates ( $<10\text{mV/s}$ ) resulting in the S-shape of CV waves (Figure 6.17 and at  $10\text{mV/s}$  in Figure 6.20). This significant current increase observed at  $5\text{mV/s}$  demonstrates that the current is kinetic dominated. In this case, the current becomes independent of the scan rate approaching a limiting value (Figure 6.18a). The cathodic current plateau effect is more pronounced at lower pyridine concentrations, indicating an efficient reprotonation for a given  $\text{CO}_2$  concentration as observed for  $\sim 10\mu\text{M}$  pyridine (Figure 6.19, slow scan rates).

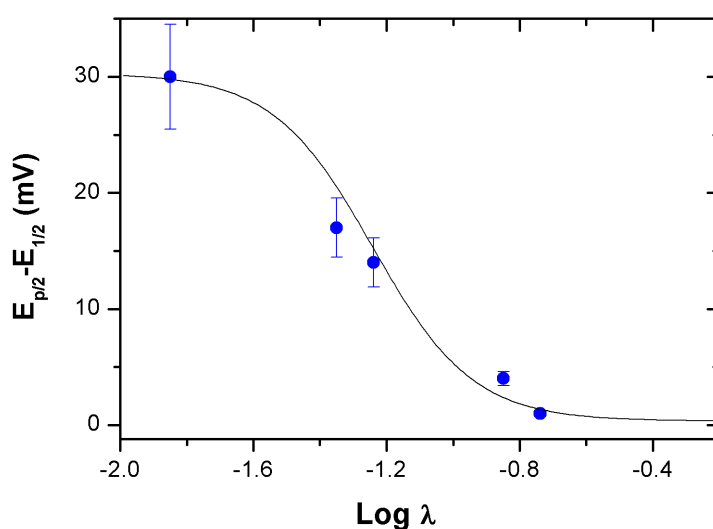


Figure 6.21 Nicholson and Shain criteria for  $EC'$  mechanism. The variation of the half peak potential with  $\log \lambda$ .  $\lambda = k_f/a$ , with  $a = nFv/RT$ . line-Nicholson characteristic curve for  $EC'$ , symbols-this work data. ( $k_f$  is the forward rate)

Figure 6.21 depicts the diagnostic criteria for the mechanism of the system under study. The variation of the peak potential as a function of the logarithm of  $\lambda = k_f/a$ , with  $a = nFv/RT$  (Figure 6.21). At high scan rates, where the coupled chemical reaction is not detectable, the half peak potential is close to  $30\text{mV}$  typical for a reversible system. However, at low scan rates the half peak potential becomes independent of the scan rate indicating a kinetically controlled system. This characteristic feature further confirms the  $EC'$  mechanism as described by Nicholson-Shain (Nicholson & Shain 1964) and Bard (Bard & Faulkner 2002)

## 6.4 Summary

The analysis of the CVs data under  $N_2$  in acid-adjusted electrolytes at Pt electrode revealed a single electron transfer at half wave potential of  $-0.56 \pm 0.01V$ , simulated as a CEPT transfer (Reaction 2 and 3, Scheme 6.5). The current was confirmed to be diffusion controlled and hence dependent on the  $PyH^+$  concentration and the pH of the medium. The pyridinium reduction process displays three pH-dependent distinctive features: (1)  $pH > 7$ , (2)  $3 < pH < 5.5$  and (3)  $pH < 3$ . At  $pH \sim 7$ , a pyridinium-related weak cathodic wave emerges which is not observable at more basic pH. However, at  $3 < pH < 5.5$  the pyridinium related CV wave is observed at  $-0.56 \pm 0.01V$  (Reaction 3, Scheme 6.5). As the proton concentration is increased beyond 1mM ( $pH < 3$ ), two waves are observed: the original at  $-0.56 \pm 0.01V$  and a new wave at  $-0.43 \pm 0.01V$ . The first wave reflects the proton reduction, while the second wave represents the pyridinium reduction. These reactions are coupled to the  $PyH^+$  deprotonation reaction, leading to the molecular hydrogen formation.

Upon the introduction of  $CO_2$  into the system, a current enhancement is observed as compared to the inert atmosphere. The current increase observed in the  $CO_2$  saturated medium was shown to be merely the reprotonation of pyridine (Reaction 1, Scheme 6.6) by the protons released from  $CO_2$  hydration and  $H_2CO_3$  dissociation (Reactions 4 and 5, Scheme 6.6). The  $CO_2$  hydration step is the limiting chemical reaction coupled to the electrode reaction. The reprotonation was found to be more efficient at elevated pressure where an excess  $CO_2$  is present. Since, the system under high  $CO_2$  pressure displays features characteristic of the catalytic coupled chemical reaction EC'. The  $CO_2$  effect is reflected in the Reactions (4) and (5) in Scheme 6.7 which are either considered as preceding chemical reaction (CE) to the hydrated protons reduction (2), or a subsequent catalytic reprotonation of pyridine (EC') of the pyridinium electrode Reaction (3). The EC' route dominates for the analytical pyridine concentrations ( $> 1mM$ ), while CE route is dominant at low concentrations ( $< 1mM$ ). The EC' catalytic mechanism proposed herein based on the experimental observations, numerical CV simulations and Nicholson diagnostic criteria was confirmed at 55bar of  $CO_2$  and different pyridine concentrations.

Analysis of all results revealed that CO<sub>2</sub>-pyridine system is merely pyridinium assisted molecular hydrogen formation under all the conditions investigated. There is no observable direct contribution of CO<sub>2</sub> in the reduction process. This outcome is in-line with the Savéant group's work. Bocarsly group's original mechanism (Figure 6.1) supporting CO<sub>2</sub> involvement in the charge transfer observed in CV curves was ruled out. In addition, the subsequently proposed route of the contribution to the current from both direct CO<sub>2</sub> reduction and HER was purely based on the product Faradaic yields rather than the voltammetric analysis in the presence of CO<sub>2</sub>. Moreover, no evidence has been found in this work for direct reduction of CO<sub>2</sub> from the CV analysis.

## References of Chapter 6

- Bard, A. & Faulkner, L., 2002. Allen J. Bard and Larry R. Faulkner, *Electrochemical Methods: Fundamentals and Applications*, New York: Wiley, 2001. *Russian Journal of Electrochemistry*.
- Barton Cole, E. et al., 2010. Using a one-electron shuttle for the multielectron reduction of CO<sub>2</sub> to methanol: Kinetic, mechanistic, and structural insights. *Journal of the American Chemical Society*, 132(33), pp.11539–11551.
- Barton Cole, E.E. et al., 2014a. Substituent Effects in the Pyridinium Catalyzed Reduction of CO<sub>2</sub> to Methanol: Further Mechanistic Insights. *Topics in Catalysis*, 58(1), pp.15–22.
- Barton, E.E., Rampulla, D.M. & Bocarsly, A.B., 2008. Selective solar-driven reduction of CO<sub>2</sub> to methanol using a catalyzed p-GaP based photoelectrochemical cell. *Journal of the American Chemical Society*, 130(20), pp.6342–6344.
- Bocarsly, A.B. et al., 2012. Comparative study of imidazole and pyridine catalyzed reduction of carbon dioxide at illuminated iron pyrite electrodes. *ACS Catalysis*, 2(8), pp.1684–1692.
- Boston, D.J. et al., 2013. Photochemical reduction of carbon dioxide to methanol and formate in a homogeneous system with pyridinium catalysts. *Journal of the American Chemical Society*, 135(44), pp.16252–5.
- Cole, E.B. et al., 2010. Using a one-electron shuttle for the multielectron reduction of CO<sub>2</sub> to methanol: kinetic, mechanistic, and structural insights. *Journal of the American Chemical Society*, 132(33), pp.11539–51.
- Costentin, C. et al., 2013. Electrochemistry of acids on platinum. Application to the reduction of carbon dioxide in the presence of pyridinium ion in water. *Journal of the American Chemical Society*, 135(47), pp.17671–4.
- Ertem, M.Z. et al., 2013. Functional Role of Pyridinium during Aqueous Electrochemical Reduction of CO<sub>2</sub> on Pt(111). *The Journal of Physical Chemistry Letters*, 4(5), pp.745–748.
- Keith, J. a & Carter, E. a, 2013. Electrochemical reactivities of pyridinium in solution: consequences for CO<sub>2</sub> reduction mechanisms. *Chemical Science*, 4(4), pp.1490–1496.
- Keith, J. a & Carter, E. a, 2012. Theoretical insights into pyridinium-based photoelectrocatalytic reduction of CO<sub>2</sub>. *Journal of the American Chemical Society*, 134(18), pp.7580–3.
- Lebègue, E. et al., 2014. The Role of Surface Hydrogen Atoms in the Electrochemical Reduction of Pyridine and CO<sub>2</sub> in Aqueous Electrolyte. *ChemElectroChem*, 1(6), pp.1013–1017.

- Liao, K. et al., 2015. Electrochemical Reduction of Aqueous Imidazolium on Pt(111) by Proton Coupled Electron Transfer. *Topics in Catalysis*, 58(1), pp.23–29.
- Lucio, A.J. & Shaw, S.K., 2015. Pyridine and Pyridinium Electrochemistry on Polycrystalline Gold Electrodes and Implications for CO<sub>2</sub> Reduction. *The Journal of Physical Chemistry C*, 119(22), pp.12523–12530.
- Mairanovskii, S.G., 1963. The theory of catalytic hydrogen waves in organic polarography. *Journal of Electroanalytical Chemistry (1959)*, 6(2), pp.77–118.
- Morris, A.J., McGibbon, R.T. & Bocarsly, A.B., 2011. Electrocatalytic carbon dioxide activation: The rate-determining step of pyridinium-catalyzed CO<sub>2</sub> reduction. *ChemSusChem*, 4(2), pp.191–196.
- Nicholson, R.S. & Shain, I., 1964. Theory of Stationary Electrode Polarography. *Analytical chemistry*, 36(4), pp.706–723.
- Pletcher, D. & Sotiropoulos, S., 1994. Hydrogen adsorption?desorption and oxide formation?reduction on polycrystalline platinum in unbuffered aqueous solutions. *Journal of the Chemical Society, Faraday Transactions*, 90(24), p.3663.
- Polievktov, M. K; Mairanovskii, S.G., 1965. Influence Of The Concentration And Nature Of The Cation Of Indifferent Electrolytes On The Polarographic Catalytic Waves Of Hydrogen Induced By Pyridine In Unbuffered Solutions. *Journal of the Academy of Sciences*, pp.400–405.
- Portenkirchner, E. et al., 2014. A Comparison of Pyridazine and Pyridine as Electrocatalysts for the Reduction of Carbon Dioxide to Methanol. *ChemElectroChem*, 1(9), pp.1543–1548.
- Priyantha, N. & Malavipathirana, S., 1996. Effect of chloride ions on the electrochemical behavior of platinum surfaces. *Journal of the National Science Council of Sri Lanka*, 24(3), pp.237–246.
- Seshadri, G., Lin, C. & Bocarsly, A.B., 1994. A new homogeneous electrocatalyst for the reduction of carbon dioxide to methanol at low overpotential. *Journal of Electroanalytical Chemistry*, 372(1-2), pp.145–150.
- De Tacconi, N.R. et al., 2012. Electrocatalytic Reduction of Carbon Dioxide Using Pt/C-TiO<sub>2</sub> Nanocomposite Cathode. *Electrochemical and Solid-State Letters*, 15(1), p.B5.
- Yan, Y., Zeitler, E.L., et al., 2013. Electrochemistry of aqueous pyridinium: Exploration of a key aspect of electrocatalytic reduction of CO<sub>2</sub> to methanol. *Journal of the American Chemical Society*, 135(38), pp.14020–14023.
- Yan, Y., Gu, J. & Bocarsly, A.B., 2014. Hydrogen bonded pyridine dimer: A possible intermediate in the electrocatalytic reduction of carbon dioxide to methanol. *Aerosol and Air Quality Research*, 14(2), pp.515–521.

Zeng, G. et al., 2014. CO<sub>2</sub> Reduction to Methanol on TiO<sub>2</sub>-Passivated GaP Photocatalysts. *ACS Catalysis*, 4(10), pp.3512–3516.

Zhan, D., Velmurugan, J. & Mirkin, M. V, 2009. Adsorption/desorption of hydrogen on Pt nanoelectrodes: evidence of surface diffusion and spillover. *Journal of the American Chemical Society*, 131(41), pp.14756–60.

# Chapter 7 Pyridinium Assisted CO<sub>2</sub> Reduction on Pt Electrode at 1bar and 55 bar

## 7.1 Introduction

In the last few decades, the electrochemical reaction pathways of pyridine and its derivatives have been extensively studied by polarography in aqueous electrolytes (Mairanovskii 1963) and by voltammetry in aprotic solvents on Pt (Yasukouchi et al. 1979). It is well agreed that protonated pyridine (C<sub>5</sub>H<sub>5</sub>N) ‘pyridinium’ has an excellent catalytic activity toward the hydrogen evolution reaction (HER) (Mairanovskii 1963) (Yasukouchi et al. 1979). More recently, the pyridinium cation was reported to have an additional catalytic activity in conjunction with metal surfaces (Seshadri et al. 1994) and semiconductors (Barton et al. 2008) towards methanol formation by electrochemical reduction of CO<sub>2</sub>. Near 100% methanol Faradaic yields (FY) were achieved on p-GaP by CO<sub>2</sub>-pyridinium reduction in aqueous electrolytes; and ~30% Faradaic yield of methanol was reported on hydrogenated Pd (Seshadri et al. 1994). However, these reports did not provide enough information on the evolution of the alcohol yield with the supplied charge and hence it still remains unclear whether these FY are constant over time.

More recently, this system was investigated at other material electrodes (Boston et al. 2013)(Lucio & Shaw 2015) (Zeng et al. 2014) (de Tacconi et al. 2012) (Contentin et al. 2013). Some of these studies confirmed the production of methanol (Boston et al. 2013)(de Tacconi et al. 2012)(Zeng et al. 2014), while others could not detect the alcohol or any other carbon based product (Contentin et al. 2013)(Lucio & Shaw 2015). Thus, the aim of investigating the controversial methanol formation in such system, CO<sub>2</sub> reduction assisted by pyridinium was studied in aqueous electrolytes at Pt electrodes. The potentiostatic and galvanostatic electrolyses of the CO<sub>2</sub>-pyridine reduction process results are reported in the first part of this Chapter for atmospheric CO<sub>2</sub> pressure (1bar) electrolysis. The concentration of dissolved gaseous CO<sub>2</sub> is limited

to ~30mM at 25°C in aqueous solutions at 1bar, this restricts the CO<sub>2</sub> availability at the electrode. Therefore, in the second part of the present study the concentration of the reactant, CO<sub>2</sub>, was increased by increasing its pressure (up to 55bar at 25°C). The abundance of this reactant near the electrode surface is expected to assist in increasing the CO<sub>2</sub> transport rate (Hori 2008). This ideally shifts the CO<sub>2</sub> reduction towards the product formation; hence it should enhance methanol Faradaic yields if the alcohol formation pathway is confirmed (Sreekanth & Phani 2014).

All measurements were performed with 10mM pyridine (C<sub>5</sub>H<sub>5</sub>N) (>99.99%) in aqueous (18.2 MΩ cm) KCl (0.5M, >99.99%) electrolyte of 1.5-30ml in the presence of CO<sub>2</sub> (>99.96%) unless otherwise stated. For the electrolysis experiments at 1 bar, CO<sub>2</sub> was supplied to the reaction vessel for 30minutes (by bubbling) then introduced to the headspace (blanketing) for pH buffering purposes. For elevated pressure experiments, the CO<sub>2</sub> pressure was gradually increased to the desired value. The bulk electrolyses were conducted in a batch manner. When the desired charge has been passed, the high pressure vessel was gradually depressurised and the content was analysed by gas chromatography mass spectrometry (GCMS) as described in Chapter 4. In all experiments Pt wires electrode (2.6cm<sup>2</sup>, 3cm<sup>2</sup> or 3.8cm<sup>2</sup>, 99.9%) or Pt foil (7cm<sup>2</sup>, 99.9%) were used as a working electrode/cathode (WE) and Pt mesh (~20cm<sup>2</sup>, 99.9%) was used as a counter electrode/anode (CE). The bulk electrolysis at high pressure CO<sub>2</sub> (mostly 55bar, 25°C) were referenced against a pseudo Ag/AgCl reference electrode (RE), while the bulk electrolysis at 1bar CO<sub>2</sub> and 25°C were referenced against Metrohm® Ag/AgCl reference electrode. The pseudo Ag/AgCl reference electrode used in the high pressure experiments was isolated in a Luggin capillary equipped with the ceramic frit as detailed in the experimental techniques and methods (Chapter 4, Figure 4.2). All other electrodes specifications and details are described in Chapter 4. The electrolyses products were analysed as described in the Chapter 4 and the Faradaic efficiencies calculations are detailed in Appendix A2.

This Chapter is not concerned with the photoelectrochemical reduction of CO<sub>2</sub> on semiconductors due to the complication of the combination of the photophysical and photochemical processes on semiconductors and to the instability of these interfaces in aqueous media (Barton et al. 2008). Instead, the voltammetric curve experiments and the electrolysis measurements at metal electrodes (e.g. Pt) provide more convenient and

simpler approach for the investigation of such system; which allows for any insights gained to be exported to semiconductor materials later.

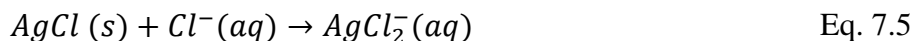
## 7.2 Optimization of the Experimental Conditions

Bulk electrolysis product yields are known to be affected by foreign ionic species in the electrolyte (Hori 2008). These ions interfere with the surface process in the electrochemical reactions on electrodes. The effect of impurities such as metal ions is observed as a decay of the electrolysis current (in controlled potential measurements) (Augustynski et al. 1996). Therefore, it is necessary: (1) to use a pure electrolyte/catalyst, (2) to perform electrolyte purification (pre-electrolysis), and (3) ensure a good isolation of the CE from the cathode electrolyte (catholyte) to minimise the interference of the CE products with the bulk electrolysis products of interest. The RE should also be well isolated from the compartments of the other two electrodes (in the case of the pseudo reference electrode). The effect of (1) the catalyst purity, (2) electrolyte purification (pre-electrolysis) and (3) CE and RE electrodes isolation on the electrolysis current are investigated in the following sections.

### 7.2.1 Effect of RE and CE Electrodes Isolation

It is critical to ensure proper isolation of both the CE and the RE electrodes as the diffusion of ions from either compartment might otherwise lead to the contamination of the catholyte and interference with the reduction products (L.D.Burke 1994). The effect of isolating both electrodes was investigated. First, the pseudo Ag/AgCl reference electrode was isolated in a glass tube ending in a medium-porosity frit. Typical potentiostatic measurements (-0.7V) (described in the introduction of the Chapter) were conducted over ~1h, cyclic voltammogram (CV) were recorded before and after electrolysis (Figure 7.1). The use of a medium-porosity glass frit resulted in ionic silver chloride contamination as shown in the subsequent CV (Figure 7.1). The silver chloride ions ( $AgCl_2^-$ ) form in the KCl medium according to Eq. 7.5 (Sawyer & Roberts 1994). The dissolved silver chloride ( $AgCl_2^-$ ) diffused through the frit to the catholyte (within ~1h) as evidenced by the appearance of extra reduction and oxidation waves (Eq.7.6

(Haynes & Sawyer 1967) at -0.096V and +0.15V respectively, Figure 7.1 detailed view).



In this case a liquid-junction potential resulted causing the mobility of ( $\text{AgCl}_2^-$ ) (Sawyer & Roberts 1994).

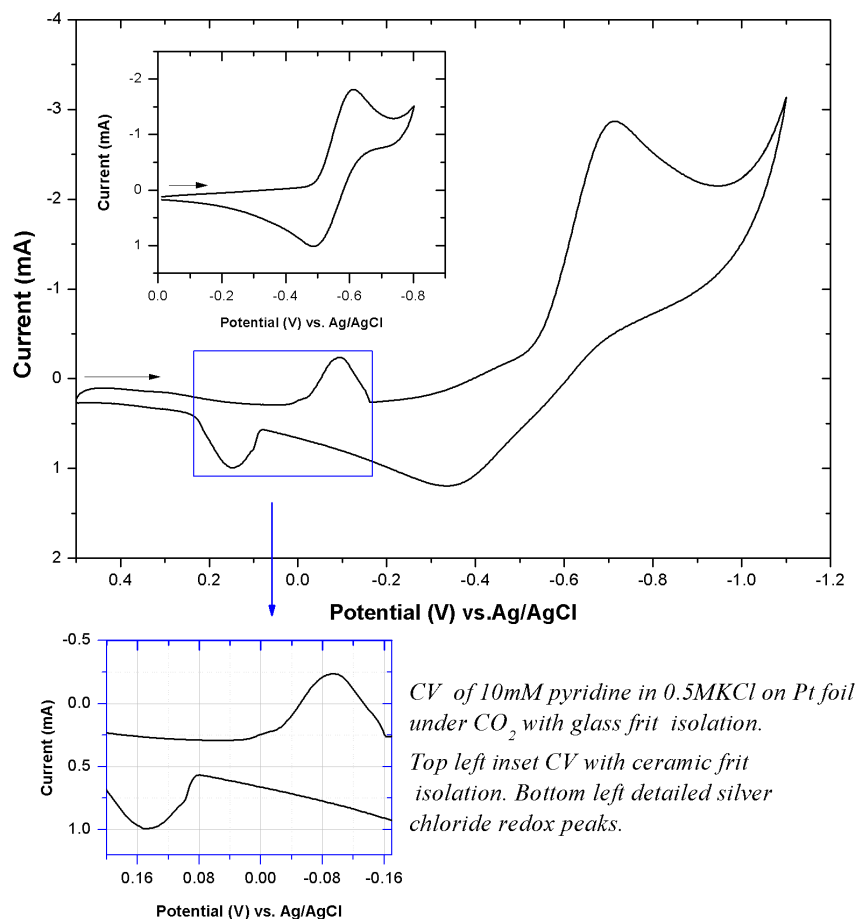


Figure 7.1 Cyclic voltammogram of 10mM pyridine in 0.5M KCl with a glass frit isolation on WE: Pt foil (7cm<sup>2</sup>).

The internal solution of Ag/AgCl reference compartment gradually leaks into the catholyte and eventually to the WE, which results in silver deposition on the surface of the electrode (Eq.7.6). These ions interfered with the usual pyridinium related wave resulting in a 4-fold increase in the peak separation and 1.5-fold increase of the reductive current (Figure 7.1).



Thus, a finer (ceramic) frit was used instead for isolation of the reference electrode compartment (as described in the introduction to this Chapter). The resulting CV is shown in Figure 7.1, inset.

## 7.2.1.1 CE Electrode Isolation

The isolation of the CE is also critical in bulk electrolysis measurements. A non-isolated CE causes the oxidation of the products of interest at the WE and/or interferences of the oxidized species produced at the CE with the reaction of interest. The interference effect manifests itself in the form of adsorption of the species (e.g. oxygen forming oxide films) which can alter the electrochemical behaviour (Bard & Faulkner 2002). An adsorbed film may partially block or inhibit the electrode reaction by a complete blockage of its surface usually observed as electrolysis current decay (de Valera 1953).

### 7.2.1.1.1. Reactions at the CE

Oxygen generation reaction takes place at the anode (Eq. 7.7):



Chlorine also forms at the anode by the oxidation of the aqueous chloride ions ( $Cl_{(aq)}^-$ ) (of the supporting KCl salt) as described by the half reaction (Eq.7.8). The chlorine formation leads to a series of reactions:



Subsequently, the dissolved chlorine reacts with water to form hydrochloric acid and hypochlorous acid as described by Eq.7.9



The hypochlorous acid may also interact with potassium to generate potassium hypochlorite (KClO). Oxygen and chlorine accumulations (Eq.7.7 and Eq.7.8) become significant at high-current density and /or prolonged electrolysis. The oxidation of products accumulation results in the diffusion of oxidized species to the cathode.

To investigate the effect of the CE isolation on the current drop, typical potentiostatic electrolyses were performed at -0.5V for ~3h at atmospheric pressure (1bar of CO<sub>2</sub>) (Only the first 2000s are shown, Figure 7.2). To ensure that the current behaviour is due to the effect of CE isolation and not to the other controllable factors investigated in the

next sections, the highest catalyst purity (>99.9%) was used and an electrolyte purification (with pre-electrolysis) was performed before the present electrolytic investigation. (1) no isolation was made for CE, where it was directly immersed in the catholyte. (2) the CE isolation was made by: the insertion of the CE electrode in a glass tube equipped with a glass frit (Refer to Chapter 4) (3) the introduction of the CE electrode in two different compartments linked with a 7cm-long salt bridge (3M KCl).

Figure 7.2 shows the potentiostatic current drop over time for: (1) no isolated CE, (2) glass tube equipped with a frit isolated CE and (3) salt bridge isolated CE. The current decay was the least severe when the frit was used for the isolation with halving of the starting current ( $\sim 7\text{mA}$ ) over 2000s. More than three-fold decrease in the current was observed by about 500s when the CE was not isolated, with the current saturating at  $\sim 1\text{mA}$ . On the other hand, the salt bridge isolation resulted in slower drop of the current up to 800s, but finally also reaching 1mA by 2000s. Thus, the bulk electrolyses were performed with a glass frit isolated CE.

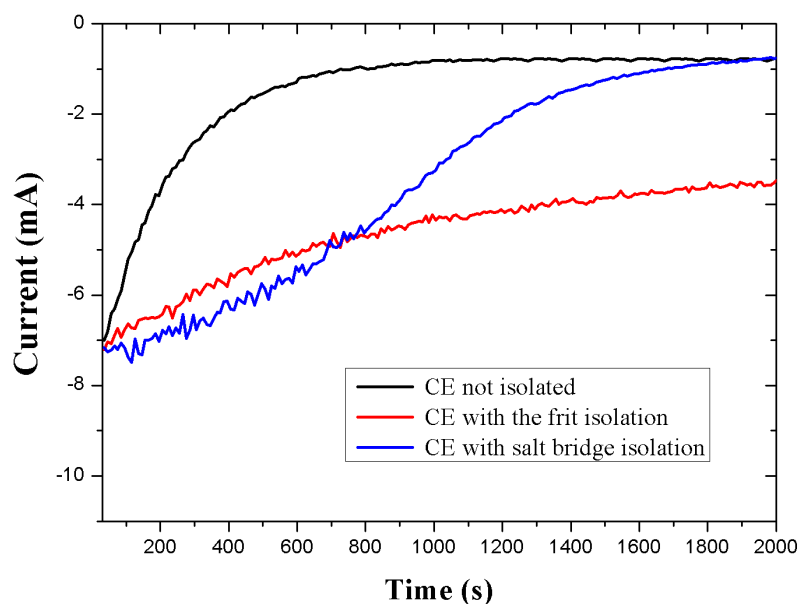


Figure 7.2 Effect of the counter electrode isolation on the electrolysis ( $-0.5\text{V}$ ) current. Electrolyte:  $10\text{mM}$  pyridine in  $0.5\text{M}$  KCl. Conditions: in the presence of  $\text{CO}_2$  ( $1\text{bar}$ ,  $25^\circ\text{C}$ ). WE: Pt foil,  $7\text{cm}^2$

## 7.2.2 Effect of Pyridine Purity on the Electrolysis

Another factor which affects the cathodic current in the electrolysis process is the purity of the substances present in the solution. Pyridine ( $C_5H_5N$ ) is used as the catalyst in the present bulk electrolysis. Therefore, potentiostatic electrolyses at  $-0.7V$  over 2000s were conducted with the glass frit isolation and with pre-electrolysed electrolytes before the addition of pyridine of different purities: (a) Sigma Aldrich, 99.9%, (b) Fisher, 99.5% distilled and (c) Sigma Aldrich, 99.99% as illustrated in Figure 7.3.

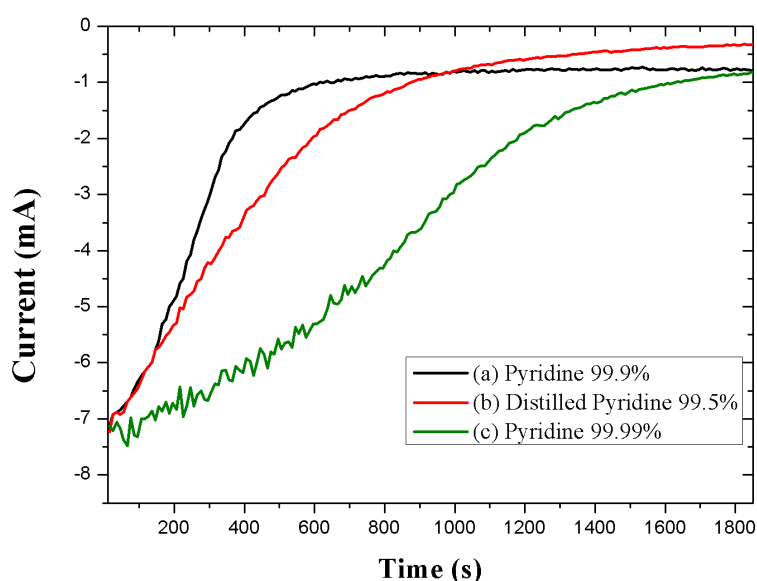


Figure 7.3 Effect of electrolyte purity on electrolysis current ( $-0.7V$ ). Electrolyte:  $10mM$  pyridine in  $0.5M$  KCl. Conditions: in the presence of  $CO_2$  (1bar,  $25^\circ C$ ). WE: on Pt foil,  $7cm^2$

In the electrolysis conducted with pyridine ( $C_5H_5N$ ) of purity (a, Figure 7.3a), the current decreases rapidly by  $\sim 86\%$  of the starting current within 600s. The current then drops further and plateaus at  $\sim 0.8mA$ . Using the catalyst of purity (b) the current decreases by  $\sim 86\%$  the starting current within 900s then drops further to  $\sim 0.5mA$ . However, the use of compound (c) results in a gradual decrease of the current (by  $\sim 86\%$  over 1700s) compared to the previous two experiments and reaches residual current value ( $\sim 0.8mA$ ). The use of the compounds of purities (a) and (b) resulted in faster and/or deeper current decay. These compounds contain (according to the manufacturer specification) higher metal ion traces (e.g. Fe, Zn and Cu) than the substance of purity (c). The presence of such impurities may have contributed to the current drop. Similar

observations of impurities in CO<sub>2</sub> reduction were reported on copper and silver electrodes (Augustynski et al. 1996), where the significant drop of the current was attributed to the presence of metal impurities in the electrolyte (Hori et al. 2005). Heavy metals such as iron (Fe) and zinc (Zn) were reported to be the main contaminants depositing on the electrode surface during electrolysis. This leaves less active sites on the electrode surface which results in its diminished activity; which is reflected in the current drop. Hori et al have studied the effect of heavy metals impurities especially Fe ion at trace level on the product yields and the Faradaic efficiencies (Hori & Suzuki 1983). The metal ions are reduced to metals and are deposited on the electrode surface (Hori 2008) as films in ~10 minutes under most electrolysis conditions.

The shape of the CVs can also be affected by contaminants in the electrolyte depending on their nature and amounts (Wasberg 1994). This characterised by a strong shift of the CV potential and higher peak to peak separation (as seen in Figure 7.1). The CV shapes and the observed negative shift can have other causes if the electrolyte is ensured impurities free (this will be discussed later in the direct CO<sub>2</sub> reduction section). The electrode poisoning usually affects the current drop and ultimately leads to low product Faradaic yields (FY). An exception to these was gold cathodes (Hori et al. 2005) (Augustynski et al. 1996), the electrodes poisoning was clearly observed but the product FY were unaffected. Therefore, it is critical to use high purity substances in bulk electrolysis experiments for trusted results.

### **7.2.3 Effect of Electrolyte Purification (Pre-Electrolysis)**

Despite the analytical grade of the chemical compounds used in the present bulk electrolyses they still contains impurities at sub-ppm level (<0.5ppm). The presence of foreign species causes interference with the electrochemical reactions on the cathode surface as was discussed in the previous sections. Thus, the electrochemical purification of the electrolyte (impurities in the supporting salt and the catalyst) was performed. The CE was isolated using the glass frit and pyridine (C<sub>5</sub>H<sub>5</sub>N) with 99.99% purity was used.

Figure 7.4 illustrates potentiometric electrolyses undertaken with and without pre-electrolysis for comparison. The pre-electrolysis was conducted at cathodically polarized Pt foil (7cm<sup>2</sup>) at ca.  $-2.8 \times 10^{-4}$  A/cm<sup>2</sup> under N<sub>2</sub> atmosphere for 20h with

medium magnetic stirring speed ca. 250 rpm. Potentiostatic electrolysis (-0.7V) was performed under CO<sub>2</sub> immediately after the pre-electrolysis treatment in the same cell with fresh Pt WE (Figure 7.4). The current decreases 3.5 fold over a very short time 200s when no pre-electrolysis was performed; while it drops by ~40% over 10 times longer time with pre-electrolysis. In this instance, the purification of the electrolyte retarded the electrolysis current decay as expected (Hori et al. 2005).

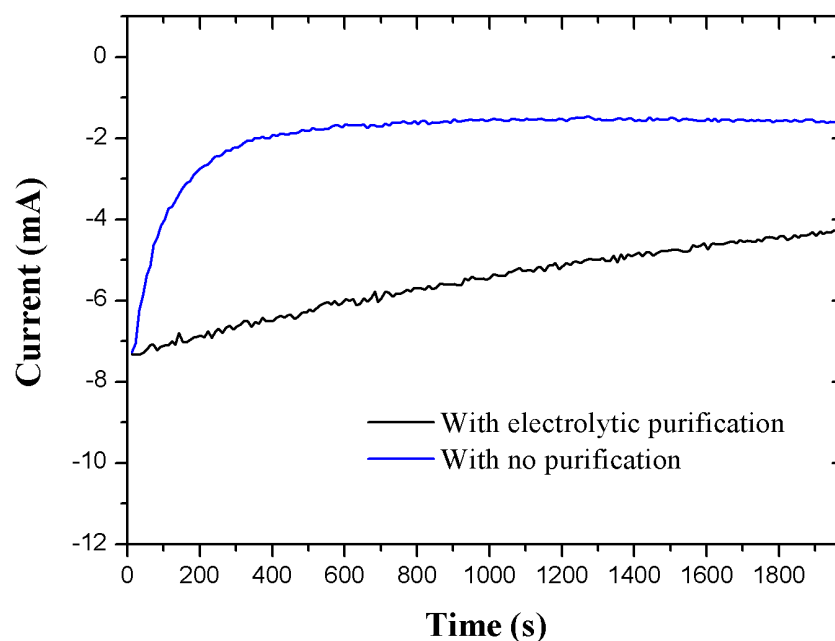


Figure 7.4 Effect of electrolytic electrolyte purification at (-0.7V). (Blue) without prior pre-electrolysis effect, (Black) with pre-electrolysis. Electrolyte: 10mM pyridine in 0.5M KCl. Conditions: in the presence of CO<sub>2</sub> (1bar, 25 °C). WE: on Pt ,ca.  $2.8 \times 10^{-4} \text{ A/cm}^2$

The above conditions are of critical importance in the bulk electrolysis procedure development. For instance the electrolytic purification was often not employed in the early CO<sub>2</sub> reduction on metals (Hori 2008) which resulted in discrepancies in the data. Hence, all bulk electrolyses were conducted with the highest purity of compounds with additional electrolytic purification, proper isolation of the CE and RE electrodes to ensure the reliability of the results.

## 7.3 Results and Discussion

### 7.3.1 Direct Electrolysis of CO<sub>2</sub> (in the absence of pyridine) at 55bar

Direct CO<sub>2</sub> potentiostatic electrolysis (-0.7V) was undertaken at its natural buffering pH (~pH4, 55bar, 25°C). Thorough cleaning of the entire setup (high pressure vessel, all electrodes, pump, the pressure regulator and the connecting tubing) was performed to ensure that the system was pyridine-free. The characteristic pyridinium CV was observed below the GCMS limit of detection (LOD) (<0.1ppm). Lower than this concentration, the pyridinium CV wave was still observed electrochemically. This observation is not surprising considering the high surface activity of pyridinium on metals (Mairanovskii 1963). The high pressure system was considered free from this compound when the usual voltammetric pyridine wave was not observed.

CVs were recorded before and after the direct CO<sub>2</sub> electrolysis at 100mV/s (Figure 7.5a and c). The CVs collected prior to electrolysis (Figure 7.5a) do not show well-defined waves contrary to what have been reported by some authors (Costentin et al. 2013), who investigated the effect of pyridine in CO<sub>2</sub> electrolysis. Instead, some features associated with species absorption/desorption on Pt are observed. The voltammetric behaviour of Pt surfaces in acidic media (Clavilier et al. 1981) (Cheng & Jandik 2009) (Srejić et al. 2011) and a neutral medium (Pletcher & Sotiropoulos 1994) were widely studied in the past. Herein, the voltammetric response under CO<sub>2</sub> shows similar behaviour to that under any other acidic medium. At negative potential scan a shoulder (-0.37V) is observed which is followed by a peak at -0.45V, these peaks are associated with the reductive hydrogen adsorption on the Pt surface (Srejić et al. 2011) (Pletcher & Sotiropoulos 1994) (Cheng & Jandik 2009).

The oxidative hydrogen desorption is observed as a peak (-0.35V) and a shoulder (-0.20V) at the reverse scan (Srejić et al. 2011) (Pletcher & Sotiropoulos 1994) (Cheng & Jandik 2009). The unusual peak separation of ~100mV and ~170mV which reflects the adsorption-desorption irreversibility of hydrogen was explained as the pH variation at the electrode surface which according to Pletcher et al results from the surface reactions themselves (Pletcher & Sotiropoulos 1994). The position of these peaks is believed to be

strongly affected by anions (e.g.  $\text{Cl}^-$ ) in the solution which are in competition with hydrogen adsorption-desorption reactions (Wasberg 1994) (Priyantha & Malavipathirana 1996).

The direct  $\text{CO}_2$  electrolysis conducted for  $\sim 2\text{h}$  is illustrated in Figure 7.5b. The current dropped to  $\sim 54\%$  of the starting value over the first hour and then plateaus at  $\sim 0.2\text{mA}/\text{cm}^2$ . Figure 7.5c shows CVs collected following the electrolysis. The CV shape is significantly distorted from the initial CV (Figure 7.5a), this is characterised by a strong negative shift ( $>300\text{mV}$ ) of the main reduction threshold and disappearance of the adsorption-induced features. Furthermore, the cathodic current on the CV increases significantly by  $\sim 88\%$  as compared to the CV current observed prior to the electrolysis.

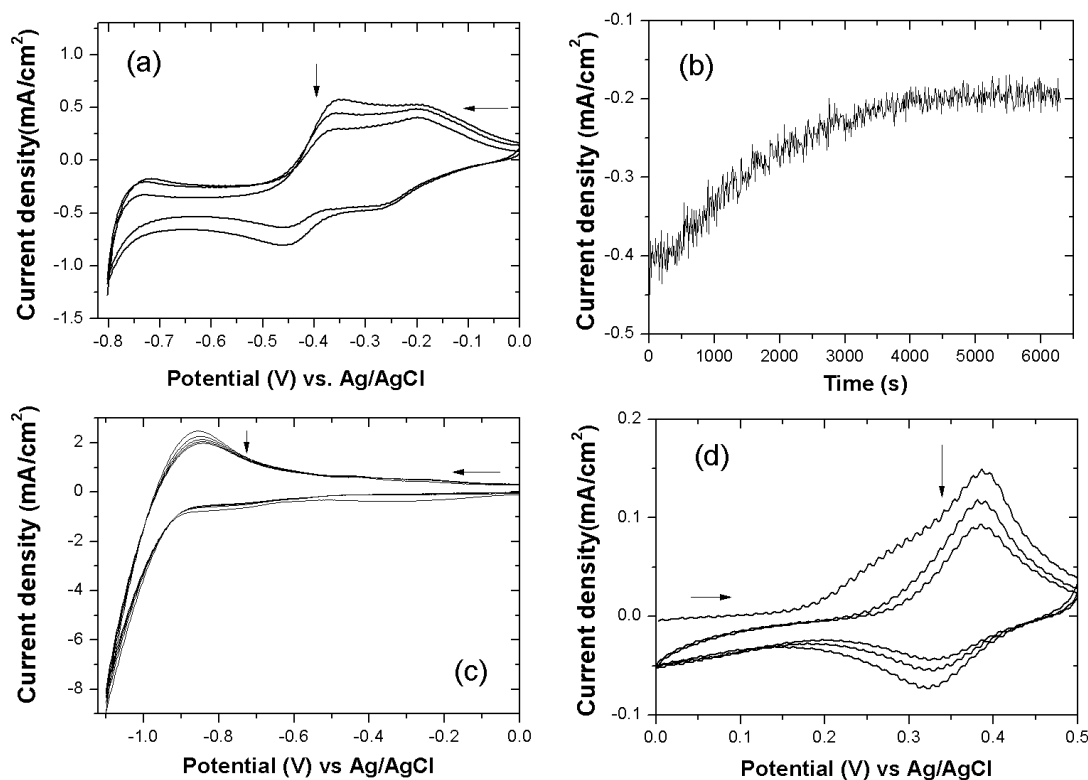


Figure 7.5 Direct electrochemical  $\text{CO}_2$  reduction (55bar,  $25^\circ\text{C}$ ): Cyclic voltammograms at  $100\text{mV}/\text{s}$  in  $0.5\text{M KCl}$  at Pt wire ( $2.6\text{cm}^2$ ) (a) cathodic CV wave before electrolysis, (b) Chronoamperometry ( $-0.7\text{V}$ ) of direct  $\text{CO}_2$ , (c) cathodic CV wave after electrolysis and (d) anodic CV wave. Horizontal arrows illustrate the scanning direction. Vertical arrows show the voltammetric cycling direction.

$\text{CO}$  and  $\text{H}_2$  are known to electrolytically form upon the reduction of  $\text{CO}_2$  on Pt electrode in aqueous electrolytes (Hori 2008). Reduced  $\text{CO}_2$  electrolyte is characterised by a

strong CO adsorption on Pt, as was initially reported by Beden et al and later confirmed by several other studies (Hori 2008). The generation of molecular hydrogen was exclusively detected with high Faradaic yields (~96%) on Pt (Hori 2008). Thus, these reactions are the most likely occurring upon electrolysis (Figure 7.5b). Lucaszewski et al have shown that the presence of CO which is referred to as CO or referred to as 'reduced CO<sub>2</sub>' competes with adsorbed hydrogen leading to partially suppressing it from the Pt surface, while it is consumed in the HER (Łukaszewski et al. 2008). Hence the adsorbed CO formation should partially block the Pt cathode surface obscuring the hydrogen adsorption-desorption CV features observed prior to electrolysis (Figure 7.5a and c). Following the direct CO<sub>2</sub> electrolysis in the acidic medium (Figure 7.5), a CV at anodic biasing was collected (Figure 7.5d). An oxidation peak appears at +0.39V (redox +0.35V) and the amplitude of the wave diminishes with subsequent cycling; this reflects the facile detachment of some reduced species from the Pt. The oxidation peaks observed were assigned to the oxidation of adsorbed CO on Pt (Priyantha & Malavipathirana 1996).

It has been suggested that the CO formation is highly favoured in acidic media (Cheng & Jandik 2009). Hence, in order to confirm the CO adsorption effect further electrolysis study was carried out in an electrolyte of different acidity. For that, the experimental conditions (CO<sub>2</sub> saturation level and passed charge ~3C) were selected to ensure that the initially acidic electrolyte was gradually displaced into the basic region during the electrolysis. This was achieved by the introduction of CO<sub>2</sub> in the aqueous electrolyte for 30min (~pH4) then the supply was cut prior to electrolysis. Figure 7.6 illustrates the direct CO<sub>2</sub> electrolysis (-0.7V) initially in acidic electrolyte over ~8h duration. The current drops by ~75% of the starting current (-0.25mA/cm<sup>2</sup> to -0.06mA/cm<sup>2</sup>) over the first hour. This represents approximately the usual current decay observed in the experiments with continuous CO<sub>2</sub> supply. The current then increases back to the starting value. In this instance, the variation of the current is reflecting the pH variation of the electrolyte in the absence of the CO<sub>2</sub> buffering effect.

Indeed, over the duration of the electrolysis significant amounts of protons are consumed (shifting the concentration from 0.1mM to negligible amounts) since the pH at the end of the electrolysis was 12.00 (measured immediately after depressurisation). Considering the highly efficient H<sub>2</sub> production (~96%) on Pt (reported above) the

protons are most likely rapidly consumed in the molecular hydrogen production. The increase of the current observed later in the experiment seems to correspond to aqueous CO<sub>2</sub>/carbonic acid exhaustion as part of its dissociation and the consumption of protons in HER and CO production (Łukaszewski et al. 2008). This indicates that the gradual consumption of protons has resulted in a pH shift to the basic region and hence promoted the CO desorption from the electrode surface. Indeed, the anodic CV recorded following the electrolysis (Figure 7.6, inset) did not show the wave observed earlier (compare to Figure 7.5d) assigned to CO. Hence, these observations indicate the partial blockage of the Pt electrode is due to the formation of adsorbed CO during the electrolysis.

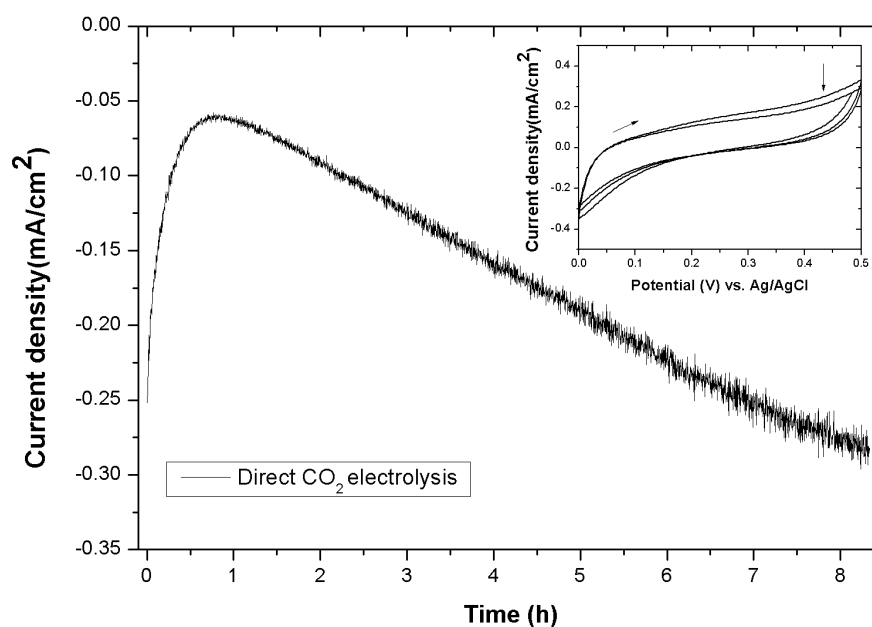


*Figure 7.6 Direct CO<sub>2</sub> electrolysis at -0.7V in initially acidic electrolyte (becoming basic electrolyte after CO<sub>2</sub> supply cut off) at Pt wire (2.6cm<sup>2</sup>) electrode. Inset: anodic CV wave after electrolysis (55bar, 25°C)*

Direct CO<sub>2</sub> electrolyses (in the absence of pyridine) were conducted in a typical electrolyte (0.5M KCl) at potentiostatic (-0.7V) and galvanostatic (2mA/cm<sup>2</sup>) conditions at 30C and 70C respectively. GCMS analysis of the direct CO<sub>2</sub> electrolysis solutions showed no methanol and no other alcohol production in the absence of pyridine. In this work the analysis is focused only on the detection/quantification of alcohols. We can conclude that this supports the statement that this molecule is involved in the process of the alcohol formation (Seshadri et al. 1994). Boston and co-workers have also

demonstrated the need of this molecule for formate and methanol formation (Boston et al. 2013).

**To summarise**, the direct CO<sub>2</sub> electrolysis experiments on Pt electrode revealed that the CVs waveforms resulting prior to electrolysis are similar to those observed in other acidic media (Clavilier et al. 1981) (Cheng & Jandik 2009) (Srejić et al. 2011) and no CO<sub>2</sub> associated waves are observed. In addition, the electrolysis current decay seems to be associated with the adsorbed CO formation which partly blocks the electrode surface. This electrode blockage is evidenced by the negative shift of the cathodic CV waves and the simultaneous appearance of the anodic wave assigned to CO formation. Furthermore, the direct CO<sub>2</sub> electrolysis in basic media has confirmed the CO formation and its close relation to the Pt blockage which is reflected in the rapid decay of the current. The analysis of the direct CO<sub>2</sub> electrolytes showed no alcohol formation, is in agreement with Bocarsly et al (Cole et al. 2010) and Boston et al (Boston et al. 2013) who were unable to detect any methanol or other alcohols in the absence of pyridine. The above observations together with the product analysis results imply that CO and molecular hydrogen are the main products of the direct CO<sub>2</sub> on Pt at these conditions. To investigate the production of methanol in the presence of pyridine electrolyses of CO<sub>2</sub>-pyridine are reported in the next sections at 1 bar and 55bar.

## **7.3.2 CO<sub>2</sub>-Pyridine Reduction at 1bar: Alcohol Faradaic Yields (FY)**

In order to investigate the controversy over the methanol production (reported in the introduction to this Chapter), potentiostatic and galvanostatic electrolyses of the CO<sub>2</sub>-pyridine system were undertaken at 1bar of CO<sub>2</sub> and 25°C. Furthermore, the electrolyses at atmospheric pressure results will serve as a reference for comparison with the high pressure experiments. The concentration of 10mM pyridine was also chosen for comparison purposes.

### **7.3.2.1 Chronoamperometric (Potentiostatic) Measurements**

To determine an optimum electrode potential for prolonged product accumulation, bulk electrolyses were carried out at different fixed potentials: -0.5V, -0.6V and -0.7V

(Figure 7.7). For -0.6V and -0.7V electrolyses, the current drops by ~84% and ~89% respectively, then approaches  $\sim 0.15\text{mA/cm}^2$  as shown in Figure 7.7. On the other hand, at -0.5V the current seems to remain virtually constant over the duration of the electrolysis (Figure 7.7). In fact, a detailed view of the electrolysis at this voltage (-0.5V) results in current decrease by ~60% which is comparable to the previous two electrolyses (Figure 7.7, inset on the left). The decrease of the current is likely to be due to the CO adsorption on the Pt surface similar to the direct  $\text{CO}_2$  electrolysis case (discussed in the previous section).

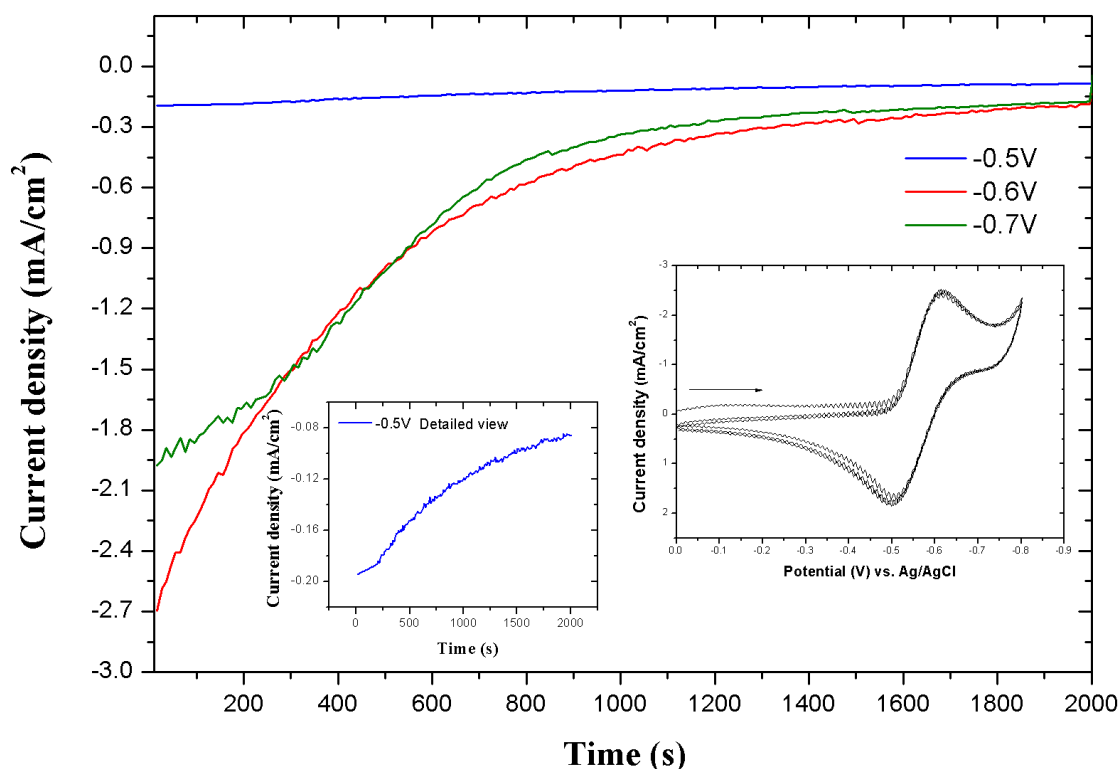


Figure 7.7 Chronoamperometric (potentiostatic) measurements at: -0.5V, -0.6V and -0.7V. Electrolyte: 10mM pyridine, 0.5 M KCl aqueous solution. Conditions: 25 °C and 1bar  $\text{CO}_2$ . WE: Pt wire  $2.6\text{cm}^2$ . Inset on the right: A typical cyclic voltamogram recorded before the electrolysis at 100mV/s. Inset on the left: Detailed view of the electrolysis at -0.5V.

Electrolyses were run under potentiostatic conditions at -0.5V, -0.6V, and -0.7V over 7-12h. Methanol Faradaic yields calculated at 12-33 C were less than 3% (Table 7.1) corresponding to concentrations of 0.20-0.30ppm. These data showed no correlation

with the charge passed in this case. In addition, no optimum potential can be revealed since methanol was detected at virtually the same level for all potentials. These results are ~7 times lower than the Faradaic efficiencies reported on Pt (22%) by Yan et al. 2014. Methanol Faradaic yields were further examined as function of electrolysis time as discussed in the next section.

Table 7.1 Methanol Faradaic efficiencies for electrolyses at controlled potential of 10mM pyridine in 0.5M KCl under CO<sub>2</sub> (1 bar, 25°C) at Pt 2.6cm<sup>2</sup>

Potential (V) vs. Ag/AgCl	Passed charge Q(C)	MeOH concentration (ppm)	MeOH Faradaic yield FY(%)
-0.5	12.44	0.20±0.07	2.07±0.72
-0.6	13.10	0.30±0.03	2.86±0.29
-0.7	32.57	0.25±0.06	0.99±0.24

### 7.3.2.2 Chronoamperometric (Potentiostatic) Measurements: Time Dependence/Charge Passed Evolution

Time dependent measurements at controlled potential -0.7V were carried out for 5h with methanol amounts analyzed every hour (Figure 7.8). The results show the formation of methanol within 1hour where the Faradaic yield is at its maximum 21% (~5C). Methanol concentration increases to a maximum of 0.17±0.01ppm corresponding to 17±2% Faradaic yield (~6C) over the second hour, then drops to 6.7±2.3% (~11C) at the end of experiment. However, the concentration of methanol remained virtually constant at <0.2ppm. Similar rapid decay of Faradaic yield observed in the bulk electrolysis was also reported for CO<sub>2</sub> reduction on Cu to hydrocarbons (DeWulf 1989) (Augustynski et al. 1996) (Noda et al. 1989). In many studies on the formation of hydrocarbons and alcohols, the reported Faradaic efficiencies are the *maximum yields* corresponding to short electrolysis times rather than steady state accumulation of products over prolonged electrolysis (Augustynski et al. 1996). There are only few exceptions where the product formation is reported at more than 6h of electrolysis (e.g.Łukaszewski et al. 2008). The results herein do not seem to differ from the reported work, where a maximum of methanol production was observed over a short

period of time followed by an important drop of the Faradaic yields. This seems to be characteristic of CO<sub>2</sub> reduction reactions on metal electrodes at ambient conditions.

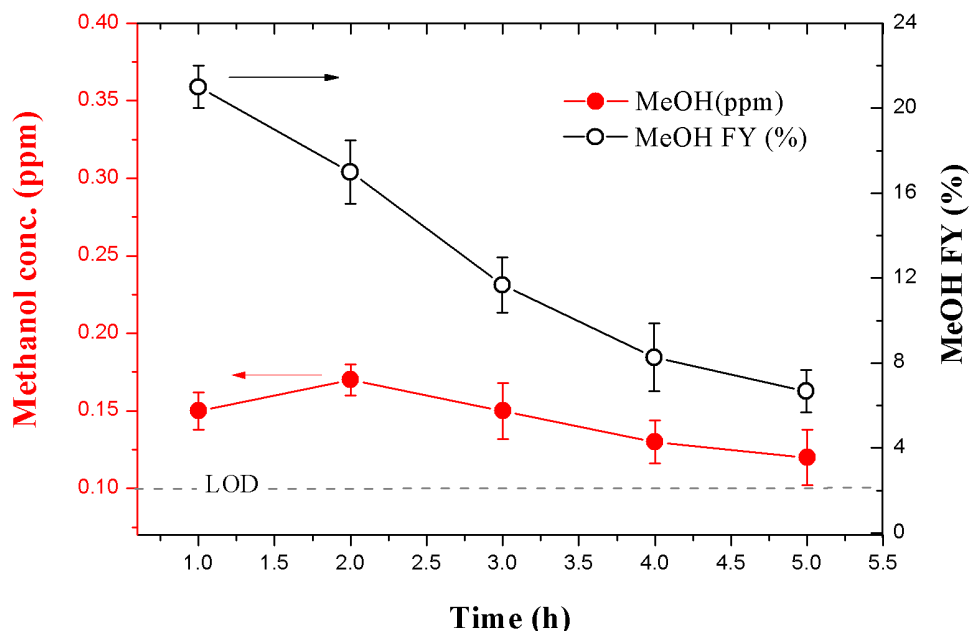


Figure 7.8 Methanol Faradaic yields and their corresponding concentrations as a function of time in potentiostatic electrolysis -0.7V: Red –Methanol concentrations (ppm), Black – Methanol Faradaic yield (%). Electrolyte: 10mM pyridine, 0.5M KCl aqueous solution. Conditions: 25 °C and 1bar CO<sub>2</sub>. LOD – limit of detection.

### 7.3.2.3 Chronopotentiometric (Galvanostatic) Measurements

Galvanostatic electrolyses were undertaken at fixed current densities of ~0.4-1.3 mA/cm<sup>2</sup>. The product concentration was monitored as function of time/charge (Figure 7.9). A maximum methanol Faradaic yield of 1.66±0.13% corresponding to 0.62±0.05ppm at 54Coulombs was achieved. Prolonged electrolyses at higher charges passed (650C) result in a drastic decrease of the FY to negligible values (0.12±0.02%) with methanol level dropping to about half the initially detected concentration. The Faradaic yields in the present galvanostatic measurements seem to exhibit a similar behavior to the FY obtained in the above described potentiostatic experiments. The electrolyses at the different biasing modes resulted in low methanol concentrations <1ppm with an apparent FY values, which seem to be strongly affected by the number

of coulombs passed. However, methanol was not the only alcohol detected in the galvanostatic experiments.

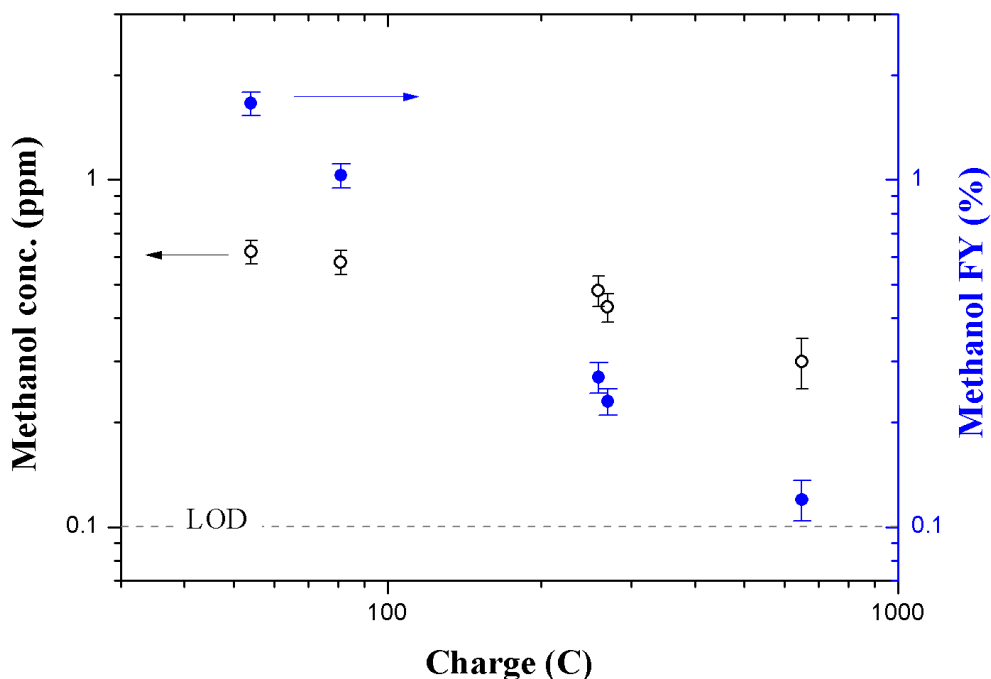


Figure 7.9 Methanol Faradaic efficiencies and their corresponding concentrations as a function of the passed charge: current densities  $\sim 0.4\text{-}1.3\text{ mA/cm}^2$ . Electrolyte: 10 mM pyridine, 0.5 M KCl aqueous solution. Conditions: 25 °C and 1bar  $\text{CO}_2$ . WE:Pt ( $3.8\text{cm}^2$ ). LOD-limit of detection

Ethanol ( $\text{C}_2\text{H}_6\text{O}$ ) and isopropanol ( $\text{C}_3\text{H}_8\text{O}$ ) were also detected (Figure 7.10). However, similar to methanol the alcohol concentrations did not exceed 1ppm regardless of the passed charge with an exception of isopropanol ( $\text{C}_3\text{H}_8\text{O}$ ). The latter alcohol was detected between 1-1.57ppm at charge of  $<200\text{C}$ . Ethanol ( $\text{C}_2\text{H}_6\text{O}$ ) and isopropanol ( $\text{C}_3\text{H}_8\text{O}$ ) were not reported on Pt previously (Barton et al. 2008). Yet, the  $\text{CO}_2$ -pyridine reduction on  $\text{TiO}_2$ -Carbon modified Pt resulted in isopropanol ( $\text{C}_3\text{H}_8\text{O}$ ) formation (de Tacconi et al. 2012).

**To summarise**, the electrolysis experiments at 1bar  $\text{CO}_2$  in the presence of pyridine were conducted in potentiostatic and galvanostatic modes. Methanol was detected as an electrolysis product in both cases. However, the concentrations of the alcohol were limited to  $\sim 0.6\text{ppm}$  irrespectively of the passed charge value and the electrolysis mode.

These measurements revealed a dynamic character of the apparent Faradaic yields which decreases significantly with higher passed charge. This dynamic character of the FY has not been reported before. On the other hand, the maximal FY values are in agreement with that reported by Bocarsly et al (Morris et al. 2011). In terms of methanol production, no critical difference between the potentiostatic and galvanostatic modes was observed.

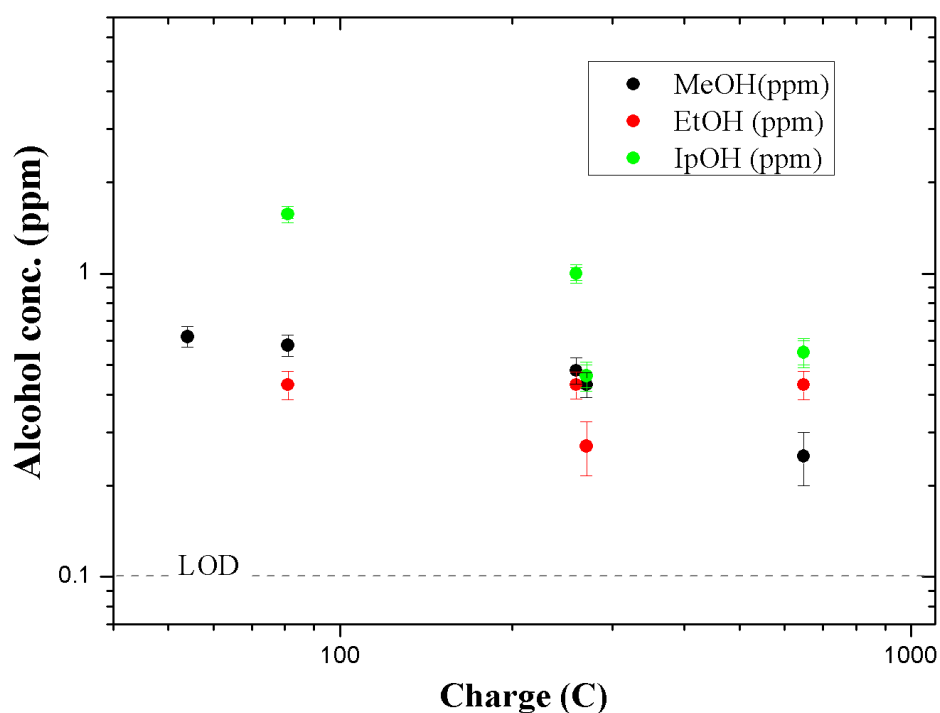


Figure 7.10 Alcohol concentrations (ppm) as function of the passed charge in potentiostatic electrolysis  $-0.7V$ : black –MeOH concentrations, Red–ethanol ( $C_2H_6O$ ) and Green–isopropanol. Electrolyte: 10mM pyridine, 0.5 M KCl aqueous solution. Conditions: 25 °C and 1bar  $CO_2$ . WE: Pt ( $3.8cm^2$ ). LOD – limit of detection.

## 7.3.3 CO<sub>2</sub>-Pyridinium Reduction at High Pressure: Alcohol Faradaic Yields (FY)

### 7.3.3.1 Chronoamperometric (potentiostatic) Electrolysis

The solubility of CO<sub>2</sub> is as low as ~30mM in water at ambient pressure and temperature (estimated from Henry's law at 1bar and 25°C) which limits the concentration of CO<sub>2</sub> to the electrode surface. In order to investigate the effect of the abundance of this reactant on the prolonged electrolyses of the CO<sub>2</sub>-pyridinium system, bulk electrolysis experiments were carried out in the presence of 10mM pyridine at 55bar of CO<sub>2</sub>. The effect of the CO<sub>2</sub> concentration increase is assessed by comparing methanol amounts and Faradaic yields at atmospheric to elevated pressure results. Potentiostatic measurements (-0.5-0.7V) were undertaken at 55bar and 25°C of CO<sub>2</sub> in the presence of pyridine (10mM).

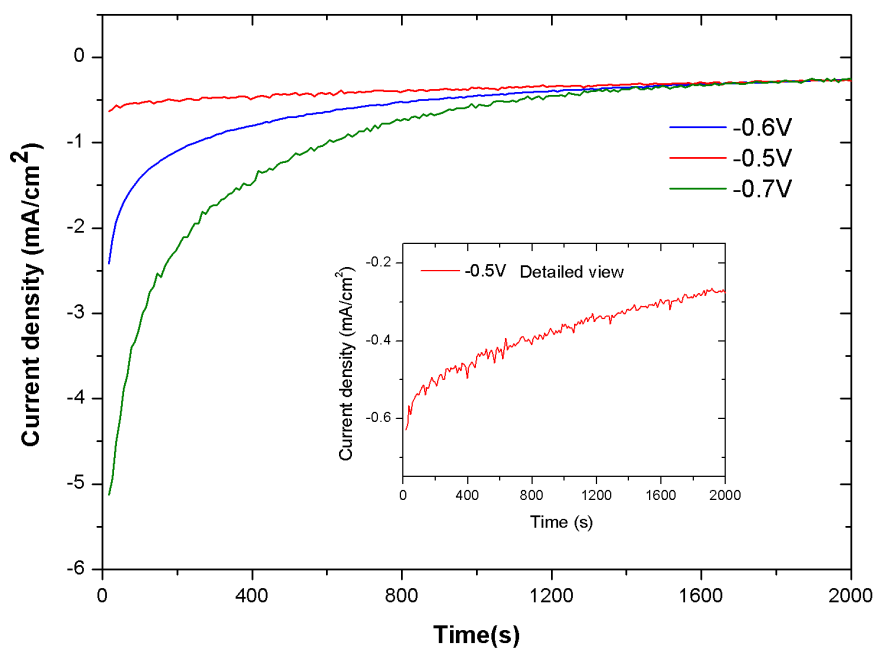


Figure 7.11 Chronoamperometric (potentiostatic) electrolyses: -0.5-0.7V. Electrolyte: 10mM pyridine, 0.5M KCl aqueous solution. Conditions: 25 °C and 55bar CO<sub>2</sub>. WE: Pt 3cm<sup>2</sup>.

Figure 7.11 shows the current decay for the potentiostatic electrolyses. The reduction current displays similar decay to the atmospheric pressure experiments. At -0.6V and -0.7V, the current decreases by ~85% over 800s then reaches a residual value of

$\sim 0.3 \text{ mA/cm}^2$  i.e. about twice that in the 1bar  $\text{CO}_2$  experiments (Figure 7.7). Similarly, the lowest potential (-0.5V) electrolysis reproduces the current decay at the atmospheric experiments with  $\sim 46\%$  decay over 2000s duration. However, the current values are approximately 3 times higher at 55bar. For the product yields estimation, potentiostatic electrolyses were undertaken at the same conditions as above and at accumulation charge of 14-19C. The average methanol Faradaic yields and the corresponding concentrations are illustrated in Figure 7.12. The error bar shown at -0.7V indicate data scatter over three independent experiments. These results show no significant difference of methanol Faradaic yields (2.5-3%) for the different reduction potentials. Similarly, methanol concentrations did not vary significantly 0.24-0.35ppm. Although the measurements were performed at the same conditions for -0.7V electrolyses and all measures were taken to ensure consistency for all electrolyses (including the -0.5V and -0.7V electrolyses), the repeatability of the accumulation results was low. Thus, no correlation of the Faradaic yields or concentrations *versus* the reduction potential can be revealed.

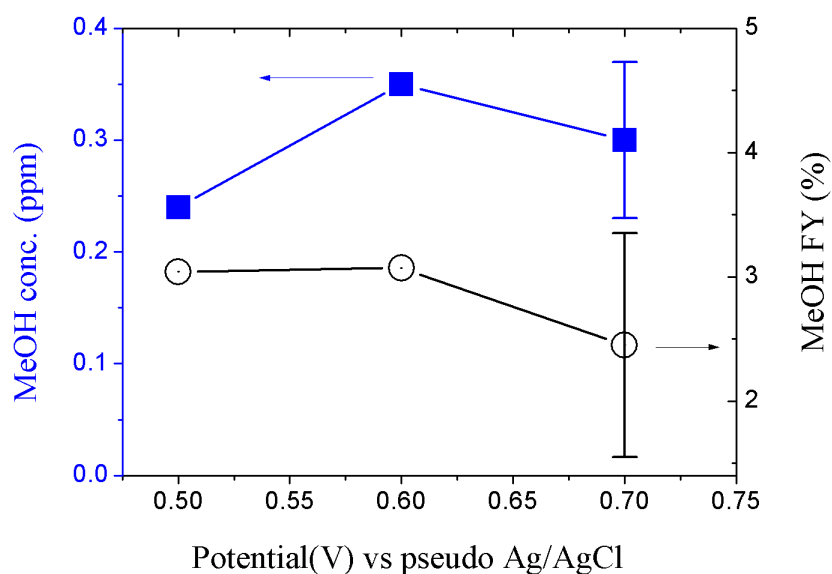


Figure 7.12 Methanol Faradaic yields and concentrations as function of the reduction potential in potentiostatic electrolysis: blue – MeOH concentrations (ppm), Black – MeOH Faradaic yield (%). Electrolyte: 10mM pyridine, 0.5 M KCl aqueous solution. Conditions: 25 °C and 55bar  $\text{CO}_2$ . Error bars indicate data scatter over three experiments at -0.7V. Other data represent single experimental runs.

### 7.3.3.2 Chronopotentiometric (galvanostatic) Measurements

Galvanostatic measurements were undertaken at 55bar of CO<sub>2</sub> and 25°C in the presence of pyridine (50mM). Two independent electrolyses were conducted at fixed reduction currents of 0.05mA/cm<sup>2</sup> and 0.5mA/cm<sup>2</sup>. For each experiment, samples were analysed at different times of the electrolysis. The sampling was performed by a complete depressurisation of the reaction vessel, which was pressurised again to 55bar for prolonged electrolyses. Methanol Faradaic yields and the corresponding concentrations at 2-72C are shown in Figure 7.13. Methanol was first observed at ~3C passed corresponding to ~2h run with 0.24±0.03ppm, the concentration then started to stabilise after ~10C and remained steady as the charge accumulates. The apparent Faradaic yields exhibit the same dynamic character as was observed at 1bar experiments. For the experiment at hand, around 7% Faradaic yield is achieved at ~3C and then it decays with the charge/time as shown in Figure 7.13.

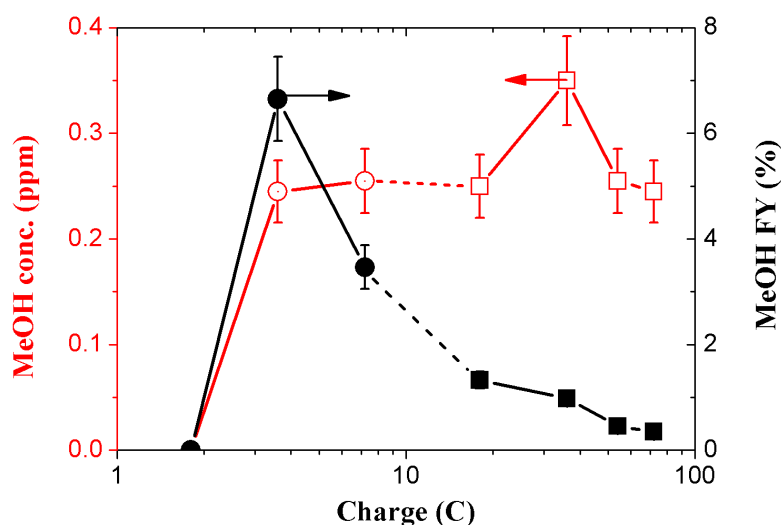


Figure 7.13 Methanol Faradaic yields and the corresponding concentrations as function of the passed charge for fixed cathodic current: circles – 0.05mA/cm<sup>2</sup>, squares – 0.5mA/cm<sup>2</sup>. Electrolyte: 50mM pyridine, 0.5M KCl aqueous solution. Conditions: 25 °C and 55bar CO<sub>2</sub>. Error bars are estimated from the errors in the GCMS analysis

In terms of methanol concentrations, similar amounts were detected on both potentiostatic and galvanostatic electrolysis regimes (compare Figure 7.12 and Figure 7.13). Moreover, within each regime, no correlation was found between the methanol



The detected methanol amounts do not seem to correlate with the pyridine concentration; instead this data is scattered over the range investigated with methanol amounts limited to <1ppm. In this instance, no optimal pyridine concentration is observed. Interestingly, methanol was produced at pyridine concentrations as low as 5  $\mu$ M with amounts closer to the GCMS detection limit (0.1ppm). Considering that pyridine was observed electrochemically at lower than the LOD of the GCMS (reported in the direct CO<sub>2</sub> electrolysis section), the concentration limit of such molecule needed for methanol production could be much lower.

In addition to methanol, other alcohols, including ethanol (C<sub>2</sub>H<sub>6</sub>O), isopropanol and butanol (C<sub>4</sub>H<sub>10</sub>O), were produced (Figure 7.15). The amounts below the LOD in Figure 7.15 represent traces alcohols at ppb level, which were often observed in these electrolyses (NB. the LOD was estimated according to strict criteria as explained in Chapter 4, Section 4.5.1 hence it is used to test the reliability of the GCMS analysis, however the alcohol concentrations below the LOD cannot be completely discarded herein).

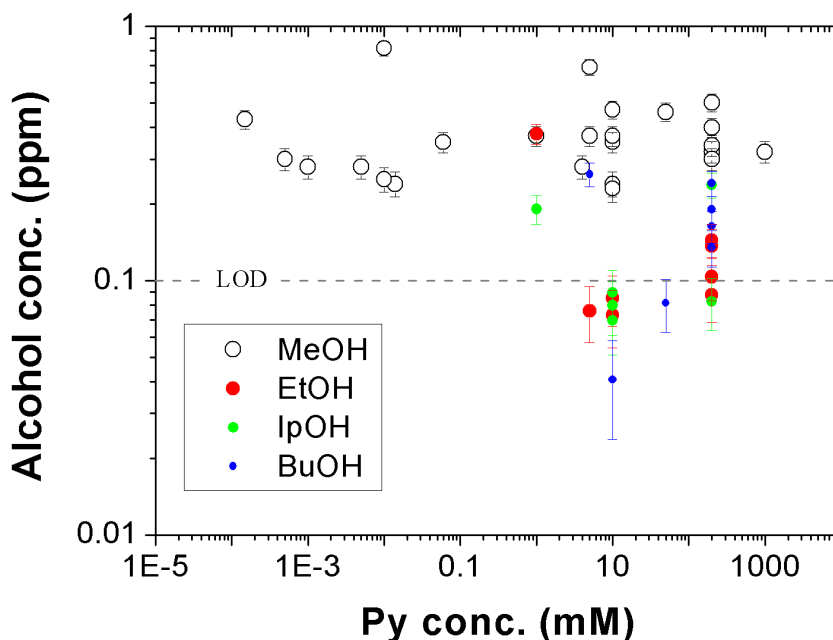


Figure 7.15 Alcohols yields (ppm) as function of the analytical pyridine concentrations. Electrolyte: 0.5M KCl. Accumulation charge  $\geq 9$  C. Conditions: 25 °C and 55bar CO<sub>2</sub>. Each symbol represents Faradaic yield of the alcohol: open circles – potentiostatic electrolysis at - 0.5-0.8V; filled circles – galvanostatic electrolysis at 50  $\mu$ A/cm<sup>2</sup> and

1.5mA/cm<sup>2</sup>. Red-ethanol, Green- isopropanol and Blue-butanol concentrations (ppm). LOD – limit of detection.

The alcohol concentrations above LOD are detected at slightly lower concentrations range (0.1-0.37ppm) than methanol. It is important to note that these alcohols were mainly observed at high pyridine concentrations ( $\sim \geq 1\text{mM}$ ). The alcohols apparent Faradaic yields at the conditions reported above (same dataset shown in Figure 7.14 and Figure 7.16) are presented as function of the coulombs passed in Figure 7.16. Methanol FYs seem to have the same dynamic character observed at 1bar CO<sub>2</sub> electrolyses. Similar to the observations of methanol FY behaviour, the FY of the other alcohols show a strong dependence on the coulombs consumed in the electrolyses. At less than 100C of charge all alcohol Faradaic yields range between 0.5-10%. However, as higher charge is consumed (>100C) the alcohols' Faradaic yields drop to marginal values (<0.2%). This FY limitation was not reported previously for the CO<sub>2</sub>-pyridinium process for methanol.

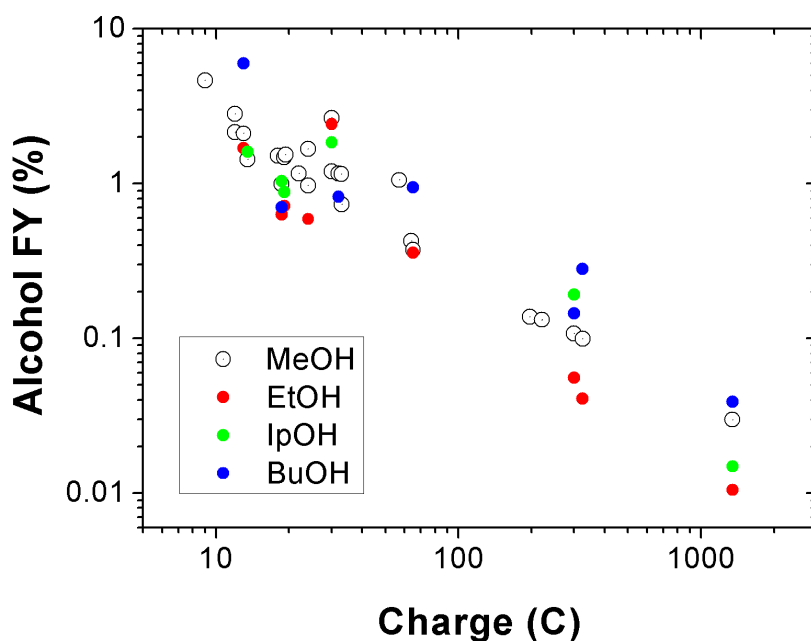


Figure 7.16 Alcohol Faradaic yields as function of the charge at analytical pyridine concentration of the range (5 $\mu\text{M}$  to 1M). Electrolyte: 0.5 M KCl aqueous solution. Accumulation charge  $\geq 9$  C. Conditions: 25  $^{\circ}\text{C}$  and 55bar CO<sub>2</sub>. Each symbol represents total Faradaic yield of the alcohol specified: Red-ethanol, Green- isopropanol and Blue-butanol.

Figure 7.17 summarises the total alcohols Faradaic yields *versus* the coulombs passed shown in Figure 7.16. The total alcohol Faradaic yields lessened with higher charge accumulated. A maximum total Faradaic yield at ~10% for a low passed charge (~10C) was observed with corresponding methanol concentrations limit of <1ppm (Figure 7.14). This Faradaic yield dynamic behaviour is clearly related to the apparent concentration limit. Importantly, the limit of this nature was not reported by Bocarsly group. Yet, the maximum observed FY of 5-10% is not very different as compared to the 20% FY reported by this group at 1bar at Pt electrodes (Seshadri et al. 1994) (Morris et al. 2011). The observed limit of the methanol yield can explain the inability to detect any methanol by Costentin et al, who used a less sensitive analytical technique than was employed in the present work (Costentin et al. 2013).

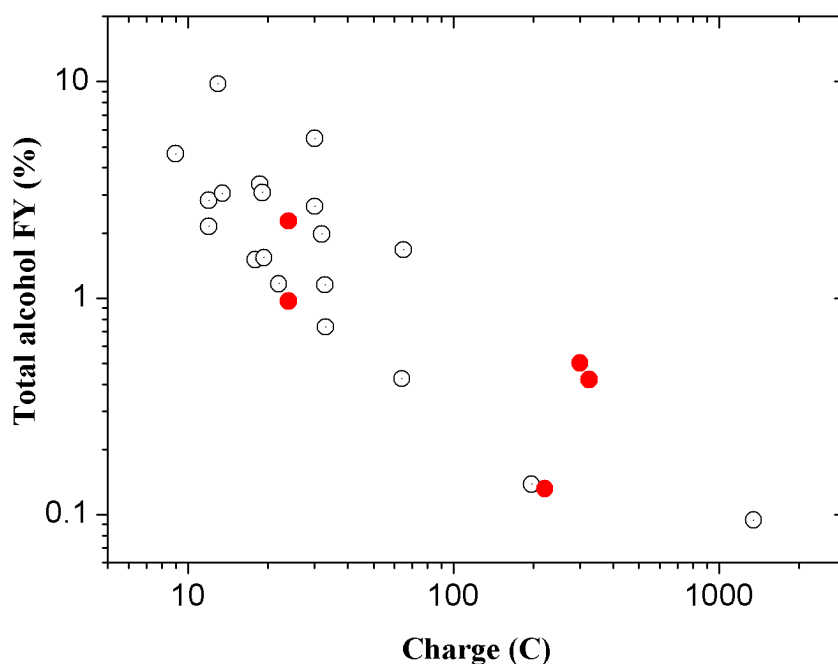


Figure 7.17 Total alcohol Faradaic yields as function of the charge at analytical pyridine concentration (0.5 $\mu$ M to 1M). Electrolyte: 0.5 M KCl aqueous solution. Accumulation charge  $\geq$ 9 C. Conditions: 25  $^{\circ}$ C and 55bar CO<sub>2</sub>. Each symbol represents total Faradaic yield at each experiment: open circles – potentiostatic electrolysis; filled circles – galvanostatic electrolysis. LOD – limit of detection.

In an attempt to maximise methanol amounts, an independent potentiostatic electrolysis (-0.7V) of 10mM pyridine was undertaken at 55bar of CO<sub>2</sub> on a WE with ~7-times higher electrode area (~20cm<sup>2</sup>) than employed in typical experiments and in ~16 times

lower electrolyte volume (1.5ml). However, after ~25C or ~350C only typical methanol concentrations were detected (0.25-0.3ppm). This approaches did not seem to have any effect on the methanol yields.

### 7.3.3.4 Discussion

Under the conditions investigated, methanol was persistently produced at sub-ppm level in all experiments. Over the entire pyridine concentration range no correlation with the methanol amounts produced could be revealed. However, higher alcohols appeared at pyridine concentrations  $\sim >1\text{mM}$ . The higher alcohol formation was not reported for the  $\text{CO}_2$ -pyridine system on Pt or Pd metals. However, some of these alcohols were suggested to form as subsequent step to the methanol formation on different materials (semiconductor or composite electrode) in the presence of pyridine or its derivatives (Bocarsly 2013). For instance, an observation supporting the up-conversion in the  $\text{CO}_2$ -pyridine process was reported on Pt/C-TiO<sub>2</sub> electrode (de Tacconi et al. 2012). Methanol was produced over 2-hours then its concentration decreased with simultaneous isopropanol formation.

The up-conversion pathway seems common in the  $\text{CO}_2$  reduction process. In this context, a rapid formic acid consumption to form N, N-dimethylformamide (DMF) was observed in the catalytic reduction of  $\text{CO}_2$  (Jessop et al. 1994). Hori has also shown the increase of the Faradaic yields of formic acid with a simultaneous drop of carbon monoxide (Hori 2008). In view of the unexpected higher alcohols appearance in the present work and the persistently low methanol concentrations produced, one may be led to consider the up-conversion route. However, there is no evidence for such process herein and the limitation of methanol concentration is more likely to be due to other reasons such as electrode poisoning.

The ambiguous results obtained herein characterised by limited production of methanol amounts production raise questions in terms of the practical applicability of the pyridine-assisted  $\text{CO}_2$  reduction to methanol system and its proposed mechanism (Cole et al. 2010). On the other hand, the decrease of the Faradaic yields in the bulk  $\text{CO}_2$  reduction electrolyses seems to be a common issue which is less addressed in the recent related work. In fact, most of the reported studies are not steady-state FY but maximum Faradaic yields estimated at a short electrolysis time (Augustynski et al. 1996). In the

late 80s, however, Hori et al have addressed this issue by extensively studying the time dependence CO<sub>2</sub> electrolyses on Cu electrodes (Hori et al. 2005) (Hori & Suzuki 1983) (Hori 2008). These authors observed that the reduction of CO<sub>2</sub> to methane, ethylene, and ethanol (C<sub>2</sub>H<sub>6</sub>O) on Cu electrodes ceased after 20-40min of continuous prolonged electrolysis which was replaced by HER (Augustynski et al. 1996). Moreover, DeWulf et al have reported severe drop of the Faradaic yields of methane and ethylene on Cu electrode (DeWulf 1989). These groups believe the FY decay is due either to the deactivation of the electrode (blockage/poisoning) due to the presence of heavy metal electrodes (Hori 2008), the formation of carbonaceous compounds during the reduction (DeWulf 1989), or to other organic substances adsorbed on the electrode surface (Jessop et al. 1994). The deactivation of the electrode was also reported on gold (Kedzierzawski 1994) and silver (Augustynski et al. 1996) electrodes.

In the present work, the electrolysis purification (pre-electrolysis) of the electrolyte did not assist in enhancing the methanol concentrations/Faradaic yields. These experiments aimed at suppressing the ionic impurities interference resulted in typical amounts of methanol of sub-ppm level (reported earlier). This implies that the blockage of the Pt electrode with foreign species is unlikely to be responsible for the limited methanol production. However, the Pt electrode poisoning by intermediates/products effect on FY cannot be excluded. In the absence of pyridine, the direct CO<sub>2</sub> electrolysis clearly displayed the Pt WE blockage behaviour (reported earlier). This effect was shown to be due to CO species adsorption. In order to investigate the electrode poisoning effect on the electrolysis current in the presence of pyridine, potentiostatic electrolysis (-0.7V) of CO<sub>2</sub>-pyridine system was undertaken at the typical experimental conditions as illustrated in Figure 7.18.

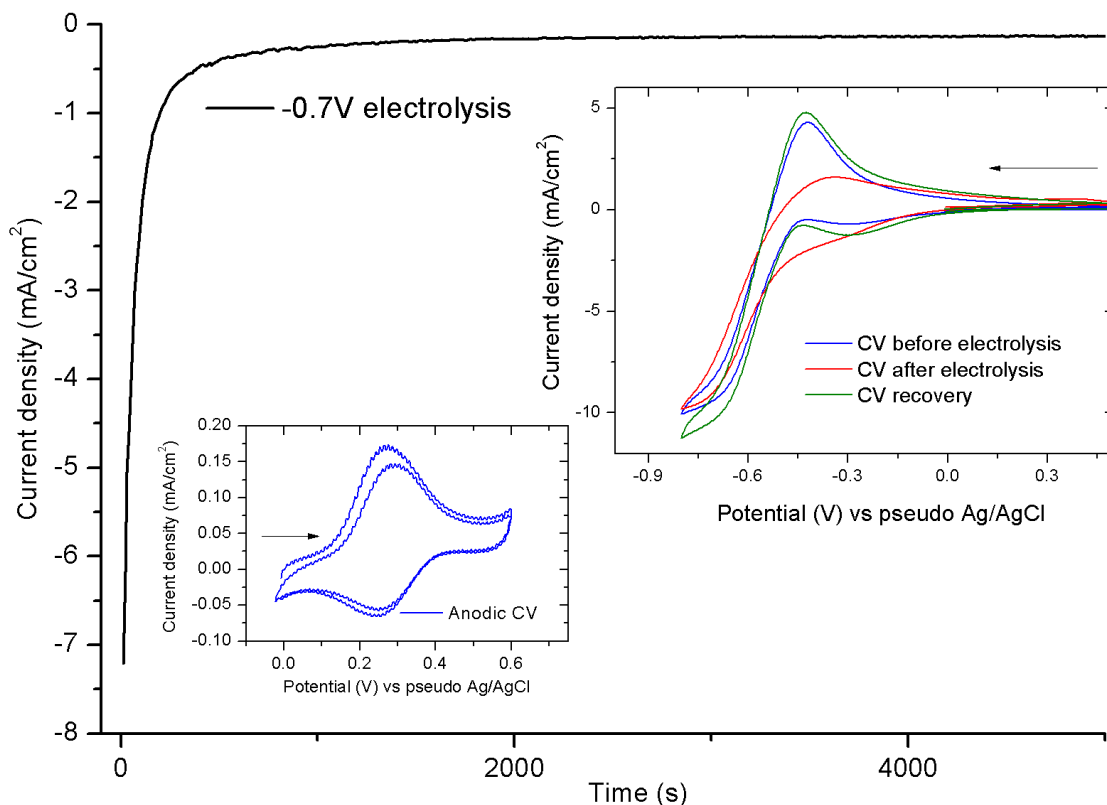


Figure 7.18 Potentiostatic electrolysis at  $-0.7\text{ V}$  at Pt electrode, showing current variation with time. Inset on the right: Cyclic voltammograms: Blue curve—before the electrolysis, red curve—after electrolysis and Green curve—after the anodic stripping at  $+0.5\text{ V}$ . Inset on the left: anodic wave. Electrolyte:  $10\text{ mM}$  of pyridine in  $0.5\text{ M KCL}$ . Conditions:  $55\text{ bar}$  of  $\text{CO}_2$  at  $25\text{ }^\circ\text{C}$ . Horizontal arrows illustrate the scanning direction.

The analysis of the CVs and the current decay reveals clear signs of the electrode blockage. The current drops by  $\sim 90\%$  of the starting current over  $\sim 400\text{ s}$  of the electrolysis time. The current eventually stabilises at  $\sim 0.3\text{ mA/cm}^2$ . The CV wave collected after the electrolysis displays a significant cathodic shift reflected in the CV shape distortion as observed in Figure 7.18 right inset. Similar to the direct  $\text{CO}_2$  experiments, the anodic peak is observed at  $\sim +0.3\text{ V}$ , which is assigned to oxidative desorption (anodic stripping) of CO from Pt surface. The polarisation at  $+0.5\text{ V}$  for few minutes (or several voltammetric cycles, Figure 7.18 left inset) results in a diminished amplitude of the anodic CV wave (which ultimately disappears) concomitant with the original CV waveform restoration (Figure 7.18 right inset). Further electrolysis following the anodic stripping, results in reoccurrence of the electrode blockage in a relatively shorter time (20-25 min). This can be explained by quicker poisoning by CO

already available in the bulk electrolyte from the preceding electrolysis step. These observations further confirm the blockage of the electrode by adsorbed CO species.

### **7.3.3.5 Techniques for Elevating Electrode Surface Poisoning**

The methanol Faradaic yield limit is suspected to be connected to the significant current decay caused by the electrode surface blockage. To investigate the possible electrode deactivation/blockage effect on methanol FY, two-step galvanostatic electrolysis ( $1.7\text{mA/cm}^2$ ) was conducted under typical experimental conditions. The first electrolysis was conducted for a charge of  $\sim 30\text{C}$ . A subsequent electrolysis ( $\sim 70\text{C}$ ) was performed in the same electrolyte with a fresh WE electrode (same area). This procedure resulted in the typical methanol concentrations of 0.2-0.3ppm amounts being detected after each electrolysis step. Hence, further physical/electrochemical techniques aimed at minimising/suppressing the CO species from Pt electrode and thus enhancing the FY, are presented below.

First, a periodic anodic biasing regime was adopted in bulk electrolysis over  $\sim 10\text{h}$ . Figure 7.19 illustrates chronoamperometric electrolysis at  $-0.7\text{V}$  with a periodic (2min at every  $\sim 30\text{min}$ ) anodic biasing of  $+0.5\text{V}$ . The current displayed periodical decreases with subsequent recovery. This electrochemical procedure did not assist in enhancing the methanol FY since in the typical methanol concentration range of 0.25-0.3ppm was detected.

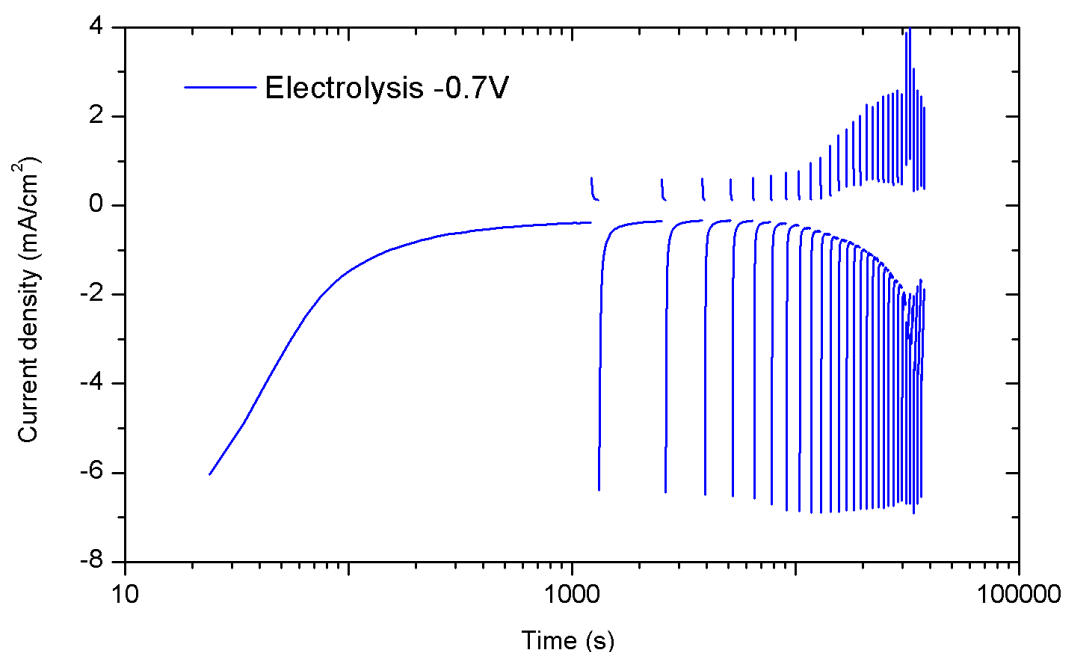


*Figure 7.19 Potentiostatic electrolysis at -0.7V with periodic anodic biasing as function of time. Electrolyte: 10mM pyridine in 0.5M KCl aqueous solution. Conditions: 25 °C and 55bar CO<sub>2</sub>*

A second electrochemical technique was tested to alleviate the electrode poisoning. Contrast electrode polarisation program was conducted by periodic potentiostatic biasing at 0V- 0.9V (Figure 7.20a), 0V-1V (Figure 7.20b) and 0V-0.65V (Figure 7.20c). For the 0V-1V biasing mode the reduction potential is switched from -1V to -0V for ~1min over the electrolysis duration (~3h). This was followed by -0V-0.65V biasing every ~1min for ~10h. Finally, the system was left for ~24h under the 0V- 0.9V regime for 2 min at every 30 minutes. At -0.9-1V bias, gas bubbles were intensively formed on the electrode surface. This technique clearly assisted in achieving high average electrolysis current density ~3mA/cm<sup>2</sup> (Figure 7.20c). Considering that HER is very efficient on Pt electrode in acid solutions (Hori 2008), the gas bubbles generated at such (relatively) high bias are most likely to be hydrogen macro bubbles which were intensively generated (visually observed). These bubbles are expected to be efficient in replacing the adsorbed CO or preventing CO adsorption, hence freeing the electrode surface from these species (Swaddle & Tregloan 1999). However, no enhancement of the methanol FY was observed with 0.25-0.5ppm concentration range detected after each experiment.

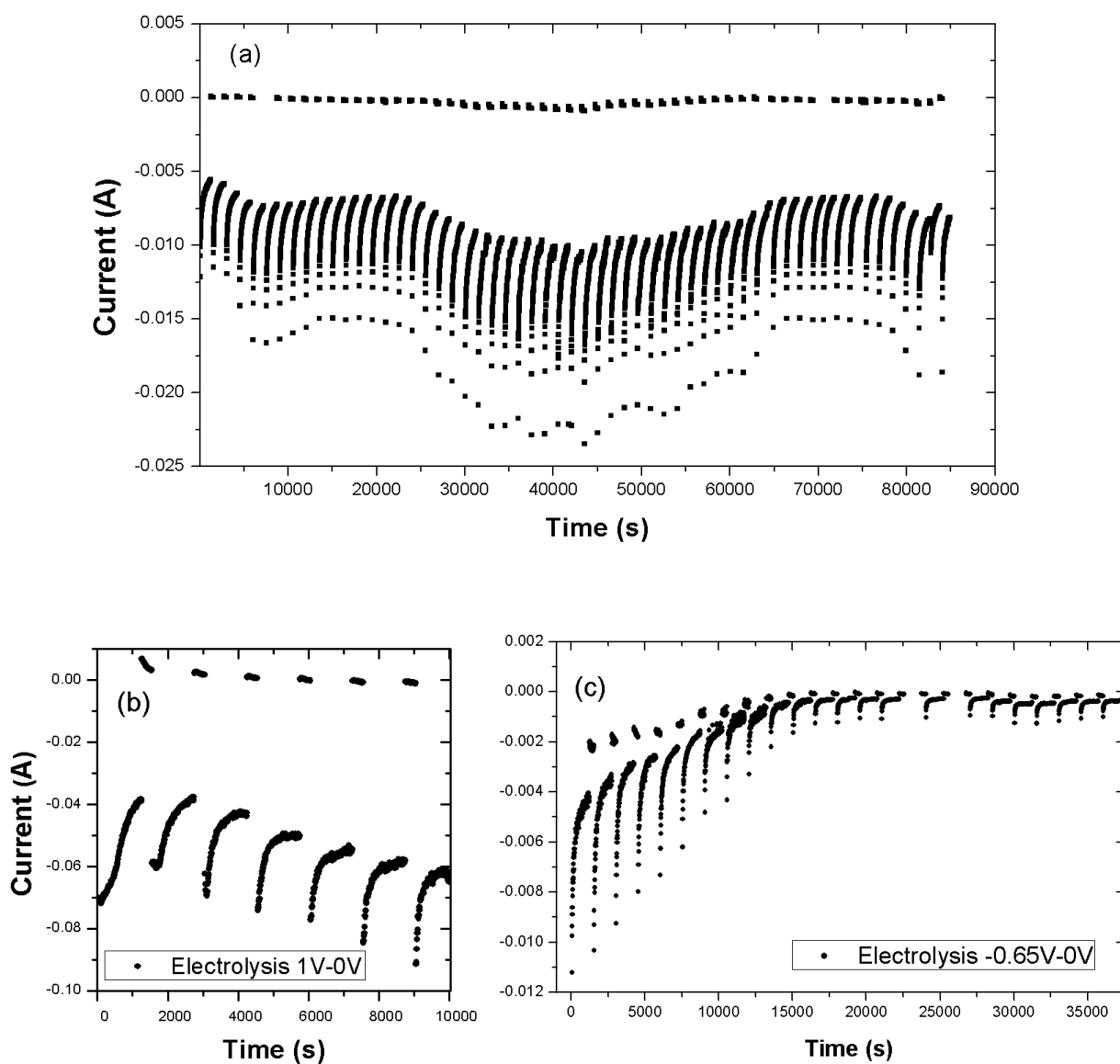


Figure 7.20 Potentiostatic electrolyses at alternating potential as function of time. Electrolyte: 200mM pyridine in 0.5MKCl aqueous solution. Conditions: 25°C and 55bar CO<sub>2</sub>. (a) 0V-0.9V, (b) 0V-1V and (c) 0V-0.65V

Another attempt, which aimed at FY enhancement by CO suppression, was performed with a periodic CO<sub>2</sub> pressure variation programme. The pressure programme was performed in a galvanostatic mode at  $-150\mu\text{A}/\text{cm}^2$  for ~20h total electrolysis duration (Figure 7.21).

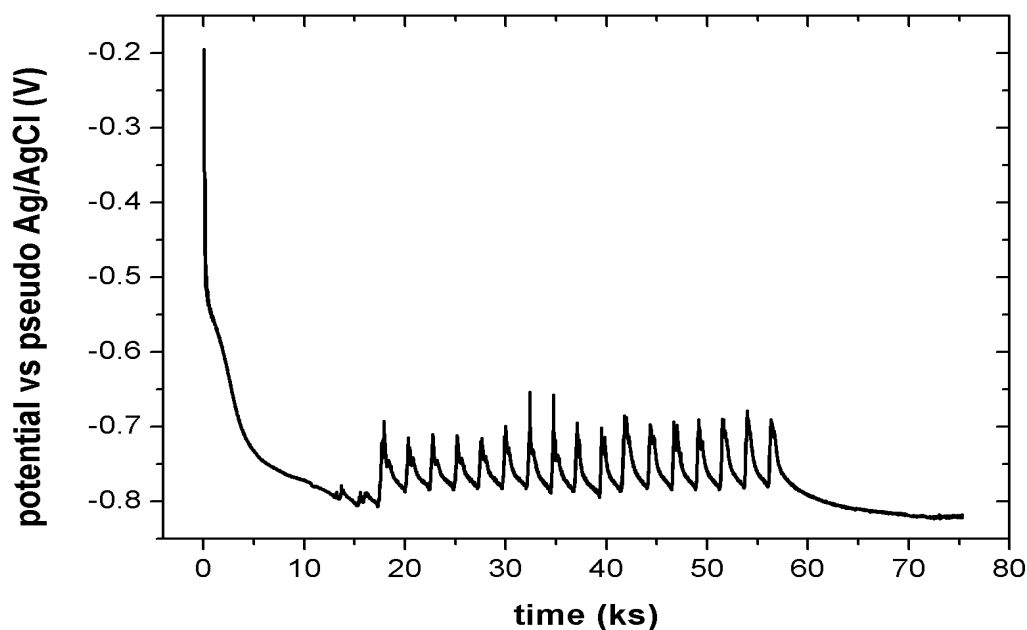
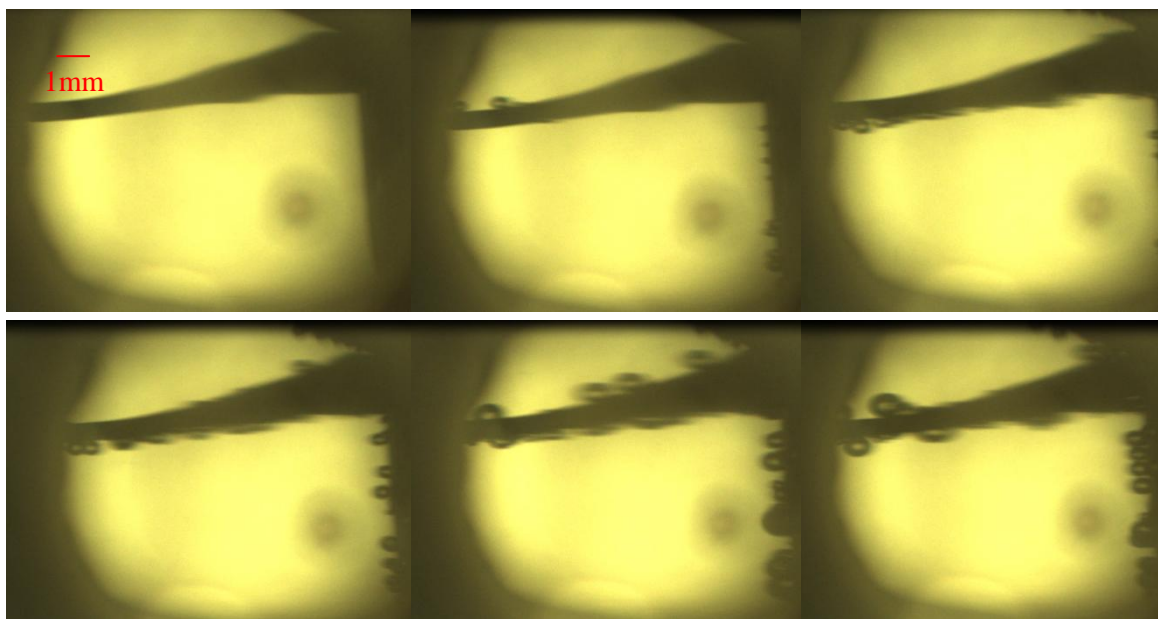


Figure 7.21 Galvanostatic electrolysis ( $-150 \mu\text{A}/\text{cm}^2$ ) at alternating  $\text{CO}_2$  pressure (63-40bar) as function of time. Electrolyte: 200mM pyridine in 0.5 M KCl aqueous solution. Conditions: 25 °C.

The programme consisted of sequences of pressure variations over ~10h. First, the pressure was gradually increased to 63bar; then it was quickly decreased to 40bar over 20min. The sudden decrease of the pressure induces the formation of  $\text{CO}_2$  micro bubbles on the Pt surface growing into macro bubbles as shown in Figure 7.22. The  $\text{CO}_2$  micro-bubbles were expected to replace the adsorbed CO on the Pt surface. The experiment conducted by this procedure did not differ from the previous method. Methanol amounts detected in all these experiments ranged between 0.25-0.5ppm with Faradaic yields  $<0.1\%$ . The different techniques of reactivation of the WE (by means of  $\text{H}_2$  or  $\text{CO}_2$  bubbles), clearly indicates that the FY limit is unlikely to be related to the electrode poisoning by any adsorbed intermediate(s).



*Figure 7.22*  $\text{CO}_2$  macro bubbles formation corresponding to the galvanostatic electrolysis at alternating  $\text{CO}_2$  pressure (63-40bar) of Figure 7.21. The formation proceeds in the following sequence: (1) top left, (2) top middle, (3) top right, (4) bottom left, (5) bottom middle and (6) bottom right. Electrolyte: 200mM pyridine in 0.5 M KCl aqueous solution. Conditions: 25 °C.

### 7.3.3.6 Underpotential $\text{CO}_2$ -pyridine Reduction

Surprisingly, methanol was also produced at a cathodic potential below the equilibrium potentials of both of HER (-0.42V at pH7 or -0.36V at pH5) and reduction of  $\text{CO}_2$  to methanol (-0.38V at pH7 or -0.32V at pH5). Galvanostatic electrolysis was conducted at low current density ( $50 \mu\text{A}/\text{cm}^2$ ) over ~2days. The variation of the electrode potential for such an experiment is shown in Figure 7.23. For the entire duration of electrolysis, the potential did not exceed -0.3V. This observation is consistent with the previously reported production of formate at potentials lower than the potential of hydrogen production on a Pd electrode (Hori et al. 2005).

Another noteworthy observation of methanol production was revealed by hydrogenated Pd electrode experiments at atmospheric pressure (1bar  $\text{CO}_2$ ). Pre-hydrogenated Pd wire ( $2.56\text{cm}^2$  at  $-2.3\text{mA}/\text{cm}^2$  for ~100C charge passed) was immersed in  $\text{CO}_2$  saturated (by bubbling) electrolyte (10mM pyridine in 0.5M KCl). The experiments were performed in a sealed vial and stored at room temperature for ~30h. Methanol was detected with  $0.2 \pm 0.02\text{ppm}$  and  $0.35 \pm 0.03\text{ppm}$  in two identical conditions experiments. In the above described experiments, methanol production process seems to be unrelated to the charge

transfer on the electrode. This is in agreement with the observed insensitivity of the methanol production to the electrode current density and the biasing potential reported earlier. The observations suggest that the electrochemically produced hydrogen is subsequently reacting with CO<sub>2</sub> to form the alcohol. Rather than the direct reduction of CO<sub>2</sub> on the electrode surface to form methanol suggested by Bocarsly and co-workers (Cole et al. 2010).

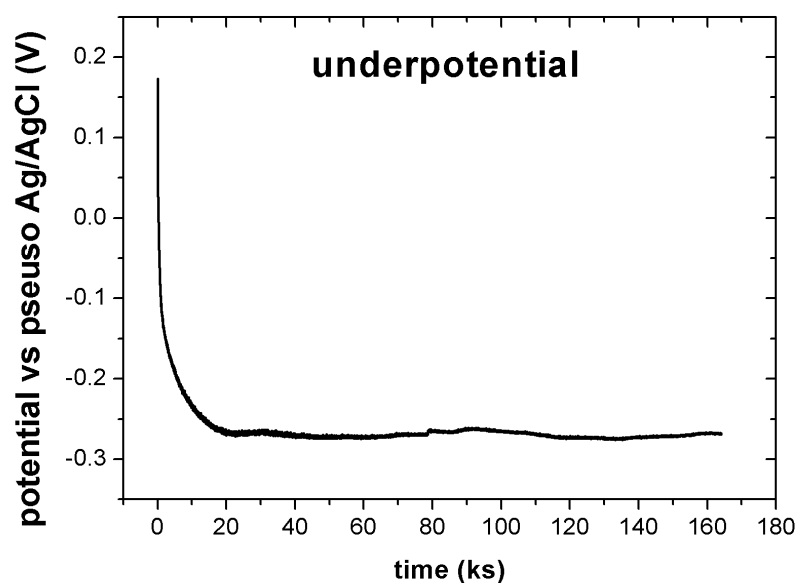


Figure 7.23 Variation of the potential in (underpotential) galvanostatic electrolysis at  $50\mu\text{A}/\text{cm}^2$ : Electrolyte: 200mM pyridine in 0.5M KCl. Conditions: 55bar of CO<sub>2</sub> and 25 °C.

### 7.3.3.7 Summary

The present bulk electrolysis experiments have confirmed the methanol production in the CO<sub>2</sub>-pyridinium reduction at Pt electrode. In addition to methanol higher alcohols were detected in such system. Pyridine proved to be essential in this process since direct CO<sub>2</sub> reduction resulted in no formation of methanol or any other alcohols. However, no optimal pyridine concentration for methanol production could be revealed. At Pt electrodes and the experimental conditions studied, methanol Faradaic yield was found to be limited to a maximum of ~10% for a low charge passed (~10C); corresponding to sub-ppm concentration level (<1ppm). High CO<sub>2</sub> concentrations do not seem to be critical in this process as comparable methanol yields were observed in high pressure and atmospheric pressure experiments. Furthermore, the limitation of the FY did not

correlate with the selected potential or the current density as methanol was formed in the low concentration range regardless of the biasing regime.

The limit on methanol Faradaic yield observed was initially linked to the significant decrease of the electrolytic current. Accordingly, attempts were made to solve the current decay issue. Although, the electrolytic purification assisted in maintaining reasonably steady state currents this procedure did not seem to be effective in enhancing the Faradaic yields. On the other hand, the electrolytic current drop was found to be severely affected by the CO adsorption on the cathode surface. Most importantly, this drop does not seem to be directly related to the methanol Faradaic yields. The attempts to activate the electrode by alleviating the adsorption of intermediate(s)/product species from the electrode surface also did not prove effective, since the methanol amounts remained at the typical low concentration level. The reason for the FY limit remains unclear. Yet, the limit of methanol production does not seem to be hindered by the lack of available hydrogen. At the same time, the methanol formation appears to be unrelated to the charge transfer on the electrode. This is evidenced by the detection of typical amounts at underpotential below the equilibrium methanol potential. The limited methanol production under all the above conditions suggests a lack of support for a direct CO<sub>2</sub> reduction to methanol at the cathode, which is supported by the chemical production of methanol on hydrogenated Pd. Further investigation of the methanol production via this route is needed.

## References of Chapter 7

- Augustynski, J., Jermann, B. & Kedzierzawski, P., 1996. Electroreduction of Carbon Dioxide in Aqueous Solutions at Metal Electrodes. *American Chemical Society Division Fuel Chemistry*, 41, pp.1420–1424.
- Bard, A. & Faulkner, L., 2002. Allen J. Bard and Larry R. Faulkner, *Electrochemical Methods: Fundamentals and Applications*, New York: Wiley, 2001. *Russian Journal of Electrochemistry*.
- Barton, E.E., Rampulla, D.M. & Bocarsly, A.B., 2008. Selective solar-driven reduction of CO<sub>2</sub> to methanol using a catalyzed p-GaP based photoelectrochemical cell. *Journal of the American Chemical Society*, 130(20), pp.6342–6344.
- Bocarsly, A.B., 2013. Conversion of CO<sub>2</sub> to organic products. *Patent Application Publication*, 1(19), pp.1–10.
- Boston, D.J. et al., 2013. Photochemical reduction of carbon dioxide to methanol and formate in a homogeneous system with pyridinium catalysts. *Journal of the American Chemical Society*, 135(44), pp.16252–5.
- Cheng, J. & Jandik, P., 2009. Electroactivity of nitriles on platinum electrodes and its use in chromatographic detection. *Electrochemistry Communications*, 11(8), pp.1615–1617.
- Clavilier, J. et al., 1981. Electrochemical adsorption behaviour of Pt(100) in sulphuric acid solution. *Journal of Electroanalytical Chemistry and Interfacial Electrochemistry*, 127(1-3), pp.281–287.
- Cole, E.B. et al., 2010. Using a one-electron shuttle for the multielectron reduction of CO<sub>2</sub> to methanol: kinetic, mechanistic, and structural insights. *Journal of the American Chemical Society*, 132(33), pp.11539–51.
- Costentin, C. et al., 2013. Electrochemistry of acids on platinum. Application to the reduction of carbon dioxide in the presence of pyridinium ion in water. *Journal of the American Chemical Society*, 135(47), pp.17671–4.
- DeWulf, D.W., 1989. Electrochemical and Surface Studies of Carbon Dioxide Reduction to Methane and Ethylene at Copper Electrodes in Aqueous Solutions. *Journal of The Electrochemical Society*, 136(6), p.1686.
- Hara, K., Kudo, A. & Sakata, T., 1995. Electrochemical reduction of carbon dioxide under high pressure on various electrodes in an aqueous electrolyte. *Journal of Electroanalytical Chemistry*, 391(1-2), pp.141–147.
- Hara, K. & Sakata, T., 1995. Electrochemical reduction of high pressure carbon dioxide on Fe electrodes at large current density. *Journal of Electroanalytical Chemistry and Interfacial Electrochemistry*, 386, pp.257–260.

- Hori, Y. et al., 2005. "Deactivation of copper electrode" in electrochemical reduction of CO<sub>2</sub>. *Electrochimica Acta*, 50(27), pp.5354–5369.
- Hori, Y., 2008. Electrochemical CO<sub>2</sub> Reduction on Metal Electrodes. In *Modern Aspects of Electrochemistry*. pp. 89–189.
- Hori, Y., Kikuchi, K. & Suzuki, S., 1985. Production of CO and CH<sub>4</sub> in electrochemical reduction of CO<sub>2</sub> at metal electrodes in aqueous hydrogencarbonate solution. *Chemistry Letters*, (11), pp.1695–1698.
- Hori, Y. & Suzuki, S., 1983. Cathodic reduction of carbon dioxide for energy storage. *J. Res. Inst. Catal., Hokkaido Univ.*, 30(Copyright (C) 2011 American Chemical Society (ACS). All Rights Reserved.), pp.81–88.
- L.D.Burke, 1994. Noble Metal. *Platinum Metals Review*, 38(4), pp.166–173.
- Le, M. et al., 2011. Electrochemical Reduction of CO<sub>2</sub> to CH<sub>3</sub>OH at Copper Oxide Surfaces. *Journal of The Electrochemical Society*, 158(5), p.E45.
- Łukaszewski, M., Siwek, H. & Czerwiński, a., 2008. Electrosorption of carbon dioxide on platinum group metals and alloys—a review. *Journal of Solid State Electrochemistry*, 13(6), pp.813–827.
- Mairanovskii, S., 1962. Polarographic determination of the protonation rate constants of pyridine and some of its homologs as affected by water. , (Iii), pp.731–734.
- Morris, A.J., McGibbon, R.T. & Bocarsly, A.B., 2011. Electrocatalytic carbon dioxide activation: The rate-determining step of pyridinium-catalyzed CO<sub>2</sub> reduction. *ChemSusChem*, 4(2), pp.191–196.
- Pletcher, D. & Sotiropoulos, S., 1994. Hydrogen adsorption?desorption and oxide formation?reduction on polycrystalline platinum in unbuffered aqueous solutions. *Journal of the Chemical Society, Faraday Transactions*, 90(24), p.3663.
- Priyantha, N. & Malavipathirana, S., 1996. Effect of chloride ions on the electrochemical behavior of platinum surfaces. *Journal of the National Science Council of Sri Lanka*, 24(3), pp.237–246.
- Sawyer, D.T.T.A.M.U. & Roberts, J.L.J.U.O.R., 1994. Electrochemistry for Chemists Second Edition. *JOHN WILEY SONS INC*, p.133.
- Seshadri, G., Lin, C. & Bocarsly, A.B., 1994. A new homogeneous electrocatalyst for the reduction of carbon dioxide to methanol at low overpotential. *Journal of Electroanalytical Chemistry*, 372(1-2), pp.145–150.
- Srejić, I. et al., 2011. Oxygen reduction on polycrystalline Pt and Au electrodes in perchloric acid solution in the presence of acetonitrile. *International Journal of Electrochemical Science*, 6(8), pp.3344–3354.

- Swaddle, T.W. & Tregloan, P.A., 1999. Electrode reactions of metal complexes in solution at high pressures. *Coordination Chemistry Reviews*, 187(1), pp.255–289.
- De Tacconi, N.R. et al., 2012. Electrocatalytic Reduction of Carbon Dioxide Using Pt/C-TiO<sub>2</sub> Nanocomposite Cathode. *Electrochemical and Solid-State Letters*, 15(1), p.B5.
- De Valera, V., 1953. On the theory of electrochemical chlorate formation. *Transactions of the Faraday Society*, 49(1338), p.1338.
- Wasberg, M., 1994. Isopotential point: A singularity in the voltammetric behaviour of platinum metal electrodes characterising adsorption competition. *Journal of Electroanalytical Chemistry*, 379(1-2), pp.541–544.
- Yang, Y.-F. & Denuault, G., 1998. Scanning electrochemical microscopy (SECM): study of the formation and reduction of oxides on platinum electrode surfaces in Na<sub>2</sub>SO<sub>4</sub> solution (pH=7). , 8.
- Yasukouchi, K. et al., 1979. Cathodic reduction of pyridinium ion in acetonitrile. *Journal of Electroanalytical Chemistry and Interfacial Electrochemistry*, 105(2), pp.403–408.
- Zhan, D., Velmurugan, J. & Mirkin, M. V, 2009. Adsorption/desorption of hydrogen on Pt nanoelectrodes: evidence of surface diffusion and spillover. *Journal of the American Chemical Society*, 131(41), pp.14756–60.

# Conclusions

The key conclusions drawn from this project are as follows:

- The bulk electrolysis experiments of the CO<sub>2</sub> reduction in pyridine-containing electrolytes confirmed the methanol production reported by several groups (Boston et al. 2013) (Cole et al. 2010) (Zeng et al. 2014). In the absence of pyridine, the product analysis of the direct CO<sub>2</sub> electrolysis showed no alcohol formation. This explicitly confirms the importance of pyridine in the studied CO<sub>2</sub> to methanol reduction process. At the same time, no correlation with the methanol amount produced could be revealed over the entire pyridine concentration range studied (~1 μM to 1M).
- However, the produced methanol amounts were limited to the sub-ppm level irrespectively of the passed charge and the electrolysis mode. This is reflected in a dynamic character of the methanol Faradaic yield, which was found to be comparable (~10%) to that reported by the Bocarsly group for a low charge passed (~10C), but was decreasing steadily with higher passed charge. This very important feature has not been reported before.
- In order to investigate the observed limit on methanol production, an effect of possible electrode deactivation caused by deposition of either cationic impurities or reaction intermediates/products was evaluated. It was found that electrolyte purification by pre-electrolysis do not assist in enhancing the methanol concentration. Several physical and electrochemical methods of electrode re-activation also did not prove effective. Hence, the reason for the methanol production limit remains unclear however it is unlikely to be due to electrode deactivation during the electrolysis.
- High CO<sub>2</sub> pressure (concentration) does not seem to be critical for the reduction process as comparable methanol yields were observed in the high pressure and the atmospheric pressure experiments. However, at high CO<sub>2</sub> pressure, higher alcohols were detected in addition to the methanol after electrolysis at pyridine

concentrations  $\sim >10\text{mM}$ . The formation of higher alcohols was not reported before for the pyridine-assisted  $\text{CO}_2$  reduction on Pt (or Pd) electrode.

- Analysis of the cyclic voltammetry data supported by simulation revealed that the electrode reduction in  $\text{CO}_2$ -pyridine system is merely pyridinium assisted molecular hydrogen production under all conditions investigated. Based on the voltametric studies no evidence of direct  $\text{CO}_2$  contribution into the electrode reduction process was found.
- The electrochemical behaviour of pyridine (pyridinium) on Pt electrode revealed a simple weak acid behaviour. Specifically, the electrochemical activity of pyridine is best represented (simulated) as a combination of two electrode reactions. One is the common reduction of hydrated protons and the second is a direct pyridinium reduction (via termolecular reaction), leading in both cases to molecular hydrogen formation. The relative contribution of each electrode reaction is defined by the particular combination of the pyridine concentration and the acidity of the medium. Both reactions can be clearly distinguished at low pH as two CV waves at  $-0.43\pm 0.01\text{V}$  and  $-0.56\pm 0.01\text{V}$  are observed corresponding to the hydrated protons reduction and the pyridinium reduction respectively.
- The effect of  $\text{CO}_2$  on the reduction processes in pyridine-containing electrolyte at Pt electrode has three distinctive features:
  - (1) When pyridinium reduction is the dominating electrode reaction (in weakly acidic medium  $\text{pH} > 4.5$  or large pyridine concentrations ( $>1\text{mM}$ )), the effect of  $\text{CO}_2$  simply represents a re-protonation source for pyridine. Hence it replenishes the exhausted pyridinium concentration in the vicinity of the electrode and increases the current. The re-protonation cycle is sourced by protons released from  $\text{H}_2\text{CO}_3$  dissociation, which in turn is produced via the hydration of dissolved  $\text{CO}_2$ . The overall reaction system was characterised as an EC' mechanism (coupled catalytic chemical reaction), where the  $\text{CO}_2$  hydration reaction is the rate-limiting step. The system is characterised by an increased current under  $\text{CO}_2$  is higher at slow scan rates as compared to fast scan speeds.

- (2) At low pH and low pyridine concentration ( $<1\text{mM}$ ), the effect of pyridine on the reduction current is negligible, in this case the direct proton reduction is the dominant electrode process. At these conditions, the effect of  $\text{CO}_2$  is reflected in replenishment of the proton concentration in the vicinity of the electrode and hence the increase of the current. Correspondingly, the overall reaction system is of CE type (preceding coupled chemical reaction).
- (3) Since in any case the enhancement of the reduction current is proportional to the excess of dissolved  $\text{CO}_2$ , the reduction current was observed to increase with  $\text{CO}_2$  pressure. The limit of the current enhancement observed above  $\sim 50$  bar is related to the saturation limit of  $\text{CO}_2$  dissolution in aqueous electrolyte.

The cumulative evidence of the results discussed in this thesis show that the methanol formation process seems to be decoupled from the charge transfer on the electrode. Instead the results suggest that methanol is rather being produced chemically via interaction of  $\text{CO}_2$  molecules with electrochemically generated hydrogen, mediated by pyridine (pyridinium) molecules and probably by Pt surface. This is further supported by the experiments with production of methanol on hydrogenated Pd in pyridine solution. Further investigation of the methanol production *via* this route could be promising. The bulk production of methanol using  $\text{CO}_2$ -pyridinium system where hydrogen is pre- electrochemically generated is worth the investigation. The optimisation of the chemical reaction conditions might lead to better methanol yields.

## Appendix A

### A.1 Reversible Nernstian System: Randle Sevcik Equation Derivation

The direct use of Laplace transform to solve this boundary problem is produced in the form of an equation. However the differential equations can be converted into integral equations by taking the Laplace transform of equations 1-4 solving for the transform of the surface concentrations in terms of the transform of the surface fluxes, then applying the convolution theorem

$$C_O(0, t) = C_O^* - \frac{1}{\sqrt{\pi D_O}} \int_0^t \frac{f(\tau) d\tau}{\sqrt{t - \tau}}$$

$$C_R(0, t) = \frac{1}{\sqrt{\pi D_R}} \int_0^t \frac{f(\tau) d\tau}{\sqrt{t - \tau}}$$

Where

$$f(t) = D_O \left( \frac{\partial C_O}{\partial x} \right)_{x=0} = i/nFA$$

If we combine equation with equations we obtain

$$\int_0^t \frac{i(\tau)}{\sqrt{t - \tau}} d\tau = \frac{nFA \sqrt{\pi D_O} C_O^*}{e^{(nF/RT)(E_i - E^0)} e^{-(nF/RT)vt} \sqrt{D_O/D_R}}$$

To obtain the current-time curve numerical solution or the current-potential for the latter is proportional to time (equation) some substitutions needs to be made (i.e. the current as a function of time  $i(t)$  can be changed to the current as a function of potential  $i(E)$  and the potential scan rate-time to the potential difference (equation)). Integrating equation and rearranging gives

$$i = nFAC_O^* \sqrt{\pi D_O (nF/RT)v} \chi((nF/RT)vt)$$

This equation relates the current to the variables at any point on the linear sweep voltammetry curve. The term  $\sqrt{\pi} \chi((nF/RT)vt)$  was calculated by Nicholson and Shain. The current reaches maximum limit at  $\sqrt{\pi} \chi((nF/RT)vt) = 0.4463$  and the peak current  $i_p$  is given by

$$i_p = 0.4463 \sqrt{F^3/RT} n^{3/2} A D_O^{1/2} C_O^* v^{1/2}$$

If  $A$  is in  $\text{cm}^2$ ,  $D_O$  in  $\text{cm}^2/\text{s}$ ,  $C_O^*$  in  $\text{mol}/\text{cm}^3$ , and  $v$  in  $\text{V}/\text{s}$  we calculate the second term of equation at  $25^\circ\text{C}$  we obtain

$$i_p = (2.69 \times 10^5) n^{3/2} A D_O^{1/2} C_O^* v^{1/2}$$

## A.2 Methanol Faradaic Efficiency Calculation

The charge transferred defined as current by the time (theoretical charge)

$$Q = I \cdot t \quad (1)$$

Where  $Q$  in Coulomb,  $I$  current in A and  $t$  in seconds. The experimental charge is defined as:

$$Q = n_{\text{moles}} \cdot n_{e^-} \cdot F \quad (2)$$

Where  $F$  is Faraday Number ( $\text{coulomb} \cdot \text{mol}^{-1}$ ),  $n_{\text{moles}}$  is the numbers of moles and  $n_e$  is the number of electrons:

$$n_{e^-} \cdot F = 96485.33392$$

At 100% Faradaic efficiency the theoretical charge equals to the experimental charge:

$$(1)=(2) \quad \equiv \quad I \cdot t = n_{\text{moles}} \cdot n_{e^-} \cdot F$$

$$I \cdot t = n_{\text{moles}} \times 96485.33392$$

The number of moles of electrons:

$$n_{\text{moles}} = \frac{I \cdot t}{96485.33392} \text{ moles}$$

The number of moles for methanol (6 moles of electrons are required to produce, 1 mole of methanol)

$$\text{moles of methanol (mol)} = \frac{n_{\text{moles}}}{6} = \frac{I \cdot t}{6 \times 96485.33392} \text{ moles}$$

The concentration of methanol in part per million

$$\text{Concentration of methanol (ppm)} = \frac{\text{Moles of methanol}}{\text{Moles of water}}$$

If 20ml of aqueous electrolyte is taken in consideration

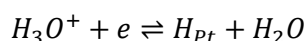
$$\text{moles of water (mol)} = \frac{\text{Mass of water}}{\text{Molar mass of water}}$$

$$\text{mass of water (mg)} = \frac{\text{Volume (cm}^3\text{)}}{\text{density of water (}\frac{\text{mg}}{\text{cm}^3}\text{)}}$$

$$\text{Concentration of methanol (ppm)} = \frac{\text{Moles of methanol}}{\text{Moles of water}} = \frac{I \cdot t}{0.58} * 10^{-6} = c_{\text{ppm}}$$

### A.3 Derivation of the Redox Potential Equation: Interrelation of the Simulated Electrode Reactions

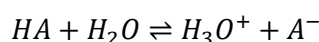
The redox equation is thermodynamically (Nernst equation) derived for hydrated proton reduction from a weak acid (pyridinium).



The redox potential of the hydrated protons reaction is written in terms of Gibbs energy equation:

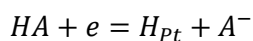
$$E_{H^+/H_{Pt}} = -(G_{H_{Pt}} + G_{H_2O} - G_e - G_{H_3O^+})/nF$$

Nernst equation is written for the acid dissociation



$$G_{A^-} + G_{H_3O^+} - G_{H_2O} - G_{HA} = -RT \ln K_a = 2.303RT \text{ p}K_a$$

Similarly the redox potential of the pyridinium reduction is written in terms of Gibbs energy equation:



$$E_{HA/H_{Pt},A^-} = -(G_{H_{Pt}} + G_{A^-} - G_e - G_{HA})/nF$$

Finally the redox potential equation relating the protons reduction to the pyridinium is written as follows:

$$E_{HA/H_{Pt},A^-} = E_{H^+/H_{Pt}} - (0.059/n)pK_a$$

#### A.4 Non-Faradaic Currents Equation Derivation

The non-Faradaic current  $i$  flowing at time  $t$  when potential  $E$  is applied is derived by the sum of the charge  $q$  on a capacitor as function of the potential and the voltage across a resistor:

$$E = E_R + E_C = iR + \frac{q}{C}$$

Rearranging and taking in consideration  $i=dq/dt$ , gives:

$$\frac{dq}{dt} = \frac{-q}{RC} + \frac{E}{R}$$

If the uncharged capacitor is considered ( $q=0$  at  $t=0$ ), the solution is given by:

$$q = EC[1 - \exp\left(\frac{-t}{RC}\right)]$$

By differentiation this equation, the following is obtained:

$$i = \frac{E}{R} e^{-t/RC}$$

## Appendix B

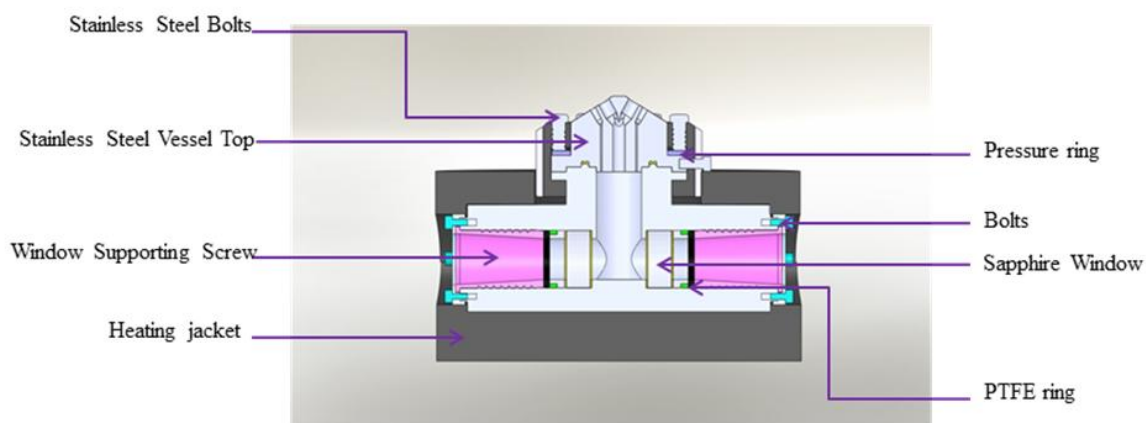


Figure B.1 Longitudinal view of the initially designed high pressure vessel

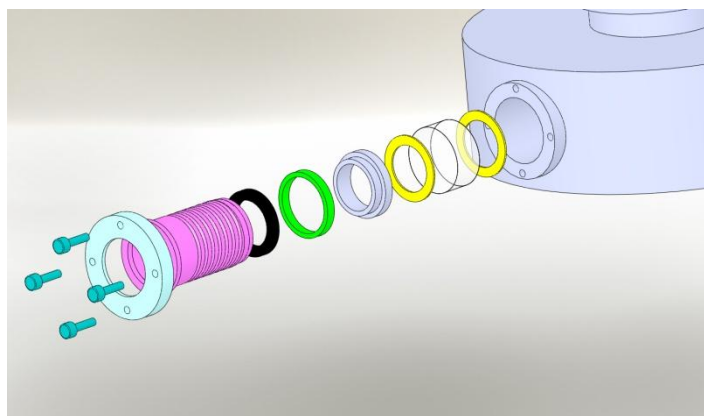


Figure B.2 Close view of the window sealing (Solid works) PTFE film (yellow), sapphire window (transparent), pressure ring (gray), PTFE high pressure seal (green) pressure distributing ring (black), and pressure screw (pink).

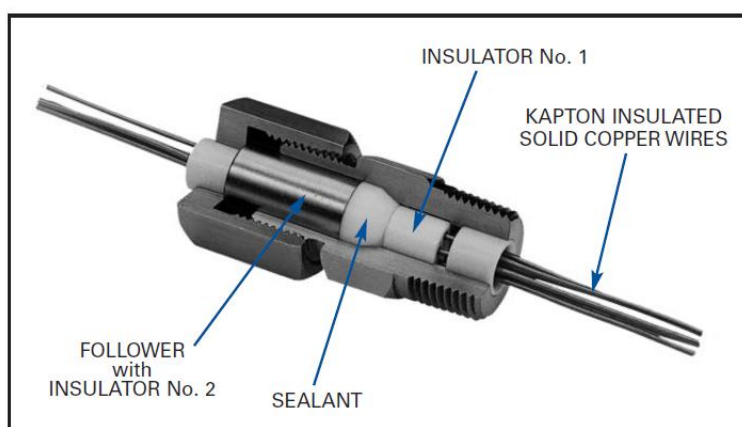


Figure B.3 Conax<sup>®</sup> sealing for electrode wires



## Appendix C

### C.1 Matlab Scripts Used for the Ionic Concentrations Calculations

#### C.1.1 Ionic Species Calculations in Aqueous Pyridine Solution

```
clear
kb=1.6e-9; % basic pyridine equilibrium constant
kw=1e-14; % water equilibrium constant
s=zeros(14,3);
N=14;
spacer=-1:0.1:N;
pyt=10.^(-spacer);
counter1=(N+1)/0.1+1;
s=zeros(counter1,3);

for i=1:counter1;
    p=[-1 -kb pyt(i)*kb+kw kb*kw]; % Cubic equation obtained in Chapter 5
    s(i,1:3)=roots(p);
    for j=1:3;
        if s(i,j)>0;
            OH(i)=s(i,j);
            H(i)=kw/OH(i);
            pH(i)=-log10(H(i));
        end
    end
    pyh(i)=(pyt(i)*kb)/(OH(i)+kb); % Pyridinium concentration

    py(i)=pyt(i)-pyh(i); % Pyridinium concentration
end

figure
plot(pyt,H,pyt,py,pyt,pyh)

PYratio=pyh./py;

figure
plot(pyt,PYratio);
figure
plot(H,PYratio);
```

## C.1.2 Ionic Species Calculations in Aqueous Pyridine-Strong Acid System

```
clear
ka=6.3e-6; % acidic pyridine equilibrium constant
kw=1e-14; % water equilibrium constant
s=zeros(14,3);
N=14;
M=10;

spacer=[0:0.1:N];
H=10.^(-spacer);
pH=-log10(H);
OH=kw./H;
counter=N/0.1+1;

spacer2=[0:1:M];
pyt=10.^(-spacer2); % multiply this by 2(*2) or 5 to get the desired
concentration(e.g.50mM or 200mM)
counter2=M+1;

pyh=zeros(counter,counter2);
py=zeros(counter,counter2);
s=zeros(counter,2);

    for j=1:counter2;% changing pyridine total concentration
        for i=1:counter;% changing pH/OH
            pyh(i,j)=pyt(j)*H(i)/(ka+H(i));
            py(i,j)=pyt(j)-pyh(i,j);
        end
    end

plot(H,pyh,H,py)
PYratio=pyh./py;
figure
plot(H,PYratio);
```

### C.1.3 Ionic Species Calculations in Aqueous Pyridine-CO<sub>2</sub> System

```
clear
ka2=3.55e-6;% acidic pyridine equilibrium constant
kw=1e-14;
ka1=4.45e-7;% CO2 equilibrium constant
co2=0.3522;% Calculated CO2 concentration at 20°C by Diamond program
% kh=0.0338;

%N=14;% maximum value of pH
M=10;% maximum value of Py total
% P=55;% maximum CO2 pressure (bar)

spacer2=[0:1:M];
pyt=10.^(-spacer2);
counter2=M+1;

pyh=zeros(counter2,1);
py=zeros(counter2,1);
H=zeros(counter2,1);
OH=zeros(counter2,1);
s=zeros(counter2,2);

for j=1:counter2;%changing py total concentration
% for i=1:counter3;%changing CO2 pressure
d=[-1 -ka2-pyt(j) (ka1*co2)+kw (ka1*ka2*co2)+kw*ka2];
s(j,1:3)=roots(d);
for n=1:counter2;
if s(n,2)>0;
H(j)=s(n,2);
OH(j)=kw/H(j);
pH(j)=-log10(H(j));
end
pyh(j)=(pyt(j)*kb)/(OH(j)+kb);
end
oh=OH(j);
hco(j)=(ka1*co2*oh)/kw;%bicarbonate ions concentration
py(j)=pyt(j)-pyh(j);
end

plot(pyt,H)
PYratio=pyh./pyt;
pytt=pyt';
plot(co2,py);
```

## Appendix D

### D.1 CVs under N<sub>2</sub> at different concentrations

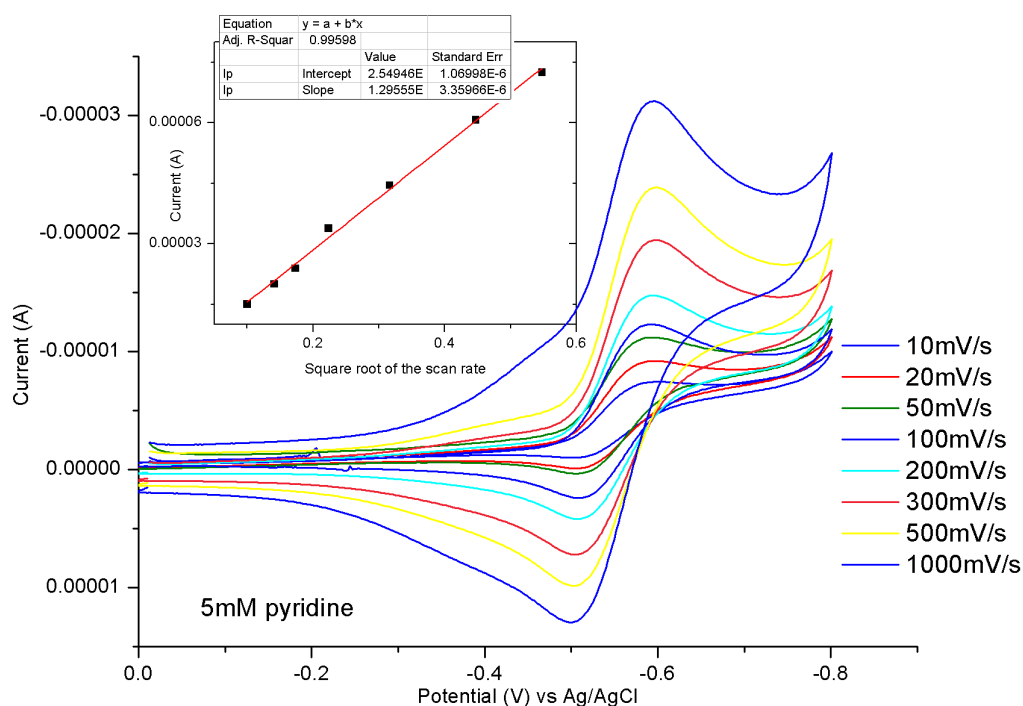


Figure D.1 CVs under N<sub>2</sub> of 5mM pyridine in 0.5M KCl at atmospheric pressure 20°C on Pt wire (0.07cm<sup>2</sup>). Inset: current vs. square root of the scan rates < 300mV/s

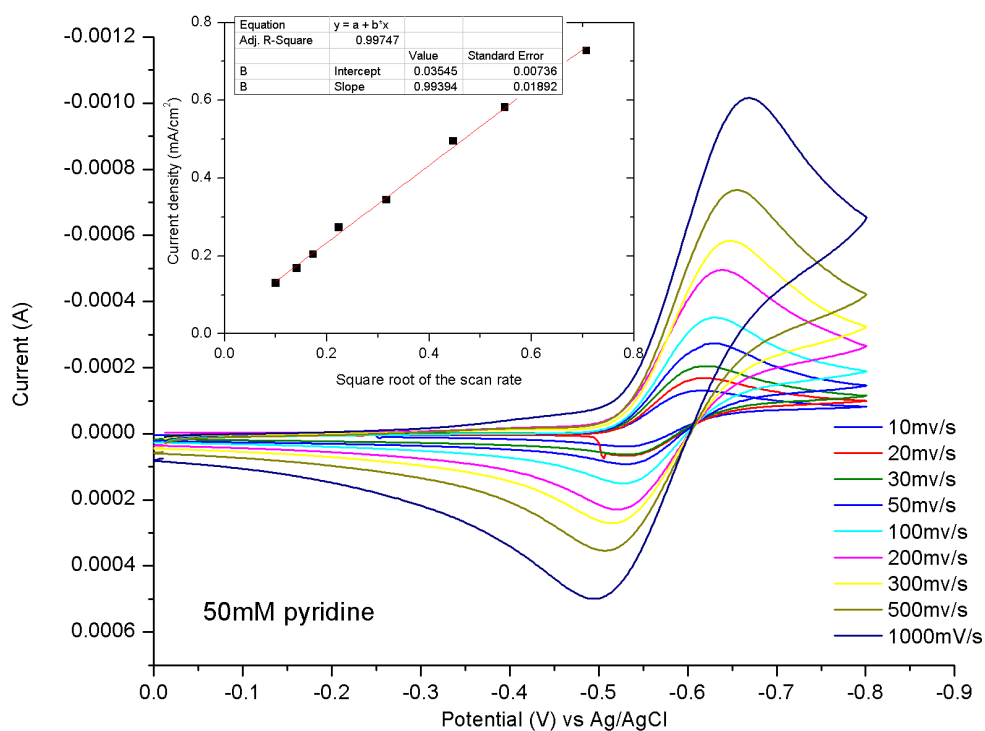


Figure D.2 CVs under N<sub>2</sub> of 50mM pyridine in 0.5M KCl at atmospheric pressure 20°C on Pt wire (0.07cm<sup>2</sup>). Inset: current vs. square root of the scan rates < 300mV/s

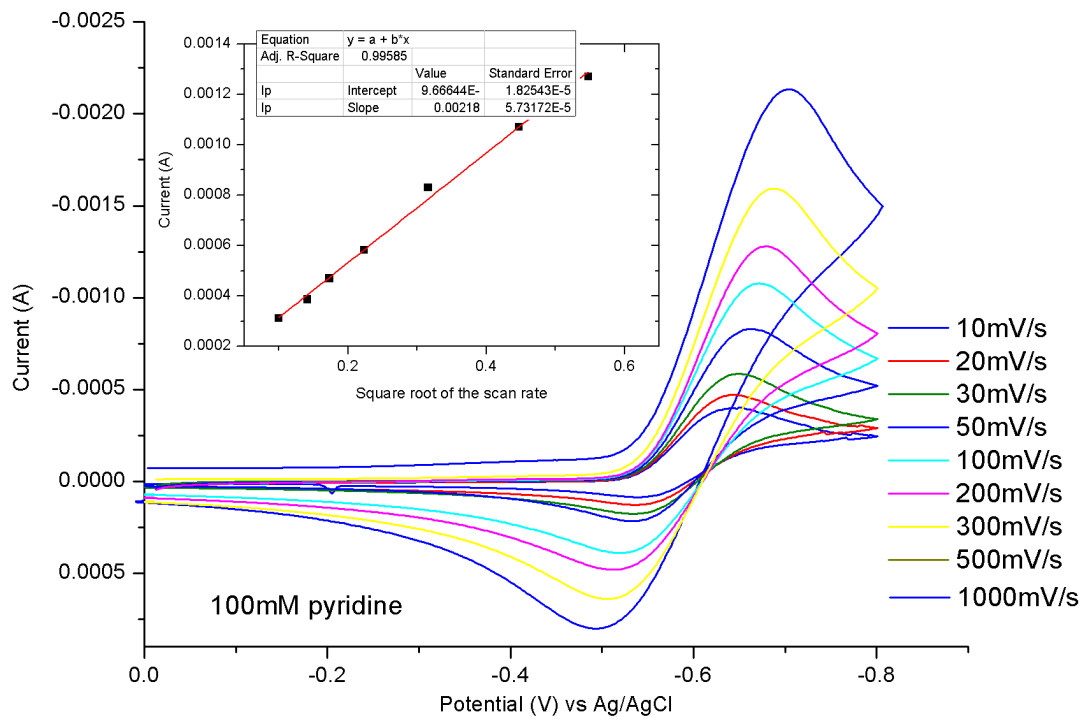


Figure D.3 CVs under  $N_2$  of 100mM pyridine in 0.5MKCl at atmospheric pressure 20°C on Pt wire ( $0.07\text{cm}^2$ ). Inset: current vs. square root of the scan rates  $< 300\text{mV/s}$

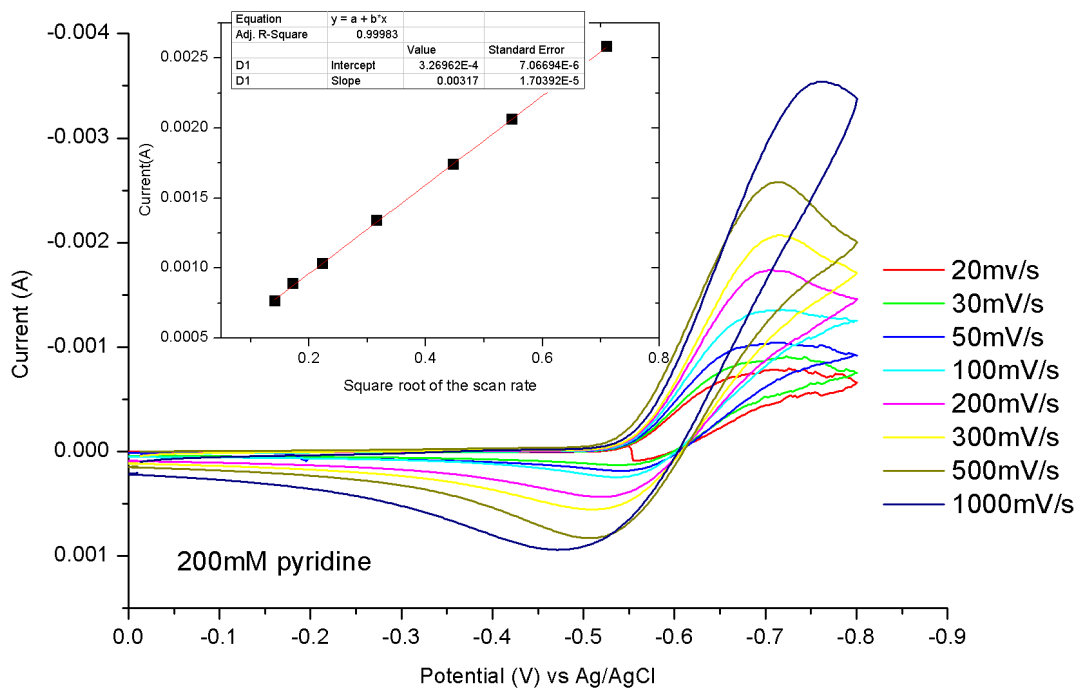


Figure D.4 CVs under  $N_2$  of 200mM pyridine in 0.5MKCl at atmospheric pressure 20°C on Pt wire ( $0.07\text{cm}^2$ ). Inset: current vs. square root of the scan rates  $< 300\text{mV/s}$

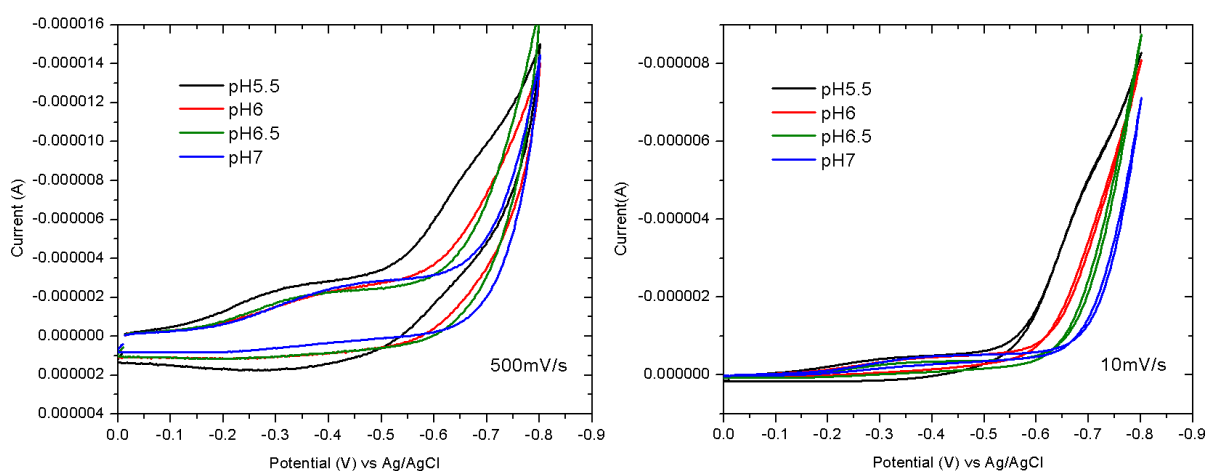


Figure D.5 CVs under  $N_2$  of 200mM pyridine in 0.5MKCl at atmospheric pressure 20°C on Pt wire ( $0.07\text{cm}^2$ ). Inset: current vs. square root of the scan rates  $<300\text{mV/s}$

## D.2 CVs under $\text{CO}_2$ at different concentrations at atmospheric pressure

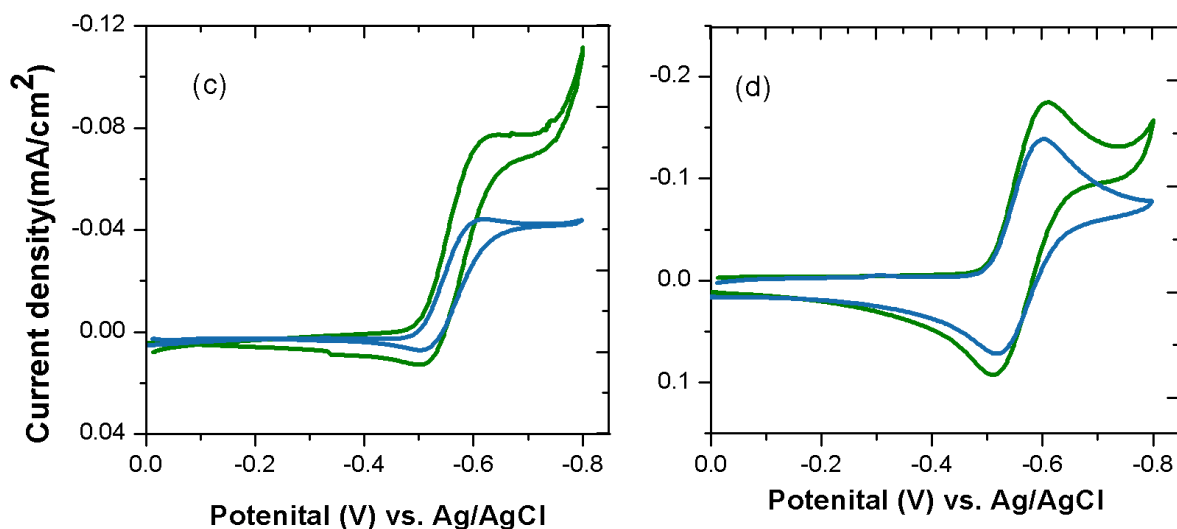


Figure D.6 CVs of 10mM pyridine in 0.5MKCl at atmospheric pressure 25°C (blue) under nitrogen, (green) under  $\text{CO}_2$  at (a) 5mV/s, (b) 500mV/s on Pt disk ( $100\mu\text{m}$  diameter). (c) 5mV/s, (d) 100mV/s on Pt  $0.6\text{cm}^2$  area.

### D.3 CVs under CO<sub>2</sub> at different concentrations at atmospheric pressure

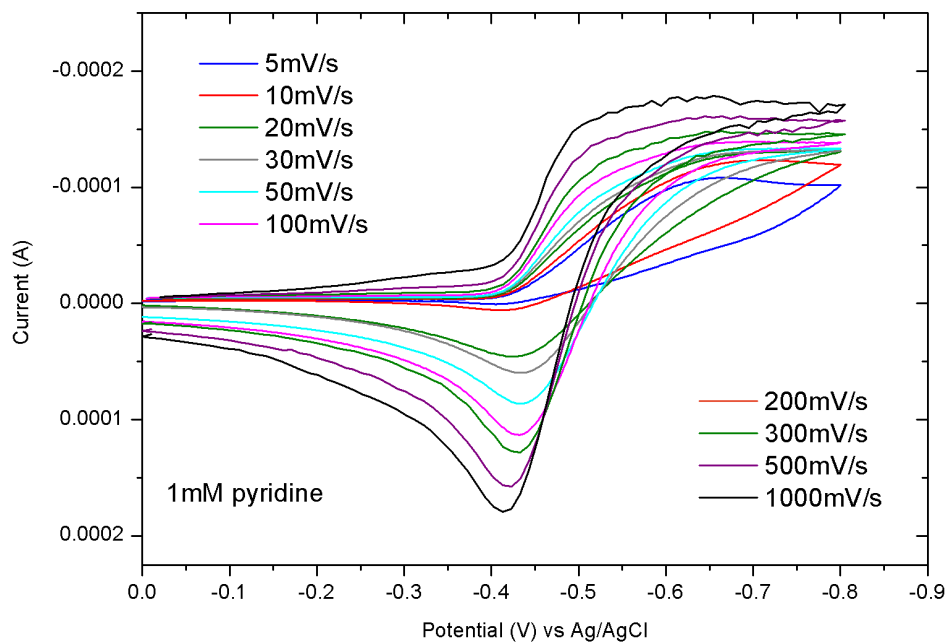


Figure D.7 CVs under 55bar CO<sub>2</sub> of 1mM pyridine in 0.5MKCl 20°C on Pt wire (0.07cm<sup>2</sup>).

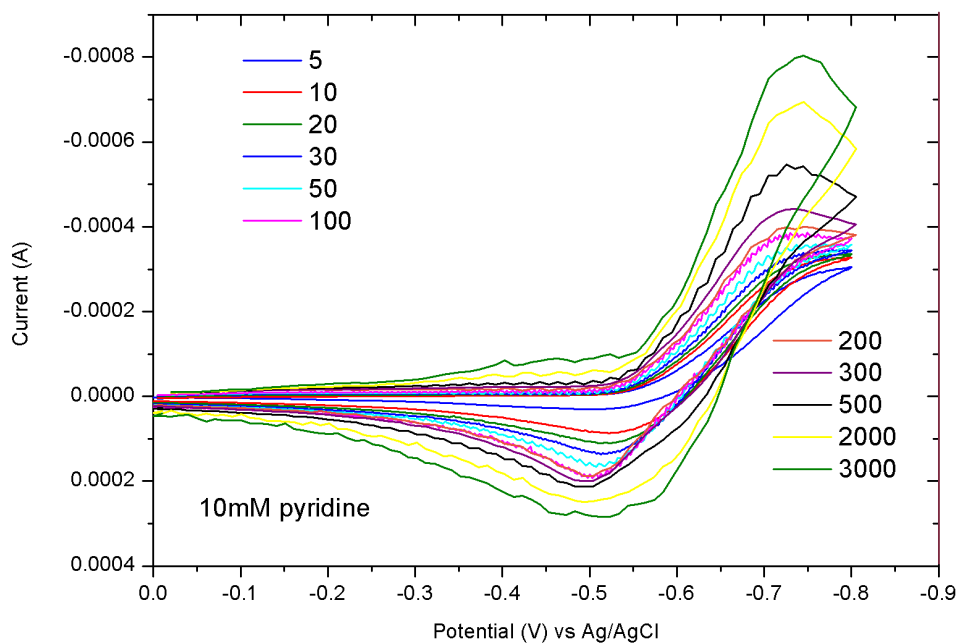


Figure D.8 CVs under 55bar CO<sub>2</sub> of 10mM pyridine in 0.5MKCl 20°C on Pt wire (0.07cm<sup>2</sup>).

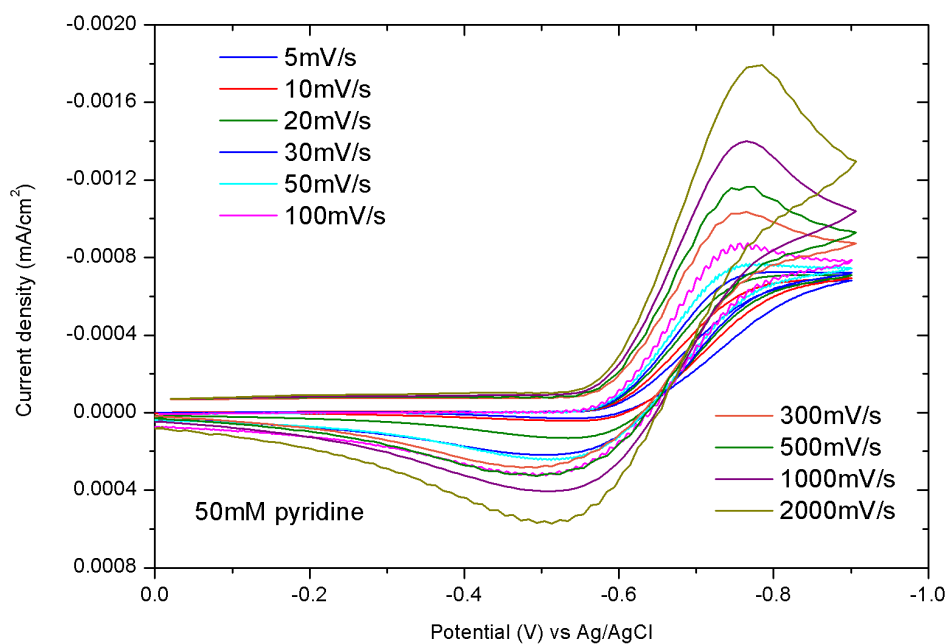


Figure D.9 CVs under 55bar CO<sub>2</sub> of 50mM pyridine in 0.5MKCl 20°C on Pt wire (0.07cm<sup>2</sup>).

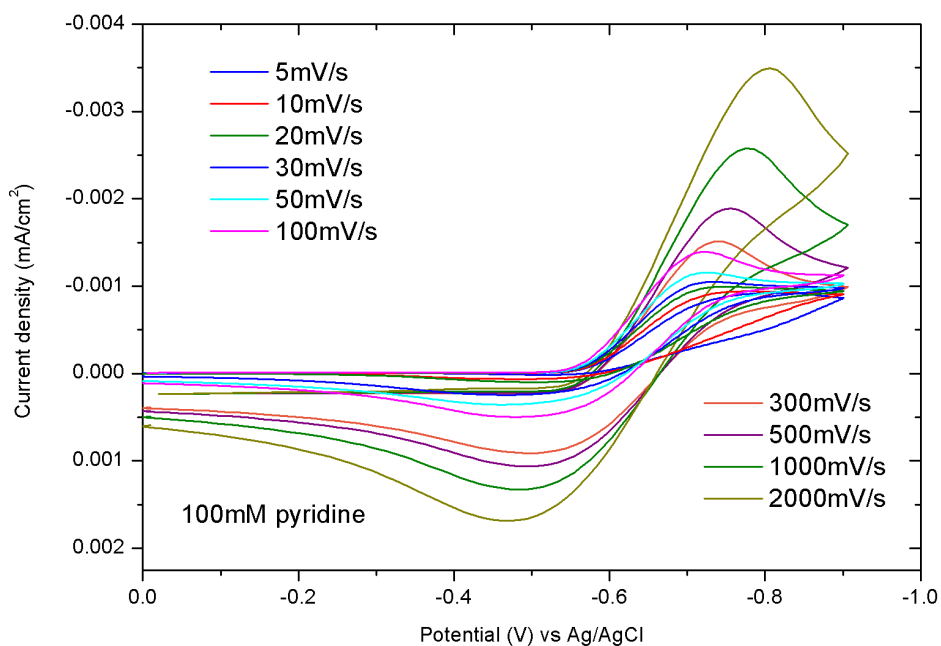


Figure D.10 CVs under 55bar CO<sub>2</sub> of 100mM pyridine in 0.5MKCl 20°C on Pt wire (0.07cm<sup>2</sup>).

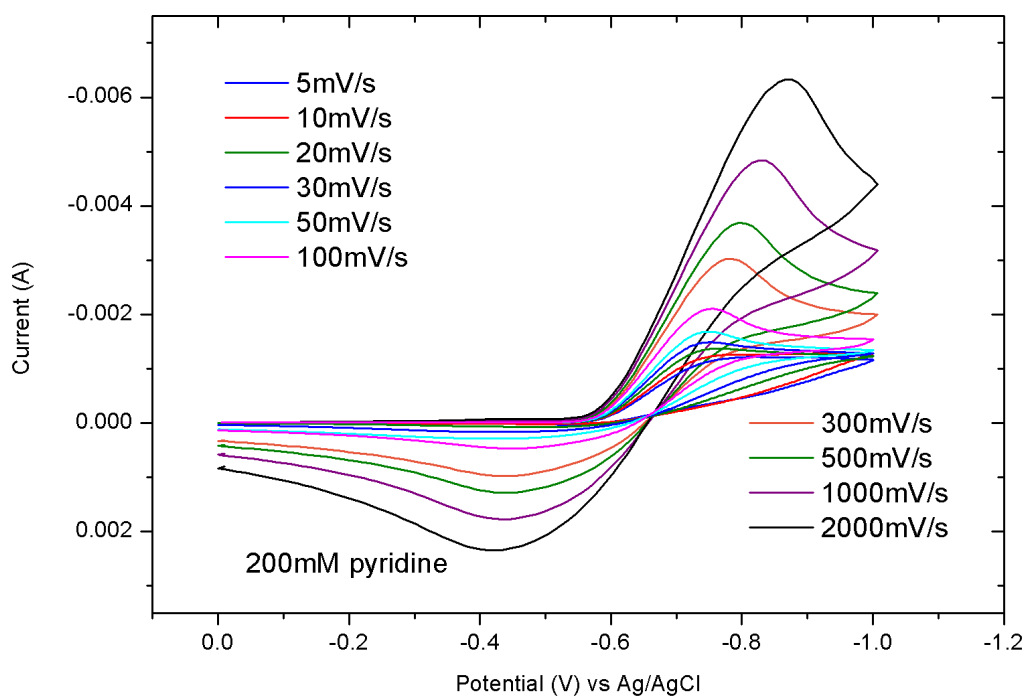


Figure D.11 CVs under 55bar CO<sub>2</sub> of 100mM pyridine in 0.5MKCl 20°C on Pt wire (0.07cm<sup>2</sup>).

## D.4 Mass spectra of methanol (CH<sub>3</sub>OH), ethanol (C<sub>2</sub>H<sub>6</sub>O), isopropanol (C<sub>3</sub>H<sub>8</sub>O), pyridine and butanol

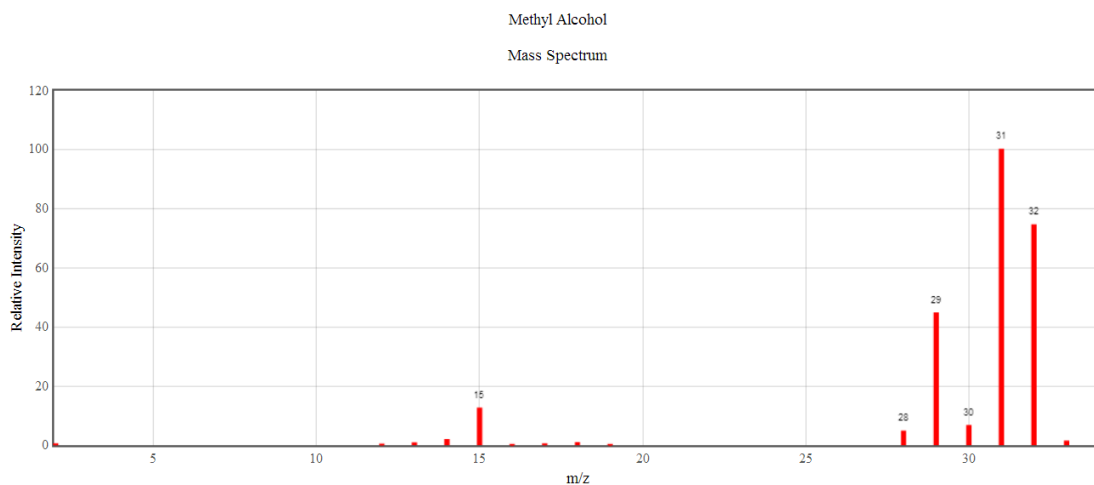


Figure D.12 Mass spectrum of methanol

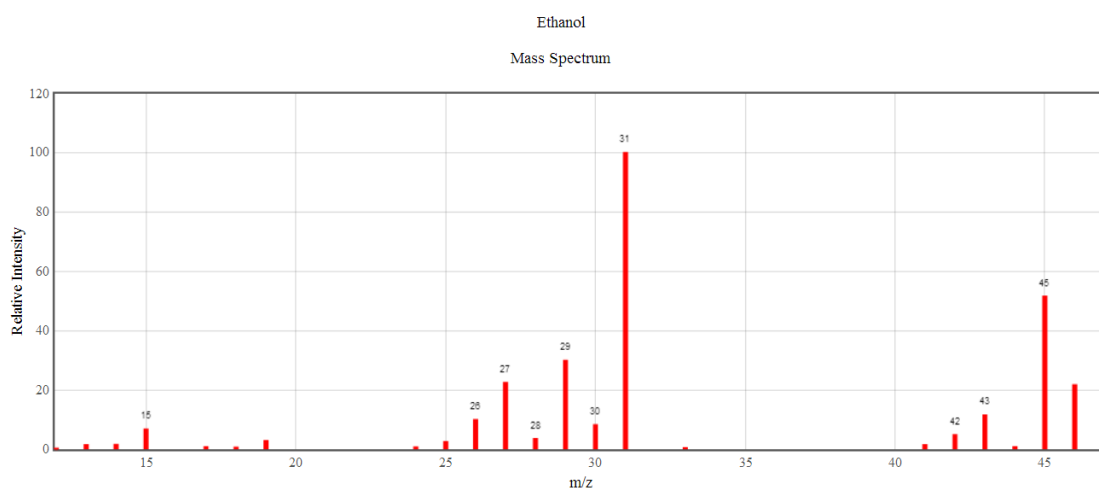


Figure D.13 Mass spectrum of ethanol (C<sub>2</sub>H<sub>6</sub>O)

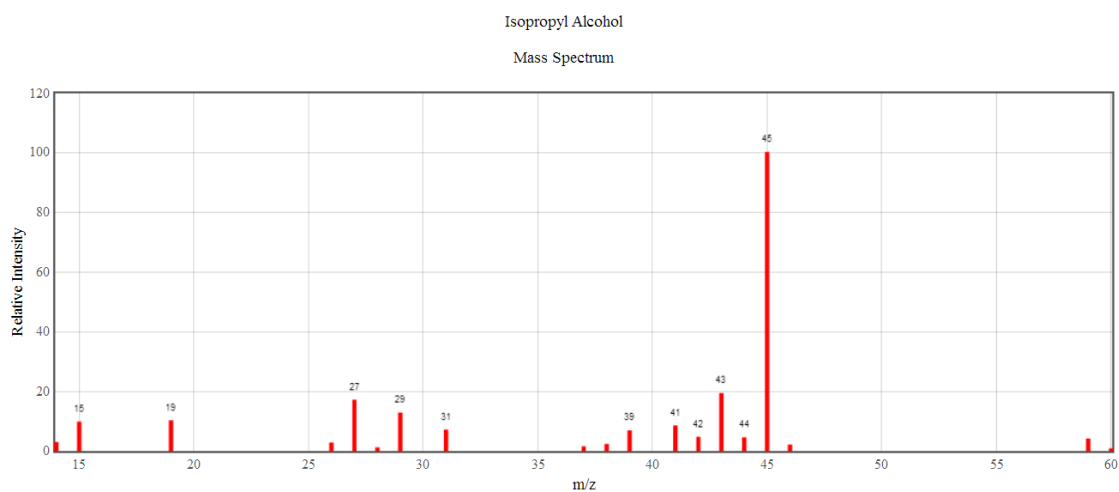


Figure D.13 Mass spectrum of isopropanol

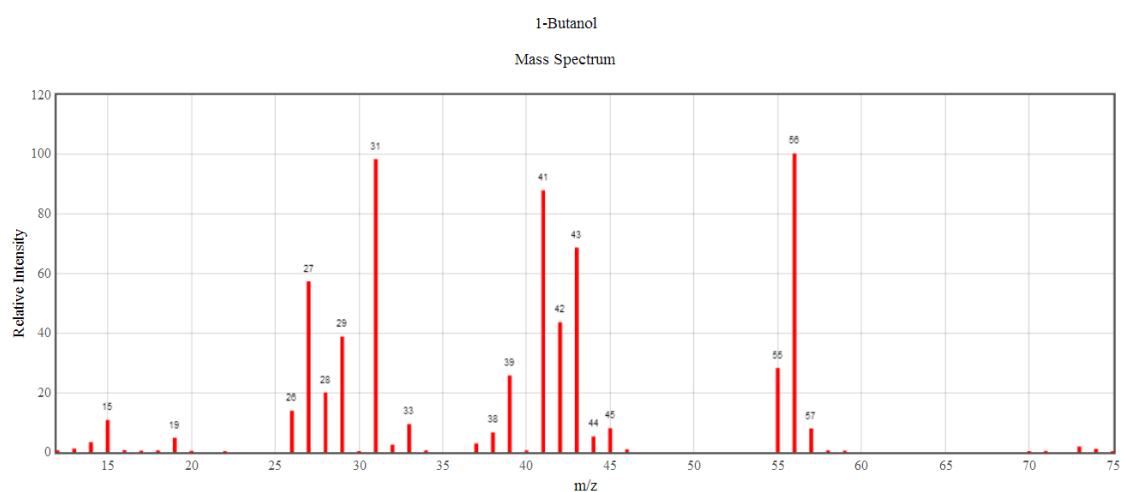


Figure D.14 Mass spectrum of butanol

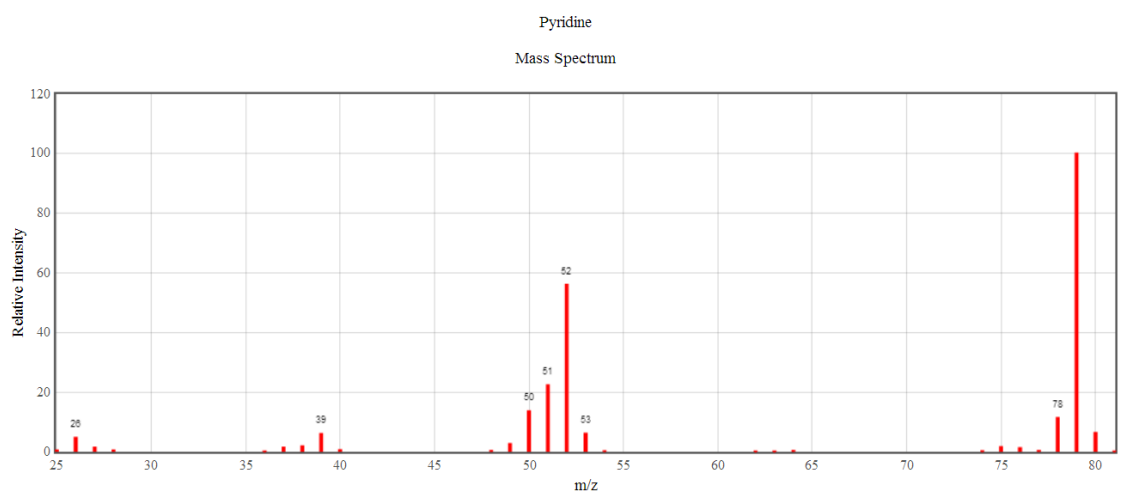
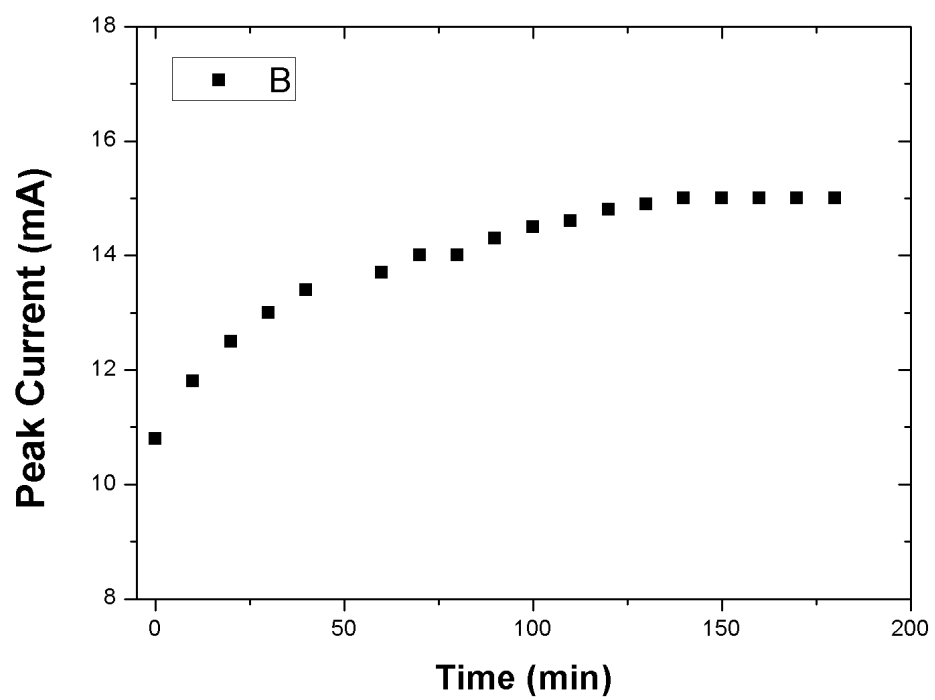


Figure D.15 Mass spectrum of pyridine



*Figure D.16 CO<sub>2</sub> saturation of aqueous electrolyte containing 10mM pyridine at 50bar*

## D.5 HS GC-MSD Method Development (samples specification/GC conditions)

Table D1 Head space method development

Sample Number	Thermal Gradient °C/Min	Pressure Psi	Initial Temp °C	Temp holding time /Min	Time Delay /Min	Syringe Type
300	20	3.5	40	0.5	0.5	Agilent
301	20	4.5	40	0.5	0.5	Agilent
302	20	4	40	0.5	0.5	Agilent
303	20	4	50	0.5	0.5	Agilent
304	20	4	50	0.5	0.5	Agilent
305	25	4	50	0.5	0.5	Agilent
306	20	3.5	40	1	1	Agilent
307	20	3	40	1	1	Agilent
308	20	2	40	1.5	1.5	Agilent
309	30	2	40	1	1	Agilent
310	30	2	40	1.5	1.5	Agilent
311	30	2	40	1.5	1.5	Agilent
312	40	2	40	1.5	1.5	Agilent
313	30	2.5	40	1.5	1.5	Agilent
314	30	4	50	1	1	Agilent
315	20	4	50	0.5	0.5	Agilent
316	20	4	50	0.5	0.5	Agilent
317	20	4	50	0.5	0.5	Agilent
318	20	2	50	1	1	Agilent
319	30	2	40	1.5	1.5	Agilent
320	30	2	40	1.5	1.5	Agilent
321	30	2	40	1.5	1.5	Agilent
322	30	2	40	1.5	1.5	Agilent
323	30	2	40	1.5	1.5	Agilent
324	30	2	40	1.5	1.5	Agilent
325	30	2	40	1.5	1.5	Hamilton
326	30	2	40	1.5	1.5	Hamilton



Best at pressure 4 psi



Best at pressure 2psi



Conditions to investigate